MULTIFACETED CARBON DOTS: THE NEXT GENERATION NANO- PLATFORM FOR OPTICAL AND BIOMEDICAL APPLICATIONS

Ph.D. Thesis

By

NAVPREET KAUR

DEPARTMENT OF BIOSCIENCES & BIOMEDICAL ENGINEERING

INDIAN INSTITUTE OF TECHNOLOGY INDORE

April 2022

MULTIFACETED CARBON DOTS: THE NEXT GENERATION NANO- PLATFORM FOR OPTICAL AND BIOMEDICAL APPLICATIONS

A THESIS

Submitted in partial fulfillment of the
requirements for the award of the degree
of

DOCTOR OF PHILOSOPHY

by

NAVPREET KAUR

DEPARTMENT OF BIOSCIENCES & BIOMEDICAL ENGINEERING
INDIAN INSTITUTE OF TECHNOLOGY INDORE
April 2022

INDIAN INSTITUTE OF TECHNOLOGY INDORE

I hereby certify that the work which is being presented in the thesis entitled **MULTIFACETED CARBON DOTS: THE NEXT GENERATION NANO- PLATFORM FOR OPTICAL AND BIOMEDICAL APPLICATIONS** in the partial fulfillment of the requirements for the award of the degree of **DOCTOR OF PHILOSOPHY** and submitted in the **DEPARTMENT OF BIOSCIENCES & BIOMEDICAL ENGINEERING, INDIAN INSTITUTE OF TECHNOLOGY INDORE**, is an authentic record of my own work carried out during the time period from OCTOBER 2016 to APRIL 2022 under the supervision of Dr. Shaikh M. Mobin, Associate Professor, Indian Institute of Technology Indore.

The matter presented in this thesis has not been submitted by me for the award of any other degree of this or any other institute.

Signature of the student with date
NAVPREET KAUR (08.04.2022)

This is to certify that the above statement made by the candidate is correct to the best of my knowledge.

Signature of Thesis Supervisor with date
Dr. SHAIKH. M. MOBIN (08.04.2022)

NAVPREET KAUR has successfully given her Ph.D. Oral Examination held on_____

27.07.2022
Signature of Thesis Supervisor with date
Dr. SHAIKH. M. MOBIN

ACKNOWLEDGEMENTS

I would like to acknowledge and extend my deepest gratitude for the suggestions, help, guidance, and continuous support offered by numerous people for completing this thesis in its current form.

At the outset, I would like to express gratitude to my advisor Dr. Shaikh M. Mobin, for believing in me and giving me this opportunity even after my carrier gap. I thank him for always leading from the front and being a pillar during academic and research activities, providing all necessary facilities, and his expertise, motivation, and tireless support for all these years. The Special mention goes to the freedom he offered to try new things and smoothly execute the research efforts. I sincerely appreciate his enormous efforts towards getting the work published in journals of international repute. It would be impossible to count all the ways he helped me in my career. I must thank him for being supportive in my personal life as well. He has been so caring and supportive during my pregnancy. I am always thankful to him for being so kind and understanding. He also helped me prepare for the transition of returning to work and made it a lot easier. I owe him a lot.

I sincerely express my gratitude to PSPC members Prof. Sampak Samanta and Dr. Sharad Gupta for closely monitoring my research progress and helping me with their suggestions and comments. I want to thank Mr. Mukesh Patidar, who gave me the initial guidance to enter the research world and inspired me to do a Ph.D.

I am thankful to the faculty and staff of the Department of Biosciences and Biomedical Engineering, IIT Indore, for their support during my research. I am hugely appreciative to the staff members of SIC, IIT Indore, Mr. Ravindra Kumar, Mr. Kinny Pandey, Mr. Ghanshyam Bhavasar, and Mr. Nitin Upadhyay for their help in performing the necessary characterization. I am also thankful to SAIF IIT Bombay, MRC-MNIT Jaipur, CeNSE IISc, and CIF IIT Gandhinagar for characterization facilities.

Special thanks to my group members and close friends, Dr. Pranav and Dr. Vinay, who supported me and guided me in every important aspect of my research. Pranav helped me immensely at all

stages of my Ph.D. with his valuable suggestions and problem-solving attitude. I am also thankful to my other group members Dr. Archana Chaudhary, Dr. Sandeep K. Singh, Dr. Prakash, Dr. Veenu Mishra, Dr. Anoop Gupta, Dr. Sanjay Verma, Dr. Akbar Mohammad, Dr. Anoop Saini, Dr. Ajeet Singh, Dr. Pratibha, Dr. Khursheed, Dr. Mohit, Dr. Kaushik, Ms. Richa, Dr. Shagufi, Dr. Topi, Mr. Pawan, Ms. Neha, Mr. Praveen, Mr. Rakesh. Ms. Nirmiti, Dr. Viresh, Mr. Zahir, Mr. Nisaar, and Mr. Keshav, for their generous support, affection, and cooperation in making my work successful. I want to give a special thanks to Ms. Chanchal for giving me joyful company and motivating me in each difficulty related to my personal and professional life.

Nothing can be successful without having a bunch of friends, so first of all, I would like to thank my best friend, Dr. Varinder, who is my inspiration in joining Ph.D. She always has my back through all thick and thin of my Ph.D. journey. I also want to thank Monika di, Arpana, Meha di, Komal, Manisha, Nishtha, Noopur, Aphipsa, and Anita. They were always behind me to support me and gave valuable suggestions throughout.

I want to express my sincere thanks to my loving family. I express my deep gratitude to my parents, Mrs. Sarabjit Kaur, Mr. Amarjit Singh, Mrs. Chitra Robert, and Mr. Samuel Robert, to whom I have dedicated my thesis, for the love and faith they kept in my dreams. No words can express my heartfelt gratitude to my loving sister Mrs. Harmanjit Kaur, my Inspiring brother-in-law Mr. Bharat Bhushan, my dear sister-in-law Ms. Deepti Robert, my sweet nephews Dhruv and Jashan, my brother Gurjit Singh and sister-in-law Rajbir Kaur for their sacrifices, endless love, unconditional support, and tireless encouragement. My special thanks to all my extended family members for their moral support and encouragement throughout this roller coaster ride of my Ph.D.

And last but not least, I would like to acknowledge the two most important persons in my life, my loving husband, Mr. Akash Robert, and my son Mr. Aanav Singh Robert. I would appreciate Akash for being there during my hard times in the journey of my Ph.D. His unconditional endless love and moral support always gave me the strength to do better. I would like to appreciate his selflessness and kindness for giving me wings to fly high and helping me fulfill all my

dreams without any restrictions and demands. I couldn't have completed my Ph.D. without the significant adjustments made by my little son, who struggled with me in the final stages of my Ph.D. journey. I was not always available for him, but the smile on his face in the evening when I returned home inspired me to get going. He deserves enormous appreciation as he has contributed significantly to getting my degree. I am sincerely thankful to God for the blessings he has bestowed upon me and for giving me the strength and wisdom to achieve my dream destination.

Words are short of expressing my deep sense of gratitude, but at the end of this journey, it is my great pleasure to thank them all who contributed in many ways to my success and made it an unforgettable experience for me.

Thank You!!!!!

(Navpreet Kaur)

DEDICATED TO MY
Family

TABLE OF CONTENTS

ABSTRACT

The investigations embodied in the thesis entitled "**MULTIFACETED CARBON DOTS: THE NEXT GENERATION NANO- PLATFORM FOR OPTICAL AND BIOMEDICAL APPLICATIONS"** were initiated in October 2016 in the Department of Biosciences & Bio-Medical Engineering, Indian Institute of Technology Indore.

This thesis aims to design and construct multifunctional carbon dots for biomedical and bio-sensing applications. The focal points of the thesis are as follows-

1. Sustainable carbon dots from green and chemical sources for explosive detection, chemical sensing, and pharmaceutical sense.
2. Modulation of fluorescence performance of carbon dots through functional group tuning for bioimaging and intracellular sensing.
3. Surface engineering of carbon dots for their diversified applications in environment safety, anticancer agent, photosensitizer, and microbial disinfection.
4. To develop carbon dots as efficient carriers for drug delivery in biological systems.

This thesis comprises six chapters. It begins with a general introduction to the topic and literature review (**Chapter 1**), followed by the use of green carbon dots for photo-triggered theranostics, selective and sensitive sensing of extracellular and intracellular iron (III), and multicolor live-cell imaging (**Chapter 2**), synthesis of photoactivatable carbon dots for picric acid detection and light-induced bacterial inactivation (**Chapter 3**), Synthesis of Fe-N@Carbon dots and Fe_3O_4-Carbon dot hybrid nanoparticles for doxycycline detection and degradation (**Chapter 4**) and to construct a sustainable fluorescent system for the delivery of 5-fluorouracil in vitro,

Co^{2+} ion detection, and cell imaging (**Chapter 5**). The thesis outlines the future perspective in (**Chapter 6**).

This thesis's introductory chapter (**Chapter 1**) illustrates the brief background and literature review of carbon dots synthesis and their surface modulation via doping. Furthermore, the bio-medical applications of carbon dots, including antibacterial activity, optical bio-sensing, bioimaging, and photodynamic therapy, are elaborated sufficiently in detail.

Fluorescent C-dots have drawn increasing attention due to their superior properties, such as high aqueous solubility, optical absorptivity, favorable biocompatibility, and appreciable photoluminescence. Nature offers various precursors for synthesizing green C-dots like fruits, vegetables, flowers, animal derivatives, etc. **Chapter 2** described the synthesis of nitrogen-doped C-dots (**N@VRCD**) by an economical, one-step hydrothermal method using "Vigna radiata" sprouts as the sole carbon precursor and ethylenediamine as the sole carbon precursor of the nitrogen source, which was optimized for enhanced optical properties. The **N@VRCD** shows the highest known quantum yield (~58%) using green precursor for synthesis. Importantly, **N@VRCD** also exhibits significant light-induced phototoxicity to cancerous cells, enabling the possibility of using it as a potential theranostics agent. Further, the **N@VRCD** displays highly sensitive and selective sensing behavior towards Fe^{3+} ions by fluorescence "turn-off" with a detection limit as low as 140 nM. Moreover, **N@VRCD** shows biocompatible and hemocompatible nature with the potential for multicolor live-cell imaging and intracellular Fe^{3+} detection, validated by confocal microscopy and flow cytometry.

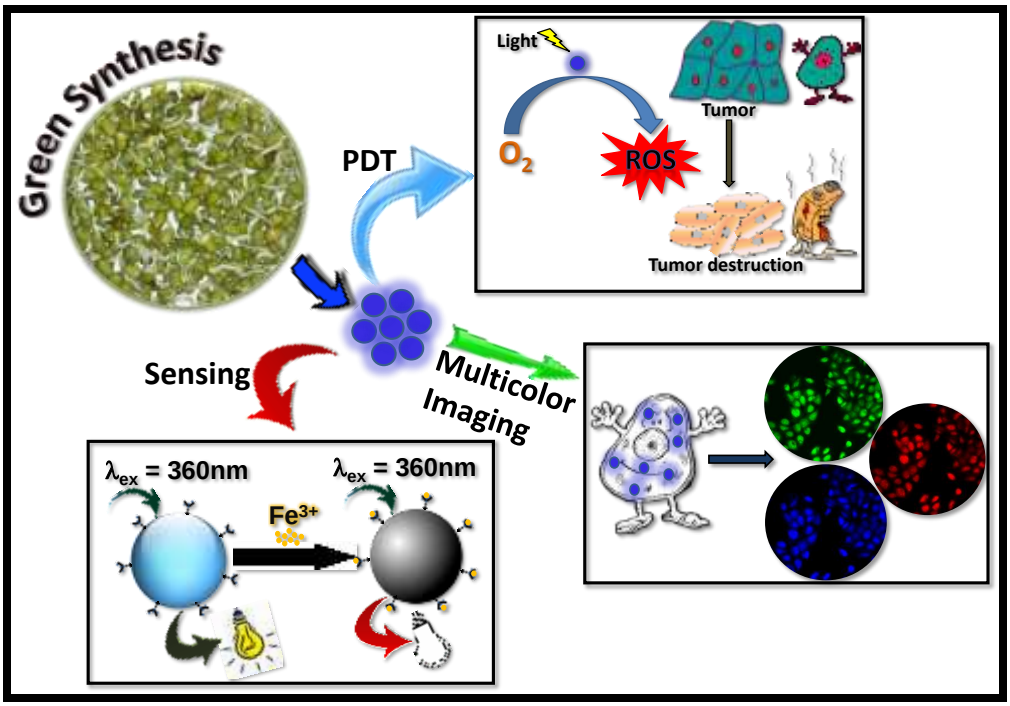

Scheme 1. Representation of green CDs for optical sensing, multicolor bioimaging, and its use as a photosensitizer for PDT

The zero-dimensional carbon nanostructure known as carbon dots showed attractive attributes such as multicolor emission, very high quantum yield, up-conversion, excellent aqueous solubility, eco-friendliness, and excellent biocompatibility. These outstanding features of the carbon dots have raised significant interest among the research community worldwide. **Chapter 3** highlights the synthesis of a metal-doped carbon dot to combat the challenges of faster and easy detection of picric acid and microbial disinfection. Water-soluble nitrogen, silver, and gold co-doped bimetallic carbon dots (**BCDs**) were prepared using the one-pot hydrothermal method with citric acid as a sole carbon source. **BCDs** showed size in the 4-8 nm range and excitation-independent emission behavior, with maximum emission observed at 427 nm. Additionally, these **BCDs** showed a very high quantum yield value of 50% and a fluorescence lifetime value of 10.1 ns. Interestingly, prepared **BCDs** selectively sense picric acid (PA) by exhibiting "selective fluorescence turn-off" behavior in the presence of PA

with a limit of detection value (LOD) of 46 nM. Further, prepared **BCDs** were explored for photodynamic therapy to inactivate bacterial growth in the presence of light (400-700 nm) by generating singlet oxygen. Thus, prepared **BCDs** offer many potentials to use a nanoprobe to detect picric acid in an aqueous medium and design next-generation antibacterial materials.

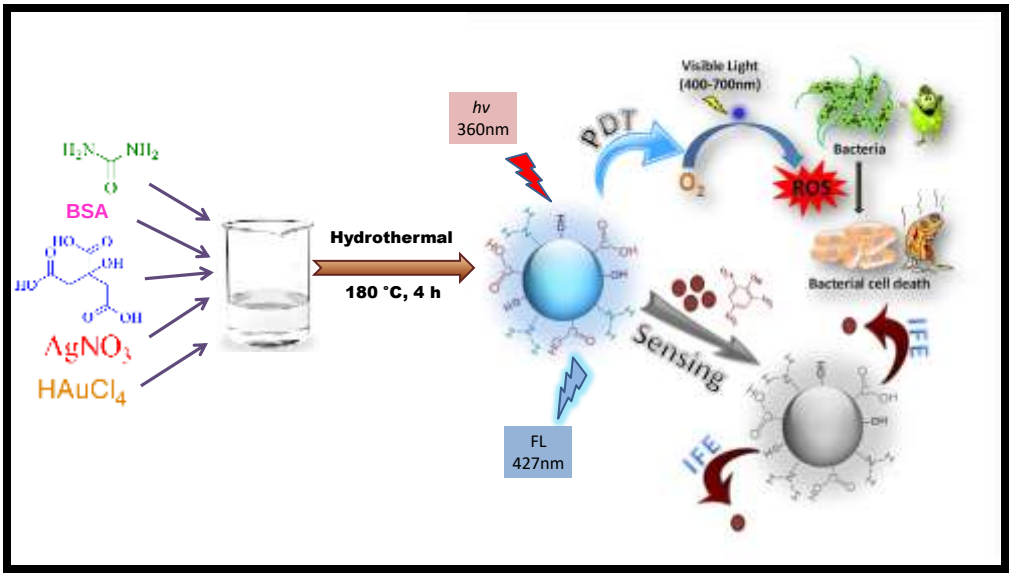

Scheme 2. Fluorescent system for detecting picric acid in an aqueous medium and its ROS mediated antibacterial activity.

The overuse of antibiotics in recent years presents a huge challenge to society for their removal from the environment. The prolonged presence of antibiotics as environmental pollutants results in the emergence of drug-resistant bacteria faster than new antibiotics to treat diseases they cause. Therefore, a rapid, sensitive, and cost-effective method is urgently required to detect and degrade. Given this, **Chapter 4** demonstrates a novel strategy for synthesizing Fe-doped carbon dots (**Fe-N@CDs**) and iron oxide-carbon dot hybrid nanoparticles (**Fe_3O_4-CDs**) in a single step for doxycycline detection and its degradation. For the very first time, the formation of two simultaneous products, i.e., **Fe-N@CDs** (0 D fluorescent carbon dots) and **Fe_3O_4-CDs** (magnetic nanoparticles) in a single step hydrothermal carbonization process by using sole iron salt ($FeCl_2$) and carbon precursor

(citric acid) in the presence of ethylenediamine is reported. As prepared, **Fe-N@CDs** selectively detect doxycycline with a limit of the detection value of 66 ng mL^{-1} and in the linear range from 0 mg mL^{-1} to 50 mg mL^{-1}, whereas other formed products, i.e., **Fe_3O_4-CDs** degrades doxycycline by 70.26 % in just 5 min by applying sheer force using simply a kitchen blender. The results demonstrated the suitability and application scope in food and environment safety.

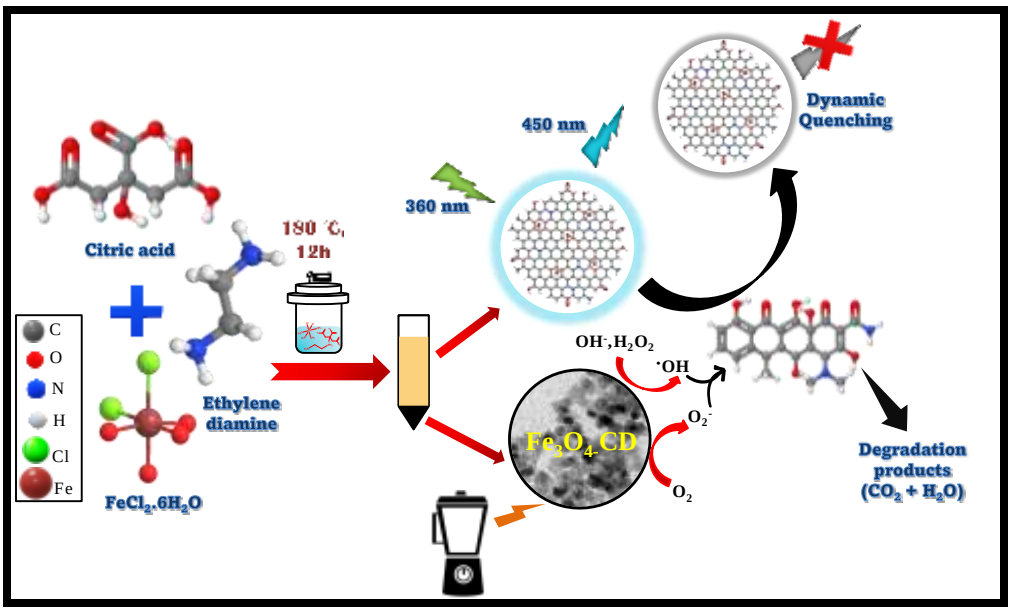

Scheme 3. Fe-doped carbon dots (**Fe-N@CDs**) and iron oxide-carbon dot hybrid nanoparticles (**Fe_3O_4-CDs**) for doxycycline detection and degradation.

In nanomedicine, the synthesis of intelligent hybrid material to assimilate diagnosis and treatment is crucial. **Chapter 5** presents a simple and facile method to synthesize multitalented blue emissive carbon dots using trimesic acid and polyethylene glycol as carbon precursors and ethylenediamine for nitrogen doping. The as-prepared carbon dots show various fascinating properties. The synthesized carbon dots are used as a selective drug carrier for 5FU to form **5FU-N@PEGCDs**, showing enhanced release at acidic pH. The mode of action of nanoconjugate has also been explored by performing

wound healing assay, DCFDA assay for ROS generation, and Hoechst staining. The drug conjugated with carbon dots showed less toxicity to normal cells compared to cancer cells making it a perfect candidate to be studied for designing a next-generation drug delivery carrier. The synthesized **N@PEGCDs** were further employed for assaying cobalt with LOD as low as 6 nM. Moreover, the biocompatible nature of **N@PEGCDs** makes it a more sensitive imaging probe than dyes.

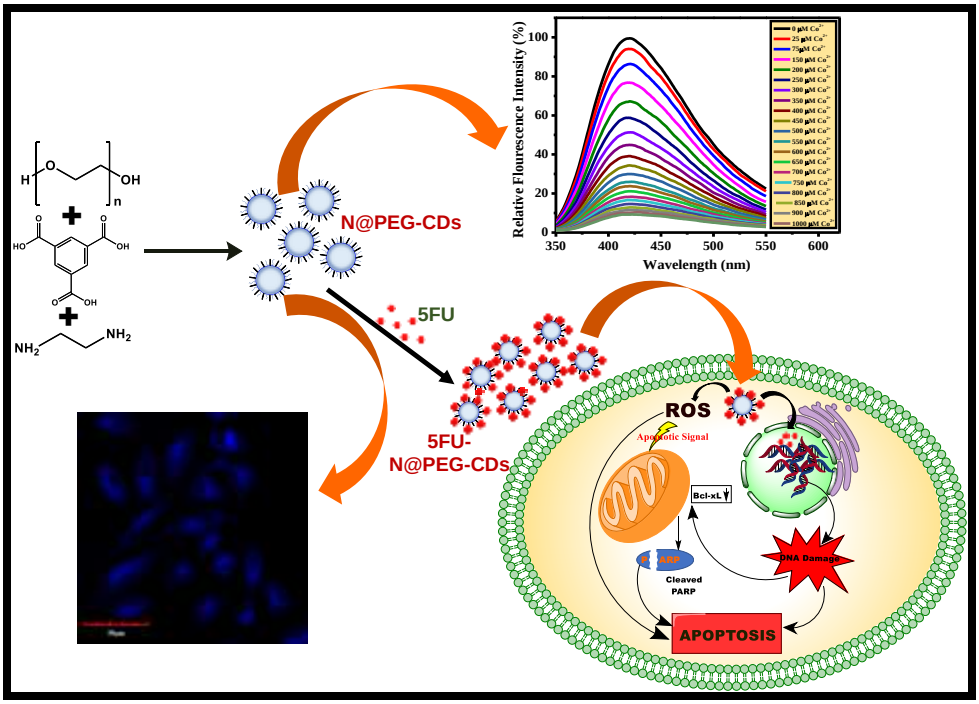

Scheme 4. Biocompatible CDs for sensing, bioimaging, and drug delivery.

Chapter 6 outlines the future perspective of this work.

LIST OF PUBLICATIONS

1. **Kaur, N**., Sharma, V., Tiwari, P., Saini, A.K., Mobin S.M. (2019), "*Vigna radiata*" based green C-dots: Photo-triggered theranostics, a fluorescent sensor for extracellular and intracellular iron (III) and multicolor live-cell imaging probe, Sens Actuators B Chem., 291, 275-286 (DOI: 10.1016/j.snb.2019.04.039)
2. **Kaur, N**., Tiwari, P., Mate, N., Sharma, V. Mobin S.M. (2022), Photoactivatable carbon dots as a label-free fluorescent probe for picric acid detection and for light-induced bacterial inactivation, J. Photochem. Photobiol. B, 229, 112412 (DOI: 10.1016/j.jphotobiol.2022.112412)
3. **Kaur, N**., Tiwari, P., Kapoor, K. S., Saini, A. K., Sharma, V., Mobin S.M. (2020), Metal-Organic Framework based Antibiotic Release and Antimicrobial Response: An Overview, CrystEnggCommun., 22, 7513-7527 (DOI: 10.1039/D0CE01215G)
4. **Kaur, N**., Tiwari, P., Abbas, Z., Mobin S.M. (2022) Doxycycline detection and degradation in aqueous media via simultaneous synthesis of Fe-N@Carbon dots and Fe_3O_4-Carbon dot hybrid nanoparticles: one arrow two hawk approach, J. Mater. Chem. B, 10, 5251-5262 (DOI: 10.1039/D2TB00475E)
5. Sharma, V$^{\#}$., Tiwari, P$^{\#}$., **Kaur, N**$^{\#}$. and Mobin S.M. (2021), Optical nanosensors based on fluorescent carbon dots for the detection of water contaminants: a review, Environ. Chem. Lett., 19, 3229–3241 (# equal contribution) (DOI: 10.1007/s10311-021-01241-8)
6. **Kaur, N.**, Tiwari, P., Kumar, P., Mobin S.M. A sustainable fluorescent system for the delivery of 5-fluorouracil in vitro, Co^{2+} ion detection, and cell imaging. (Communicated)
7. Sharma, V., **Kaur, N.**, Tiwari, P., Saini, A.K. Mobin S.M. (2018), Multifunctional fluorescent "Off-On-Off" nanosensor for Au^{3+} and S^{2-} by N-S co-doped carbon-dots, Carbon, 139,393-403 (DOI: 10.1016/j.carbon.2018.07.004)
8. Sharma, V., **Kaur, N.**, Tiwari, P. Mobin S.M. (2018), Full color emitting fluorescent carbon material as reversible pH sensor with multicolor live cell imaging, J. Photochem. Photobiol. B, 182, 137-145 (DOI: 10.1016/j.jphotobiol.2018.04.006)
9. Tiwari, P., **Kaur, N.**, Sharma, V., Mobin S.M. (2018), High yield graphene production arising from the synergistic effect of inflated temperature and gelatin offers higher stability and cellular compatibility,

Phys. Chem. Chem. Phys, 20, 20096-20107 (DOI: 10.1039/C8CP02263A)

10. Tiwari, P., **Kaur, N.**, Sharma, V., Kang, H., Uddin, J., Mobin S.M. (2019), Cannabis sativa-derived carbon dots co-doped with N–S: highly efficient nanosensors for temperature and vitamin B12, New J. Chem., 43, 17058-17068 (DOI: 10.1039/C9NJ04061G)
11. Tiwari, P., Sharma, V., **Kaur N.**, Ahmad K., Mobin S.M. (2019), Sustainable Graphene Production: New Insights into Cannabis sativa Engineered Carbon Dots Based Exfoliating Agent for Facile Production of Graphene, ACS Sustainable Chem., 07, 11500-11510 (DOI: 10.1021/acssuschemeng.9b01353)
12. Tiwari, P., **Kaur, N.**, Sharma, V Mobin S.M. (2020), A spectroscopic investigation of Carbon dots and its reduced state towards fluorescence performance, J. Photochem. Photobiol. A, 403,112847 (DOI: 10.1016/j.jphotochem.2020.112847)
13. Kumar, P., Kumar, V., **Kaur, N.**, Mobin S.M., Kaur. P., Singh. K. (2022), A fluorene-based probe: Synthesis and "turn-on" water sensitivity of the in-situ formed Cu^{2+} complex: Application in bio-imaging, Analytica Chimica Acta, 1189, 339211 (DOI: 10.1016/j.aca.2021.339211)
14. Kumar, V., Sony, S., **Kaur, N.**, Mobin S.M., Kaur, P., Singh, K., (2022), Thiazolothiazole based donor-π-acceptor fluorophore: Protonation/deprotonation triggered molecular switch, sensing and bio-imaging applications, Analytica Chimica Acta, 1206, 339776 (DOI: 10.1016/j.aca.2022.339776)
15. Parth., **Kaur, N.,** Korkor, C., Mobin S.M., Chibale, K., Singh, K., Fluorene-Chloroquine Hybrids: Synthesis, in vitro Antiplasmodial Activity, and Inhibition of Heme detoxification machinery of Plasmodium falciparum (Communicated)

Conferences/Workshop attended and oral/poster presentation.

1. **Oral Presentation** at International Symposium on Functional Materials (ISFM-2018): Energy and Biomedical Applications on "Synthesis of N-doped Carbon Dots with High Quantum Yield using *Vigna radiata* Sprouts for Effective Fluorescent Sensing of Iron (III) and Live Cell Imaging" held during April 13–15, 2018 at Chandigarh, India by Indian Institute of Technology Kanpur.
2. **Oral Presentation** at Two Days National Webinar "Recent Trends in Chemistry at the Interface with Biology" on "Photoactivatable C-Dots for bacterial killing and label-free fluorescent probe for picric acid-sensing" held during Aug 30-31, 2020 at Bagnan College, Howrah, in collaboration with IQAC, Bagnan College.
3. **Oral Presentation at** 7th International Conference on Advanced Nanomaterials and Nanotechnology (ICANN2021) held during Dec.14-17, 2021, at Indian Institute of Technology Guwahati.
4. **Poster Presentation** at 4th National Workshop "NEMS/MEMS and Theranostic Devices" on "Synthesis of N-doped Carbon Dots with High Quantum Yield using *Vigna radiata* Sprouts for Effective Fluorescent Sensing of Iron (III) and Live Cell Imaging" held during Feb. 26-28, 2018, at Indian Institute of Technology Guwahati. (**BEST POSTER AWARD**)
5. **Poster Presentation** at Madhya Pradesh Vigyan Sammelan & Expo (MPVS-2021) on "Multifunctional fluorescent green carbon–dots for Sensing, Bioimaging, Exfoliation and Theranostics" held during Dec. 22-25, 2021, jointly organized by IIT Indore, MPCST, and Vigyan Bharati at Indore, India. (**BEST POSTER AWARD)**
6. **Poster Presentation** at "2019 #RSCPoster Twitter Conference" held online on March 5, 2019.
7. **Poster Presentation** at RSC-IIT Indore symposium on Advances in chemical sciences held on January 30, 2018, at Indian Institute of Technology Indore, India.
8. **Poster Presentation** in Indo-UK Virtual Conference on "Current Innovations and the Future of Therapeutic Developments (CIFTD-2020)" held during June 1-3, 2020. (**BEST E-POSTER AWARD)**
9. **Poster Presentation** in International Conference on "Emerging Areas in Biosciences and Biomedical Technologies-2 (eBBT-2)", held during February 7-9, 2020, at IIT Indore, India.

10. **Participated** in GIAN course on "Human infectious disease and animal models" held during July 05-15, 2017, conducted by Dr. Siddappa Byrareddy, University of Nebraska Medical Center, USA at IIT Indore.
11. **Participated** in GIAN course on "Inorganic chemistry of imaging: Magnetic resonance and optical imaging with coordination complexes" held during January 08 - 12, 2018, conducted by Prof. Janet R. Morrow, University at Buffalo, USA at IIT Indore.

LIST OF ABBREVIATIONS

ICP–OES	Inductively coupled plasma- optical emission spectrometry
ICP-MS	Inductively coupled plasma-mass spectrometry
SEM	Scanning electron microscope
TEM	Transmission electron microscope
EDAX	Energy Dispersive X-Ray Analysis
PXRD	Powder X-ray diffraction
FT-IR	Fourier transform - Infrared spectroscopy
XPS	X-ray photoelectron spectroscopy
UV	Ultraviolet
TCS-PC	Time-correlated single-photon counting
VSM	Vibrating-sample magnetometer
DMSO	Dimethyl sulfoxide
DCM	Dichloromethane
LOD	limit of detection
RT	Room temperature
DNA	Deoxyribonucleic acid
EDTA	Ethylenediaminetetraacetic acid
MTT	3-(4,5-dimethylthiazol-2-yl)-2,5-diphenyltetrazolium bromide

DPBF	1, 3-diphenylisobenzofuran
DCF-DA	2', 7'- dichlorofluorescein diacetate
MCF–7	Breast cancer cell line
A375	Skin melanoma cell line
HeLa	Cervical cancer cell line
HEK	Human Embryonic Kidney cell line
c-dot	Carbon-dots
N@VRCDs	Nitrogen-doped *Vigna radiata* derived carbon dots
VRCDs	*Vigna radiata* derived carbon dots
BCDs	Bimetallic doped carbon dots
Fe-N@CDs	Iron and Nitrogen-doped carbon dots
Fe_3O_4-CDs	Iron oxide carbon dots composite
N@PEGCDs	Nitrogen-doped PEG derived carbon dots
5-FU-N@PEGCDs	5FU loaded N@PEGCDs
PET	Photoinduced electron transfer
IFE	Inner Filter Effect
FRET	Fluorescence Resonance Energy Transfer
HOMO	Highest Occupied Molecular Orbital
LUMO	Lowest Unoccupied Molecular Orbital
DFT	Density-functional theory

IC_{50}	Half maximal inhibitory concentration
FITC	Fluorescein isothiocyanate
5FU	5 Fluorouracil
PEG	Polyethylene glycol
TA	Terephthalic Acid
MEM	Minimum essential medium
PBS	Phosphate-buffered saline
ppm	Parts per million
WHO	World Health Organization
BSA	Bovine serum albumin
HSA	Human serum albumin
RBC	Red blood cells
K_{sv}	Quenching constant
QY	Quantum yield
MIC	Minimum inhibition concentration
MBC	Minimum bactericidal concentration
ROS	reactive oxygen species
PDT	Photo-Dynamic therapy
PS	Photo-sensitizer
PARP	Poly (ADP-ribose) polymerase

E. coli	*Escherichia coli*
(°)	degree
Å	Angstrom
nm	Nanometer
nM	Nanomolar
π	pi
θ	theta

LIST OF SCHEMES

LIST OF FIGURES

LIST OF TABLES

LIST OF ANNEXURES

CHAPTER 1

Introduction

The knowledge of the omnipresence of naturally existing nanoparticles for billions of years and their use in various ways by humans for thousands of years has made the field of nanotechnology exciting [1]. A legendary physicist Richard Feynman predicted the future of nanotechnology in his talk “There is plenty of room at the bottom” in 1959. He indicated what needed to be done and how it might be done before anyone would have seen an atom with a microscope. His talk became a roadmap for nanotechnology. He looked into the future and predicted how technology might make things smaller, even the size of an atom.

The European Commission defines a ‘nanomaterial’ as any indigenous or engineered material that exhibits one or more external dimensions in the size range of 1 nanometer (nm) to 100 nm. The precisely controlled sizes, shapes, and compositions of these engineered nanoscale architectures result in differences in properties compared to their bulk correlative.

There has been a massive swirling of research techniques to build application-oriented nanomaterials for over a decade to improve the quality of life and change the way we live. The exciting properties of c-dots such as strong absorption, excellent photoluminescence, superior light stability, resistance to photobleaching, low toxicity, environment-friendliness, enhanced biocompatibility, easy preparation, intriguing physio-chemical properties have brought them to the forefront of various applications ranging from supercapacitors, optoelectronics, sensors, catalysis, agriculture, aerospace, environment and even in the bio-medical field. The biomedical application of c-dots is extended to antibacterial, anticancer, photothermal therapy (PDT), targeted drug delivery, cellular imaging, diagnosis, bio-sensing, and intracellular monitoring.

1.1. Carbon dots

The small-sized carbon nanoparticles (c-dots) have emerged as glowing members of the carbon family with sizes less than 10 nm. These have excellent optical features such as elevated quantum yield, wavelength modulated emission, and capability to up-convert. Their ability to exhibit fluorescence has assisted them in becoming the swiftly growing and favorite material in the carbon family lately. After the accidental discovery of these fluorescent carbon nanoparticles by Xu *et al*. [2] in 2004, Sun *et al.* [3] synthesized and named them c-dots or carbon quantum dots (CQDs) in 2006.

The optical properties of c-dots differ remarkably based on starting material used for their synthesis. The precursor could vary from chemical molecules to natural organic carbon sources [4]. The optical properties of these nano lights could be tuned easily via surface passivation. Various elements have been used as dopants like nitrogen, phosphorus, sulfur, magnesium, and even metals like Zn, Au, Ag, and Fe.

1.2. Synthesis of carbon-dots

The dependence of various properties of c-dots on their synthesis method leads to the utilization of many new synthesis strategies. Laser ablation, arc-discharge, ultrasonication, chemical and electrochemical oxidation, etc., are used as a top-down method of c-dots synthesis. Whereas plasma treatment, hydrothermal carbonization, microwave pyrolysis, thermal decomposition, and template-based synthesis form another group as bottom-up synthesis strategies. A summarized representation of the synthetic approach is shown in **Figure 1.1.**

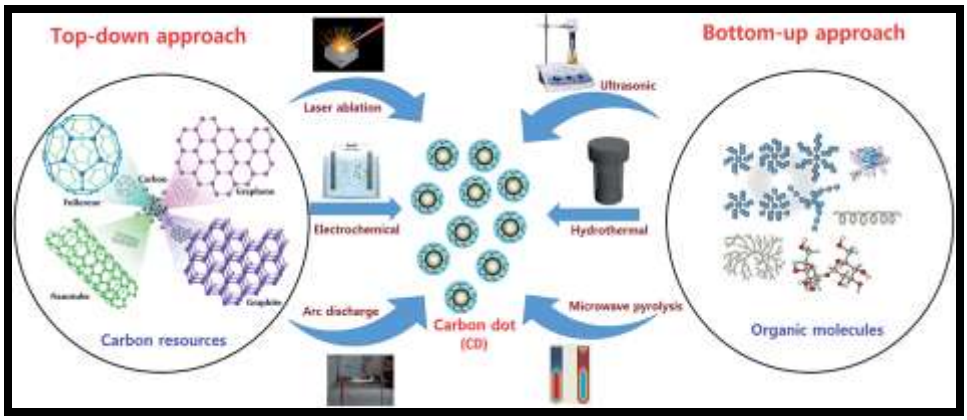

Figure 1.1. Schematic representation of top-down and bottom-up methods of carbon dot preparation. [5]

A variety of precursors were investigated for the synthesis of c-dots. A significant number of chemical and green precursors are utilized for c-dots synthesis. Interestingly, the precursor, dopant, temperature, and synthesis method substantially influence the characteristics of c-dots.

The synthesis modes are categorized as chemical or green methods depending on the type of carbon precursor used.

1.2.1. Chemical Synthesis

Citric acid, urea, thiourea, benzene, ammonium citrate, ethylene glycol, phenylenediamine, phytic acid, EDTA, etc., are shared among the various chemical precursors used to synthesize c-dots so far. C-dots with QY of ~30% were prepared by Zhai *et al.* [6] utilizing citric acid through the microwave pyrolysis method. The carboxylic group assists in the dehydration and carbonization of the precursor citric acid. The c-dots are surface passivated using amines. In another study by Yang *et al.* [7], ammonium citrate was utilized for carbon-rich dots synthesis by following hydrothermal carbonization at 160 °C. The product formed is purified via a silica gel column where methanol and di-chloromethane are used as eluent, and the QY of the purified product was 13.5%.

EDTA was carbonized by Zhou *et al.* [8] at 400 °C. The QY of so-formed c-dots was 11%. The c-dots prepared by Wang *et al.* [9] using phytic acid as a carbon source were surface passivated through microwave treatment at 700 W, found to be rich in phosphorous; the purified c-dots extract using organic solvents like methanol, tetrahydrofuran, ethanol, and acetonitrile showed QY in the range of 11.1% to 19.5%.

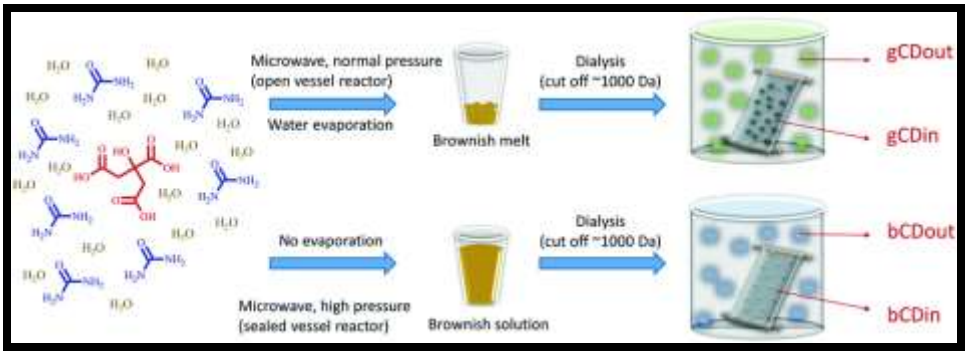

Figure 1.2. Schematic synthesis of c-dots. The microwave pyrolysis of citric acid and urea results in c-dot synthesis. The dialysis helps in cutting off different molecular weight fragments. A closed and an open vessel condition results in a blue carbon dot (bCD) and a green carbon dot (gCD). [10]

1.2.2. Green Synthesis

The easy availability of carbon-rich sources naturally leads researchers to use them as a precursor for synthesizing c-dots. It doesn't take much time to use green sources profusely to synthesize green c-dots [4]. Coffee grounds and grass [11, 12] were the first sources to synthesize green c-dots.

The self-passivation is an attractive advantage of green c-dots over others, leading to the formation of auto-doped c-dots. Self-passivated c-dots rich in nitrogen with QY 6-8% were synthesized by Wang *et al.* [13] through a one-step hydrothermal synthesis strategy using chicken egg as a carbon source. The hydrophilic nitrogen-doped c-dots with a good quantum yield

of 23% had been synthesized by Atchudan *et al.* [14], and Arul *et al.* had made exciting use of *Actinidia deliciosa* for the synthesis of c-dots with good biocompatibility and low cytotoxicity [15] shown in **Figure 1.3.**

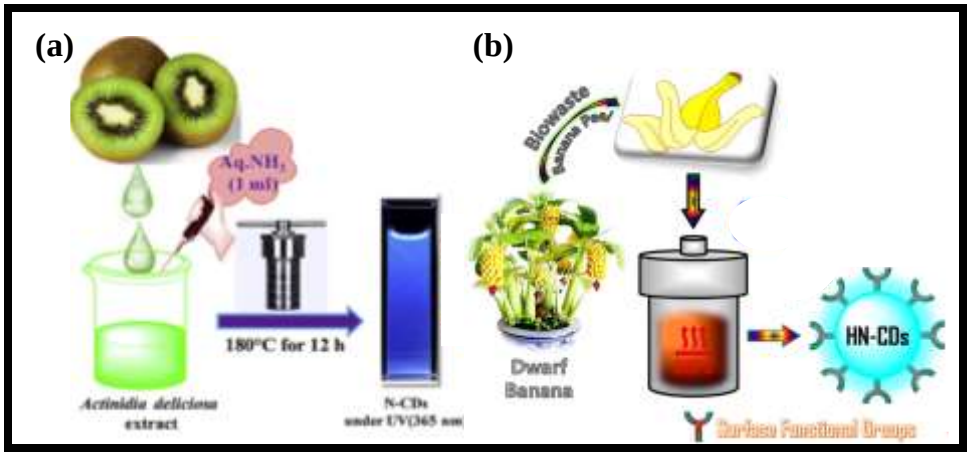

Figure 1.3. (a) Hydrothermal preparation of c-dots using *Actinidia deliciosa.* [15] (b) Preparation of hydrophilic nitrogen-doped c-dots from biowaste using dwarf banana peel. [14]

Various other consumable sources such as orange, papaya, grapes, mango, apple, strawberry, lychee, watermelon, sugarcane, banana, yam, carrot, potato, onion, kitchen waste, coffee, beer, milk, tea, etc. [16–35] were investigated for c-dots synthesis. Other non-consumable resources, including human hair and urine, feathers, Bombyx mori silk, silkworm chrysalis, pigskin, crab shell, etc. [36–42], were also used as carbon precursors to synthesize green c-dots. The massive increase in the use of the green source for the synthesis of c-dots has started a new era of c-dots, and so far, a variety of green sources have been explored, as shown in **Figure 1.4.**

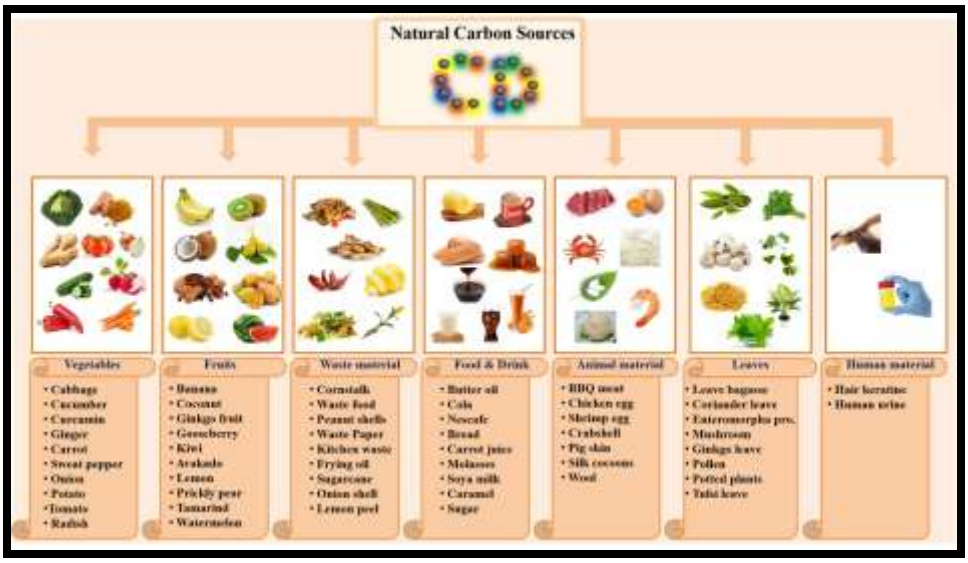

Figure 1.4. Illustration of some green sources used to develop green c-dots. [43]

1.3. Properties of Carbon-dots

The source of carbon used for c-dots synthesis greatly influences its properties because of the ingrained amalgamation of carbon, functional groups, and hetero-atom dopants [44]. "Carbonization or pyrolysis" of carbon precursor is a regularly used method for c-dots synthesis. Condensation, polymerization, carbonization, and passivation are the steps involved in the synthesis process of c-dots [45]. The structural and optical properties of the c-dots so formed are discussed in the following section.

1.3.1. Structural properties

Powder x-ray diffraction (PXRD) and high-resolution transmission electron microscopy (HR-TEM) are two top techniques used to characterize c-dots. These two techniques mainly revealed the amorphous or occasionally crystalline structure of c-dots, with an average size of around 10 nm. The usual amorphous nature of c-dots was confirmed by a broad hump in $2\theta = 20^{o}$-25^{o} arises in PXRD [39]. The most common morphology displayed in electron microscopy is spherical. However, sometimes lattice fringes were visualized at very high magnification in a

few c-dots. A very small-sized 2-9 nm c-dots were obtained using cellulose waste paper by Jeong *et al.* [46]. The "d" value of 0.24 nm obtained using lattice fringes corresponds to the (100) graphitic plane. The high crystallinity was confirmed via a ring-selected area electron diffraction pattern (SAED). The two broader peaks of Raman spectra of c-dots, one at "1300 cm^{-1}" due to deformed "D" band appeared because of a structural defect or doping agent and the other at "1580 cm^{-1}" consisting of "G" band which became apparent due to ordered sp2 hybridized carbon atoms, were obtained most commonly [47]. Structurally the c-dots primarily consist of C, H, and O elements N, S, P, etc. are the most common dopants used so far. X-ray photoelectron spectroscopy (XRD) and Fourier transform infrared (FTIR) spectroscopy are specialized techniques for surface functionality studies of c-dots which assist in calculating the elemental percentage and determining various surface functional groups present [4].

1.3.2. Optical Properties

The c-dots are known to show exciting optical behavior leading to greater interest in them. n-π*and π-π* is the most common transition shown by the absorption spectra of c-dots, sp^2 hybridized carbon core, and the functional groups with lone pairs [48]. The absorption peak of UV-vis spectra at the lower wavelength (230-280 nm) is assigned to the π-π* transition (C=C) bond; however, the peak at a higher wavelength (300-320 nm) appears due n-π* transition (C=O) bond [49, 50]. Another exciting property of c-dots arises due to several mechanisms like the degree of surface oxidation [51, 52], quantum confinement [53, 54], and molecular fluorescence [55].

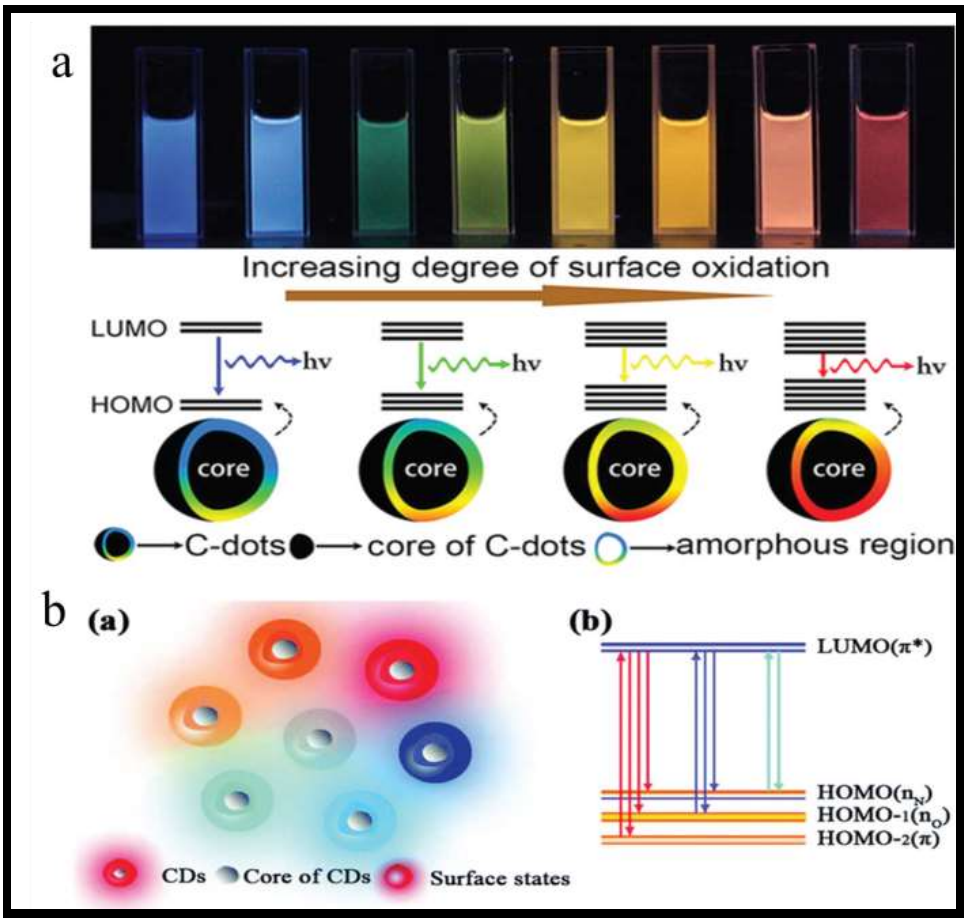

Figure 1.5. The optical transitions in c-dots. (a) Fluorescence origination from the degree of surface oxidation (b) Structure and electronic transition diagram of c-dots. [45]

As the surface oxidation increases, the emission spectra also span over a broad range [56], the reason for which could be reduced bandgap on the surface of c-dots results in a redshift, as shown in **Figure 1.5.** Similar multi-color fluorescent emitting tunable c-dots, which were nitrogen-doped, were reported by Zhang *et al.* [57]. The detailed studies revealed the mechanism behind this phenomenon is the formation of new energy levels due to doping. Kim *et al.* [53] prepared c-dots of various sizes (5-35 nm) comprising different morphologies manifesting size-dependent absorption and fluorescence spectra. The study reveals that the emission spectra showed a redshift as the size increased. Concurrently, few studies

provide evidence to support the synergistic effect of quantum confinement and the surface state towards fluorescence of c-dots.

The multiphoton activation process leads to fluorescence up-conversion of c-dots in which the absorption of two or more photons leads to emission at a shorter wavelength. This captivating feature of c-dots makes them a promising and forthcoming candidate in sensing and biomedical applications, especially in biomedical imaging and biosensing [48].

1.4. Application of carbon dots in optical sensing

A large number of c-dots-based sensors have been reported for sensing various analytes. Detecting hazardous materials, molecules of biological importance, toxic wastes, pharmaceuticals, etc., is of utmost importance. Many poisonous or dangerous compounds like dyes, nitro explosives, and organic molecules have been used extensively in our day-to-day lives in many ways and products, namely textile, food, cosmetics, plastic, security, and agriculture. Recently, c-dots have been a milestone in optical sensing due to their exceptional physical and chemical properties. Their favorable optical properties have made these c-dots as preferred sensing agent for various analytes. The facile synthesis, excellent quantum yield, small size but a large surface area, enhanced biocompatibility, water-solubility, resistance to photobleaching, and surface passivation are few of the qualities which make c-dots a unique candidate to be used in sensors. The wide application of c-dots based sensors in the real world is due to their water-soluble nature, which helps them get utilized for sensing in an aqueous system. The selectivity, specificity, sensitivity, and recovery in real water samples are up to par.

The large number of functional groups present on the surface of c-dots react selectively and specifically with different analytes, resulting in a change in their optical properties as either turn-on (fluorescence enhancement) or turn-off (fluorescence quenching). The phenomenon

behind this change in optical behavior could be electron transfer (ET), Forster resonance energy transfer (FRET), inner filter effect (IFE), aggregation-induced emission (AIE), aggregation-induced quenching (AIQ), static or dynamic quenching, charge transfer, bonding, etc.

The c-dots have been used extensively for sensing various analytes such as anions, cations, biomolecules (different metabolites, enzymes, amino acids, glucose, cholesterol, nucleic acids, vitamins, etc.), drugs, pesticides, nitroaromatic explosives, pollutants, and a variety of other small molecules (**Figure 1.6**) [45]. The c-dots were also utilized for sensing microorganisms, including bacteria, fungi, and protozoans, along with selectively targeting the ability toward cancerous cells, which could be attained via surface functionalization [58].

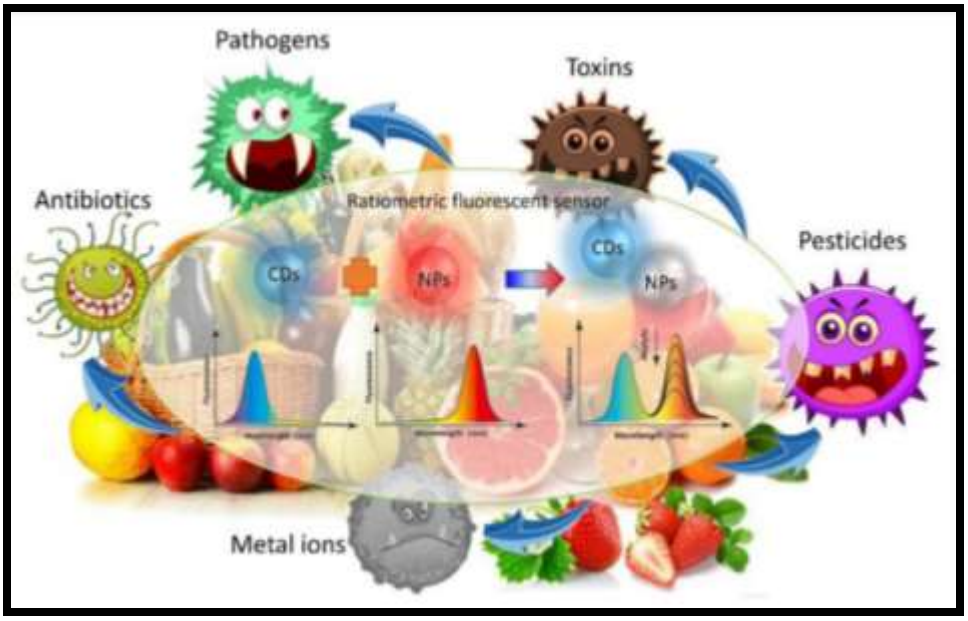

Figure 1.6. Use of c-dots as a ratiometric fluorescent sensor in food safety. [59]

1.5. Biomedical applications of carbon dots

C-dots' small size and exciting optical properties made their use obvious for biomedical applications and theranostics. The fluorescent c-dots with ingrained therapeutic proficiency are complete packages used in therapeutic and diagnostic nanomedicines.

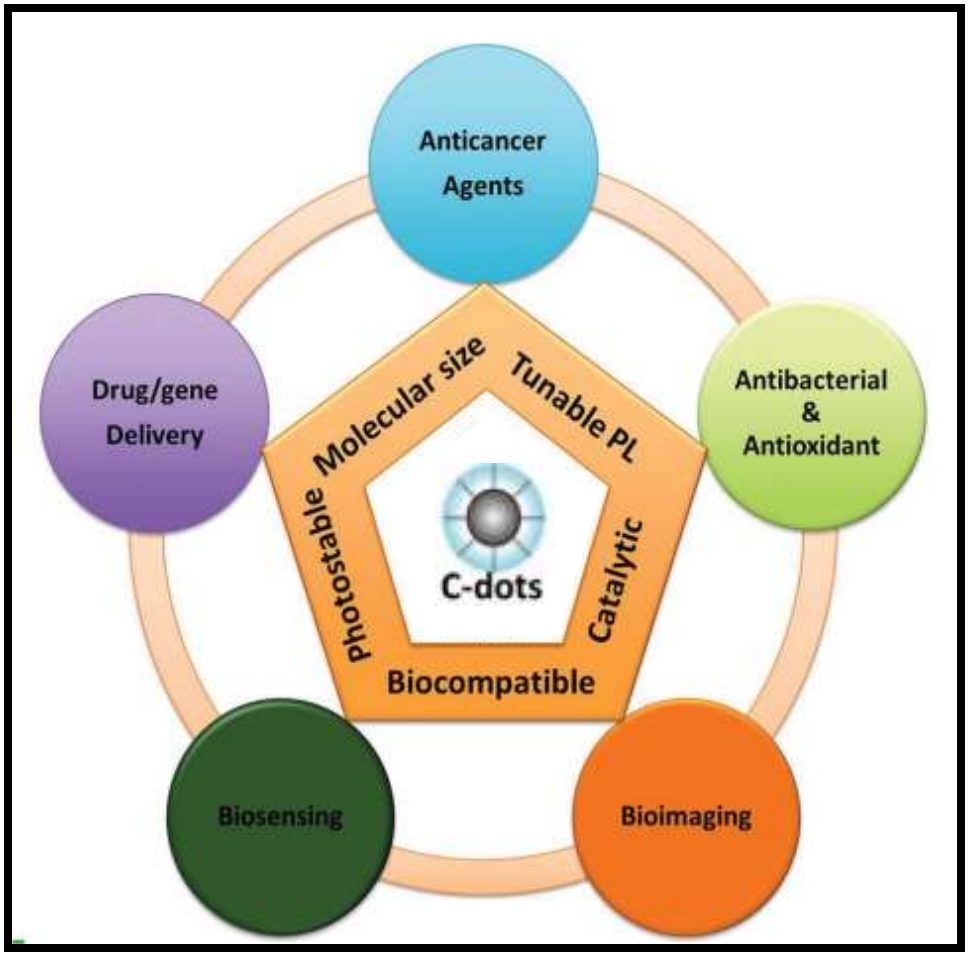

Figure 1.7. Biomedical applications of c-dots. [60]

1.5.1. Antibacterial activity of carbon dots.

Among the various biological applications of c-dots, their role as an antibacterial agent has gained much interest in the last decade. There are many reports where c-dots act as an antibacterial agent. The surface

functionalization of such c-dots is always helpful in enhancing their antibacterial activity to a great extent in one way or another. The increased drug resistance among pathogenic bacteria is a concern [61]. Many conventional antibiotics are already proved non-responsive to various bacterial species [62]. Increased drug resistance almost in all bacterial strains leads to a significant burden on the healthcare system. Therefore, developing alternative measures against pathogens is the need of the hour. A large number of materials have been studied for their antibacterial activities. Among them, c-dots have emerged as a very effective and efficient antibacterial agent due to their biocompatible nature, photoinduced redox properties, low-cost facile synthesis, easy surface passivation, fluorescence behavior, and stability. Predominantly, c-dots act against bacterial cells via photo-induced toxicity [63].

The use of visible light for photodynamic therapy against bacteria is explored for the first time by Meziani *et al.* [64]. The c-dots prepared by them are surface-functionalized using 2,2′-(ethylenedioxy)bis(ethylamine) (EDA). They have estimated the antibacterial action of EDA functionalized c-dots against gram-negative *E. coli* both in liquid media and on agar. The 30 min exposure to visible light decreases the viability of bacteria by four folds compared to control. However, when the same experiment was performed in the dark condition, the viability decreased by one-fold only. A similar effect of visible irradiation was also seen on cell viability by the presence of very few bacterial colonies on agar. The photodynamic nature of c-dots was proposed to be responsible for their action against bacteria reported earlier for cancer cell killing.

In another study by Yang *et al.* [65], carboxyl-amine functionalized c-dots were prepared and explored for antibacterial activities. These c-dots could also discriminate between gram-positive and gram-negative bacteria. The antibacterial action of c-dots was investigated against gram-positive and gram-negative bacteria. The MIC values were 8 μg mL^{-1}, 6

μg mL^{-1}, and 12 μg mL^{-1} against *S. aureus*, *M. luteus*, and *B. subtilis* (all gram-positive), respectively. These highly biocompatible c-dots were also checked for their antibacterial activity *in-vivo* and displayed similar results as in-vitro studies. However, the gram-negative bacteria remain unaffected at lower treatment concentrations. The disruption of the cell membrane was the main reason behind the toxicity of c-dots towards bacterial cells.

Li *et al.* [66], Nie *et al.* [67], Travlou *et al.* [68], and Wang *et al.* [69] have also found similar results where c-dots can act as photosensitizers and are crucial in bacterial killing via ROS generation. The surface coatings have also been made using such material in healthcare systems and in our daily lives. The biocompatible nature of c-dots is beneficial in making them a material of choice in biological systems in-vivo and in-vitro. A better understanding of the underlying mechanism and synthesizing c-dots with even better properties could be beneficial in replacing the traditional antibiotics. The problem of antibiotic resistance in microbes could also be solved effectively with great ease using c-dots.

The common mechanism of action is ROS generation. The oxidative stress caused by c-dots could be light-dependent or light-independent. The ROS production is enhanced when c-dots are functionalized using electron-donating groups like $–NH_2$. The reduction in the HOMO-LUMO gap is the reason behind it [70]. C-dots as photosensitizers are gaining popularity due to their effectiveness. After photoexcitation, the ground state is achieved via nonradiative photoactive decay, producing a photothermal effect and ROS, which results in more killing. The ROS generation also causes permanent membrane damage, dis-functioning various cellular organelles like mitochondria and endoplasmic reticulum, and irreversible damage to genetic material [71]. The lipid extraction and inhibition of primary metabolism are also plausible mechanisms for the antibacterial action of carbon nanomaterials [72]. Figure 1.7 represents the proposed mechanisms for c-dots induced antibacterial activity.

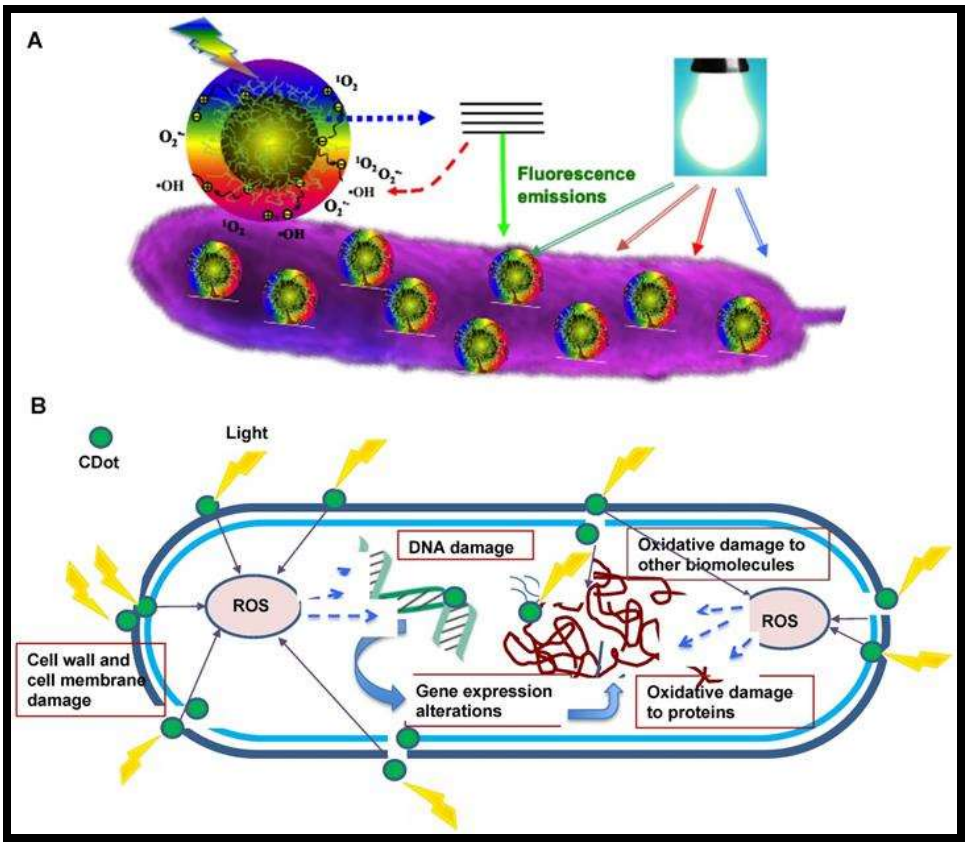

Figure 1.8. Mechanisms for antibacterial activity of c-dots. [62]

1.5.2. Bioimaging

The excellent characteristics of c-dots as high photostability, resistance to photobleaching, aqueous solubility, elevated QY, non-cytotoxic nature, stable fluorescent behavior under various physiological or biological conditions, easy cellular uptake, and enhanced biocompatibility provide an advantage to c-dots over traditional dyes or molecules used in bioimaging. These favorable properties of c-dots attract the researcher's attention to exploring their use in bioimaging. The c-dots have been used substantially for bioimaging for the last fifteen years. The bioimaging studies performed so far have led to the division of this field into two different groups in vivo and in vitro bioimaging. In-vitro bioimaging covers using c-dots for fluorescent staining of different types of cells and cellular

organelles. In contrast, the in vitro bioimaging pivoted the uptake and dissemination of c-dots in mice and zebrafish and their use in therapeutics.

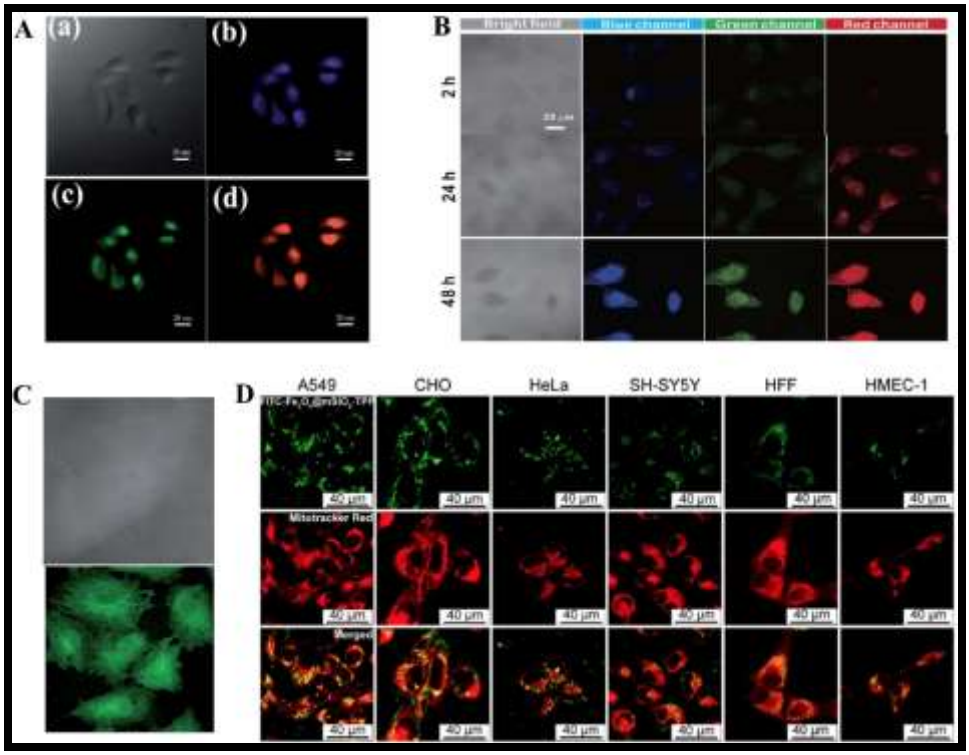

Figure 1.9. Multicolor imaging of A549 (A) HeLa cells (B) Microtubule imaging (C) Mitochondria targeting ability of c-dots (D). [82]

Cao et al. first explored the use of c-dots in the field of bioimaging in 2007 using breast cancer cell line MCF7 [73]. This work opened the ground for using c-dots for live-cell imaging, and many researchers have reported bioimaging of various cells since then [11, 41, 74, 75]. The c-dots show potential for cellular visualization using fluorescent microscopy. The staining of cells using c-dots is generally nonspecific, i.e., spread throughout the cytoplasm [54, 76, 77]. Still, certain reports show the specific targeting of cellular organelles using c-dots [78–81]. The excitation-dependent emission behavior of c-dots was utilized for multicolor imaging of various cells (Figure 1.9). Huang *et al.* in 2013 carried out multi-color imaging in A549 cells. In contrast, Chen *et al.*

prepared a nanoconjugate of c-dots with α-tubulin specific antibodies for fluorescent targeting of microtubules of A549 cells. Jung et al. in 2015 synthesized zwitterionic c-dots for nucleus targeting, and mitochondria targeting was achieved by mitochondria-targeting nanoplatform using c-dots.

1.5.3. Photo-Dynamic therapy

Due to the plenty of side effects of conventional cancer treatment therapies, there is a massive demand for new strategies with better therapeutic efficiency and lesser adverse effects. The captivating physical, chemical, and biological features of c-dots have attracted the attention of researchers to explore their anti-cancerous activity. It was not until later in the last decade that c-dots' reactive oxygen species generation activity was investigated.

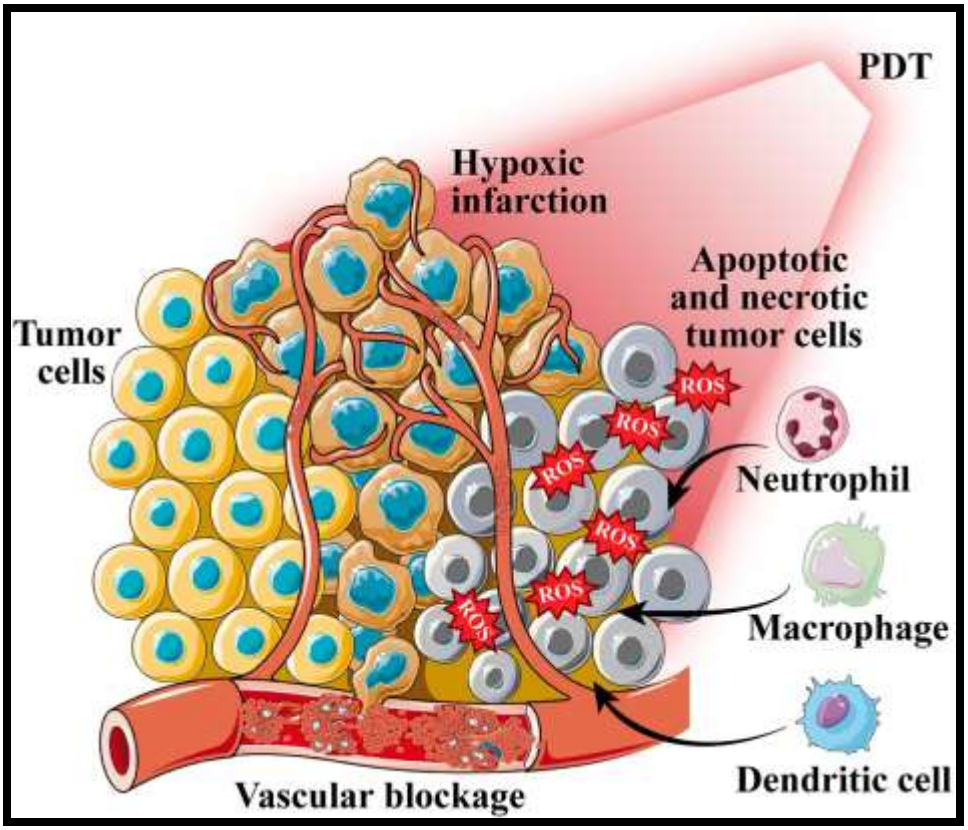

Figure 1.10. Various ways of killing tumor cells via PDT**.** [84]

The c-dots could be used as photosensitizers to generate free radicals in visible or near-infrared light [83]. Photodynamic therapy (PDT) is a new therapeutic strategy that utilizes light sources to treat diseases like cancer. The defined mechanism behind PDT has not yet been clarified. But broadly, after treating tumor cells with photosensitizer and light irradiation, the tumor cells would die either by autophagy, apoptosis, cell cycle arrest, or all three can happen at once [84], as shown in **Figure 1.10.** The red emissive c-dots were prepared by Zhao *et al.* using the simple hydrothermal method, which could effectively kill lung cancer cells and tumors in mice by generating ROS on light irradiation [85]. Wang et al. suggested the successful inhibition of 3D multicellular spheroids growth by using copper dopped c-dots as photosensitizer [86]. The singlet oxygen quantum yield was calculated to be 36% when an LED lamp (400-700nm) was used for irradiation. The use of carbon dot as an *in-vivo* PDT agent was also checked by Jia et al. by injecting carbon dot nanospheres into tumor-bearing mice [87]. The porphyrin-based c-dots were established by li et al. to treat hepatoma with the help of light irradiation [88], as shown in **Figure 1.11.a**. Interestingly, Xu *et al*. had synthesized Se/N-doped c-dots explicitly used to penetrate and produce ROS inside the nucleus of the cancer cells, thus enhancing cell death significantly [89] (**Figure.1.11.b**).

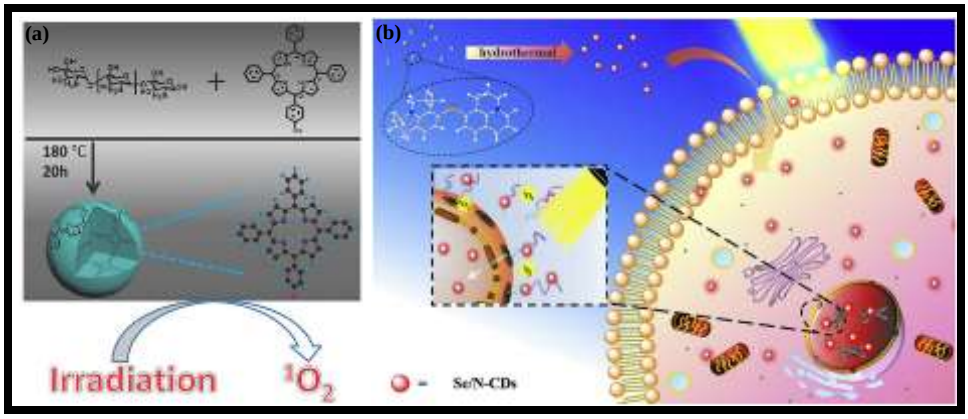

Figure 1.11. Use of c-dots as a photosensitizer in PDT. [88,89]

1.5.4. Carbon dots for drug delivery

Delivering the drug to the target site is the key to enhancing the treatment's effectiveness. Due to intrinsic fluorescence properties, high biocompatibility, and accessible surface modification, c-dots emerge as a perfect candidate for a cargo carrier. The delivery could easily be tracked due to the fluorescent nature of c-dots. To check the ability of c-dots as a nanocarrier, Tang *et al.* developed folic acid-modified c-dots loaded with Doxorubicin (CD-FA-DOX) to deliver it at the site of interest [90]. The quenched fluorescence of c-dots in CD-FA-DOX conjugate due to FRET was regained when DOX detached from the carbon dot surface (**Figure 1.12**). The FA functionalization led to targeted delivery, followed by a more significant apoptosis percentage.

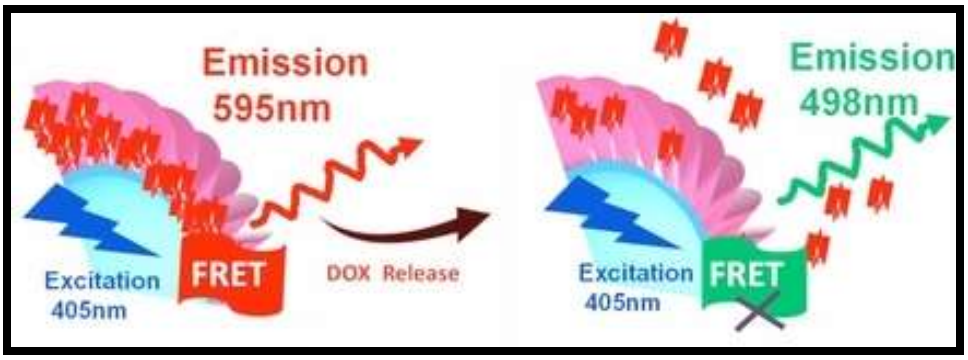

Figure 1.12. Doxorubicin delivery using folic acid functionalized c-dots. [90]

The mesoporous silica nanoparticles–c-dots (MSNs–CDs) nanohybrid was prepared in situ by Zhao *et al.* [91] for the successful delivery of DOX to folic acid overexpressing cancer cells (**Figure 1.13**). This nanocarrier can be tracked and showed reduced toxicity toward normal cells. There are various reports of using carbon dot as a cargo carrier for different drugs, biomolecules, genes, photosensitizers, etc., for stimuli-responsive release at the targeted site [92–95]. The astonishing results of c-dots in drug delivery encourage their use in cancer treatment for better therapeutic efficacy.

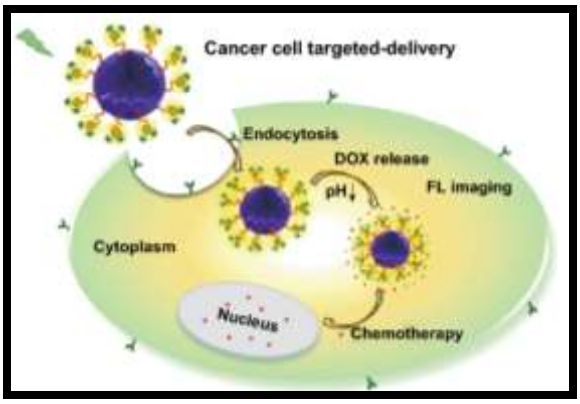

Figure 1.13. Targeted delivery of doxorubicin using c-dots nanohybrid with silica nanoparticles. [91]

There are many other reports in which c-dots' diagnostic and therapeutic ability have been explored. Indeed, it opens up new horizons of nanomedicine.

1.6. Scope of Present Work

The synthesis strategies, properties, and applications of c-dots discussed in previous sections highlight the importance of c-dots in optical and biomedical applications, including fluorescence sensing of various analytes, biosensing, cellular imaging, antibacterial potential, and photodynamic therapy to combat multiple diseases and drug delivery. The present thesis work highlights the development of c-dots using green and chemical precursors tuned for enhancement in optical properties, particularly by doping. The motivation is to use these c-dots for optical sensing, intracellular sensing, and live-cell imaging, along with their use in different biomedical applications.

The focal points of the thesis work are as follows-

1. Sustainable synthesis of c-dots from green and chemical sources for explosive detection, chemical sensing, and bioimaging.
2. Modulation of fluorescence performance of c-dots through functional group tuning.

3. C-dots' surface engineering for their diversified applications in environment safety, anticancer agent, photosensitizer, and microbial disinfection.
4. C-dots as carriers for the development of drug delivery systems.

1.7. References

[1] Wagner, S., Gondikas, A., Neubauer, E., Hofmann, T., von der Kammer, F. (2014), Spot the Difference: Engineered and Natural Nanoparticles in the Environment—Release, Behavior, and Fate. Angew. Chem. Int. Ed., 53, 12398–12419 (DOI: 10.1002/anie.201405050)

[2] X. Xu, R. Ray, Y. Gu, H.J. Ploehn, L. Gearheart, K. Raker, W.A. Scrivens (2004), Electrophoretic analysis and purification of fluorescent single-walled carbon nanotube fragments, J. Am. Chem. Soc., 126, 12736–12737 (DOI:10.1021/ja040082h)

[3] Sun, Y.-P., Zhou, B., Lin, Y., Wang, W., Fernando, K.A.S., Pathak, P., Meziani, M.J., Harruff, B.A., Wang, X., Wang, H., Luo, P.G., Yang, H., Kose, M.E., Chen, B., Veca, L.M., Xie, S.-Y. (2006), Quantum-Sized Carbon Dots for Bright and Colorful Photoluminescence, J. Am. Chem. Soc., 128, 7756–7757 (DOI: 10.1021/ja062677d)

[4] Sharma, V., Tiwari, P., Mobin, S.M. (2017), Sustainable carbon-dots: recent advances in green carbon dots for sensing and bioimaging, J. Mater. Chem. B., 5, 8904–8924 (DOI: 10.1039/C7TB02484C)

[5] Sciortino, A., Cannizzo, A., Messina, F. (2018), Carbon Nanodots: A Review—From the Current Understanding of the Fundamental Photophysics to the Full Control of the Optical Response, C. 4, 67 (DOI: 10.3390/c4040067)

[6] Zhai, X., Zhang, P., Liu, C., Bai, T., Li, W., Dai, L., Liu, W. (2012), Highly luminescent carbon nanodots by microwave-assisted pyrolysis, Chem. Commun., 48, 7955–7957 (DOI: 10.1039/C2CC33869F)

[7] Yang, Z., Xu, M., Liu, Y., He, F., Gao, F., Su, Y., Wei, H., Zhang, Y. (2014), Nitrogen-doped, carbon-rich, highly photoluminescent carbon dots from ammonium citrate, Nanoscale, 6, 1890–1895 (DOI: 10.1039/C3NR05380F)

[8] Zhou, L., Li, Z., Liu, Z., Ren, J., Qu, X. (2013), Luminescent Carbon Dot-Gated Nanovehicles for pH-Triggered Intracellular Controlled Release and Imaging, Langmuir, 29, 6396–6403 (DOI: 10.1021/la400479n)

[9] Wang, W., Li, Y., Cheng, L., Cao, Z., Liu, W. (2013), Water-soluble and phosphorus-containing carbon dots with strong green fluorescence for cell labeling, J. Mater. Chem. B, 2, 46–48 (DOI: 10.1039/C3TB21370F)

[10] Kasprzyk, W., Świergosz, T., Bednarz, S., Walas, K., Bashmakova, N.V., Bogdał, D. (2018), Luminescence phenomena of carbon dots derived from citric acid and urea – a molecular insight, Nanoscale, 10, 13889–13894 (DOI: 10.1039/C8NR03602K)

[11] Hsu, P.-C., Shih, Z.-Y., Lee, C.-H., Chang, H.-T. (2012), Synthesis and analytical applications of photoluminescent carbon nanodots, Green Chem., 14, 917–920 (DOI: 10.1039/C2GC16451E)

[12] Liu, S., Tian, J., Wang, L., Zhang, Y., Qin, X., Luo, Y., Asiri, A.M., Al-Youbi, A.O., Sun, X. (2012), Hydrothermal Treatment of Grass: A Low-Cost, Green Route to Nitrogen-Doped, Carbon-Rich, Photoluminescent Polymer Nanodots as an Effective Fluorescent Sensing Platform for Label-Free Detection of Cu(II) Ions, Adv. Mater., 24, 2037–2041 (DOI: 10.1002/adma.201200164)

[13] Wang, J., Wang, C.-F., Chen, S. (2012), Amphiphilic Egg-Derived Carbon Dots: Rapid Plasma Fabrication, Pyrolysis Process, and Multicolor Printing Patterns, Angew. Chem. Int. Ed., 51, 9297–9301 (DOI: 10.1002/anie.201204381)

[14] Atchudan, R., Edison, T.N.J.I., Perumal, S., Muthuchamy, N., Lee, Y.R. (2020), Hydrophilic nitrogen-doped carbon dots from biowaste using the dwarf banana peel for environmental and biological applications, Fuel, 275, 117821 (DOI: 10.1016/j.fuel.2020.117821)

[15] Arul, V., Sethuraman, M.G. (2018), Facile green synthesis of fluorescent N-doped carbon dots from Actinidia deliciosa and their catalytic activity and cytotoxicity applications, Opt. Mater., 78, 181–190 (DOI: 10.1016/j.optmat.2018.02.029)

[16] Zhou, J., Sheng, Z., Han, H., Zou, M., Li, C. (2012), Facile synthesis of fluorescent carbon dots using watermelon peel as a carbon source, Mater. Lett., 66, 222–224 (DOI: 10.1016/j.matlet.2011.08.081)

[17] Sahu, S., Behera, B., Maiti, T.K., Mohapatra, S. (2012), Simple one-step synthesis of highly luminescent carbon dots from orange juice: application as excellent bio-imaging agents, Chem. Commun., 48, 8835–8837 (DOI: 10.1039/C2CC33796G)

[18] De, B., Karak, N. (2013), A green and facile approach for the synthesis of water-soluble fluorescent carbon dots from banana juice, RSC Adv., 3, 8286–8290 (DOI: 10.1039/C3RA00088E)

[19] Huang, H., Lv, J.-J., Zhou, D.-L., Bao, N., Xu, Y., Wang, A.-J., Feng, J.-J. (2013), One-pot green synthesis of nitrogen-doped carbon nanoparticles as fluorescent probes for mercury ions, RSC Adv., 3, 21691–21696 (DOI: 10.1039/C3RA43452D)

[20] Prasannan, A., Imae, T. (2013), One-Pot Synthesis of Fluorescent Carbon Dots from Orange Waste Peels, Ind. Eng. Chem. Res., 52, 15673–15678 (DOI: 10.1021/ie402421s)

[21] Huang, H., Xu, Y., Tang, C.-J., Chen, J.-R., Wang, A.-J., Feng, J.-J. (2014), Facile and green synthesis of photoluminescent carbon nanoparticles for cellular imaging, New J. Chem., 38, 784–789 (DOI: 10.1039/C3NJ01185B)

[22] Jeong, C.J., Roy, A.K., Kim, S.H., Lee, J.-E., Jeong, J.H., In, I., Park, S.Y. (2014), Fluorescent carbon nanoparticles derived from natural materials of mango fruit for bio-imaging probes, Nanoscale, 6, 15196–15202 (DOI: 10.1039/C4NR04805A)

[23] Xu, J., Lai, T., Feng, Z., Weng, X., Huang, C. (2015), Formation of fluorescent carbon nanodots from kitchen wastes and their application for detection of Fe^{3+}, Luminescence, 30, 420–424 (DOI: 10.1002/bio.2754)

[24] Kasibabu, B.S.B., D'souza, S.L., Jha, S., Kailasa, S.K. (2015), Imaging of Bacterial and Fungal Cells Using Fluorescent Carbon Dots Prepared from Carica papaya Juice, J. Fluoresc., 25, 803–810 (DOI: 10.1007/s10895-015-1595-0)

[25] Mehta, V.N., Jha, S., Basu, H., Singhal, R.K., Kailasa, S.K. (2015), One-step hydrothermal approach to fabricate carbon dots from apple juice for imaging of mycobacterium and fungal cells, Sens. Actuators B Chem., 213, 434–443 (DOI: 10.1016/j.snb.2015.02.104)

[26] Xue, M., Zou, M., Zhao, J., Zhan, Z., Zhao, S. (2015), Green preparation of fluorescent carbon dots from lychee seeds and their application for the selective detection of methylene blue and imaging in living cells, J. Mater. Chem. B., 3, 6783–6789 (DOI: 10.1039/C5TB01073J)

[27] Vandarkuzhali, S.A.A., Jeyalakshmi, V., Sivaraman, G., Singaravadivel, S., Krishnamurthy, K.R., Viswanathan, B. (2017), Highly fluorescent carbon dots from Pseudo-stem of banana plant: Applications as nanosensor and bio-imaging agents, Sens. Actuators B Chem., 252, 894–900 (DOI: 10.1016/j.snb.2017.06.088)

[28] Yang, R., Guo, X., Jia, L., Zhang, Y., Zhao, Z., Lonshakov, F. (2017), Green preparation of carbon dots with mangosteen pulp for the selective detection of Fe^{3+} ions and cell imaging, Appl. Surf. Sci., 423, 426–432 (DOI: 10.1016/j.apsusc.2017.05.252)

[29] Sharma, V., Kaur, N., Tiwari, P., Mobin, S.M. (2018), Full color emitting fluorescent carbon material as reversible pH sensor with multicolor live cell imaging, J. Photochem. Photobiol. B, 182, 137–145 (DOI: 10.1016/j.jphotobiol.2018.04.006)

[30] Li, Z., Ni, Y., Kokot, S. (2015), A new fluorescent nitrogen-doped carbon dot system modified by the fluorophore-labeled ssDNA for the analysis of 6-mercaptopurine and Hg (II), Biosens. Bioelectron., 74, 91–97 (DOI: 10.1016/j.bios.2015.06.014)

[31] Mehta, V.N., Jha, S., Singhal, R.K., Kailasa, S.K. (2014), Preparation of multicolor emitting carbon dots for HeLa cell imaging, New J. Chem., 38, 6152–6160 (DOI: 10.1039/C4NJ00840E)

[32] Hu, Y., Zhang, L., Li, X., Liu, R., Lin, L., Zhao, S. (2017), Green Preparation of S and N Co-Doped Carbon Dots from Water Chestnut and Onion as Well as Their Use as an Off–On Fluorescent Probe for the Quantification and Imaging of Coenzyme A, ACS Sustain. Chem. Eng., 5, 4992–5000 (DOI: 10.1021/acssuschemeng.7b00393)

[33] Jiang, C., Wu, H., Song, X., Ma, X., Wang, J., Tan, M. (2014), Presence of photoluminescent carbon dots in Nescafe® original instant coffee: Applications to bioimaging, Talanta, 127, 68–74 (DOI: 10.1016/j.talanta.2014.01.046)

[34] Wang, L., Zhou, H.S. (2014), Green Synthesis of Luminescent Nitrogen-Doped Carbon Dots from Milk and Its Imaging Application, Anal. Chem., 86, 8902–8905 (DOI: 10.1021/ac502646x)

[35] Wei, J., Liu, B., Yin, P. (2014), Dual functional carbonaceous nanodots exist in a cup of tea, RSC Adv., 4, 63414–63419 (DOI: 10.1039/C4RA11152D)

[36] Wen, X., Shi, L., Wen, G., Li, Y., Dong, C., Yang, J., Shuang, S. (2016), Green and facile synthesis of nitrogen-doped carbon nanodots for multicolor cellular imaging and Co^{2+} sensing in living cells, Sens. Actuators B Chem., 235, 179–187 (DOI: 10.1016/j.snb.2016.05.066)

[37] Yao, Y.-Y., Gedda, G., Girma, W.M., Yen, C.-L., Ling, Y.-C., Chang, J.-Y. (2017), Magnetofluorescent Carbon Dots Derived from Crab Shell for Targeted Dual-Modality Bioimaging and Drug Delivery, ACS Appl. Mater. Interfaces., 9, 13887–13899 (DOI: 10.1021/acsami.7b01599)

[38] Guo, Y., Zhang, L., Cao, F., Leng, Y. (2016), Thermal treatment of hair for the synthesis of sustainable carbon quantum dots and the applications for sensing Hg^{2+}, Sci. Rep., 6, 35795 (DOI: 10.1038/srep35795)

[39] Essner, J.B., Laber, C.H., Ravula, S., Polo-Parada, L., Baker, G.A. (2015), Pee-dots: biocompatible fluorescent carbon dots derived from the upcycling of urine, Green Chem., 18, 243–250 (DOI: 10.1039/C5GC02032H)

[40] Liu, R., Zhang, J., Gao, M., Li, Z., Chen, J., Wu, D., Liu, P. (2014), A facile microwave-hydrothermal approach towards highly photoluminescent carbon dots from goose feathers, RSC Adv., 5, 4428–4433 (DOI: 10.1039/C4RA12077A)

[41] Wu, Z.L., Zhang, P., Gao, M.X., Liu, C.F., Wang, W., Leng, F., Huang, C.Z. (2013), One-pot hydrothermal synthesis of highly luminescent nitrogen-doped amphoteric carbon dots for bioimaging from Bombyx mori silk – natural proteins, J. Mater. Chem. B., 1, 2868–2873 (DOI: 10.1039/C3TB20418A)

[42] Feng, J., Wang, W.-J., Hai, X., Yu, Y.-L., Wang, J.-H. (2016), Green preparation of nitrogen-doped carbon dots derived

from silkworm chrysalis for cell imaging, J. Mater. Chem. B, 4, 387–393 (DOI: 10.1039/C5TB01999K)

[43] Alas, M.O., Alkas, F.B., Aktas Sukuroglu, A., Genc Alturk, R., Battal, D. (2020), Fluorescent carbon dots are the new quantum dots: an overview of their potential in emerging technologies and nanosafety, J. Mater. Sci., 55, 15074–15105 (DOI: 10.1007/s10853-020-05054-y)

[44] Sharma, V., Singh, S.K., Mobin, S.M. (2019), Bioinspired carbon dots: from rose petals to tunable emissive nanodots, Nanoscale Adv., 1, 1290–1296 (DOI: 10.1039/C8NA00105G)

[45] Liu, M.L., Chen, B.B., Li, C.M., Huang, C.Z. (2019), Carbon dots: synthesis, formation mechanism, fluorescence origin and sensing applications, Green Chem., 21, 449–471 (DOI: 10.1039/C8GC02736F)

[46] Jeong, Y., Moon, K., Jeong, S., Koh, W.-G., Lee, K. (2018), Converting Waste Papers to Fluorescent Carbon Dots in the Recycling Process without Loss of Ionic Liquids and Bioimaging Applications, ACS Sustain. Chem. Eng., 6, 4510–4515 (DOI: 10.1021/acssuschemeng.8b00353)

[47] Mazrad, Z.A.I., Lee, K., Chae, A., In, I., Lee, H., Park, S.Y. (2018), Progress in internal/external stimuli responsive fluorescent carbon nanoparticles for theranostic and sensing applications, J. Mater. Chem. B, 6, 1149–1178 (DOI: 10.1039/C7TB03323K)

[48] Wang, R., Lu, K.-Q., Tang, Z.-R., Xu, Y.-J. (2017), Recent progress in carbon quantum dots: synthesis, properties and applications in photocatalysis, J. Mater. Chem. A, 5, 3717–3734 (DOI: 10.1039/C6TA08660H)

[49] Wang, W.-J., Xia, J.-M., Feng, J., He, M.-Q., Chen, M.-L., Wang, J.-H. (2016), Green preparation of carbon dots for intracellular pH sensing and multicolor live cell imaging, J. Mater. Chem. B, 4, 7130–7137 (DOI: 10.1039/C6TB02071B)

[50] Ramanan, V., Thiyagarajan, S.K., Raji, K., Suresh, R., Sekar, R., Ramamurthy, P. (2016), Outright Green Synthesis of Fluorescent Carbon Dots from Eutrophic Algal Blooms for In Vitro Imaging, ACS Sustain. Chem. Eng., 4, 4724–4731 (DOI: 10.1021/acssuschemeng.6b00935)

[51] Shi, L., Yang, J.H., Zeng, H.B., Chen, Y.M., Yang, S.C., Wu, C., Zeng, H., Yoshihito, O., Zhang, Q. (2016), Carbon dots with high fluorescence quantum yield: the fluorescence originates from organic fluorophores, Nanoscale, 8, 14374–14378 (DOI: 10.1039/C6NR00451B)

[52] Shen, J., Chen, G., Vu, A.-M., Fan, W., Bilsel, O.S., Chang, C.-C., Han, G. (2013), Engineering the Upconversion Nanoparticle Excitation Wavelength: Cascade Sensitization of Tri-doped Upconversion Colloidal Nanoparticles at 800 nm, Adv. Opt. Mater., 1, 644–650 (DOI: 10.1002/adom.201300160)

[53] Kim, S., Hwang, S.W., Kim, M.-K., Shin, D.Y., Shin, D.H., Kim, C.O., Yang, S.B., Park, J.H., Hwang, E., Choi, S.-H., Ko, G., Sim, S., Sone, C., Choi, H.J., Bae, S., Hong, B.H. (2012), Anomalous Behaviors of Visible Luminescence from Graphene Quantum Dots: Interplay between Size and Shape, ACS Nano., 6, 8203–8208 (DOI: 10.1021/nn302878r)

[54] Jiang, K., Sun, S., Zhang, L., Lu, Y., Wu, A., Cai, C., Lin, H. (2015), Red, Green, and Blue Luminescence by Carbon Dots: Full-Color Emission Tuning and Multicolor Cellular Imaging, Angew. Chem., 127, 5450–5453 (DOI: 10.1002/ange.201501193)

[55] Essner, J.B., Kist, J.A., Polo-Parada, L., Baker, G.A. (2018), Artifacts and Errors Associated with the Ubiquitous Presence of Fluorescent Impurities in Carbon Nanodots, Chem. Mater., 30, 1878–1887 (DOI: 10.1021/acs.chemmater.7b04446)

[56] Ding, H., Yu, S.-B., Wei, J.-S., Xiong, H.-M. (2016), Full-Color Light-Emitting Carbon Dots with a Surface-State-Controlled Luminescence Mechanism, ACS Nano., 10, 484–491 (DOI: 10.1021/acsnano.5b05406)

[57] Zhang, Y., Yuan, R., He, M., Hu, G., Jiang, J., Xu, T., Zhou, L., Chen, W., Xiang, W., Liang, X. (2017), Multicolour nitrogen-doped carbon dots: tunable photoluminescence and sandwich fluorescent glass-based light-emitting diodes, Nanoscale. 9, 17849–17858 (DOI: 10.1039/C7NR05363K)

[58] Sun, X., Lei, Y. (2017), Fluorescent carbon dots and their sensing applications, TrAC Trends Anal. Chem. 89, 163–180 (DOI: 10.1016/j.trac.2017.02.001)

[59] Han, Y., Yang, W., Luo, X., He, X., Zhao, H., Tang, W., Yue, T., Li, Z. (2022), Carbon dots based ratiometric fluorescent sensing platform for food safety, Crit. Rev. Food Sci. Nutr., 62, 244–260 (DOI: 10.1080/10408398.2020.1814197)

[60] Zheng, X.T., Ananthanarayanan, A., Luo, K.Q., Chen, P. (2015), Glowing Graphene Quantum Dots and Carbon Dots: Properties, Syntheses, and Biological Applications, Small, 11, 1620–1636 (DOI: 10.1002/smll.201402648)

[61] Rabe, D.I.A., Awak, M.M.A., Yang, F., Okonjo, P.A., Dong, X., Teisl, L.R., Wang, P., Tang, Y., Pan, N., Sun, Y.-P., Yang, L. (2019), The dominant role of surface functionalization in carbon dots & photo-activated antibacterial activity, Int. J. Nanomedicine, 14, 2655–2665 (DOI: 10.2147/IJN.S200493)

[62] Dong, X., Liang, W., Meziani, M.J., Sun, Y.-P., Yang, L. (2020), Carbon Dots as Potent Antimicrobial Agents, Theranostics, 10, 671–686 (DOI: 10.7150/thno.39863)

[63] Hu, X., Huang, Y.-Y., Wang, Y., Wang, X., Hamblin, M.R. (2018), Antimicrobial Photodynamic Therapy to Control Clinically Relevant Biofilm Infections, Front. Microbiol., 0, (DOI: 10.3389/fmicb.2018.01299)

[64] Meziani, M.J., Dong, X., Zhu, L., Jones, L.P., LeCroy, G.E., Yang, F., Wang, S., Wang, P., Zhao, Y., Yang, L., Tripp, R.A., Sun, Y.-P. (2016), Visible-Light-Activated Bactericidal Functions of Carbon "Quantum" Dots, ACS Appl. Mater. Interfaces, 8, 10761–10766 (DOI: 10.1021/acsami.6b01765)

[65] Yang, J., Zhang, X., Ma, Y.-H., Gao, G., Chen, X., Jia, H.-R., Li, Y.-H., Chen, Z., Wu, F.-G. (2016), Carbon Dot-Based Platform for Simultaneous Bacterial Distinguishment and Antibacterial Applications, ACS Appl. Mater. Interfaces, 8, 32170–32181 (DOI: 10.1021/acsami.6b10398)

[66] Li, H., Huang, J., Song, Y., Zhang, M., Wang, H., Lu, F., Huang, H., Liu, Y., Dai, X., Gu, Z., Yang, Z., Zhou, R., Kang, Z. (2018), Degradable Carbon Dots with Broad-Spectrum Antibacterial Activity, ACS Appl. Mater. Interfaces, 10, 26936–26946 (DOI: 10.1021/acsami.8b08832)

[67] Nie, X., Jiang, C., Wu, S., Chen, W., Lv, P., Wang, Q., Liu, J., Narh, C., Cao, X., Ghiladi, R.A., Wei, Q. (2020), Carbon quantum dots: A bright future as photosensitizers for in vitro antibacterial photodynamic inactivation, J. Photochem. Photobiol. B, 206, 111864 (DOI: 10.1016/j.jphotobiol.2020.111864)

[68] Travlou, N.A., Giannakoudakis, D.A., Algarra, M., Labella, A.M., Rodríguez-Castellón, E., Bandosz, T.J. (2018), S- and N-doped carbon quantum dots: Surface chemistry dependent antibacterial activity, Carbon, 135, 104–111 (DOI: 10.1016/j.carbon.2018.04.018)

[69] Wang, H., Song, Z., Gu, J., Li, S., Wu, Y., Han, H. (2019), Nitrogen-Doped Carbon Quantum Dots for Preventing Biofilm Formation and Eradicating Drug-Resistant Bacteria Infection, ACS Biomater. Sci. Eng., 5, 4739–4749 (DOI: 10.1021/acsbiomaterials.9b00583)

[70] Kuo, W.S., Chen, H.H., Chen, S.Y., Chang, C.Y., Chen, P.C., Hou, Y.I., Shao, Y.T., Kao, H.F., Hsu, C.L.L., Chen, Y.C., Chen, S.J., Wu, S.R., Wang, J.Y. (2017), Graphene quantum dots with nitrogen-doped content dependence for highly efficient dual-modality photodynamic antimicrobial therapy and bioimaging. Biomaterials, 120, 185–194 (DOI: 10.1016/j.biomaterials.2016.12.022)

[71] Xin, Q., Shah, H., Nawaz, A., Xie, W., Akram, M.Z., Batool, A., Tian, L., Jan, S.U., Boddula, R., Guo, B., Liu, Q., Gong, J.R. (2019), Antibacterial Carbon-Based Nanomaterials, Adv. Mater., 31, 1804838 (DOI: 10.1002/adma.201804838)

[72] Tu, Y., Lv, M., Xiu, P., Huynh, T., Zhang, M., Castelli, M., Liu, Z., Huang, Q., Fan, C., Fang, H., Zhou, R. (2013), Destructive extraction of phospholipids from Escherichia coli membranes by graphene nanosheets, Nat. Nanotechnol., 8, 594–601 (DOI: 10.1038/nnano.2013.125)

[73] Cao, L., Wang, X., Meziani, M.J., Lu, F., Wang, H., Luo, P.G., Lin, Y., Harruff, B.A., Veca, L.M., Murray, D., Xie, S.-Y., Sun, Y.-P. (2007), Carbon Dots for Multiphoton Bioimaging, J. Am. Chem. Soc., 129, 11318–11319 (DOI: 10.1021/ja073527l)

[74] Ray, S.C., Saha, A., Jana, N.R., Sarkar, R. (2009), Fluorescent Carbon Nanoparticles: Synthesis, Characterization, and Bioimaging Application, J. Phys. Chem. C, 113, 18546–18551 (DOI: 10.1021/jp905912n)

[75] Li, Q., Ohulchanskyy, T.Y., Liu, R., Koynov, K., Wu, D., Best, A., Kumar, R., Bonoiu, A., Prasad, P.N. (2010), Photoluminescent Carbon Dots as Biocompatible Nanoprobes for Targeting Cancer Cells in Vitro, J. Phys. Chem. C, 114, 12062–12068 (DOI: 10.1021/jp911539r)

[76] Algarra, M., Pérez-Martín, M., Cifuentes-Rueda, M., Jiménez-Jiménez, J., Silva, J.C.G.E. da, Bandosz, T.J., Rodríguez-Castellón, E., Navarrete, J.T.L., Casado, J. (2014), Carbon dots obtained using hydrothermal treatment of formaldehyde. Cell imaging in vitro, Nanoscale, 6, 9071–9077 (DOI: 10.1039/C4NR01585A)

[77] Liu, J.-H., Cao, L., LeCroy, G.E., Wang, P., Meziani, M.J., Dong, Y., Liu, Y., Luo, P.G., Sun, Y.-P. (2015), Carbon "Quantum" Dots for Fluorescence Labeling of Cells, ACS Appl. Mater. Interfaces, 7, 19439–19445 (DOI: 10.1021/acsami.5b05665)

[78] Jung, Y.K., Shin, E., Kim, B.-S. (2015), Cell Nucleus-Targeting Zwitterionic Carbon Dots, Sci. Rep. 5, 18807 (DOI: 10.1038/srep18807)

[79] Wu, X., Sun, S., Wang, Y., Zhu, J., Jiang, K., Leng, Y., Shu, Q., Lin, H. (2017), A fluorescent carbon-dots-based mitochondria-targetable nanoprobe for peroxynitrite sensing in living cells, Biosens. Bioelectron., 90, 501–507 (DOI: 10.1016/j.bios.2016.10.060)

[80] Unnikrishnan, B., Wu, R.-S., Wei, S.-C., Huang, C.-C., Chang, H.-T. (2020), Fluorescent Carbon Dots for Selective Labeling of Subcellular Organelles, ACS Omega, 5, 11248–11261 (DOI: 10.1021/acsomega.9b04301)

[81] Zhang, X., Chen, L., Wei, Y.Y., Yang, Y.Z., Liu, X.G., Du, J.L., Li, Q., Yu, S.P. (2021), Advances in organelle-targeting carbon dots. Fuller. Nanotub. Carbon Nanostructures, 29, 394–406 (DOI: 10.1080/1536383X.2020.1852217)

[82] Peng, Z., Han, X., Li, S., Al-Youbi, A.O., Bashammakh, A.S., El-Shahawi, M.S., Leblanc, R.M. (2017), Carbon dots: Biomacromolecule interaction, bioimaging, and nanomedicine, Coord. Chem. Rev., 343, 256–277 (DOI: 10.1016/j.ccr.2017.06.001)

[83] Li, B., Zhao, S., Huang, L., Wang, Q., Xiao, J., Lan, M. (2021), Recent advances and prospects of carbon dots in phototherapy, Chem. Eng. J., 408, 127245 (DOI: 10.1016/j.cej.2020.127245)

[84] Hua, J., Wu, P., Gan, L., Zhang, Z., He, J., Zhong, L., Zhao, Y., Huang, Y. (2021), Current Strategies for Tumor Photodynamic Therapy Combined With Immunotherapy, Front. Oncol., 11, 738323 (DOI: 10.3389/fonc.2021.738323)

[85] Zhao, J., Li, F., Zhang, S., An, Y., Sun, S. (2019), Preparation of N-doped yellow carbon dots and N, P co-doped red carbon dots for bioimaging and photodynamic therapy of tumors, New J. Chem., 43, 6332–6342 (DOI: 10.1039/C8NJ06351F)

[86] Wang, J., Xu, M., Wang, D., Li, Z., Primo, F.L., Tedesco, A.C., Bi, H. (2019), Copper-Doped Carbon Dots for Optical Bioimaging and Photodynamic Therapy, Inorg. Chem., 58, 13394–13402 (DOI: 10.1021/acs.inorgchem.9b02283)

[87] Jia, Q., Ge, J., Liu, W., Guo, L., Zheng, X., Chen, S., Chen, M., Liu, S., Zhang, L., Wang, M., Zhang, H., Wang, P. (2017), Self-Assembled Carbon Dot Nanosphere: A Robust, Near-Infrared Light-Responsive, and Vein Injectable Photosensitizer, Adv. Healthc. Mater., 6, 1601419 (DOI: 10.1002/adhm.201601419)

[88] Li, Y., Zheng, X., Zhang, X., Liu, S., Pei, Q., Zheng, M., Xie, Z. (2017), Porphyrin-Based Carbon Dots for Photodynamic Therapy of Hepatoma, Adv. Healthc. Mater. 6, 1600924 (DOI: 10.1002/adhm.201600924)

[89] Xu, N., Du, J., Yao, Q., Ge, H., Li, H., Xu, F., Gao, F., Xian, L., Fan, J., Peng, X. (2020), Precise photodynamic therapy: Penetrating the nuclear envelope with photosensitive carbon dots, Carbon, 159, 74–82 (DOI: 10.1016/j.carbon.2019.12.002)

[90] Tang, J., Kong, B., Wu, H., Xu, M., Wang, Y., Wang, Y., Zhao, D., Zheng, G. (2013), Carbon Nanodots Featuring Efficient FRET for Real-Time Monitoring of Drug Delivery and Two-Photon Imaging, Adv. Mater., 25, 6569–6574 (DOI: 10.1002/adma.201303124)

[91] Zhao, S., Sun, S., Jiang, K., Wang, Y., Liu, Y., Wu, S., Li, Z., Shu, Q., Lin, H. (2019), In Situ Synthesis of Fluorescent Mesoporous Silica–Carbon Dot Nanohybrids Featuring Folate Receptor-Overexpressing Cancer Cell Targeting and Drug Delivery, Nano-Micro Lett., 11, 32 (DOI: 10.1007/s40820-019-0263-3)

[92] Liu, C., Zhang, P., Zhai, X., Tian, F., Li, W., Yang, J., Liu, Y., Wang, H., Wang, W., Liu, W. (2012), Nano-carrier for gene delivery and bioimaging based on carbon dots with PEI-passivation enhanced fluorescence, Biomaterials, 33, 3604–3613 (DOI: 10.1016/j.biomaterials.2012.01.052)

[93] Zhang, J., Zheng, M., Xie, Z. (2016), Co-assembled hybrids of proteins and carbon dots for intracellular protein delivery, J. Mater. Chem. B. 4, 5659–5663 (DOI: 10.1039/C6TB01622G)

[94] Huang, P., Lin, J., Wang, X., Wang, Z., Zhang, C., He, M., Wang, K., Chen, F., Li, Z., Shen, G., Cui, D., Chen, X. (2012), Light-Triggered Theranostics Based on Photosensitizer-Conjugated Carbon Dots for Simultaneous Enhanced-Fluorescence Imaging and Photodynamic Therapy, Adv. Mater., 24, 5104–5110 (DOI: 10.1002/adma.201200650)

[95] Shu, Y., Lu, J., Mao, Q.-X., Song, R.-S., Wang, X.-Y., Chen, X.-W., Wang, J.-H. (2017), Ionic liquid mediated organophilic carbon dots for drug delivery and bioimaging, Carbon, 114, 324–333 (DOI: 10.1016/j.carbon.2016.12.038)

CHAPTER 2

"*Vigna radiata*" based green C-dots: photo-triggered theranostics, a highly selective and sensitive fluorescent sensor for extracellular and intracellular iron (III) and multicolor live-cell imaging probe

2.1. Introduction

Plants and their natural products have been used profusely for ages. The use of green sources for the synthesis of C-dots is gaining attention due to its easy availability and increased environmental concerns. Moreover, the green synthesis of nanoparticles is cheap as well as efficient. Being a fresh member of the nanomaterial family, fluorescent C-dots have drawn much attention because it accentuates excitation-dependent multi-color emission, substantial biocompatibility, hemocompatibility, stable photoluminescence, resistance to photo-bleaching, and environmental friendliness [1–7]. However, maximum times C-dots synthesized from green source come up with low quantum yield (QY) [8–15]. Various green sources were explored to synthesize carbon dots like coffee beans, grass, orange juice, peanut shells, cabbage, and banana juice having QY 3.8%, 6.2%, and 26%. 9.91%, 16.5% and 8.95% respectively [9,13,16–19] (**Table 2.2**). Apart from using various edible sources, biomasses like lignin were used as the carbon source for synthesizing carbon dots [20,21]. High quantum yield is desirable for any fluorescent material to be used as an imaging agent [22]. Hence, there is a huge requirement to develop low-cost, green, high-yielding methods and good sources for preparing C-dots. The C-dots have a huge impact on advancement in the field of intracellular imaging, such as in human cell lines, fungal cells, etc. [23–25] The nitrogen doping leads to the enhancement of QY due to similar atomic size and the presence of five free valence electrons to be introduced in carbon

[26–28]. Therefore, nitrogen is the commonly used doping element for QY enhancement [29–32].

An efficient approach to treating cancer is today's world's demand [33]. Photodynamic therapy (PDT) is an upcoming therapeutic modality used for cancer treatment [34]. It is a fruitful and distinct method of killing malignant cells in a more manageable way [35–38]. Due to its minimal invasiveness, it is gaining interest widely [39]. There is an enormous demand for light-activated therapeutic agents for PDT. The primary cause associated with the effectiveness of PDT was the generation of reactive oxygen species (ROS) [40]. When C-dots are irradiated, it leads to electron transfer to H_2O, generating free radicals, thus killing nearby cells [41,42]. Semiconductor quantum dots were used in PDT, but their cytotoxic nature due to heavy metal ions limiting their use in biological systems. The other limitations of PDT agents are hydrophobicity, low ROS generation, and photobleaching.[43] Further, people have used C-dots surface passivated with the photosensitizer (PS) in PDT. The high $^1O_2$ quantum yield of a material is another favorable factor for using it as a PS agent [40,44]. So, there is an urgent need to develop a PDT agent showing good biocompatibility photostability with adequate ROS generation.

Besides using C-dots as bioimaging agents and photosensitizers, the other captivating application is metal ion sensing.[45] Transition metals like Fe^{3+} play an essential role in the chemistry of living organisms. An ample amount of iron is present in biological systems, which play a crucial role in many metabolic activities inside the body, like oxygen transportation gaseous exchange. It is part of many enzymatic reactions [46]. It is the central component of hemoglobin and an integral part of many proteins. Many diseases like anemia, sickle cell anemia and iron overload, hemochromasia, Alzheimer's, etc., happen due to decreased or elevated levels of Fe^{3+} respectively. Because of the hydrophobic nature of many available Fe^{3+} sensors, they are non-soluble in water, hindering their use in biological systems [47].

In this work, the nitrogen-doped C-dots (**N@VRCD**) were synthesized using a one-pot hydrothermal method using a sustainable resource, i.e., "Vigna radiata" sprouts that serve as an abundant source of carbon for the preparation of **N@VRCD** and ethylenediamine as the nitrogen source for doping. **N@VRCD** exhibits phototoxic behavior in the presence of visible light, which could be further explored for developing a new environment-friendly photosensitizer agent. Besides, it shows a "turn-off" response towards Fe^{3+} ions, which is further studied intracellularly using confocal microscopy and flow cytometry. Green chemistry of synthesis and the use of as prepared C-dots in photo-triggered theranostics using "*Vigna radiata*" has not been reported to date to the best of our knowledge. So, herein we present, for the first time, the synthesis of fluorescent C-dots using *"Vigna radiata"* as the sole carbon source and their evaluation for biocompatibility, live-cell imaging, photothermal therapy, and intracellular as well as extracellular Fe^{3+} ion sensing.

2.2. Results and discussion

2.2.1. Synthesis of N@VRCD

The nitrogen-doped **N@VRCD** was synthesized using the hydrothermal method at 180°C for 24 h (**Scheme 2.1**). Ethylenediamine (EDA) was used as a nitrogen source for doping. The reaction conditions were optimized to obtain a maximum quantum yield using different concentrations ranging from 200-1000 µL of ethylene diamine per 10 mL of "*Vigna radiata*" extract. The quantum yield was calculated for all the products and compounds having ethylenediamine 600 µL, 800 µL, and 1000 µL, showing almost a similar quantum yield (**Table 2.1**). The highest quantum yield was found to be ~58%. The increase in quantum yield can easily be explained based on nitrogen doping [55].

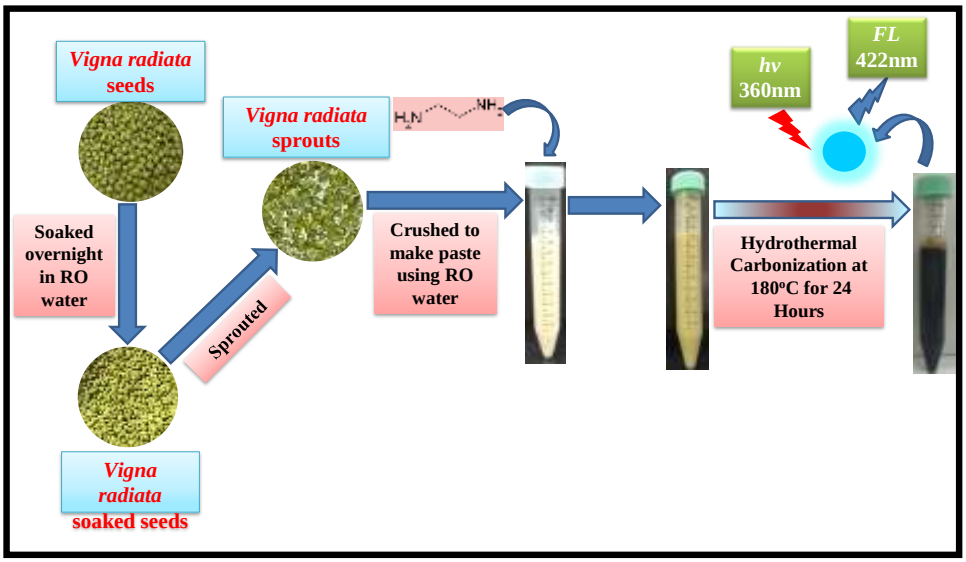

Scheme 2.1. Schematic illustration for synthesis strategy of **N@VRCD.**

For further optimization, two concentrations of ethylenediamine were chosen, i.e., 600 µL and 800 µL. Further, the two solutions of *"Vigna radiata"* extract with different concentrations of ethylenediamine were made by following the same method and were kept at 180 °C with varying times in the range of 5 h to 36 h. As there is not much difference in the quantum yield of reaction carried out for 24 h and 36 h, the minimum of

24 h had been chosen as a standard condition for maximum QY. The QY was further optimized to the maximum in varying temperatures in the range of 150 °C to 200 °C, and at 180 °C, the maximum QY was achieved. Purification could further enhance the QY, which needs further study [55].

Table 2.1. Optimization of Quantum yield of **N@VRCD** under varying conditions

S.No.	Conc. of EDA (ml/10ml of the sample)	QY[b]
1.	`200	42%
2.	400	44%
3.	600	48.37%
4.	800	48.41%
5.	1000	48.44%

S.No.	Time (h)	QY [b] (EDA 600ml/10ml)	QY[b] (EDA 800ml/10ml)
1.	5	48.37%	46.84%
2.	8	48.37%	48.41%
3.	12	53.57%	51.34%
4.	24	56.51%	55.73%
5.	36	57.27%	56.37%

S.No.	Temperature (°C)	QY [b]
1.	150	50.44%
2.	160	52.32%
3.	170	55.37%
4.	180	58.11%
5.	200	54.14%

[a] sample prepared in water, [b] determined by using quinine sulfate as the standard (Φ_{st} = 0.54, 0.1 M H_2SO_4)

Only "*Vigna radiata*" extract was also used to synthesize C-dots (VRCD) without any doping agent. The results are summarized in **Figure 2.1**. With the addition of EDA, the relative fluorescence intensity increases

drastically by more than 80%. Further, a more evident difference can be seen in the fluorescence intensity of VRCD and **N@VRCD** at emission wavelength@422nm. Thus, with nitrogen doping, fluorescence emission gets enhanced of **N@VRCD** w.r.to VRCD.

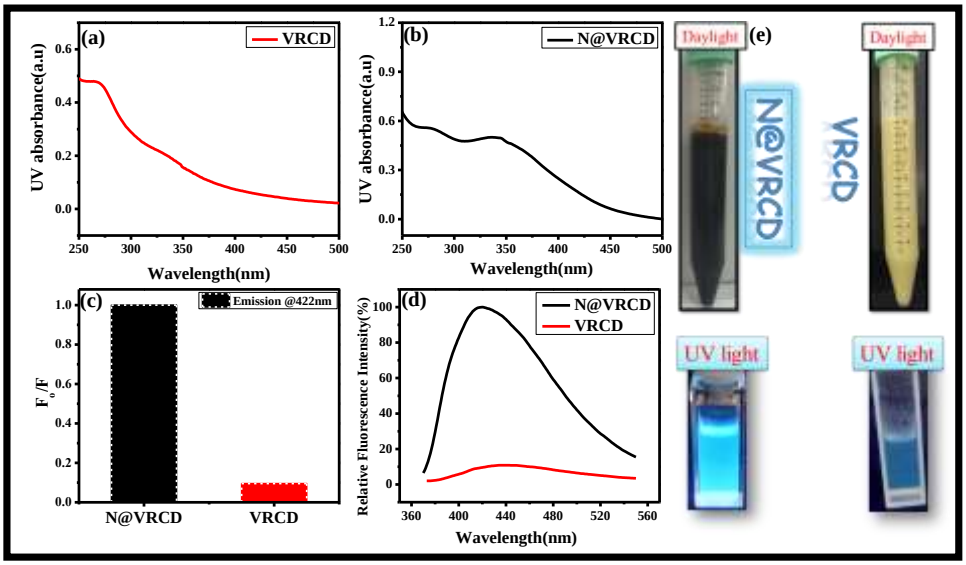

Figure 2.1. Comparison of **VRCD** and **N@VRCD** (a) Relative fluorescence intensity (b) Relative fluorescence intensity at emission wavelength 422nm (c) UV-vis spectra of **VRCD** (d) UV-Vis spectra of **N@VRCD** (e) Images of as-synthesized **N@VRCD** and **VRCD** in daylight and UV light.

2.2.2 Characterization of *N@VRCD*

The X-ray diffraction pattern showed one broad peak centered at 20.9° with the interlayer spacing of 4.2 Å, which is greater than graphite (3.3 Å), attributed to distorted sp^2 carbon structure (**Figure 2.2.a**). The surface ligands were analyzed using FT-IR, which shows prominent absorbance peaks of functional groups at 3428 cm^{-1} and 2925 $cm^{-1,}$ which includes stretching mode of C-H, O-H, and N-H, along with the vibrational mode of C=O at 1664 cm^{-1} and bending vibrations of CH_2 at 1401 cm^{-1} with an epoxide peak at 1048 cm^{-1} (**Figure 2.2.b**) [3,13].

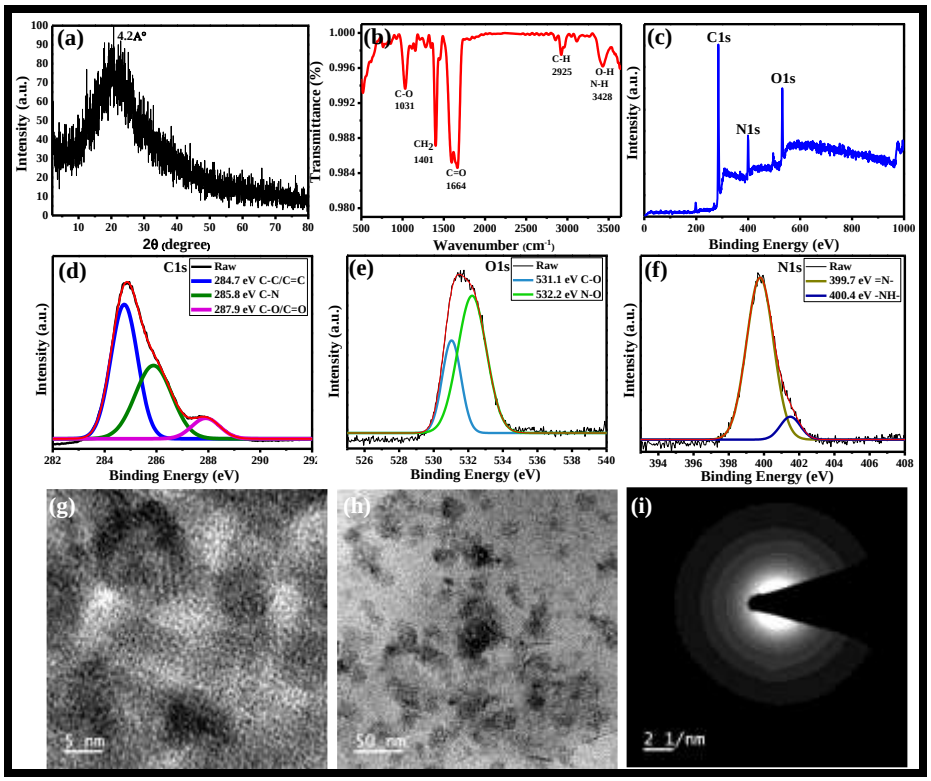

Figure 2.2. Structural characterization of **N@VRCD** (a) PXRD (b) FT-IR (c) XPS survey spectra. (d-f) High-resolution XPS spectra of C1s, N1s, and O1s, respectively (g) TEM micrograph (h) HR-TEM (i) SAED pattern.

X-ray photoelectron spectroscopy (XPS) was carried out to further structural information analysis. The survey spectrum of **N@VRCD** shown in **Figure 2.2.c** shows three peaks with binding energies of 284.8 eV, 399.2 eV, and 531.2 eV, which reveals the presence of graphitic or aliphatic carbon (C1s), nitrogen (N1s), and oxygen (O1s), respectively [11]. In the high-resolution XPS spectrum of C1s, three peaks of binding energies, 284.7 eV, 285.8 eV, and 287.9 eV, were obtained after deconvolution, which attributed to C-C/C=C (graphitic or aromatic carbon), C-N and C–O (epoxy and alkoxy), and C=O species respectively [11,56] (**Figure 2.2.d**). The deconvoluted spectrum of N1s exhibited N atom of both pyridinic type (399.7 eV) and pyrrolic type (400.4 eV),

which shows successful doping of C-dots with nitrogen (**Figure 2.2.e**). The high-resolution O1s spectrum could be deconvoluted into two peaks of energies 531 eV and 532.2 eV, which exhibit the presence of C-O and N-O bonds, respectively **Figure 2.2.f**. [57–59]. Further, the morphology of **N@VRCD** was explained by TEM (**Figure 2.2.g**). It exhibits that the shape is primarily spherical, and the size of C-dots is less than 10 nm. The HR-TEM image (**Figure 2.2.h**) displays clear lattice fringes, which indicate the crystallinity of **N@VRCD** [60]. SAED pattern is shown in **Figure 2.2.i,** it also confirms the poor crystallinity of **N@VRCD**. The presence of crystalline, as well as amorphous particles is similar to previous reports of C-dots.

2.2.3 Photo-physical properties of N@VRCD

The aqueous solution of **N@VRCD** shows two distinctive absorbance peaks at 276 and 344 nm (**Figure 2.3.a(i)**). The former peak is attributed to the π–π^* transition of the aromatic sp^2 domain and later n-π^* transition of C=O [61]. The absorbance peaks in the longer wavelength region are often seen after surface passivation. As we can observe in the absorbance plot of **VRCD** (**Figure 2.1.a),** there is no peak in the longer wavelength region [62]. Concurrently, **Figure 2.3.a** (inset) shows visual changes in the light-yellow colored solution of **N@VRCD** to a bright blue fluorescence when irradiated with a UV trans-illuminator at 365 nm.

The fluorescence spectra have been measured as a function of excitation wavelength (**Figure 2.3.a (ii), (iii)**). Emission maxima centered at 422 nm were obtained at 360 nm excitation wavelength, along with the excitation-dependent emission wavelength, which is the prominent feature of C-dots (**Figure 2.3.b**) [63]. Emission maxima range from about 410 nm to 530 nm, which could be utilized in multicolor imaging [64].

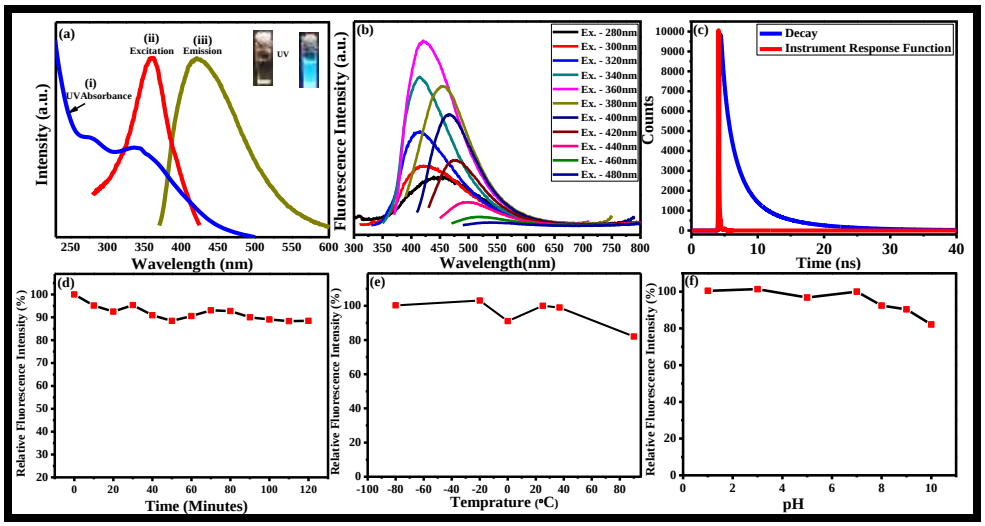

Figure 2.3. Optical characterization of **N@VRCD** (a) (i) UV–vis absorption spectrum of **N@VRCD** (ii) Fluorescence excitation spectra, (iii) emission spectra of **N@VRCD**. (Right inset) color of **N@VRCD** solution without & with UV irradiation (360 nm), (b) excitation-dependent emission (c) fluorescence lifetime decay (d-f) Stability of **N@VRCD**: at varying UV illumination (d), at different temperatures (e) and at the variable time (f).

Time-correlated single-photon counting (TCSPC) (**Figure 2.3.c**) was performed to obtain insight into the fluorescence response's kinetics of **N@VRCD** using a 375 nm diode laser. The data obtained after the best three-exponential function fitting showed the average lifetime of **N@VRCD** alone is 2.67 ns. Such a short average lifetime indicates that the fluorescence of **N@CRCD** is radiative recombination in nature [65,66]. Further, the fluorescence stability was determined under UV irradiation by the varying temperatures, time, and *p*H. **N@VRCD** shows exceptional stability after UV irradiation, as depicted in **Figure 2.3.d**. sample exposed to a 125 W UV (365 nm) lamp for 120 min retains 88% of initial fluorescence intensity. Similarly, fluorescence was stable at different temperatures up to 82% when kept at -80 ^{o}C, -20 ^{o}C, 0 ^{o}C, 25 ^{o}C, 37 ^{o}C and 90 ^{o}C for 2 h (**Figure 2.3.e**). After about 160 days of synthesis,

about 88% of initial fluorescence intensity was retained (**Figure 2.3.f**). The fluorescence ability of **N@VRCD** is also relatively stable in the *p*H range of 2-10. Thus**, N@VRCD** was highly stable under harsh conditions, and suitable for bio-imaging and intracellular sensing.

2.2.4 Evaluation of cellular response towards N@VRCD

2.2.4.1 Cell viability and cell imaging

Besides optical superiority, excellent biocompatibility is needed for **N@VRCD** for its biomedical applications. The cell viability studies were performed on HeLa and A375 cells (a human cervical cancer cell line and melanoma cell line, respectively) to determine the biocompatibility of **N@VRCD**. The results shown in **Figure 2.6.a** illustrate more than 75% cell viability after treatment with high concentrations ranging from 50 μg mL^{-1} to 1000 μg mL^{-1} for 24 h.

Further, when Hela cells and A375 cells were excited with 405 nm, 488 nm, and 559 nm lasers after 2 h incubation with **N@VRCD**, they showed blue, green, and red color fluorescence, respectively (**Figure 2.4**). The staining pattern confirms the membrane permeability of **N@VRCD,** and it also perpetuates its multicolor emission property in the cellular environment. However, the accurate localization could not be interpreted because **N@VRCD** emission spread over a wide range.

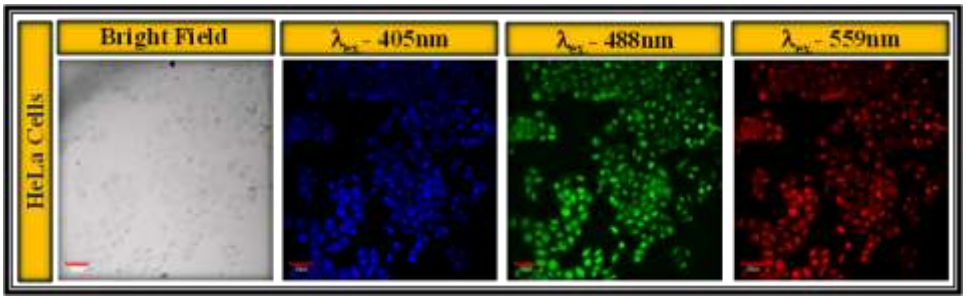

Figure 2.4. Bio-imaging of HeLa cells using **N@VRCD** (50 μg mL^{-1}) at 37 ℃ for 2 h at various excitation wavelengths.

2.2.4.2 Hemocompatibility

To check the human blood compatibility, a hemolysis ratio test was performed. Due to the health implications of C-dots, it's essential to understand their effect on red blood cells (RBCs). The results obtained from the hemolysis study shown in **Figure 2.5** ratify the hemocompatible nature of **N@VRCD**. Less than 5% hemolysis was observed even when RBCs were exposed to a very high concentration of 50 mg mL^{-1}. Positive control clearly shows the red color of the supernatant due to the presence of free hemoglobin. In contrast, the treated samples do not offer any red color of the supernatant, and their color resembles that of negative control (**Figure 2.5.b**). Any material showing less than 5% hemolysis is considered hemocompatible [67]. The SEM images of RBCs treated with varying concentrations of **N@VRCD** further confirm the biconcave morphology of RBCs and support the hemocompatible nature (**Figure 2.5.c**). Thus, surface passivation helped the non-hemolytic nature of **N@VRCD** consistent with earlier reports.[68].

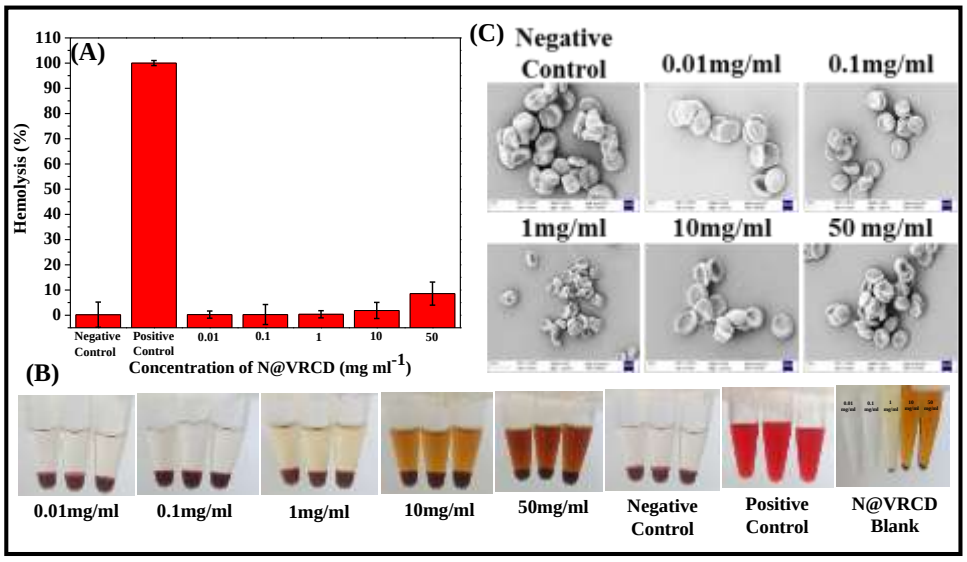

Figure 2.5. Hemocompatibility of **N@VRCD** (A) graphical representation of % hemolysis after 1 h incubation of RBCs with different concentrations of **N@VRCD** (B) Camera images of control and experimental samples. (C) SEM images of **N@VRCD** treated RBCs.

2.2.4.3 Photo-cytotoxicity

Bioimaging studies have already established that **N@VRCD** is being taken up by the cells and is non-cytotoxic. However, phototoxicity of carbon nanomaterials such as graphene quantum dots was investigated [40] for further applicability. Thus, photo cytotoxicity of **N@VRCD** was investigated here. The photocytotoxicity profile in the presence of visible light (400-700 nm) was studied to evaluate the photodynamic capability of **N@VRCD**, which was calculated in terms of IC_{50} value in HeLa and A375 cells by using a MTT assay. **N@VRCD** was surprisingly photo cytotoxic with an IC_{50} value in Hela and A375 cells having concentrations of 505 μg mL^{-1} and 310 μg mL^{-1}, respectively (**Figure 2.6**) when exposed to visible light while being non-cytotoxic in the dark. The plausible mechanism of cytotoxicity was the generation of reactive oxygen species (ROS). To get further insights into the mechanism, ROS generation was determined using a singlet oxygen scavenger DPBF in vitro. In contrast, intracellular ROS generation was determined by using DCF-DA, ROS detection assay.

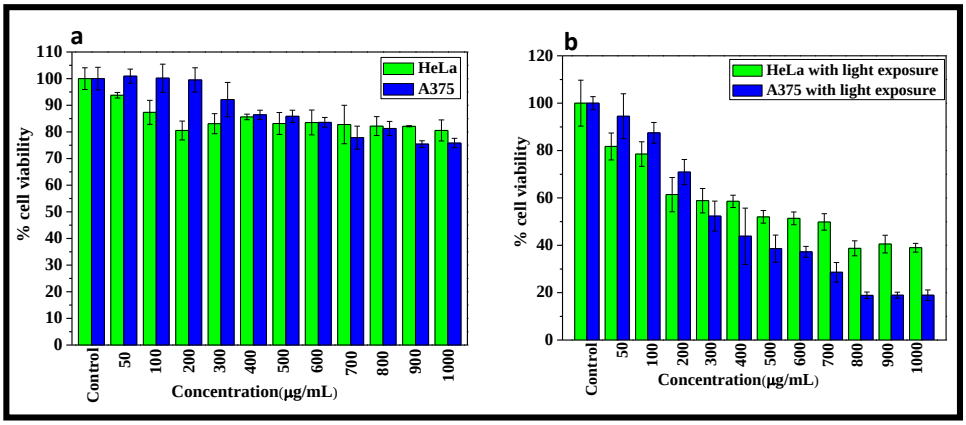

Figure 2.6. (a) Cell viability of A375 and HeLa after 24 h with various concentrations of **N@VRCD** (50μg mL-1 – 1000 μg mL-1) (b) Cell viability of A375 and HeLa cells after 1 h exposure to visible light (400-700nm)

2.2.4.4 Singlet oxygen measurement

To foresee the possibility of intracellular ROS generation, the ability of **N@VRCD** to generate singlet oxygen was studied. One of a photosensitizer's most important photochemical properties is singlet oxygen production. The singlet oxygen produced by **N@VRCD** upon irradiation reacts with DPBF, leading to a decrease in the absorbance at 414 nm. As shown in **Figure 2.7** absorbance value was taken after each irradiation with a time interval of 5 sec. The significant and gradual decrease in absorbance indicates the formation of photo-induced singlet oxygen in the solution of **N@VRCD** in DCM. At the same time, when the only **N@VRCD** solution in DCM with DPBF was irradiated, no change in absorbance value indicated any degradation of **N@VRCD** in the presence of light. The singlet oxygen quantum yield ($\Phi\Delta$) was found to be 0.41. The obtained results indicate the role of ROS in photo-induced cell death. A linear relationship between time and absorbance value was shown in **Figure 2.7.b**.

According to earlier reports, when specific nanoparticles are irradiated with light, they get excited and react with molecular oxygen present in the system, producing ROS and cytotoxicity. Carbon dots upon photoexcitation show electron excitation from the valence band to the conduction band and form electron-hole pair. However, when these electrons combine with surface-bound molecules such as oxygen, free radicals are formed, which lead to hydroxyl radical formation.[42]

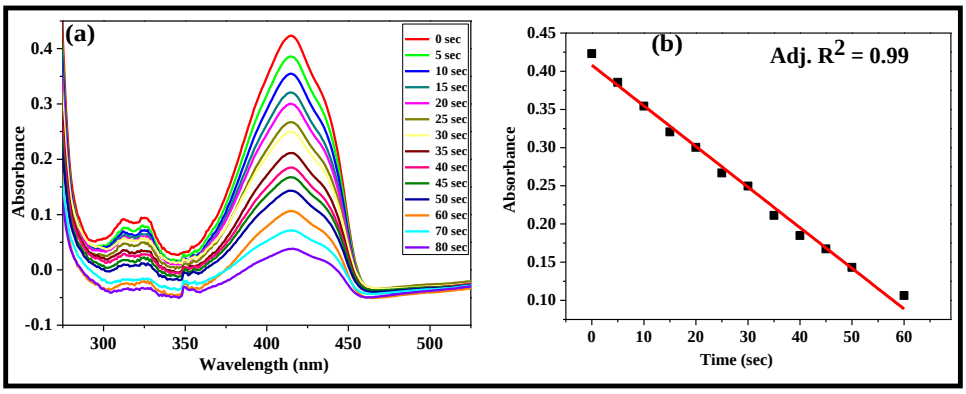

Figure 2.7. (a)The absorbance decay spectra of DPBF in the presence of **N@VRCD** with various irradiations (b) Relationship between the absorbance of DPBF with irradiation time in the presence of **N@VRCD**

2.2.4.5 Intracellular ROS generation assay

To further confirm the intracellular generation of ROS in the presence of light, a DCFDA assay was carried out, which was widely used to measure the cell's redox state. 2′-7′-dichlorodihydrofluorescein diacetate (DCFDA), a non-fluorescent compound that can quickly enter the cell via cell membrane and accumulate inside the cell, which on oxidation by ROS species provides a highly fluorescent compound 2',7'-dichlorofluorescein (DCF). The concentration of DCF could be measured by exciting it by 485nm, which gives emission maxima at 530 nm. The studies were carried out on the A375 cell line. The samples were only cells (control), only DCFDA treated cells, and cells treated with DCFDA and **N@VRCD** after irradiation for 1 h with visible light of 400-700 nm or in the dark (as control). A clear shift was readily observed in the fluorescence data obtained using FACS of cells treated with **N@VRCD** then exposed to light compared to those treated with **N@VRCD** alone or with **N@VRCD** and DCFDA in the dark (**Figure 2.8**). This infers ROS formation by **N@VRCD** on visible light exposure; however, no such observation was observed when placed in the dark, which supports lower cell viability due to ROS arbitrated cell death. To the best of our knowledge, the present

work is the first report investigating the photo-toxic nature of green carbon dots on human cell lines (**Table 2.3**).

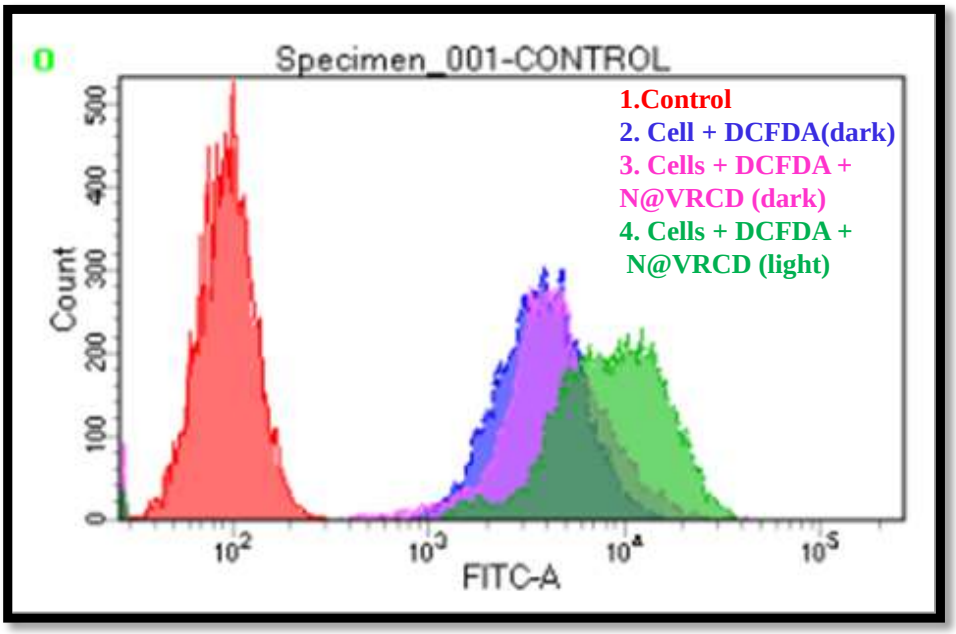

Figure 2.8. The study of shift in fluorescence intensity of only cells (control) compared with the addition of different additives under different conditions as mentioned in A375 cells shown as a histogram, done using a flow cytometer.

2.2.5 Analytical sensor response of N@VRCD

The dual ability of C-dots to act as an electron acceptor and electron donor leads to fluorescence quenching due to the electron transfer between metal and the C-dots. The water-soluble nature of **N@VRCD** makes it a potential candidate to be a sensor in biological systems.

The fluorescence "turn off" response of water-soluble **N@VRCD** towards Fe^{3+} was one of the interesting findings and was consistent with the earlier reports.[69] As shown in **Figure 2.9**, the fluorescence quenching was observed when the aqueous solution of Fe^{3+} in the range of 0-3000µM was added to the **N@VRCD** solution. A good linear correlation was found between 100-1000 µM and 1000-2000 µM, for which an adj. R^2 value is

0.98 and 0.99 respectively (**Figure 2.9.b**). The following equation was used to calculate the limit of detection [51].

Limit of detection (LOD) = 3.3(σ/S) (3)

In this equation, S represents the calibration curve's slope, and σ represents standard error. LOD was found to be as low as 140 nM. Further, the fluorescence intensity gradually decreased to 13% of the initial intensity of **N@VRCD** after the addition of 3000 µM Fe^{3+} solution.

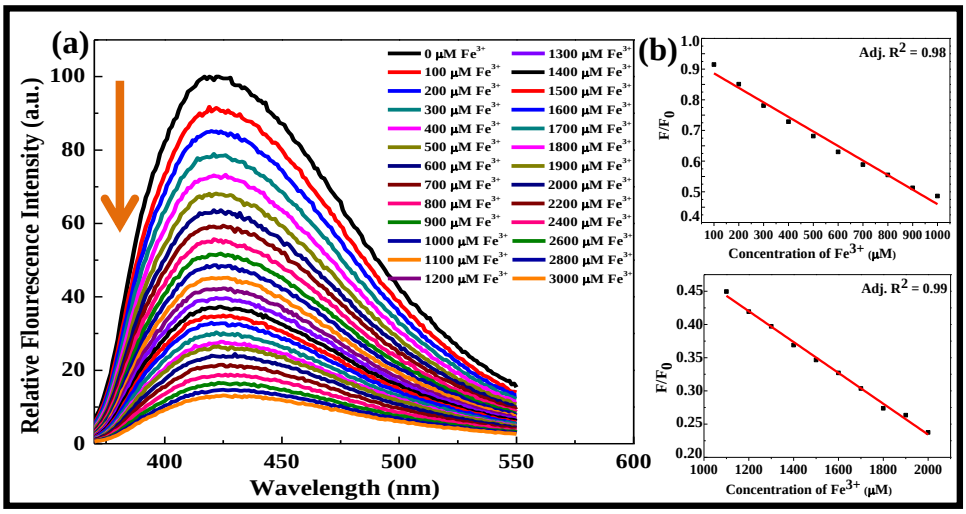

Figure 2.9. (a) **N@VRCD's** Fluorescence spectra after addition of Fe3+ (concentration range from 100 µM - 3000 µM) (b) Relationship between concentration of Fe^{3+} and F/F_0.

2.2.6 The mechanism for fluorescence quenching of N@VRCD

According to previous reports, the "turn-off" behavior of **N@VRD** can be explained by the electron transfer mechanism and formation of the metal-fluorophore complex [8,28,70]. As elaborated in **Figure 2.10,** plentiful phenolic hydroxyl group (-OH) present on the surface of **N@VRCD** form specific coordination interaction with Fe^{3+}. The formation of this complex leads to the splitting of the d orbital of Fe^{3+}, which facilitates the non-radiative electron-hole recombination, leading to significant fluorescence quenching. The Quencher molecule (Fe^{3+} in this case) reacts with the fluorophore (**N@VRCD**) either at the ground state or excited state leading

to static or dynamic quenching.[71] Apart from this, the redox potential of Fe^{3+}/Fe^{2+} is in the middle of the conduction and valence bands of **N@VRCD**, so photo-induced electrons can be transferred to the complexed Fe^{3+} from **N@VRCD's** surface, resulting in fluorescence quenching [72,73].

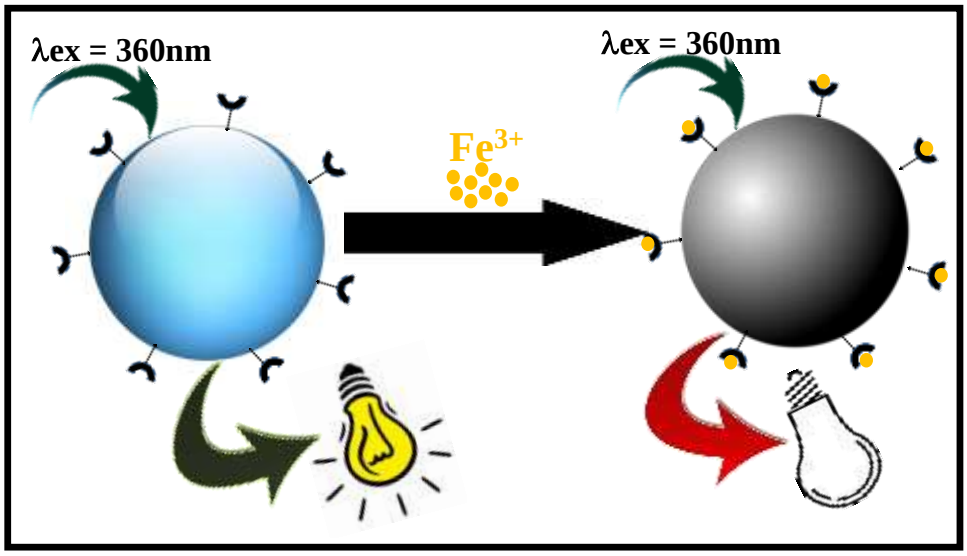

Figure 2.10. The mechanism for fluorescence quenching of **N@VRCD**

To confirm the electronic communication between the **N@VRCD** system and Fe(III), theoretical calculations were performed based on density functional calculation. Two types of basic sets were used in DFT calculations, (i) 6-31G basic sets were used for carbon (C), hydrogen (H), Oxygen (O), and Nitrogen (N), and (ii) LanL2DZ basic was used for Fe (III). The energy and geometry optimization was performed using Gaussian 09 program. [74,75] HOMO and LUMO energy of the N@VRCD system was found to be -4.2936 eV and -2.9124 eV, respectively. The LUMO energy of N@VRCD was higher than that of the standard reduction potential of the Fe^{2+}/Fe^{3+} system, which is 0.77 V, which indicates the favorable electron transfer from **N@VRCD** to Fe(III). Moreover, the HOMO and LUMO energy of the **N@VRCD** system was calculated to be -4.2936 eV and -2.9124 eV, respectively. While in the

case of **N@VRCD** –Fe(III), HOMO and LUMO energy were found to be -4.5970 eV and -3.2977 eV, respectively. Moreover, The theoretical band gaps of **N@VRCD** and **N@VRCD** –Fe(III) were found to be 1.38 and 1.29 eV, respectively (**Figure 2.11**).

Systems	HOMO	LUMO	Band-gap
N@VRCD	 **-4.2936 eV**	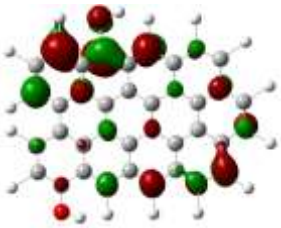 **-2.9124 eV**	**1.38 eV**
N@VRCD -Fe^{3+}	 **-4.5970 eV**	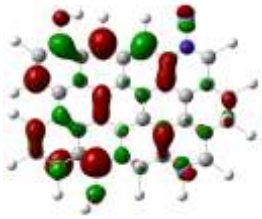 **-3.2977 eV**	**1.29 eV**

Figure 2.11. Frontier molecular diagrams of **N@VRCD** and **N@VRCD-Fe(III)** systems at 0.03 iso values.

Further, to get insights into fluorescence response kinetics of **N@VRCD**, TCSPC was done using a 375 nm diode laser with and without the addition of Fe^{3+} in **N@VRCD** solution in water. The results are obtained in **Figure 2.12. a** revealed that there is not much difference in average life

lime of the control sample, i.e., **N@VRCD** alone and after adding various concentrations of Fe^{3+} solution, indicating the static quenching in the **N@VRCD**-Fe^{3+} system.

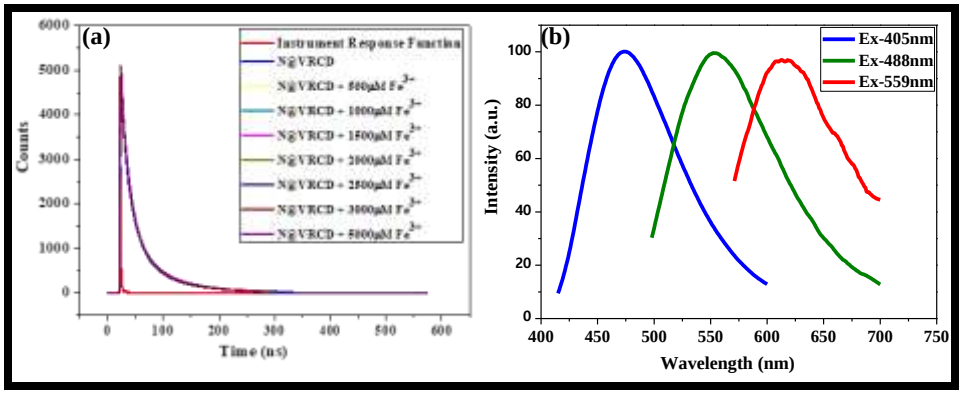

Figure 2.12. (a) Fluorescence lifetime decay of **N@VRCD** in the absence and presence of Fe^{3+} (b) Emission spectra of **N@VRCD** excited at 405 nm, 488 nm, and 559 nm, respectively

2.2.7 Selectivity and sensitivity studies of N@VRCD towards Fe^{3+}

Furthermore, to evaluate the selectivity of the sensor specifically towards the $Fe^{3+,}$ the fluorescence quenching effect of various metal ions and anions (Co^{2+}, Li^{+}, K^{+}, Zn^{2+}, Al^{3+}, Mn^{2+}, V^{+}, Mo^{+}, Sn^{2+}, Ag^{+}, Ba^{2+}, Mg^{2+}, Ga^{3+}, Fe^{2+}, Na^{2+}, Cd^{2+}, Cr^{2+}, Ca^{2+}, Cu^{2+}, La^{3+}, Pt^{+}, Hg^{2+}, Ni^{2+}, S^{2-}, $CH3COO^{-}$, CO_3^{2-}, No^{3-}, PO_4^{3-}, $S_2O_8^{2-}$ and SO_4^{2-}) on **N@VRCD** was investigated. As depicted in **Figure 2.13.a** Fe^{3+} exhibits the most significant effect on fluorescence quenching among all the metal ions. Moreover, competitive selectivity studies were performed to check the impact of other anions and cations on the sensing behavior of **N@VRCD**. As shown in **Figure 2.13.b-c**, even in the presence of various other anions and cations, the **N@VRCD** could sense Fe^{3+} effectively. The quenched fluorescence of **N@VRCD**/Fe^{3+} was recovered up to 32% of the original when Phosphate ions were added to the mixture. No other anion or cation showed any such effect, as shown in **Figure 2.13.a(inset)**. This could be

due to the competitive interaction of **N@VRCDs** between phosphate molecules and Fe^{3+}.

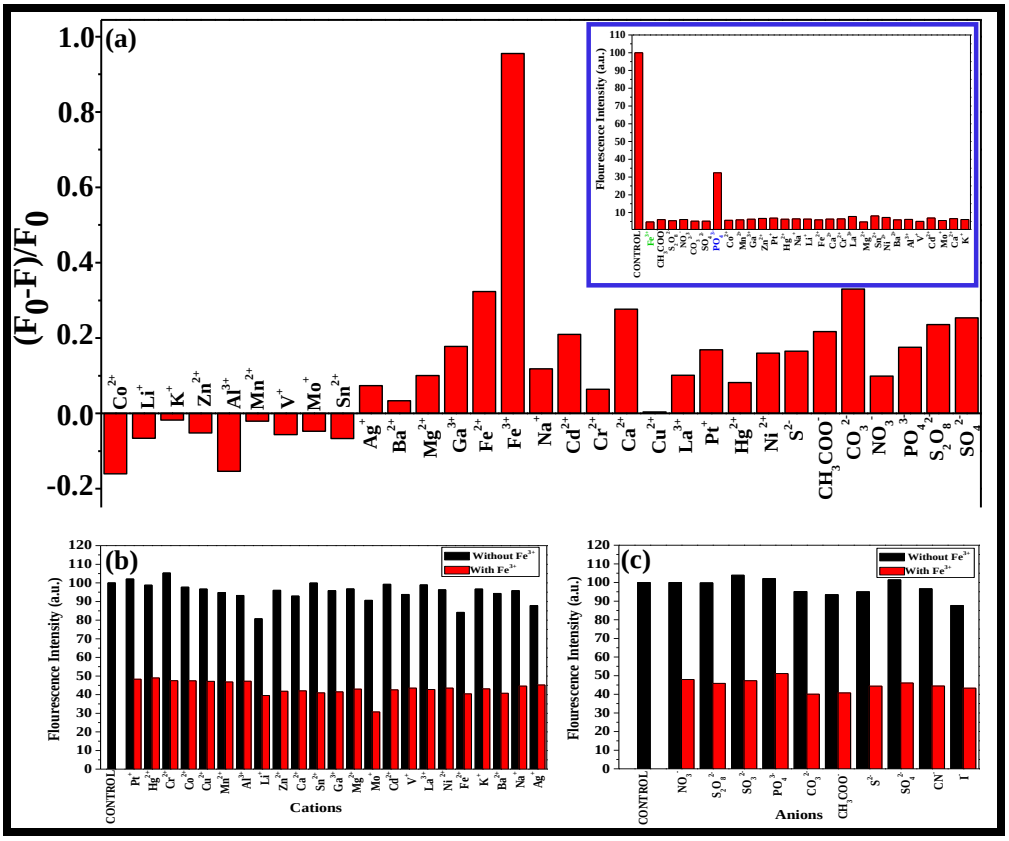

Figure 2.13. (a)Selectivity in the sensing response of various metal ions (c = 1.0×10^{-2} M) with **N@VRCD** (0.5mg mL^{-1} in water) (inset) Fluorescent recovery after quenching with Fe^{3+} upon addition of various cations and anions. (b-c) Competitive Selectivity in the sensing response of **N@VRCD** in the presence of cations and anions (c = 1.0×10^{-2} M).

2.2.8 In-vitro intracellular Fe^{3+} ion sensing

The suitability of **N@VRCD** as an intracellular Fe^{3+} sensing agent was checked using confocal microscopy and flow cytometry. The fluorescence was quenched completely when cells treated with **N@VRCD** were incubated with Fe^{3+} (**Figure 2.14.a-c**), which verified the authenticity of spectroscopic studies. The flow cytometry experiment endorsed fluorescence quenching after adding Fe^{3+} ions (**Figure 2.14.g-i**). It must

be mentioned here that **N@VRCDs** act as a nanosensor for sensing of $Fe^{3+,}$ having excellent sensing capability with a better limit of detection and broader liner range w.r.to other reported literature (**Table 2.4**).

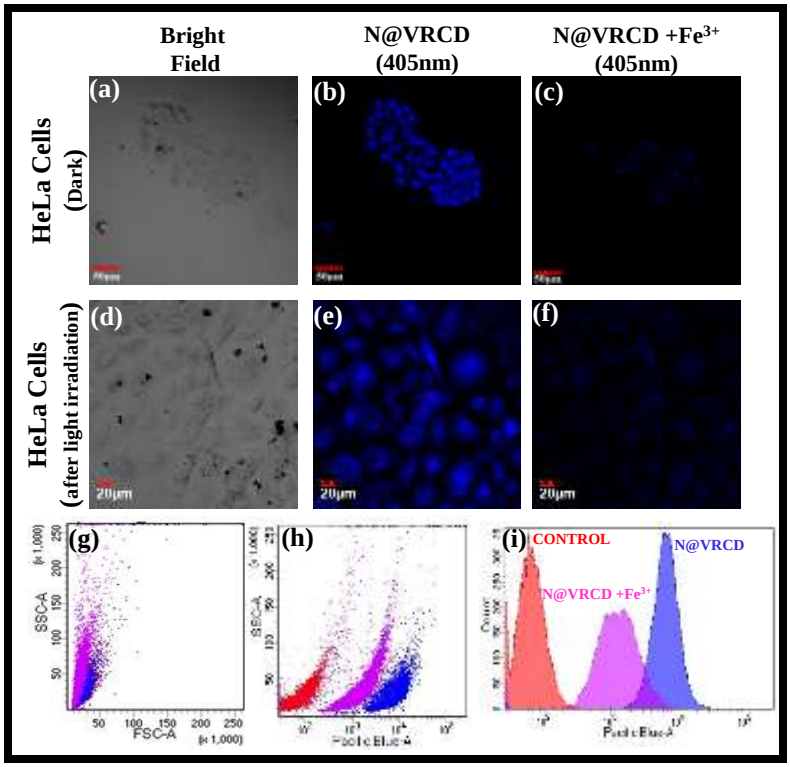

Figure 2.14. Intracellular sensing of Fe^{3+} in HeLa cells treated with **N@VRCD** (50 μg mL^{-1}) at 37°C for 2 h with the help of confocal microscopy (a,d) Bright field (b,e) at $\lambda_{ex}/\lambda_{em}$ = 405/450 ± 25 nm (c) **N@VRCD**+ 500μM of Fe^{3+} (f) **N@VRCD**+ 500μM of Fe^{3+} (after light irradiation) (g-i) Intracellular fluorescence intensity determination of control, **N@VRCD** treated and **N@VRCD** + Fe^{3+} treated HeLa cells using flow cytometry.

Also, the green synthetic approach, very high quantum yield, excellent bio, and hemocompatibility make **N@VRCD** a potential candidate for its application in Fe^{3+} sensing. Moreover, ROS is being generated only in the presence of light. For Fe^{3+} determination, no such condition is required. Still, we have checked the effect of ROS on Fe^{3+} determination in live

cells by determining it after exposing the cells to light for one hour. As per our expectations, Fe^{3+} still be determined without any difficulty, even in the ROS-containing cells (**Figure 2.14.d-f)**.

Table 2.2. Various Green precursors for the synthesis of C-dots and their quantum yield

S.no	Green source	QY	Ref.
1.	Konjac flour	22%	**[10]**
2	Hair	17%	**[11]**
3	Grass	6.2%	**[17]**
4	Coffee grounds	3.8%	**[16]**
5	Banana juice	8.9%	**[13]**
6	*Chionanthus retusus*	9%	**[8]**
7	Milk	12%	**[14]**
8	Silkworm chrysalis	46%	**[61]**
9	Peanut shells	9.91%	**[76]**
10	*S. officinarum* juice	5.76%	**[15]**
11	Oatmeal	37.40%	**[77]**
12	Crab shells	19.84%	**[78]**
13	Lactobacillus plantarum	16%	**[79]**
14	Sweet pepper	19.3%	**[80]**
15	*Phyllanthus acidus*	14%	**[81]**
16	*Vigna radiata*	58%	**Present work**

Table 2.3. The comparison of C-dots prepared using "*Vigna radiata*" with other recently reported green precursor-derived C-dots.

	Green Precursor	Bio-imaging	Sensing	Hemo-Compatibility	Intra-cellular sensing	ROS	Ref.
1	Black pepper	✓	x	x	x	x	**[82]**
2	Pork	x	Uric Acid	x	x	x	**[83]**
3	Vege-table waste	x	Alka-line phos-phate	x	x	x	**[84]**
4	Rose-heart radish	✓	Fe^{3+}	x	✓	x	**[85]**
5	Caffeine	x	Ag^{+}	x	x	x	**[86]**
6	Date kernel	✓	Zole-dronic acid	x	x	x	**[87]**
7	Peanut shells	✓	x	x	x	x	**[76]**
8	Jinhua bergamot	x	Hg^{2+} and Fe^{3+}	x	x	x	**[88]**
9	Water Chestnut and Onion	✓	Co-enzyme A	x	✓	x	**[89]**
10	***"Vigna radiata"***	✓	✓	✓	✓	✓	**Present work**

Table 2.4. Performance comparison of various fluorescence-based Fe^{3+} sensors.

S. No.	Sensing Element	Green Sensor	Method	Linear Range	LOD	Ref.
1	Nitrogen-doped carbon dots	No	Flu. "Turn Off"	0.010 –1.8 ppm	10 ppb	**[90]**
2	Nitrogen-doped carbon dots	No	Flu. "Turn Off"	X	20 nM	**[91]**
3	C-dots	Yes	Flu. "Turn Off"	0.025–100 µM	0.075 µM	**[88]**
4	N and S doped carbon dots	No	Flu. "Turn Off"	6.0–200 µM	0.80 µM	**[92]**
5	Carbon nanodots	No	Flu. "Turn Off"	X	0.04 µM	**[47]**
6	1,8-naphthalimide dye	No	Flu. "Turn Off"	1.33×10^{-7}– 4.00×10^{-4} mol L^{-1}	X	**[93]**
7	Fluorescent carbon nanoparticles	No	Flu. "Turn Off"	0.1 – 500 µM	30 nM	**[94]**
8	CDs	No	Flu. "Turn Off"	x	1 ppm	**[95]**
9	N-CDs	Yes	Flu. "Turn Off"	0-2 mM	70 mM	**[8]**
10	Nitrogen-doped carbon dots	No	Flu. "Turn Off"	0–1000 µM	79 nM	**[96]**
11	FNCDs	Yes	Flu. "Turn Off"	2–25 µM	0.9 µM	**[81]**
12	PProDOTCB-salt	No	Flu. "Turn Off"	0.047–0.084 mM	0.023 mM	**[97]**
13	Bis(rhodamine)	No	Flu. "Turn On"	150-237.5 µM	x	**[98]**
14	Derivative of naphthalimide	No	Flu. "Turn Off"	1µM - 1000 µM	4.5 µM	**[99]**
15	*Syzygium cumini*	Yes	Flu. "Turn Off"	0.01–100 µM	0.001 µM	**[69]**
16	*Solanum lycopersicum*	Yes	Flu. "Turn Off"	0.1 - 2.0 µM	X	**[71]**
17	**N@VRCD**	Yes	Flu. "Turn Off"	100- 2000 µM	140 nM	**Present work**

2.3. Conclusion

A new green source, "*Vigna radiata*," was explored to efficiently synthesize multi-talented C-dots doped with nitrogen to get the highest quantum yield (~58%) reported using a green source. The nitrogen-doped surface passivated C-dots (**N@VRCD**) exhibited excellent water solubility and bright multicolor fluorescence with great photo-stability. The as-prepared green C-dots were photo-toxic due to ROS formation in the presence of light. They were observed by singlet oxygen measurement and intracellular ROS detection studies. The novelty of the present work opens grounds to explore **N@VRCD** for making a new chemotherapeutic agent for cancer treatment. Moreover, it showed a highly selective and sensitive "turn-off" response towards Fe^{3+} ions. The reasonable biocompatibility and hemocompatibility make it a promising multicolor fluorescent agent for live-cell imaging, bio labeling, and intracellular Fe^{3+} ion sensing.

2.4. Experimental section

2.4.1. Materials and reagents

The purchasing of "*Vigna radiata*" (green gram) seeds was done locally. Ethylenediamine was attained from sigma-Aldrich. The anions and metal salts were procured from sigma-Aldrich and Merck. No further purification was done of the received analytical grade chemicals. The work was completed using the Sartorius Milli-Q system's Deionized water (DI).

2.4.2. Instruments

The X-ray diffraction (XRD) was analyzed using a Rigaku, RINT 2500 V X-ray diffractometer with Cu Kα radiation (1.5406 Å). The Varian Cary 100 Bio UV-visible spectrophotometer was used to perform UV-visible spectroscopic studies. A Fluoromax spectrofluorometer was used to conduct fluorescence studies. IR spectra (4000–400 cm^{-1}) and X-ray photoelectron spectroscopy (XPS) were recorded using the Bio-Rad FTS 3000MX instrument and AXIS ULTRA. TEM images were recorded using a FEI Tecnai G2- F20 Transmission Electron Microscope. The cellular imaging studies were carried out using an Olympus laser scanning microscope. Synergy H1 Biotek microplate reader used for absorption studies of MTT assay. Flow cytometric analysis was performed on BD LSR Fortessa.

2.4.3. Synthesis of N@VRCD

Hydrothermal carbonization was used for the synthesis of **N@VRCD**. "*Vigna radiata*" seeds (250 gram) were washed thoroughly with running tap water and were immersed in 500 mL of RO water for 12 h. To get sprouts, soaked seeds were kept covered with a damp cloth for 24 h. The sprouts were ground using a domestic mixer by adding 200 mL of RO water to get a thick "*Vigna radiata*" extract. Further, 10 mL of "*Vigna radiata*" extract was mixed with different concentrations from 200 μL to 1000 μL of ethylenediamine. The mixture was sonicated for 10 min to

achieve a homogenous solution. The solution was then transferred to a Teflon-lined autoclave followed by hydrothermal treatment at 180^{o}C for a period of 24 h. The autoclave was kept at room temperature for cooling down. The product suspension was centrifuged at high speed to remove large particles to purify. Black sticky product (**N@VRCD**) was obtained by lyophilization and was re-suspended in water as per requirement.

2.4.4. Calculation of quantum yield

The quantum yield was calculated according to the procedure suggested in the manual "A Guide to Recording Fluorescence Quantum Yields" by HORIBA Jobin Yvon IBH Ltd. and the published procedure [48]. The fluorescence quantum yield (ΦF) of **N@VRCD** was calculated by using equation (1), where quinine sulfate dissolved in 0.1M H_2SO_4 was taken as the standard (Φst = 0.54)

$$\Phi F = \Phi_{st} \times S_s / S_{st} \times A_{st} / A_s \times n2_s / n2_{st} \quad (1)$$

where ΦF is the emission quantum yield of the sample, Φst is the emission quantum yield of the standard, i.e., quinine sulfate (0.54) [49], A_{st} and A_s represent the absorbance of the standard, and the sample at the excitation wavelength, respectively. At the same time, S_{st} and S_s are the slopes from the plot of the integrated fluorescence intensity vs. the absorbance of the standard and the sample at different concentrations, respectively, and n_{st} and n_s are the solvent refractive index of the standard and the sample. Subscripts s and st refer to the sample and the standard, respectively. The procedure followed is as written below:

(1) Integrated fluorescence intensities were measured at excitation wavelength 345 nm when the absorbance was set as 0.02, 0.04, 0.06, 0.08, and 0.1 at 345 nm of QS.

(2) The integrated fluorescence intensity vs. the absorbance of QS was plotted, and the slope was calculated (**Figure 2.15**).

(3) Similarly, Integrated fluorescence intensities were measured at excitation wavelength 360 nm when the absorbance was set as 0.02, 0.04, 0.06, 0.08, and 0.1 at 360 nm of **N@VRCD.**

(4) The integrated fluorescence intensity vs. the absorbance of **N@VRCD** were plotted, and the slope was calculated.

(5) The final calculations were made by putting values in equation 1.

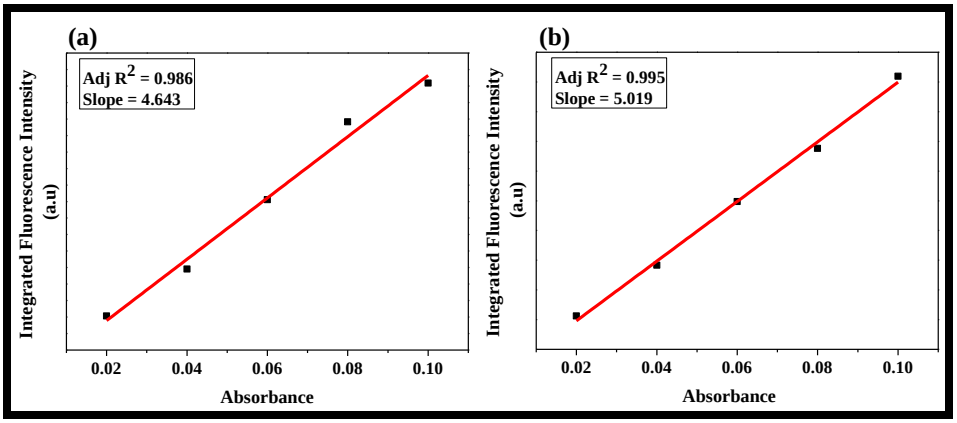

Figure 2.15. (a) The plot of integrated Fluorescence intensity (excited at 345 nm) against absorbance values at 345 nm of quinine sulfate (QS) (b) Plot of integrated Fluorescence intensity (excited at 360 nm) against absorbance values at 360 nm of **N@VRCD**.

2.4.5. Fe (III) ions detection and selectivity studies.

The metal ions detection procedure was as follows.

The fluorescence spectrum of 2 mL aqueous solution of **N@VRCD** was recorded at $\lambda_{ex.}$ 360 nm and maximum intensity were set as control (F_0). In the meantime, all the metal solutions were prepared by dissolving salts of Na^+, Zn^{2+}, Ba^{2+}, Al^{3+}, Fe^{3+}, Mg^{2+}, Mn^{2+}, Cu^{2+}, Fe^{2+}, Cd^{2+}, Cr^{3+}, Ni^{2+}, and K^+ in milli-Q water to get a final concentration of 10 mM. The solution of different metal ion as-synthesized was mixed with the **N@VRCD** solution, and fluorescence spectra were recorded at λ_{ex}. 360 nm. All the experiments were done at room temperature under similar conditions. The highly sensed metal ion was determined, and further sensing experiments were conducted at lower concentrations (0-1000 μM). Subsequently, competitive selectivity for Fe^{3+} was done in the presence of other metal ions.

2.4.6. Cytotoxicity, Bio-Imaging, and Flow Cytometric Studies.

Cell viability was studied using HeLa (cervical cancer cell line) and A375 (human melanoma cell line) by performing 3-(4,5-dimethylthiazole-2-yl)-2,5-diphenyltetrazolium bromide (MTT assay) [50,51]. The purple-colored formazan produced by reducing yellow tetrazolium by metabolically active cells was quantified by dissolving them in DMSO and recording the absorbance at 570 nm. Dulbecco's modified Eagle medium supplemented with 1% antibiotics penicillin/streptomycin, 10,000 U $mL^{-1,}$ and 10% (v/v) fetal bovine serum was used to grow cells in a 96-well plate. $1x10^4$ cells in 100 μL of growth media were seeded in each well and allowed to grow using a 5% CO_2 humidified atmosphere at 37 ℃ for 24 h. Different concentrations of **N@VRCD** ranging from 50 μg mL^{-1} to 1000 μg mL^{-1} were added to the wells in triplicates. The wells containing growth media only were taken as control. After 24 h incubation, the **N@VRCD** containing media was replaced with fresh media having MTT (0.5 mg mL^{-1}) dissolved in it, which was further incubated for 4 h. The purple formazan crystals so formed were dissolved in 100 μL of DMSO. The absorbance was read at 570 nm. The percent cell viability was calculated using the following equation (2).

$$\% \text{ Cell Viability} = \text{Abs}_{(\text{Exp.})} / \text{Abs}_{(\text{Control})} \times 100 \quad (2)$$

Bio-imaging was done using HeLa and A375 cells grown in confocal dishes for 24 h and treated with **N@VRCD** (250 μg mL^{-1}) for 2 h. The cells were washed with 1X PBS twice after treatment, and live-cell images were taken using a confocal laser scanning microscope using blue, red, and green laser sources.

The flow cytometric studies were carried out to investigate further the staining abilities of **N@VRCD** and its sensing behavior towards Fe^{3+} ions. Cells were grown in a 6-well plate until they achieved 100% confluency. Cells of wells without treatment were taken as control. The stained sample consists of cells treated with **N@VRCD** (250 μg mL^{-1}) for 2 h. For Fe^{3+} ion sensing, the cells were first treated with **N@VRCD** and then exposed

to the Fe^{3+} solution. The cells were trypsinized, and the pallet was collected after centrifugation, and further dissolved in 1X PBS for flow cytometric analysis.

2.4.7. In-vitro PDT effect

Photo-toxicity studies were performed similarly to that of cytotoxicity studies. Two 96 well plates were divided into dark control and light experiment groups. Cells were grown for 24 h. Treatment of **N@VRCD** was given from 50 μg mL^{-1} to 1000 μg mL^{-1} in both plates. After 4 h of treatment, cells of 96 well plates belonging to the light experiment group were exposed to the visible light lamp (400-700 nm) for 1 h and again incubated for the next 20 h. The other dark control 96 well plate was kept under identical conditions but without irradiation. As mentioned above, cell viability was measured by MTT assay, and % cell viability were calculated subsequently.

2.4.8. Intracellular reactive oxygen species (ROS) generation assay

2', 7'- dichlorofluorescein diacetate (DCF-DA) was used to determine the generation of Intracellular reactive oxygen species (ROS) in live cells. The ROS generation studies used HeLa and A375 cell lines (plated in duplicate). After 24 h of growth, the cells were incubated in the presence and absence of **N@VRCD** (treatment concentration = IC_{50} value in the presence of light), dispersed in DMEM, and incubated for 4 h. Further, one set was photo-irradiated, and the other was kept in the dark. DCF-DA (30 μM) was added, and the plates were incubated in the dark at 37 °C for 30 min. Cells without DCF-DA were treated as a negative control. All the cells were trypsinized, centrifuged, suspended in 1X PBS, and analyzed in the flow cytometer using $\lambda_{exc.}$= 488 nm.

2.4.9. Singlet oxygen ($^1O_2$) measurements by DPBF chemical trapping

The singlet oxygen ($^1O_2$) generation capability of **N@VRCD** was assessed by using 1, 3-diphenylisobenzofuran (DPBF) as a detection probe [52]. DPBF act as a $^1O_2$ scavenger [53]. A visible light (400-700 nm) was used for irradiation experiment. **N@VRCD** mixed with DPBF ($3x10^{-5}$ M) and

irradiated. The decrease in absorbance value of DPBF at 414 nm was observed spectrophotometrically. The singlet oxygen quantum yield (ΦΔ) was calculated by using Methylene blue (MB) (ΦΔ=0.57 in dichloromethane) as standard [54].

2.4.10. Hemolytic assay

The hemolytic activity of **N@VRCD** was investigated further to check its hemocompatibility. Fresh blood was collected from a healthy human in a sodium citrate vial. The blood was centrifuged at 3000 rpm for 10 min, and supernatant plasma was discarded. The collected RBCs were washed three times with 1X PBS and treated with **N@VRCD** in the concentration range of 0.01 mg mL^{-1} to 50 mg mL^{-1}. Subsequently, the tubes were incubated for 60 min at 37 °C and centrifuged at 700× g for 10 min. The amount of free hemoglobin in the supernatant was determined by measuring the absorbance of the supernatant at 540 nm in the microplate reader. Sterile saline solution and Triton X 100 (0.2%) were used to set negative and positive controls, respectively [3]. All the experiments were run in triplicates. To investigate any change in the morphology of RBCs, SEM was done after fixing cells in 4% glutaraldehyde followed by dehydration with 30%, 50%, 70%, 90%, and 100% ethanol serially. Institute Human Ethics Committee (IHEC), IIT Indore, was consulted to use a human blood sample.

2.5. References

[1] Ramanan, V., Thiyagarajan, S.K., Raji, K., Suresh, R., Sekar, R., Ramamurthy, P. (2016), Outright Green Synthesis of Fluorescent Carbon Dots from Eutrophic Algal Blooms for In Vitro Imaging, ACS Sustain. Chem. Eng., 4, 4724–4731(DOI: 10.1021/acssuschemeng.6b00935)

[2] Baker, S.N., Baker, G.A. (2010), Luminescent Carbon Nanodots: Emergent Nanolights, Angew. Chem. Int. Ed., 49, 6726–6744 (DOI: 10.1002/anie.200906623)

[3] Das Purkayastha, M., Manhar, A.K., Das, V.K., Borah, A., Mandal, M., Thakur, A.J., Mahanta, C.L. (2014), Antioxidative, hemocompatible, fluorescent carbon nanodots from an "end-of-pipe" agricultural waste: exploring its new horizon in the food-packaging domain, J. Agric. Food Chem., 62, 4509–4520 (DOI: 10.1021/jf500138f)

[4] Liu, J.-H., Cao, L., LeCroy, G.E., Wang, P., Meziani, M.J., Dong, Y., Liu, Y., Luo, P.G., Sun, Y.-P. (2015), Carbon "Quantum" Dots for Fluorescence Labeling of Cells, ACS Appl. Mater. Interfaces., 7, 19439–19445 (DOI:10.1021/acsami.5b05665)

[5] Sarkar, S., Das, K., Das, P.K. (2017), Estradiol Hemisuccinate-Modified Surface-Engineered Carbon Dots: Target-Specific Theranostic Agent, ACS Sustain. Chem. Eng., 5, 8356–8369 (DOI: 10.1021/acssuschemeng.7b02130)

[6] Liu, M.L., Yang, L., Li, R.S., Chen, B.B., Liu, H., Huang, C.Z. (2017), Large-scale simultaneous synthesis of highly photoluminescent green amorphous carbon nanodots and yellow crystalline graphene quantum dots at room temperature, Green Chem., 19, 3611–3617 (DOI: 10.1039/C7GC01236E)

[7] Zhao, A., Chen, Z., Zhao, C., Gao, N., Ren, J., Qu, X. (2015), Recent advances in bioapplications of C-dots, Carbon, 85, 309–327 (DOI: 10.1016/j.carbon.2014.12.045

[8] Atchudan, R., Edison, T.N.J.I., Chakradhar, D., Perumal, S., Shim, J.-J., Lee, Y.R. (2017), Facile green synthesis of nitrogen-doped carbon dots using Chionanthus retusus fruit extract and investigation of their suitability for metal ion sensing and biological applications, Sens. Actuators B Chem., 246, 497–509 (DOI: 10.1016/j.snb.2017.02.119)

[9] Sahu, S., Behera, B., Maiti, T.K., Mohapatra, S. (2012), Simple one-step synthesis of highly luminescent carbon dots from orange juice: application as excellent bio-imaging agents, Chem. Commun., 48, 8835–8837 (DOI: 10.1039/C2CC33796G)

[10] Teng, X., Ma, C., Ge, C., Yan, M., Yang, J., Zhang, Y., Morais, P.C., Bi, H. (2014), Green synthesis of nitrogen-doped carbon dots from konjac flour with "off–on" fluorescence by Fe^{3+}

and L-lysine for bioimaging, J. Mater. Chem. B., 2, 4631–4639 (DOI: 10.1039/C4TB00368C)
[11] Liu, S.-S., Wang, C.-F., Li, C.-X., Wang, J., Mao, L.-H., Chen, S. (2014), Hair-derived carbon dots toward versatile multidimensional fluorescent materials, J. Mater. Chem. C., 2, 6477–6483 (DOI: 10.1039/C4TC00636D)
[12] Jia, X., Li, J., Wang, E. (2012), One-pot green synthesis of optically pH-sensitive carbon dots with upconversion luminescence, Nanoscale, 4, 5572–5575 (DOI: 10.1039/C2NR31319G)
[13] De, B., Karak, N. (2013), A green and facile approach for the synthesis of water soluble fluorescent carbon dots from banana juice, RSC Adv., 3, 8286–8290 (DOI: 10.1039/C3RA00088E)
[14] Wang, L., Zhou, H.S. (2014), Green Synthesis of Luminescent Nitrogen-Doped Carbon Dots from Milk and Its Imaging Application, Anal. Chem., 86, 8902–8905 (DOI: 10.1021/ac502646x)
[15] Mehta, V.N., Jha, S., Kailasa, S.K. (2014), One-pot green synthesis of carbon dots by using Saccharum officinarum juice for fluorescent imaging of bacteria (Escherichia coli) and yeast (Saccharomyces cerevisiae) cells, Mater. Sci. Eng. C., 38, 20–27 (DOI: 10.1016/j.msec.2014.01.038)
[16] Hsu, P.-C., Shih, Z.-Y., Lee, C.-H., Chang, H.-T. (2012), Synthesis and analytical applications of photoluminescent carbon nanodots, Green Chem., 14, 917–920 (DOI: 10.1039/C2GC16451E)
[17] Liu, S., Tian, J., Wang, L., Zhang, Y., Qin, X., Luo, Y., Asiri, A.M., Al-Youbi, A.O., Sun, X. (2012), Hydrothermal treatment of grass: a low-cost, green route to nitrogen-doped, carbon-rich, photoluminescent polymer nanodots as an effective fluorescent sensing platform for label-free detection of Cu(II) ions, Adv. Mater. Deerfield Beach Fla., 24, 2037–2041 (DOI: 10.1002/adma.201200164)
[18] Alam, A.-M., Park, B.-Y., Ghouri, Z.K., Park, M., Kim, H.-Y. (2015), Synthesis of carbon quantum dots from cabbage with down- and up-conversion photoluminescence properties: excellent imaging agent for biomedical applications, Green Chem., 17, 3791–3797 (DOI: 10.1039/C5GC00686D)
[19] Sharma, V., Tiwari, P., Mobin, S.M. (2017), Sustainable carbon-dots: recent advances in green carbon dots for sensing and bioimaging, J. Mater. Chem. B., 5, 8904–8924 (DOI: 10.1039/C7TB02484C)
[20] Si, M., Zhang, J., He, Y., Yang, Z., Yan, X., Liu, M., Zhuo, S., Wang, S., Min, X., Gao, C., Chai, L., Shi, Y. (2018), Synchronous and rapid preparation of lignin nanoparticles and

carbon quantum dots from natural lignocellulose, Green Chem., 20, 3414-3419 (DOI: 10.1039/C8GC00744F)

[21] Ding, Z., Li, F., Wen, J., Wang, X., Sun, R. (2018), Gram-scale synthesis of single-crystalline graphene quantum dots derived from lignin biomass, Green Chem., 20, 1383–1390 (DOI: 10.1039/C7GC03218H)

[22] Sharma, V., Kaur, N., Tiwari, P., Mobin, S.M. (2018), Full color emitting fluorescent carbon material as reversible pH sensor with multicolor live cell imaging, J. Photochem. Photobiol. B., 182, 137–145 (DOI: 10.1016/j.jphotobiol.2018.04.006)

[23] Wang, X., Qu, K., Xu, B., Ren, J., Qu, X. (2011), Microwave assisted one-step green synthesis of cell-permeable multicolor photoluminescent carbon dots without surface passivation reagents, J. Mater. Chem., 21, 2445–2450 (DOI: 10.1039/C0JM02963G)

[24] Mehta, V.N., Jha, S., Singhal, R.K., Kailasa, S.K. (2014), Preparation of multicolor emitting carbon dots for HeLa cell imaging, New J. Chem., 38, 6152–6160 (DOI: 10.1039/C4NJ00840E)

[25] Mehta, V.N., Jha, S., Basu, H., Singhal, R.K., Kailasa, S.K. (2015), One-step hydrothermal approach to fabricate carbon dots from apple juice for imaging of mycobacterium and fungal cells, Sens. Actuators B Chem., 213, 434–443 (DOI: 10.1016/j.snb.2015.02.104)

[26] Li, Y., Zhao, Y., Cheng, H., Hu, Y., Shi, G., Dai, L., Qu, L. (2012), Nitrogen-Doped Graphene Quantum Dots with Oxygen-Rich Functional Groups, J. Am. Chem. Soc., 134, 15–18 (DOI: 10.1021/ja206030c)

[27] Ding, C., Zhu, A., Tian, Y. (2014), Functional surface engineering of C-dots for fluorescent biosensing and in vivo bioimaging, Acc. Chem. Res., 47, 20–30 (DOI: 10.1021/ar400023s)

[28] Zhang, H., Chen, Y., Liang, M., Xu, L., Qi, S., Chen, H., Chen, X. (2014), Solid-phase synthesis of highly fluorescent nitrogen-doped carbon dots for sensitive and selective probing ferric ions in living cells, Anal. Chem., 86, 9846–9852 (DOI: 10.1021/ac502446m)

[29] Das, R.K., Mohapatra, S. (2017), Highly luminescent, heteroatom-doped carbon quantum dots for ultrasensitive sensing of glucosamine and targeted imaging of liver cancer cells, J. Mater. Chem. B., 5, 2190–2197 (DOI: 10.1039/C6TB03141B)

[30] Shi, W., Guo, F., Han, M., Yuan, S., Guan, W., Li, H., Huang, H., Liu, Y., Kang, Z. (2017), N,S co-doped carbon dots as a stable bio-imaging probe for detection of intracellular temperature and tetracycline, J. Mater. Chem., B. 5, 3293–3299 (DOI: 10.1039/C7TB00810D)

[31] Bandi, R., Dadigala, R., Gangapuram, B.R., Guttena, V. 2018), Green synthesis of highly fluorescent nitrogen – Doped carbon dots from Lantana camara berries for effective detection of lead(II) and bioimaging, J. Photochem. Photobiol. B., 178, 330–338 ((DOI: 10.1016/j.jphotobiol.2017.11.010)

[32] Rong, M., Feng, Y., Wang, Y., Chen, X. (2017), One-pot solid phase pyrolysis synthesis of nitrogen-doped carbon dots for Fe^{3+} sensing and bioimaging, Sens. Actuators B Chem., 245, 868–874 (DOI: 10.1016/j.snb.2017.02.014)

[33] Ferlay, J., Shin, H.-R., Bray, F., Forman, D., Mathers, C., Parkin, D.M. (2010), Estimates of worldwide burden of cancer in 2008: GLOBOCAN 2008, Int. J. Cancer., 127, 2893–2917 (DOI: 10.1002/ijc.25516)

[34] Agostinis, P., Berg, K., Cengel, K.A., Foster, T.H., Girotti, A.W., Gollnick, S.O., Hahn, S.M., Hamblin, M.R., Juzeniene, A., Kessel, D., Korbelik, M., Moan, J., Mroz, P., Nowis, D., Piette, J., Wilson, B.C., Golab, J. (2011), Photodynamic therapy of cancer: An update, CA Cancer J. Clin., 61, 250–281 (DOI: 10.3322/caac.20114)

[35] Brown, S.B., Brown, E.A., Walker, I. (2004), The present and future role of photodynamic therapy in cancer treatment, Lancet Oncol., 5, 497–508 (DOI: 10.1016/S1470-2045(04)01529-3)

[36] Sharman, W.M., Allen, C.M., van Lier, J.E. (1999), Photodynamic therapeutics: basic principles and clinical applications, Drug Discov. Today., 4, 507–517 (DOI: 10.1016/S1359-6446(99)01412-9)

[37] Zhou, Z., Song, J., Nie, L., Chen, X. (2016), Reactive oxygen species generating systems meeting challenges of photodynamic cancer therapy, Chem. Soc. Rev., 45, 6597–6626 (DOI: 10.1039/C6CS00271D)

[38] Ethirajan, M., Chen, Y., Joshi, P., K. Pandey, R. (2011), The role of porphyrin chemistry in tumor imaging and photodynamic therapy, Chem. Soc. Rev., 40, 340–362 (DOI: 10.1039/B915149B)

[39] Liu, X., Su, H., Shi, W., Liu, Y., Sun, Y., Ge, D. (2018), Functionalized poly(pyrrole-3-carboxylic acid) nanoneedles for dual-imaging guided PDT/PTT combination therapy, Biomaterials, 167, 177–190 (DOI: 10.1016/j.biomaterials.2018.03.030)

[40] Ge, J., Lan, M., Zhou, B., Liu, W., Guo, L., Wang, H., Jia, Q., Niu, G., Huang, X., Zhou, H., Meng, X., Wang, P., Lee, C.-S., Zhang, W., Han, X. (2014), A graphene quantum dot photodynamic therapy agent with high singlet oxygen generation, Nat. Commun., 5, 4596 (DOI: 10.1038/ncomms5596)

[41] Albert, K., Hsu, H.-Y. (2016), Carbon-Based Materials for Photo-Triggered Theranostic Applications, Mol. Basel Switz., 21, (DOI: 10.3390/molecules21111585)
[42] Fu, P.P., Xia, Q., Hwang, H.-M., Ray, P.C., Yu, H. (2014), Mechanisms of nanotoxicity: Generation of reactive oxygen species, J. Food Drug Anal., 22, 64–75 (DOI: 10.1016/j.jfda.2014.01.005)
[43] He, H., Zheng, X., Liu, S., Zheng, M., Xie, Z., Wang, Y., Yu, M., Shuai, X. (2018), Diketopyrrolopyrrole-Based Carbon Dots for Photodynamic Therapy, Nanoscale, (DOI: 10.1039/C8NR02643B)
[44] Peng, H., Jing, L., Xiansong, W., Zhe, W., Chunlei, Z., Meng, H., Kan, W., Feng, C., Zhiming, L., Guangxia, S., Daxiang, C., Xiaoyuan, C. (2012), Light-Triggered Theranostics Based on Photosensitizer-Conjugated Carbon Dots for Simultaneous Enhanced-Fluorescence Imaging and Photodynamic Therapy, Adv. Mater., 24, 5104–5110 (DOI: 10.1002/adma.201200650)
[45] Zhou, L., Lin, Y., Huang, Z., Ren, J., Qu, X. (2012), Carbon nanodots as fluorescence probes for rapid, sensitive, and label-free detection of Hg^{2+} and biothiols in complex matrices, Chem. Commun. 48, 1147–1149 (DOI: 10.1039/C2CC16791C)
[46] Eichhorn, G.L. (1964), The function of iron in biochemistry. In: Iron Metabolism, Springer, Berlin, Heidelberg, pp. 9–23
[47] Qu, S., Chen, H., Zheng, X., Cao, J., Liu, X. (2013), Ratiometric fluorescent nanosensor based on water soluble carbon nanodots with multiple sensing capacities. Nanoscale. 5, 5514–5518 (DOI: 10.1039/C3NR00619K)
[48] Bao, L., Zhang, Z.-L., Tian, Z.-Q., Zhang, L., Liu, C., Lin, Y., Qi, B., Pang, D.-W. (2011), Electrochemical Tuning of Luminescent Carbon Nanodots: From Preparation to Luminescence Mechanism. Adv. Mater. 23, 5801–5806 (DOI: 10.1002/adma.201102866)
[49] Melhuish, W.H. (1961), Quantum efficiencies of fluorescence of organic substances: effect of solvent and concentration of the fluorescent solute, J. Phys. Chem., 65, 229–235 (DOI: 10.1021/j100820a009)
[50] Carmichael, J., DeGraff, W.G., Gazdar, A.F., Minna, J.D., Mitchell, J.B. (1987), Evaluation of a tetrazolium-based semiautomated colorimetric assay: assessment of chemosensitivity testing, Cancer Res., 47, 936–942
[51] Sharma, V., Saini, A.K., Mobin, S.M. (2016), Multicolour fluorescent carbon nanoparticle probes for live cell imaging and dual palladium and mercury sensors, J. Mater. Chem. B., 4, 2466–2476 (DOI: 10.1039/C6TB00238B)

[52] Zhang, D., Wen, L., Huang, R., Wang, H., Hu, X., Xing, D. (2018), Mitochondrial specific photodynamic therapy by rare-earth nanoparticles mediated near-infrared graphene quantum dots, Biomaterials, 153, 14–26 (DOI: 10.1016/j.biomaterials.2017.10.034)
[53] Meng, A.-N., Chaihu, L.-X., Chen, H.-H., Gu, Z.-Y. (2017), Ultrahigh adsorption and singlet-oxygen mediated degradation for efficient synergetic removal of bisphenol A by a stable zirconium-porphyrin metal-organic framework, Sci. Rep., 7, 6297 (DOI: 10.1038/s41598-017-06194-z)
[54] Majumdar, P., Yuan, X., Li, S., Guennic, B.L., Ma, J., Zhang, C., Jacquemin, D., Zhao, J. (2014), Cyclometalated Ir(iii) complexes with styryl-BODIPY ligands showing near IR absorption/emission: preparation, study of photophysical properties and application as photodynamic/luminescence imaging materials, J. Mater. Chem. B., 2, 2838–2854 (DOI: 10.1039/C4TB00284A)
[55] Wang, X., Cao, L., Yang, S.-T., Lu, F., Meziani, M.J., Tian, L., Sun, K.W., Bloodgood, M.A., Sun, Y.-P. (2010), Bandgap-Like Strong Fluorescence in Functionalized Carbon Nanoparticles, Angew. Chem. Int. Ed., 49, 5310–5314 (DOI: 10.1002/anie.201000982)
[56] Rodríguez-Padrón, D., Algarra, M., Tarelho, L.A.C., Frade, J., Franco, A., de Miguel, G., Jiménez, J., Rodríguez-Castellón, E., Luque, R. (2018), Catalyzed Microwave-Assisted Preparation of Carbon Quantum Dots from Lignocellulosic Residues, ACS Sustain. Chem. Eng., 6, 7200–7205 (DOI: 10.1021/acssuschemeng.7b03848)
[57] Sun, C., Zhang, Y., Wang, P., Yang, Y., Wang, Y., Xu, J., Wang, Y., Yu, W.W. (2016), Synthesis of Nitrogen and Sulfur Co-doped Carbon Dots from Garlic for Selective Detection of Fe^{3+}, Nanoscale Res. Lett., 11, (DOI: 10.1186/s11671-016-1326-8)
[58] Dong, Y., Pang, H., Yang, H.B., Guo, C., Shao, J., Chi, Y., Li, C.M., Yu, T. (2013), Carbon-Based Dots Co-doped with Nitrogen and Sulfur for High Quantum Yield and Excitation-Independent Emission, Angew. Chem. Int. Ed., 52, 7800–7804 (DOI: 10.1002/anie.201301114)
[59] Datta, K.K.R., Qi, G., Zboril, R., Giannelis, E.P. (2016), Yellow emitting carbon dots with superior colloidal, thermal, and photochemical stabilities, J. Mater. Chem. C., 4, 9798–9803 (DOI: 10.1039/C6TC03452G)
[60] Niu, J., Gao, H., Wang, L., Xin, S., Zhang, G., Wang, Q., Guo, L., Liu, W., Gao, X., Wang, Y. (2014), Facile synthesis and optical properties of nitrogen-doped carbon dots, New J. Chem., 38, 1522–1527 (DOI: 10.1039/C3NJ01068F)
[61] Feng, J., Wang, W.-J., Hai, X., Yu, Y.-L., Wang, J.-H. (2016), Green preparation of nitrogen-doped carbon dots derived

from silkworm chrysalis for cell imaging, J. Mater. Chem. B., 4, 387–393 (DOI: 10.1039/C5TB01999K)

[62] Miao, P., Han, K., Tang, Y., Wang, B., Lin, T., Cheng, W. (2015), Recent advances in carbon nanodots: synthesis, properties and biomedical applications, Nanoscale, 7, 1586–1595 (DOI: 10.1039/C4NR05712K)

[63] Nie, H., Li, M., Li, Q., Liang, S., Tan, Y., Sheng, L., Shi, W., Zhang, S.X.-A. (2014), Carbon Dots with Continuously Tunable Full-Color Emission and Their Application in Ratiometric pH Sensing, Chem. Mater., 26, 3104–3112 (DOI: 10.1021/cm5003669)

[64] Ye, R., Peng, Z., Metzger, A., Lin, J., Mann, J.A., Huang, K., Xiang, C., Fan, X., Samuel, E.L.G., Alemany, L.B., Martí, A.A., Tour, J.M. (2015), Bandgap engineering of coal-derived graphene quantum dots, ACS Appl. Mater. Interfaces., 7, 7041–7048 (DOI: 10.1021/acsami.5b01419)

[65] Yang, Z., Xu, M., Liu, Y., He, F., Gao, F., Su, Y., Wei, H., Zhang, Y. (2014), Nitrogen-doped, carbon-rich, highly photoluminescent carbon dots from ammonium citrate, Nanoscale, 6, 1890–1895 (DOI: 10.1039/C3NR05380F

[66] Khan, W.U., Wang, D., Zhang, W., Tang, Z., Ma, X., Ding, X., Du, S., Wang, Y. (2017), High Quantum Yield Green-Emitting Carbon Dots for Fe(III) Detection, Biocompatible Fluorescent Ink and Cellular Imaging, Sci. Rep., 7, 14866 (DOI: 10.1038/s41598-017-15054-9)

[67] Liu, H.-Y., Du, L., Zhao, Y.-T., Tian, W.-Q. (2016), In Vitro Hemocompatibility and Cytotoxicity Evaluation of Halloysite Nanotubes for Biomedical Application, J Nanomater., 16, 384 (DOI: 10.1155/2015/685323)

[68] Yildirim, A., Ozgur, E., Bayindir, M. (2013), Impact of mesoporous silica nanoparticle surface functionality on hemolytic activity, thrombogenicity and non-specific protein adsorption, J. Mater. Chem. B., 1, 1909–1920 (DOI: 10.1039/C3TB20139B)

[69] Bhamore, J.R., Jha, S., Singhal, R.K., Kailasa, S.K. 2017), Synthesis of Water Dispersible Fluorescent Carbon Nanocrystals from Syzygium cumini Fruits for the Detection of Fe^{3+} Ion in Water and Biological Samples and Imaging of Fusarium avenaceum Cells, J. Fluoresc., 27, 125–134 ((DOI: 10.1007/s10895-016-1940-y)

[70] Dong, Y., Cai, J., You, X., Chi, Y. (2015), Sensing applications of luminescent carbon based dots, Analyst, 140, 7468–7486 (DOI: 10.1039/C5AN01487E)

[71] Kailasa, S.K., Ha, S., Baek, S.H., Phan, L.M.T., Kim, S., Kwak, K., Park, T.J. (2019), Tuning of carbon dots emission color for sensing of Fe^{3+} ion and bioimaging applications, Mater. Sci. Eng. C., 98, 834–842 (DOI: 10.1016/j.msec.2019.01.002)

[72] Xue, M., Zhan, Z., Zou, M., Zhang, L., Zhao, S. (2016), Green synthesis of stable and biocompatible fluorescent carbon dots from peanut shells for multicolor living cell imaging, New J. Chem., 40, 1698–1703 (DOI: 10.1039/C5NJ02181B)

[73] Shi, B., Su, Y., Zhang, L., Huang, M., Liu, R., Zhao, S. (2016), Nitrogen and Phosphorus Co-Doped Carbon Nanodots as a Novel Fluorescent Probe for Highly Sensitive Detection of Fe^{3+} in Human Serum and Living Cells, ACS Appl. Mater. Interfaces, 8, 10717–10725 (DOI: 10.1021/acsami.6b01325)

[74] Wang, C., Ding, Y., Bi, X., Luo, J., Wang, G., Lin, Y. (2018), Carbon quantum dots-Ag nanoparticle complex as a highly sensitive "turn-on" fluorescent probe for hydrogen sulfide: A DFT/TD-DFT study of electronic transitions and mechanism of sensing, Sens. Actuators B Chem., 264, 404–409 (DOI: 10.1016/j.snb.2018.02.186)

[75] Goel, S., Velizhanin, K.A., Piryatinski, A., Tretiak, S., Ivanov, S.A. (2010), DFT Study of Ligand Binding to Small Gold Clusters, J. Phys. Chem. Lett., 1, 927–931 (DOI: 10.1021/jz1000193)

[76] Xue, M., Zhan, Z., Zou, M., Zhang, L., Zhao, S. (2016), Green synthesis of stable and biocompatible fluorescent carbon dots from peanut shells for multicolor living cell imaging, New J. Chem., 40, 1698–1703 (DOI:10.1039/C5NJ02181B)

[77] Yu, C., Xuan, T., Chen, Y., Zhao, Z., Sun, Z., Li, H. (2015), A facile, green synthesis of highly fluorescent carbon nanoparticles from oatmeal for cell imaging, J. Mater. Chem. C., 3, 9514–9518 (DOI:10.1039/C5TC02057C)

[78] Yao, Y.-Y., Gedda, G., Girma, W.M., Yen, C.-L., Ling, Y.-C., Chang, J.-Y. (2017), Magnetofluorescent Carbon Dots Derived from Crab Shell for Targeted Dual-Modality Bioimaging and Drug Delivery, ACS Appl. Mater. Interfaces., 9, 13887–13899 (DOI:10.1021/acsami.7b01599)

[79] Lin, F., Li, C., Dong, L., Fu, D., Chen, Z. (2017), Imaging biofilm-encased microorganisms using carbon dots derived from L. plantarum, Nanoscale, 9, 9056–9064 (DOI:10.1039/c7nr01975k)

[80] Yin, B., Deng, J., Peng, X., Long, Q., Zhao, J., Lu, Q., Chen, Q., Li, H., Tang, H., Zhang, Y., Yao, S. (2013), Green synthesis of carbon dots with down- and up-conversion fluorescent properties for sensitive detection of hypochlorite with a dual-readout assay, Analyst, 138, 6551–6557 (DOI:10.1039/C3AN01003A)

[81] Atchudan, R., Edison, T., Aseer, K-R., Perumal, S., Karthik, N., Lee, Y-R. (2018), Highly fluorescent nitrogen-doped carbon dots derived from Phyllanthus acidus utilized as a fluorescent probe for label-free selective detection of Fe^{3+} ions,

live cell imaging and fluorescent ink, Biosens. Bioelectron., 15, 303-311 (DOI: j.bios.2017.07.076)

[82] Vasimalai, N., Vilas-Boas, V., Gallo, J., Cerqueira, M. de F., Menéndez-Miranda, M., Costa-Fernández, J.M., Diéguez, L., Espiña, B., Fernández-Argüelles, M.T. (2018), Green synthesis of fluorescent carbon dots from spices for in vitro imaging and tumour cell growth inhibition, Beilstein J. Nanotechnol., 9, 530–544 (DOI: 10.3762/bjnano.9.51)

[83] Zhao, C., Jiao, Y., Hu, F., Yang, Y. (2018), Green synthesis of carbon dots from pork and application as nanosensors for uric acid detection, Spectrochim. Acta. A. Mol. Biomol. Spectrosc., 190, 360–367 (DOI: 10.1016/j.saa.2017.09.037)

[84] Kim, M.I., Park, S.Y., Park, K.S., Kim, S., Kim, J.-P., Lee, Y.-C., Lee, H.U., Park, H.G. (2018), Label-free fluorescent detection of alkaline phosphatase with vegetable waste-derived green carbon probes, Sens. Actuators B Chem., 262, 469–476 (DOI: 10.1016/j.snb.2018.02.007)

[85] Liu, W., Diao, H., Chang, H., Wang, H., Li, T., Wei, W. (2017), Green synthesis of carbon dots from rose-heart radish and application for Fe^{3+} detection and cell imaging, Sens. Actuators B Chem., 241, 190–198 (DOI: 10.1016/j.snb.2016.10.068)

[86] Dang, D.K., Sundaram, C., Ngo, Y.-L.T., Chung, J.S., Kim, E.J., Hur, S.H. (2018), One pot solid-state synthesis of highly fluorescent N and S co-doped carbon dots and its use as fluorescent probe for Ag^{+} detection in aqueous solution, Sens. Actuators B Chem., 255, 3284–3291 (DOI: 10.1016/j.snb.2017.09.155)

[87] Amin, N., Afkhami, A., Hosseinzadeh, L., Madrakian, T. (2018), Green and cost-effective synthesis of carbon dots from date kernel and their application as a novel switchable fluorescence probe for sensitive assay of Zoledronic acid drug in human serum and cellular imaging, Anal. Chim. Acta., (DOI: 10.1016/j.aca.2018.05.014)

[88] Yu, J., Song, N., Zhang, Y.-K., Zhong, S.-X., Wang, A.-J., Chen, J. (2015), Green preparation of carbon dots by Jinhua bergamot for sensitive and selective fluorescent detection of Hg^{2+} and Fe^{3+}, Sens. Actuators B Chem., 214, 29–35 (DOI: 10.1016/j.snb.2015.03.006)

[89] Hu, Y., Zhang, L., Li, X., Liu, R., Lin, L., Zhao, S. (2017), Green Preparation of S and N Co-Doped Carbon Dots from Water Chestnut and Onion as Well as Their Use as an Off–On Fluorescent Probe for the Quantification and Imaging of Coenzyme A, ACS Sustain. Chem. Eng., 5, 4992–5000 (DOI: 10.1021/acssuschemeng.7b00393)

[90] Gong, X., Lu, W., Paau, M.C., Hu, Q., Wu, X., Shuang, S., Dong, C., Choi, M.M.F. (2015), Facile synthesis of nitrogen-doped

carbon dots for Fe3+ sensing and cellular imaging. Anal. Chim. Acta., 861, 74–84 (DOI: 10.1016/j.aca.2014.12.045)

[91] Zhao, A., Zhao, C., Li, M., Ren, J., Qu, X. (2014), Ionic liquids as precursors for highly luminescent, surface-different nitrogen-doped carbon dots used for label-free detection of Cu^{2+}/Fe^{3+} and cell imaging. Anal. Chim. Acta., 809, 128–133 (DOI:10.1016/j.aca.2013.10.046)

[92] Lu, W., Gong, X., Nan, M., Liu, Y., Shuang, S., Dong, C. (2015), Comparative study for N and S doped carbon dots: Synthesis, characterization and applications for Fe^{3+} probe and cellular imaging. Anal. Chim. Acta., 898, 116–127 (DOI: 10.1016/j.aca.2015.09.050)

[93] Hu, Y., Wang, B., Su, Z. (2008), Synthesis and photophysical properties of a novel green fluorescent polymer for Fe^{3+} sensing. Polym. Int., 57, 1343–1350 (DOI:10.1002/pi.2479)

[94] Feng, J., Chen, Y., Han, Y., Liu, J., Ren, C., Chen, X. (2016), Fluorescent carbon nanoparticles: A low-temperature trypsin-assisted preparation and Fe^{3+} sensing. Anal. Chim. Acta., 926, 107–117 (DOI: 10.1016/j.aca.2016.04.039)

[95] Zhu, S., Meng, Q., Wang, L., Zhang, J., Song, Y., Jin, H., Zhang, K., Sun, H., Wang, H., Yang, B. (2013), Highly Photoluminescent Carbon Dots for Multicolor Patterning, Sensors, and Bioimaging. Angew. Chem., 125, 4045–4049 (DOI: 10.1002/ange.201300519)

[96] Lv, P., Yao, Y., Zhou, H., Zhang, J., Pang, Z., Ao, K., Cai, Y., Wei, Q. (2017), Synthesis of novel nitrogen-doped carbon dots for highly selective detection of iron ion. Nanotechnology., 28, 165502 (DOI: 10.1088/1361-6528/aa6320)

[97] Chen, X., Zhao, Q., Zou, W., Qu, Q., Wang, F. (2017), A colorimetric Fe^{3+} sensor based on an anionic poly(3,4-propylenedioxythiophene) derivative. Sens. Actuators B Chem., 244, 891–896 (DOI: 10.1016/j.snb.2017.01.027)

[98] Weerasinghe, A-J., Schmiesing, C., Varaganti, S., Ramakrishna, G., Sinn, E. 2010, Single- and Multiphoton Turn-On

Fluorescent Fe3+ Sensors Based on Bis(rhodamine), J. Phys. Chem. B, 114, 9413–9419 (DOI: 10.1021/jp1034568)

[99] Xu, J.-H., Hou, Y.-M., Ma, Q.-J., Wu, X.-F., Wei, X.-J. (2013), A highly selective fluorescent sensor for Fe^{3+} based on covalently immobilized derivative of naphthalimide. Spectrochim. Acta. A. Mol. Biomol. Spectrosc., 112, 116–124 (DOI: 10.1016/j.saa.2013.04.044)

CHAPTER 3

Photoactivatable carbon dots as a label-free fluorescent probe for picric acid detection in aqueous medium and light-induced bacterial inactivation

3.1. Introduction

Nitroaromatic explosives, used more recently, are hazardous for humans, animals, and the environment [1]. Among these nitroaromatic compounds, picric acid is highly water-soluble, which makes it stand out as the most hazardous environmental pollutant [2]. So, the rapid and accurate detection of highly water-soluble picric acid is an essential current research field. The detection methods and techniques, along with the newly developed sensors for picric acid determination, have recently been explored using various fluorescent probes [3–10]. The excellent water solubility of picric acid is the primary concern that makes it a dangerous water and soil contaminant, which can cause adverse effects on human and animal health [11–13]. Therefore, the determination of picric acid in an aqueous medium has gained substantial effort from the research community lately. Among the various other materials such as picric acid sensors, the carbon dots attracted immense interest from researchers due to their commendatory performance. Many properties of carbon dots distinguish them from others, like appealing optical properties, excellent water solubility, high biocompatibility, easy surface passivation, and environment-friendliness [14–19]. The carbon dots-based sensors have been used for sensing a wide range of analytes such as metal ions [20,21], biomolecules [22–25], drugs [26–28], and many more [29].

Healthy living is a prime concern in today's life, so the materials that have the potential of killing harmful bacteria and other microorganisms are gaining interest rapidly. Coating materials, as mentioned earlier, on the surfaces of everyday used items that are frequently touched by several individuals like doorbells, public swings, toys, switchboards, and phones to make them antimicrobial so that the transmission of infectious diseases could be controlled [30–32]. In many cases, improper use of antibiotics is a leading cause of antibiotic resistance, so off-the-centered plans of action are required to gear up for such infections [33,34]. Recently, photodynamic therapy for treating cancer and infectious diseases has gained interest. Photodynamic antimicrobial therapy (PDAMT) is appropriate for treating surface microbial infections such as skin infection, burn tissues infection, bedsores in elderly patients, acne, and making aseptic surfaces [35,36]. The materials that could act as photosensitizers in photodynamic antimicrobial therapy are chosen. Moreover, the chances of developing resistant strains are almost nil in this PDAMT compared to conventional antibiotic therapies. Conventionally in PDAMT, UV or NIR lights are used to irradiate photo-sensitizers to generate reactive oxygen species (ROS) for bactericidal action. UV and NIR light exposure are hazardous to humans, so visible light activatable agents have been presented with extra attention of late. Various new visible light activatable agents such as gold nano-particles, ruthenium complexes, and TiO_2 nanoparticles have been synthesized in recent years [37,38]. Surface-modified carbon dots have been showcased as efficient visible light-activated antimicrobial agents [39–42].

Given this, the present work focused on synthesizing nitrogen, silver, and gold bimetallic heteroatom doped carbon dots (**BCDs**) using citric acid as the sole carbon source having excellent quantum yield and greater aqueous solubility for the label-free detection of picric acid in an aqueous system. Synthesized, **BCDs** showed commendable sensitivity, selectivity, and precision towards picric acid detection. Additionally, these **BCDs** were

also explored as a photosensitizer for efficient bacterial elimination owing to their visible light activatable nature, which can be used to fabricate advanced biocidal surface coatings to keep surfaces free from any potential pathogenic microbes.

3.2. Results and discussion

Hydrothermal carbonization was used for the synthesis of **BCDs**. The synthesis was performed by heating the whole mixture at 180 °C for 4 h in an autoclave using the furnace. The heteroatom doping was done using different sources like $HAuCl_4$ for gold, $AgNO_3$ for silver, urea, and BSA for nitrogen, as shown in **Scheme 3.1**. The quantum yield was calculated and found to be around ~50%. The plausible mechanism behind the formation of **BCDs** includes carbonization followed by hydrolysis of carbon precursors, which can be initiated by increasing temperature followed by dehydration.

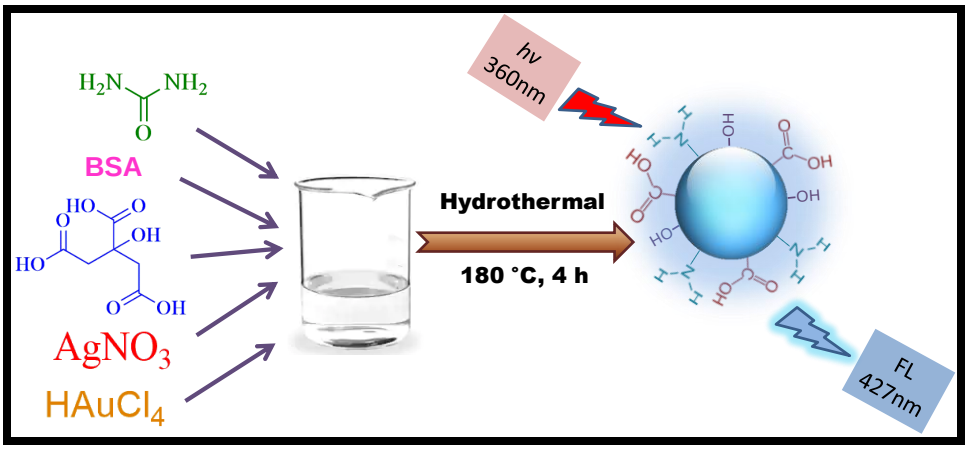

Scheme 3.1. Schematic illustration of the preparation of **BCDs.**

Further increase in temperature led to condensation, hence polymerization, which gave carbon nuclei. Rising temperatures lead to the growth of these carbon nuclei within polymeric fragments, which ultimately burst and give rise to ultra-small carbon dots [50,51]. The structural and optical characterization was performed to elucidate the insights of prepared **BCDs,** which were further investigated as a picric acid sensor and a photoactivated antibacterial agent. It must be mentioned here that nitrogen doping was performed to enhance the fluorescence characteristics of prepared carbon dots owing to its unpaired electron, whereas Au and Ag's

doping was incorporated to modulate the overall photosensitizing nature, which may lead to higher biocidal nature of as prepared **BCDs**.

3.2.1 Morphological and Structural Characterization of BCDs.

XRD, TEM, and FTIR were performed to get structural insights of BCDs. A broad hump was seen in XRD spectra, where the peak lies at 20.23°. The distorted graphite hybridization was indicated by the greater interlayer spacing of 4.3 Å (**Figure 3.1.a**). The oxygen-rich surface functional groups of carbon dots could be the reason behind distorted sp^2 hybridization and broad peak indicating amorphous nature as seen in XRD [22]. Raman spectroscopy was performed to quantify the sp^2 and sp^3 hybridized carbon atoms present in prepared **BCDs** carbon-based nanostructures contain mainly characteristic D (sp^3- hybridized) and G (sp^2- hybridized) bands. In the current work, **BCDs** exhibited two prominent Raman bands at 1311.59 cm^{-1} and 1574.31 $cm^{-1,}$ respectively (**Figure 3.1.f**). It can be mentioned here that 785 nm laser sources were used to record the spectra to minimize the fluorescence signal from **BCDs** [52]. In the present spectrum, the D band arises from the edge of sp^2 hybridized atoms, and it confirms the presence of doped elements (N, Au, and Ag) within the carbon lattice. Additionally, the higher intensity of the G band in comparison to the D band supports the higher degree of sp^2 atoms within the **BCDs** structure [53,54]. In the FT-IR spectrum of **BCDs** (**Figure 3.1.b**), a strong absorbance band is visualized at 3342 cm^{-1} attributed to the O-H stretch of the hydroxyl group and a weak absorbance band at 2093 cm^{-1} corresponds to O-H stretching of the carboxyl group [55,56]. The carbonyl in the amide bond gives rise to a strong peak of its stretching vibration at 1634 cm^{-1} [57,58]. A weak absorbance band at 1408 cm^{-1} is attributed to C-N stretching vibration [59]. The peaks visualized at 1224 cm^{-1} and 618 cm^{-1} were assigned to C-OH stretch and C-H bending, respectively [60,61]. The surface passivation with such hydrophilic functional groups helped **BCDs** achieve high aqueous solubility and stability.

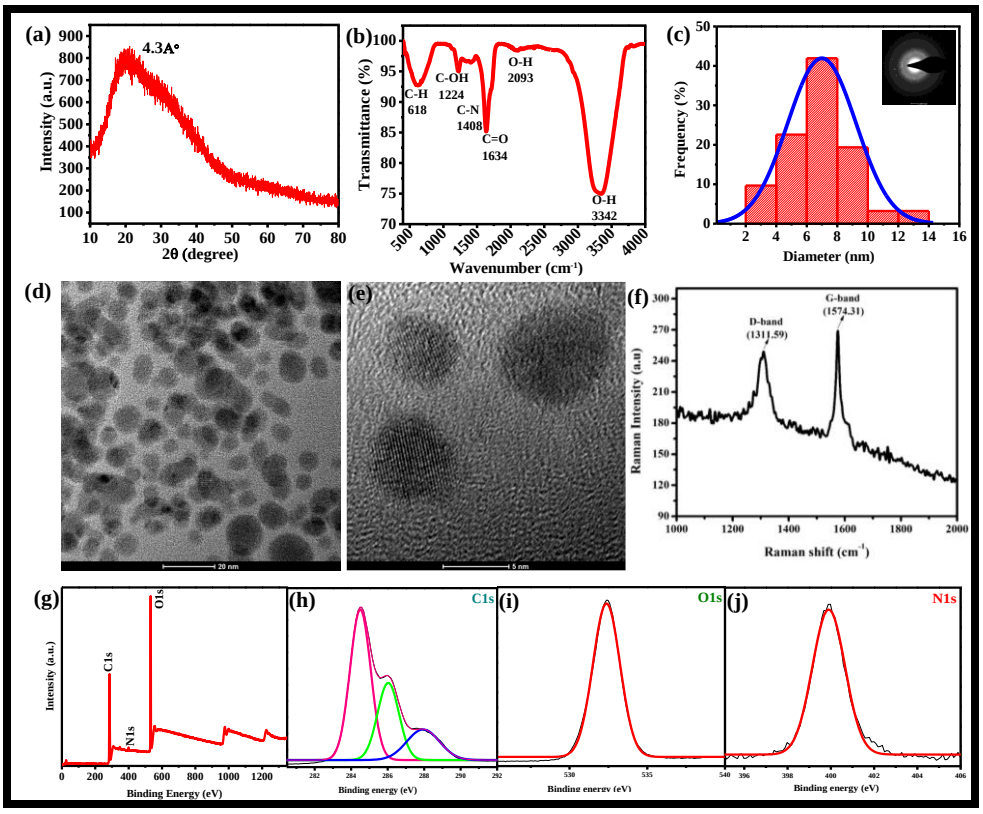

Figure 3.1. Structural and morphological characterization of **BCDs** (a) Powder X-ray diffractogram (b) FT-IR (c) Size distribution histogram of **BCDs** obtained from TEM image and SAED pattern (inset) (d) TEM (e) HR-TEM micrograph (f) Raman Spectra of **BCDs** (g) XPS survey spectra of **BCDs** (h-j) High-resolution XPS spectra of C1s, N1s, and O1s respectively

TEM micrograph (**Figure 3.1.d**) showed the size of maximum particles was in the range of 4-8 nm (**Figure 3.1.c**). The crystallinity of the **BCDs** was displayed by clear lattice fringes seen in HR-TEM images (**Figure 3.1.e**). However, the diffused selected area electron diffraction (SAED) pattern in **Figure 3.1.c (inset)** indicates the poor crystallinity of the material. In addition to that, a contrast difference was observed between the particles confirming the doping of Au and Ag, which was further supported by EDAX results suggesting the presence of Au and Ag in **BCDs**. ICP-OES analysis was performed to determine the Au and Ag

doping in the **BCDs** nanoparticles. The results show the presence of Ag and Au, 11.5272 mg L^{-1} and 0.1019 mg $L^{-1,}$ respectively. In the XPS spectra of **BCDs**, the prominent peaks of C1s and O1s and less intensity peak for N1s are found. However, no peak for Au or Ag was seen (**Figure 3.1.g-j**). From XRD and SAED, we can conclude that the **BCDs** are amorphous particles with some crystallinity, as confirmed in many previous reports of carbon dots [62].

3.2.2 Optical properties of BCDs

To determine the optical properties of **BCDs**, UV-Vis spectroscopy and fluorescence spectroscopy were performed. As shown in figure **Figure 3.2.a** (curve Abs), the aqueous solution of **BCDs** shows a typical absorbance peak at 340 nm. This peak emerges due to the n-π^* transition at the edge of carbon lattice and occurs because of the energy transfer between carbon band and dopant present within carbon lattice [63]. Such longer wavelength UV peaks generally arise due to the surface functionalization of carbon dots [64]. The bright blue fluorescence coming from a light-yellow colored solution of **BCDs** could be visualized with naked eyes when irradiated with UV light (365 nm) using a transilluminator (**Figure 3.2.a** (inset)). The maximum fluorescence emission was observed at 427 nm (**Figure 3.2.a** (Emission)) with excitation maxima at 360 nm (**Figure 3.2.b** (Excitation)). Such strong emission is observed when the surface state traps the excited state energy [65]. As illustrated in (**Figure 3.2.b**), the **BCDs** showed excitation-independent emission behavior. A slight red shift was seen from 427 nm to 433 nm when the excitation wavelength increased from 360 nm to 380 nm; however, at the same time, fluorescence intensity was decreased drastically. This behavior could be explained based on monodispersity and surface adsorbed functional groups [66]. Moreover, the uniform crystalline core shown in the HR-TEM image with very few surface layers could also be the reason behind the excitation-independent emission behavior of **BCDs** [67]. The average lifetime of **BCDs** was evaluated as

10.1 ns using a 375 nm diode laser in TCSPC, for which data is fitted to a three-exponential function. This significantly long lifetime makes **BCDs** the desired candidate to be used as a nanoprobe for fluorescence lifetime imaging in many diagnostic applications [68].

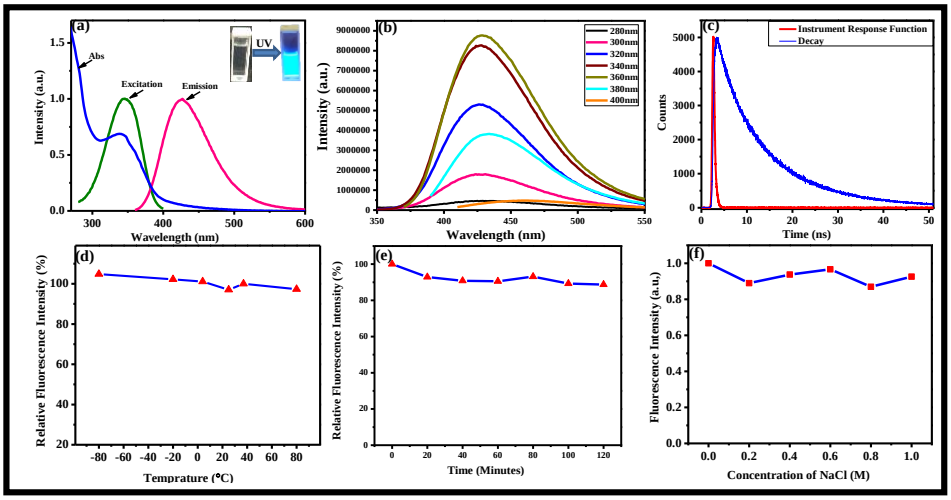

Figure 3.2. Photophysical characterization of **BCDs** (a) UV–vis absorption spectrum, excitation spectrum, and emission spectrum of **BCDs.** (Right inset) **BCDs** solution under visible light and UV light (360 nm), (b) Emission spectra of **BCDs** obtained with varying excitation wavelength (c) TCSPC (d) Stability of **BCDs** at various temperatures (e) Stability of **BCDs** under UV irradiation for 120 min (f) Stability of **BCDs** with varying NaCl concentration.

3.2.3 Fluorescence stability of BCDs

The carbon dots have the dual ability to accept electrons and donate electrons responsible for the quenching of fluorescence owing to the transfer of an electron between analyte and carbon dots. The highly water-soluble **BCDs** were checked for their sensing response towards nitroaromatic compounds. A solid optical response was observed in the presence of picric acid. The fluorescence of **BCDs** was “turned off” with the addition of picric acid in the range of 0 μM - 500 μM. There is a gradual decrease in fluorescence intensity with the addition of picric acid as shown in (**Figure 3.3.a**).

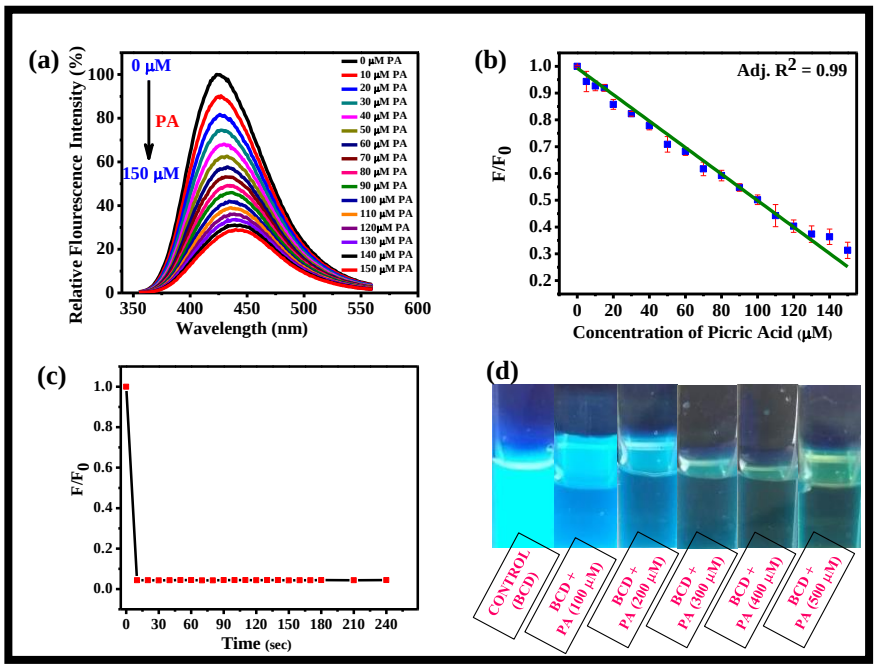

Figure 3.3. (a) The fluorescence spectra of **BCDs** with different concentrations of picric acid in the linear range (0 μM – 150 μM). (b) The linear plot shows the relationship of F/F_0 with various concentrations of picric acid. (c) Sensing response time of **BCDs** for picric acid (d) Images of an aqueous solution of **BCDs** alone (control) and after the addition of picric acid (100 μM - 500 μM) captured using a UV transilluminator (365 nm).

The fluorescence was decreased to 98.72% with 500 μM of picric acid. The fluorescence quenching efficiency was consistent with a picric acid concentration range from 0 μM-150 μM as depicted in (**Figure 3.3.a**). A perfect linear correlation was found between F/F_0 and the concentration of picric acid, which is typically described by the linear correlation equation F/F_0= 0.0049+0.993 [C], where C is the concentration of picric acid as shown in (**Figure 3.3.b**). The correlation coefficient (R^2) was found to be 0.99. The limit of detection (LOD) was calculated and found to be as low as 46 nM with signal to noise (S/N) ratio of 3. The loss of fluorescence was visible upon serial addition of picric acid under UV transilluminator

(365nm) shown in (**Figure 3.3.d**). The ideal incubation time for picric acid sensing was determined by observing fluorescence spectra of **BCDs** after the addition of picric acid. After 10 s of incubation, a stable fluorescence was recorded, as shown in (**Figure 3.3.c**); therefore, a concise time, i.e., 10 s, was chosen as the incubation time required for picric acid sensing. This observation concludes that this method of picric acid sensing using **BCDs** is expeditious. The performance of this sensor has been compared with earlier reports in **Table 3.2.** It is essential to mention that under the varying pH (1-12), the sensing ability of BCDs has not been hampered (Figure 3.4.e). The neutral pH, the *p*H of deionized water, has been selected as the optimal *p*H for performing all the experiments. Similarly, varying temperature conditions from 15 ^{o}C to 70 ^{o}C did not affect the sensing ability of **BCDs** (**Figure 3.4.f**). At low temperatures (15 ^{o}C), there is a 10% increase in fluorescence intensity. However, the fluorescence intensity decreases by 15% at high temperatures (70 ^{o}C), but the relative fluorescence quenching after adding 100 μM of picric acid is the same in all conditions. So, we have chosen room temperature as the optimum temperature for performing all the sensing experiments.

3.2.4 Selectivity of BCDs towards picric acid detection and sensing mechanism

The selectivity of the proposed sensor was checked by observing its fluorescence behavior towards various analytes, which are picric acid, 3-nitrotoluene (3-NT), 2,4-dinitrotoluene (2,4-DNT), aniline, 4-idoaniline (4-IA), nitrobenzene (NB), ortho-nitrophenol (o-NP), 4-nitrotoluene (4-NT), and 3-nitroaniline (3-NA) using the concentration 200 μM of each. It is clear from (**Figure 3.4.a**) that none other than picric acid from the above-mentioned analytes could quench fluorescence effectively. The quenching happened due to strong hydrogen bonding and π–π* interaction between the hydroxyl group of picric acid and electron-rich moieties on the surface of **BCDs** [69]. Moreover, there is a clear overlap between the emission

spectrum of **BCDs** and the absorption spectrum of picric acid (**Figure 3.4.b**); no such overlap was seen with any other analyte's absorption spectra which makes **BCDs** a selective sensor for picric acid (**Figure 3.4.d**).

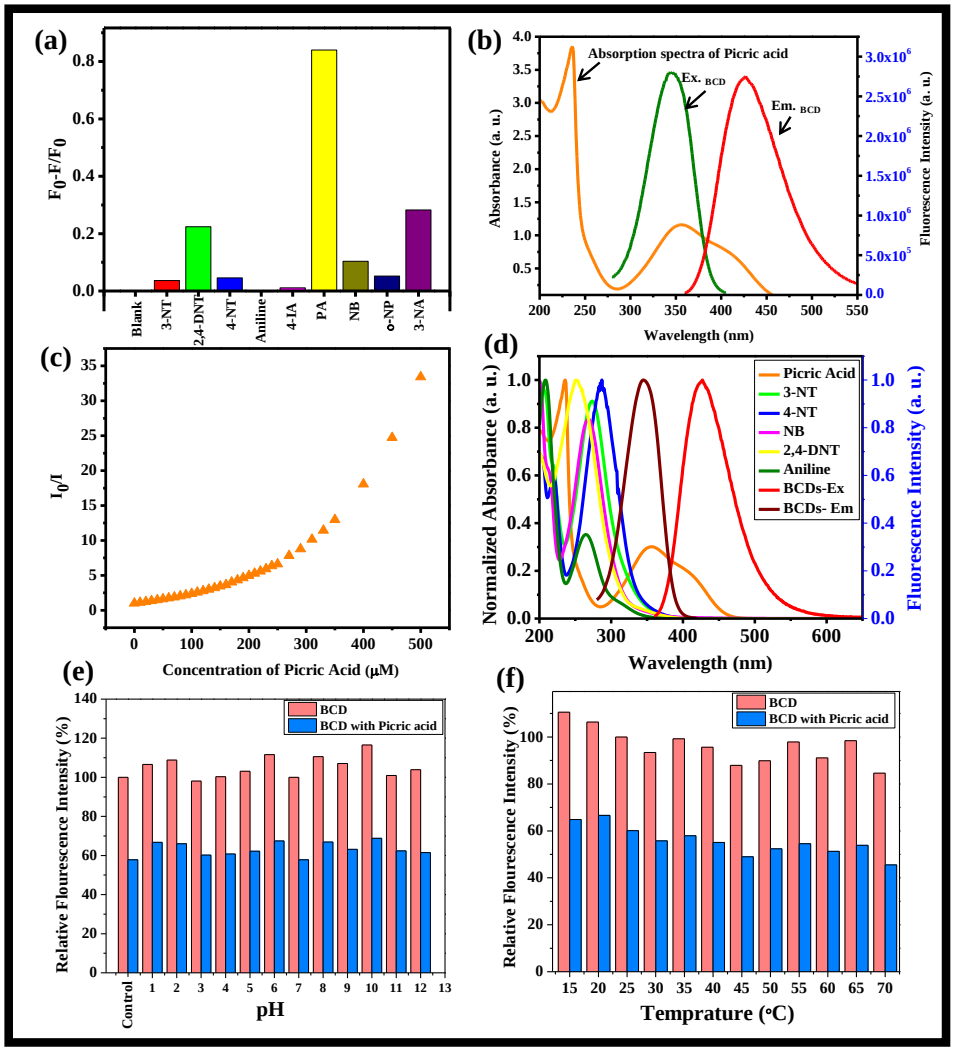

Figure 3.4. (a) Fluorescence quenching efficiency (F_0-F/ F_0) of **BCDs** after various nitroaromatics and aromatic addition. F_0 and F are initial and final fluorescence intensities, i.e., without and with multiple nitroaromatics and aromatic, respectively. (b) The absorption spectra of picric acid overlapped with excitation and emission spectra of **BCDs**. (c) Stern-Volmer plot for picric acid (d) Overlap between the absorption spectra of other nitro and aromatic analytes and the excitation and

emission spectra of **BCDs** (e-f) Effect of *p*H and temperature on sensing of picric acid using **BCDs**

Furthermore, the fluorescence quenching efficiency was measured using Stern−Volmer (SV) equation no. 1.

$$I_0/I = K_{sv}[C] + 1 \quad (1)$$

I_0 represents the fluorescence intensity of **BCDs** alone, whereas I denote the fluorescence intensity of **BCDs** after the addition of picric acid. K_{sv} is a quenching constant (M^{-1}), and [C] is the molar concentration of analyte (picric acid). In the SV plot (**Figure 3.4.c**), the graph was linear at lower analyte concentrations but started to deviate from linearity with increasing analyte concentration. The nonlinear response of the SV plot is suggestive of the energy transfer process or self-absorption between **BCDs** and picric acid. The direct fitting of the plot was used to calculate the quenching constant (K_{sv}), which was calculated as 1.358×10^4 M^{-1}.

To further investigate the mechanism behind BCDs' "turn-off" behavior in the presence of picric acid, the optical properties of both picric acid and **BCDs** were studied precisely. By looking at the overlapping of absorbance spectra of picric acid and excitation and emission spectra of **BCDs**, the phenomenon behind fluorescence quenching was expected to be either fluorescence resonance energy transfer (FRET) or inner filter effect (IFE) [24]. TCSPC was performed for the BCDs solution in the presence and absence of picric acid to investigate further. The average lifetime was reduced from 10.1 ns to 9.94 ns after adding picric acid shown in **Figure 3.5.a.** The slight change in the fluorescence lifetime after the addition of picric acid indicates that the quencher is not making any chemical bonding or forming any new complex with the fluorophore. The liquid (picric acid) binds directly with the fluorophore (BCDs) at the ground state and exhibits static quenching. The fluorophore and the quencher react chemically to form an intermediate product responsible for fluorescence quenching in FRET. So, the observation leads to the inclination sensing

mechanism towards IFE. The use of fluorophore and quencher without the formation of any chemical linking between them makes this sensor simpler and more flexible [70,71]. Additionally, when the absorbance spectrum of picric acid after the addition of **BCDs** was observed, it only showed the enhancement of absorbance value, but no new peak was seen (**Figure 3.5.b)**. It represents the fact that no new chemical complex is formed after mixing of picric acid and **BCDs** i.e., they are not reacting chemically. The completely coincided absorption spectrum of picric acid with the excitation spectrum of **BCDs,** which further extended to the emission spectrum of **BCDs,** also makes strong evidence for the self-absorption process, i.e., IFE as the primary phenomenon responsible for fluorescence quenching (**Figure 3.5.c**) [72].

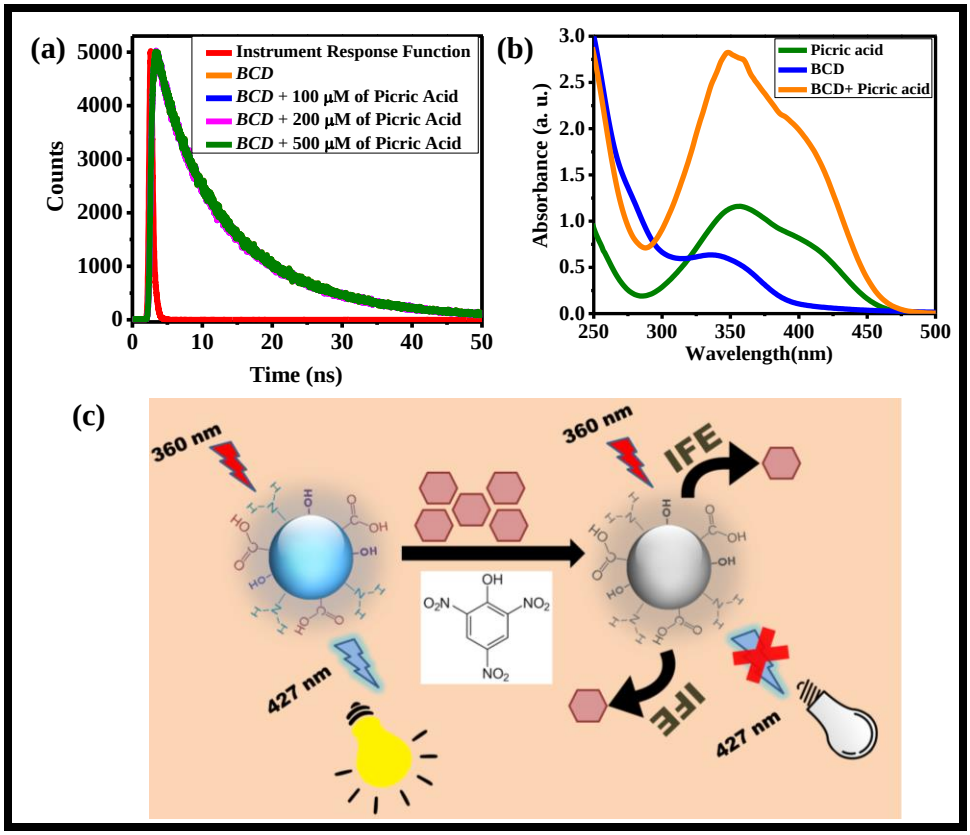

Figure 3.5. (a) TCSPC data of **BCDs** before and after addition of picric acid (b) UV-vis absorption spectra of **BCDs**, Picric acid, and

BCDs+Picric acid (c) Schematic illustration of sensing mechanism of **BCDs** for picric acid sensing.

3.2.5 Detection of picric acid in tap water

The reliability of this analytical sensor for real-time applications was checked using tap water from the laboratory. As expected, a synthesized fluorescent probe detected no picric acid in tap water. Further, water samples were prepared by adding different concentrations of picric acid, and a recovery test was performed. The recovery of picric acid was in the range of 93-97%, with a standard deviation less than 2, as shown in **Table 3.1**. The excellent recovery rate with accuracy and reliability showed the application potential of **BCDs** sensor to be used in real samples.

Table 3.1. Picric acid sensing in water samples (n=3)

Sample	Claimed Concentration (µM)	Found Concentration (µM)	Recovery (%)	SD
1	0	NF*		
2	20	18.75±0.14	93.75	0.28
3	40	39.28±0.26	98.2	0.53
4	60	57.91±0.53	96.51	1.07

* Not found

3.2.6 Visible light-activated anti-bacterial activity of BCDs

To demonstrate the anti-bacterial activity of **BCDs**, *E.coli* (DH5a) was used. The optical density measurement method (OD600) was utilized to verify BCDs' photo-activated bacterial cell growth inhibition. The results shown in (**Figure 3.6.a**) revealed the considerable effect of **BCDs** with light irradiation on *E.coli* cells. The growth of cells treated with **BCDs** alone was inhibited compared to control cells. However, the light exposure

further enhances BCDs' antibacterial nature, confirming the photodynamic antibacterial activity. To determine the use of as prepared antibacterial agent in-vivo, cellular toxicity caused by **BCDs** was studied using MCF-7 cells. However, the non-biocompatible nature of BCDs (Figure 3.6.b) renders its application for in-vitro use only. The silver nanoparticles have been explored extensively for their antibacterial activity [73], and doping of antibacterial silver ions plays a role in bacterial killing by **BCDs**, which get enhanced after photoactivation via the formation of $^1O_2$/ROS. The gold nanoparticles have been used in photodynamic therapies lately [74,75].

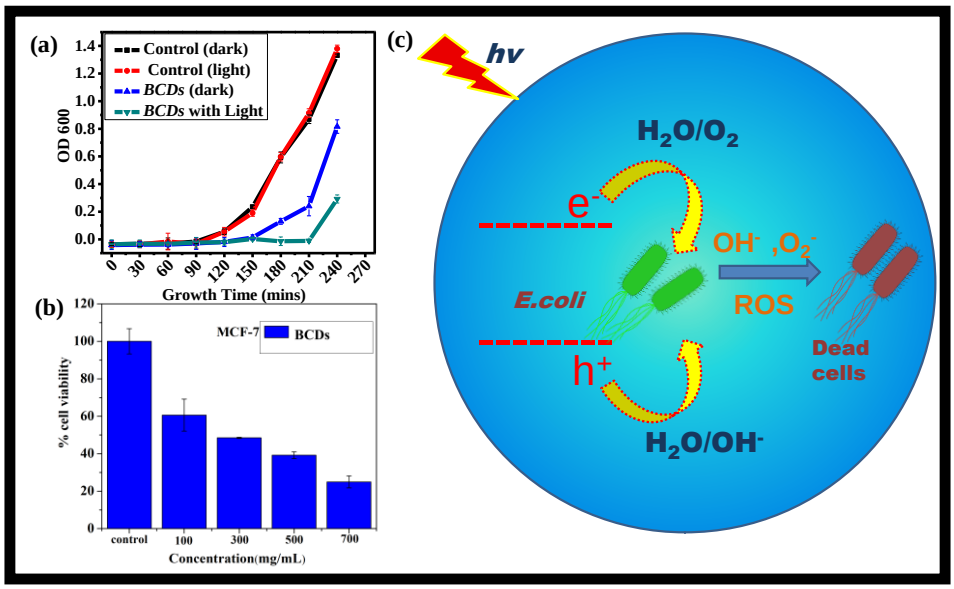

Figure 3.6. (a) Growth curves of *E. coli* cells after treatment with **BCDs** in light and dark conditions, obtained by measuring OD at 600 nm after 30 min interval. (b) Cytocompatibility of **BCDs** using MCF-7 cell line for 24 h (c) Mechanism of antibacterial activity of **BCDs** with light irradiation.

The photoinduced bactericidal activity is attributed to doping of **BCDs** with Au. When the carbon dots absorb light, electrons jump from the valence band to the conduction band, which leads to the generation of electron-hole pairs (**Figure 3.6.c**). These electrons react with available surface-bound O_2, whereas holes as oxidants react with OH^- present in the

system and lead to hydroxyl radical formation [76,77]. The ROS binds with DNA, RNA, and cellular proteins and damages cells' essential components, proving lethal for bacteria growth [76–78]. In addition to that, because of the illumination of light, the **BCDs** damage the bacterial cell structure and deform their bacterial membrane.

3.2.7 Determination of photo-biocidal nature of BCDs

The surface functionalized carbon dots with very high fluorescence quantum yield exhibited photo-toxicity to cells [79–82]. The graphene quantum dots were first studied for photo-induced toxic behavior [79]. A scavenger test using DPBF was performed to check the generation of $^1O_2$ by light irradiation. The $^1O_2$ generated by **BCDs** upon photoirradiation reacts with DPBF, which results in decreased absorbance at 414 nm with each exposure. The data collected after light exposure with 5-sec intervals were plotted and shown in (**Figure 3.7.a**).

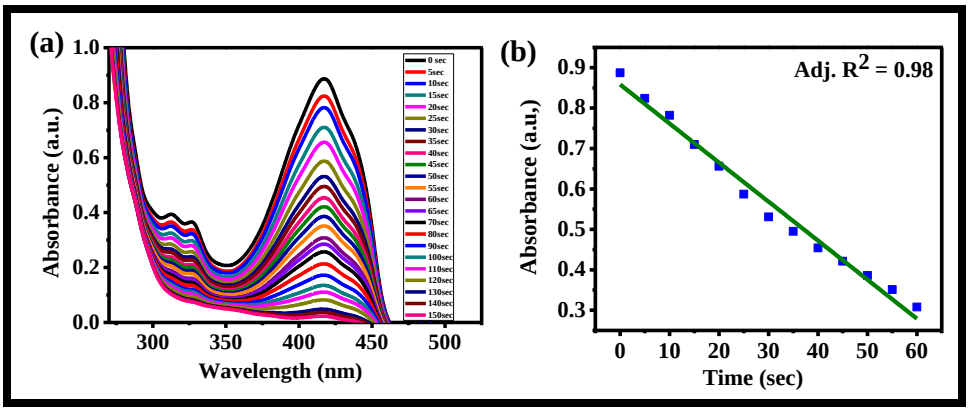

Figure 3.7. (a) The decrease in absorbance after visible light irradiation (5 sec) of DPBF in the presence of **BCDs**. (b) The linear relationship between light exposure time in the presence of **BCDs** and the absorbance of DPBF was measured at 414 nm.

The periodic decrease in absorbance value inferred photo-induced singlet oxygen generation by **BCDs** in DCM. This result stipulates that cell death occurred because of ROS produced through photo-activation of **BCDs**.

Furthermore, Au and Ag's nanoparticles have already shown enough potential for antibacterial activity; thus, doping of these elements in carbon dot lattice may produce a more synergistic effect to suppress bacterial growth and improve the overall antibacterial activity of **BCDs** [83,84]. The results produced here were in accordance with previous literature and provided many potentials to fabricate novel photo-biocidal materials to eradicate pathogens from different surfaces to different people [76,80,82,85].

Table 3.2. A comparison between the reported fluorescent sensors based on CDs and the sensor reported in the present study for detection of Picric acid

Material	QY	LOD	K_{sv} (M^{-1})	Average lifetime	Other Application	Ref.
NS-CQDs	53.19%	0.24μM	-	4.78 ns	-	**[86]**
CDs	12.6%	5.37 ng mL^{-1}	-	8.65 ns	-	**[87]**
C-dots	33.81%	30 nM.	3.86×10^4	5.38 ns	-	**[88]**
CDs	~50%	12 nM	-	-	-	**[89]**
CNDs	NA	0.36 μM	1.30×10^5	-	-	**[7]**
Cdot-PPy	0.04%	32 ppb	-	-	-	**[90]**
P-CDs	3.8%	82 nM	-	2.487 ns	-	**[91]**
N-CDs	41.4%	0.041 μmol L^{-1}	-	2.79 ns	-	**[92]**
C. dots	9.5%	3.86 nM	1.08×10^6	2.72 ns	Bilirubin Detection	**[24]**
CDs	18.67%	10 nM	-	-	-	**[93]**
CNPs	19.8%	0.25 μM	3.18×10^4	-	-	**[94]**
NS-CQDs	~37.8%	0.22 μM	0.03×10^6	9.40 ns	-	**[69]**
C-dots	12.6%	51 nM	-	3.95 ns	-	**[59]**
N-CDs	11.22%	0.046 μM	0.052×10^6	6.38 ns	-	**[95]**
C-dots	26.8%	58.5 nM	2.8×10^4	2.57 ns	-	**[72]**
BCDs	50%	46 nM	1.358×10^4	10.1 ns	Anti-bacterial	**Present work**

3.3. Conclusion

In conclusion, the bimetallic doped carbon dots (**BCDs**) were prepared by a one-pot hydrothermal method. The synthesized carbon dots exhibit an excellent quantum yield of 50% with excitation-independent emission behavior, excellent aqueous solubility, and excellent photo and thermal stability. These carbon dots further act as a superb fluorescent probe for picric acid detection in an aqueous medium. The detection process is simple, selective, and reliable based on IFE and electron transfer between carbon dots and picric acid with a notable LOD 46 nM and quenching constant (K_{SV}) 1.358×104 M^{-1}. These carbon dots were also checked for their antibacterial activity against gram-negative *E.coli*, and results showed the photoactivation of carbon dots with visible light for consequential bactericidal function. So, the present work paves the pathway for using heteroatom doped carbon dots for comprehensive sensing applications and their potential use in microbial elimination applications.

3.4. Experimental

3.4.1. Materials

All the analytical reagent grade chemicals used to prepare carbon dots and sensing were procured from Merck and Sigma-Aldrich. No further purification was done. Deionized water (DI) of the Sartorius milli-Q system was used for all the experiments.

3.4.2. Instruments

Rigaku, RINT smart lab 2500 V X-ray diffractometer was used for performing X-ray diffraction (XRD) with Cu Kα radiation (1.5406 Å). The UV-visible spectroscopic studies were performed using Varian Cary 100 Bio UV-visible spectrophotometer. The fluorescence spectrophotometry was carried out using a Fluoromax spectrofluorometer. Bio-Rad FTS 3000MX instrument was used for recording IR spectra (4000–400 cm^{-1}). FEI Tecnai G2- F20 Transmission Electron Microscope captured TEM images. Elemental mapping was done on an EDAX Octane Elite TW 55 Energy Dispersive Spectroscopy (EDS) instrument. Time-correlated single-photon counting (TCSPC) data were recorded for fluorescence lifetime studies using the TCSPC system model-Fluorocube-01-NL. The adsorption was recorded for MTT assay using Synergy H1 Biotek microplate reader. LabRAM HR (UV system) was used for Raman spectroscopy measurement using a 785 nm laser source.

3.4.3. Synthesis of bimetallic carbon dots (BCDs)

Bimetallic carbon dots were synthesized through the traditional hydrothermal method. First, 4 g citric acid was added to 20 ml of DI water. In the next step, all the other chemicals (28 mg of $HAuCl_4$, 10 mg of $AgNO_3$, 500 mg Bovine serum albumin, and 80 mg of Urea) were weighed and added to the aqueous solution of citric acid. Sonication of the mixture was done for 10 min for homogenous dispersion of all the ingredients. The solution so formed was poured into a Teflon coated

autoclave. The autoclave was kept in the furnace at 180 ℃ for 4 h for hydrothermal carbonization. After cooling at room temperature, the final suspension was centrifuged, which helped remove any solid remains. The remaining clear solution was lyophilized. The sticky lyophilized product was weighed and re-suspended to form a yellow-colored solution using DI water for further use.

3.4.4 Quantum yield

The procedure is recommended in the manual by HORIBA Jobin Yvon IBH Ltd. "A Guide to Recording Fluorescence Quantum Yields" [43] was referred for calculating Quantum Yield. Following equation (2) was used to calculate BCDs' fluorescence quantum yield (ΦF). 0.1M H_2SO_4 was used to dissolve quinine sulfate to be used as standard with a quantum yield of 0.54 [44,45]

$$\Phi F=\Phi_{st}\times S_s/S_{st}\times A_{st}/A_s\times n^2_s/n^2_{st} \quad (2)$$

ΦF and Φ_{st} are the quantum yield of the sample and standard respectively, the absorbance of the standard and sample are ascribed to A_{st} and A_s at their respective excitation wavelength. The integrated fluorescence intensity was plotted against the absorbance of the standard for calculating the slope of standard S_{st} and the slope of sample S_s at various divergent concentrations. The refractive index of solvent for standard and the sample were represented as n_{st} and n_s respectively.

3.4.5 Detection of 2,4,6-trinitrophenol (picric acid) and selectivity studies

A dispersed aqueous solution of **BCDs** was prepared according to a typical photoluminescence (PL) studies procedure. Further, in a 1 cm quartz cuvette, 3 mL of the prepared aqueous solution was poured into, recording the fluorescence response in the range of 370−730 nm upon 360 nm excitation. The maximum attained intensity was set as control (F_0). Nitroaromatics solution (10 mM) was prepared afresh for sensing studies.

The spectra of **BCDs** solution after adding different nitroaromatic were recorded at λ_{ex}. 360 nm excitation. The experimental conditions were kept the same for all the studies. Fluorescence response kinetics of **BCDs** were studied using lifetime decay data recorded at TCSPC system and analyzed using IBH DAS 6.0 software [22]. The reduced χ-square (χ2) value was used to investigate fit value, and fluorescence lifetime decay was measured using the iterative reconciliation method. The decay values were fitted with a three-exponential function by utilizing equation no. 3.

$$F(\tau) = \Sigma\, \alpha i \exp(-\tau/\tau i) \quad (3)$$

Here, $F(\tau)$ represents the fluorescence decay (normalized), α denotes the amplitude of the decay component τ. Whereas the average lifetime was calculated by utilizing equation no. 4.

$$\{\tau\} = \Sigma \alpha_i \tau_i \quad (4)$$

3.4.5 Cytotoxicity and antibacterial studies

Biocompatibility of **BCDs** was checked using MCF7 (Breast cancer cell line) via MTT assay using (3-(4,5-dimethylthiazole-2-yl) -2,5-diphenyltetrazolium bromide) [46,47]. Live cells were quantified by colorimetric analysis. The metabolically active cells reduce yellow tetrazolium to purple-colored insoluble formazan, dissolved using DMSO, whose absorbance was recorded at 570 nm. Penicillin/streptomycin (10,000 U mL^{-1}) and FBS (fetal bovine serum 10% (v/v)) were added to the growth media DMEM (Dulbecco's modified Eagle medium) to get the final media to be used for growing cells. The MTT assay was performed using 96 wells plate, and each well containing 100 μL of DMEM was seeded with $1x10^4$ cells. The optimum condition for cell growth was attained using an incubator where cells were kept at 37 ℃ under a 5% CO_2 humidified atmosphere for 24 h. The assay was performed using various concentrations of **BCDs** in triplicate. The media containing **BCDs** was replaced after 24 h with fresh media containing MTT (0.5 mg mL^{-1}) and kept in an incubator for 4 h to form purple formazan crystals. DMSO

(100 μL) was used to dissolve the insoluble formazan crystals, and absorbance was measured at 570 nm. The percent cell viability was calculated using equation no. 5, written below.

$$\%CellViability=Absorbance_{(sample)}/Absorbance_{(Control)}\times100 \quad (5)$$

All the labware was autoclaved for 15 min at 121 °C to maintain sterile conditions for antibacterial studies. Escherichia coli (*E.coli* DH5α) was cultured in Luria broth at 37 °C under continuous shaking at 120 rpm in an orbital shaker and harvested through centrifugation when the exponential growth phase reached. The optical density of the resuspended bacterial pallet in PBS was measurements at 600 nm (OD600), and the OD was adjusted to 0.1 using PBS to make a fresh inoculum. The 10 μL inoculum was added to 5 mL of fresh Luria broth for performing further experiments. The control was kept under optimal bacterial growth conditions; the other group belonging to the only light group was visible light (400-700 nm) irradiated bacteria for 30 min before incubation, the third group was the bacteria treated with BCDs (200 μg mL^{-1}) and incubated in the dark, whereas the fourth group was bacteria treated with BCDs (200 μg mL^{-1}) irradiated using visible light lamp (400-700 nm) for 30 min and then incubated. All the experiments were performed in triplicates. Absorbance was measured at 600 nm after 30 min intervals up to 240 min.

3.4.6 DPBF assay for singlet oxygen ($^1O_2$) measurements

1, 3-diphenylisobenzofuran (DPBF) was used for estimating the singlet oxygen ($^1O_2$) spawning ability of **BCDs** [48]. The $^1O_2$ generated after irradiation of **BCDs** using a visible light (400-700 nm) taken up by DPBF results in decreased absorbance value [49]. DPBF solution ($3x10^{-5}$ M) was used, into which **BCDs** were added, and the whole mixture was exposed to light. The absorbance was measured using a UV-Vis spectrophotometer at 414 nm after 5 sec light exposure till 150 sec.

3.5. References

[1] Kovacic, P., Somanathan, R. (2014), Nitroaromatic compounds: Environmental toxicity, carcinogenicity, mutagenicity, therapy, and mechanism: Nitro aromatic pollutants, J. Appl. Toxicol., 34, 810–824 (DOI: 10.1002/jat.2980)

[2] Parham, H., Zargar, B., Rezazadeh, M. (2012), Removal, preconcentration and spectrophotometric determination of picric acid in water samples using modified magnetic iron oxide nanoparticles as an efficient adsorbent, Mater. Sci. Eng. C., 32, 2109–2114 (DOI: 10.1016/j.msec.2012.05.044)

[3] Rajak, R., Saraf, M., Verma, S.K., Kumar, R., Mobin, S.M. (2019), Dy(III)-Based Metal–Organic Framework as a Fluorescent Probe for Highly Selective Detection of Picric Acid in Aqueous Medium, Inorg. Chem., 58, 16065–16074 (DOI: 10.1021/acs.inorgchem.9b02611)

[4] Niu, Q., Gao, K., Lin, Z., Wu, W. (2013), Amine-capped carbon dots as a nanosensor for sensitive and selective detection of picric acid in aqueous solution via electrostatic interaction, Anal. Methods., 5, 6228–6233 (DOI: 10.1039/C3AY41275J)

[5] Malik, A.H., Hussain, S., Kalita, A., Iyer, P.K. (2015), Conjugated Polymer Nanoparticles for the Amplified Detection of Nitro-explosive Picric Acid on Multiple Platforms, ACS Appl. Mater. Interfaces, 7, 26968–26976 (DOI: 10.1021/acsami.5b08068)

[6] Ahmad, K., Mohammad, A., Mathur, P., Mobin, S.M. (2016), Preparation of $SrTiO_3$ perovskite decorated rGO and electrochemical detection of nitroaromatics, Electrochimica Acta., 215, 435–446 (DOI: 10.1016/j.electacta.2016.08.123)

[7] Wang, B., Mu, Y., Zhang, C., Li, J. (2017), Blue photoluminescent carbon nanodots prepared from zeolite as efficient sensors for picric acid detection, Sens. Actuators B Chem., 253, 911–917 (DOI: 10.1016/j.snb.2017.07.046)

[8] Roy, B., Bar, A.K., Gole, B., Mukherjee, P.S. (2013), Fluorescent Tris-Imidazolium Sensors for Picric Acid Explosive, J. Org. Chem., 78, 1306–1310 (DOI: 10.1021/jo302585a)

[9] Sivaraman, G., Vidya, B., Chellappa, D. (2014), Rhodamine based selective turn-on sensing of picric acid, RSC Adv., 4, 30828–30831 (DOI: 10.1039/C4RA02931C)

[10] Kaur, I., Sharma, V., Mobin, S.M., Kaur, P., Singh, K. (2019), Excitation wavelength based reversible multicolor photoluminescence by a single chromophore upon aggregation: Detection of picric acid-application in bioimaging, Sens. Actuators B Chem., 281, 613–622 (DOI: 10.1016/j.snb.2018.10.161)

[11] Tanwar, A.S., Meher, N., Adil, L.R., Iyer, P.K. (2020), Stepwise elucidation of fluorescence based sensing mechanisms

considering picric acid as a model analyte, The Analyst, 145, 4753–4767 (DOI: 10.1039/D0AN00732C)
[12] Young, J.A. (2008). Picric Acid, J. Chem. Educ., 85, 492 (DOI: 10.1021/ed085p492)
[13] Gogoi, B., Sarma, N-S., (2015), Curcumin–Cysteine and Curcumin–Tryptophan Conjugate as Fluorescence Turn On Sensors for Picric Acid in Aqueous Media, ACS Applied Materials & Interfaces, 7, 11195–11202 (DOI: 10.1021/acsami.5b01102)
[14] Ramanan, V., Thiyagarajan, S.K., Raji, K., Suresh, R., Sekar, R., Ramamurthy, P. (2016), Outright Green Synthesis of Fluorescent Carbon Dots from Eutrophic Algal Blooms for In Vitro Imaging, ACS Sustain. Chem. Eng., 4, 4724–4731 (DOI: 10.1021/acssuschemeng.6b00935)
[15] Baker, S.N., Baker, G.A. (2010), Luminescent Carbon Nanodots: Emergent Nanolights, Angew. Chem. Int. Ed., 49, 6726–6744 (DOI: 10.1002/anie.200906623)
[16] Si, M., Zhang, J., He, Y., Yang, Z., Yan, X., Liu, M., Zhuo, S., Wang, S., Min, X., Gao, C., Chai, L., Shi, Y. (2018), Synchronous and rapid preparation of lignin nanoparticles and carbon quantum dots from natural lignocellulose, Green Chem., 20, 3414-3419 (DOI: 10.1039/C8GC00744F)
[17] Sharma, V., Tiwari, P., Mobin, S.M. (2017), Sustainable carbon-dots: recent advances in green carbon dots for sensing and bioimaging, J. Mater. Chem. B., 5, 8904–8924 (DOI: 10.1039/C7TB02484C)
[18] Kaur, N., Sharma, V., Tiwari, P., Saini, A.K., Mobin, S.M. (2019), “Vigna radiata” based green C-dots: Photo-triggered theranostics, fluorescent sensor for extracellular and intracellular iron (III) and multicolor live cell imaging probe, Sens. Actuators B Chem., 291, 275–286 (DOI: 10.1016/j.snb.2019.04.039)
[19] Sharma, V., Kaur, N., Tiwari, P., Mobin, S.M. (2018), Full color emitting fluorescent carbon material as reversible pH sensor with multicolor live cell imaging, J. Photochem. Photobiol. B., 182, 137–145 (DOI: 10.1016/j.jphotobiol.2018.04.006)
[20] Devi, P., Thakur, A., Bhardwaj, S.K., Saini, S., Rajput, P., Kumar, P. (2018), Metal ion sensing and light activated antimicrobial activity of aloe-vera derived carbon dots, J. Mater. Sci. Mater. Electron., 29, 17254–17261 (DOI: 10.1007/s10854-018-9819-0)
[21] Atchudan, R., Edison, T.N.J.I., Chakradhar, D., Perumal, S., Shim, J.-J., Lee, Y.R. (2017), Facile green synthesis of nitrogen-doped carbon dots using Chionanthus retusus fruit extract and investigation of their suitability for metal ion sensing and biological applications, Sens. Actuators B Chem., 246, 497–509 (DOI: 10.1016/j.snb.2017.02.119)

[22] Tiwari, P., Kaur, N., Sharma, V., Kang, H., Uddin, J., Mobin, S.M. (2019), Cannabis sativa-derived carbon dots co-doped with N–S: highly efficient nanosensors for temperature and vitamin B12, New J. Chem., 43, 17058–17068 (DOI: 10.1039/C9NJ04061G)

[23] Shen, P., Xia, Y. (2014), Synthesis-Modification Integration: One-Step Fabrication of Boronic Acid Functionalized Carbon Dots for Fluorescent Blood Sugar Sensing, Anal. Chem., 86, 5323–5329 (DOI: 10.1021/ac5001338)

[24] Roshni, V., Gujar, V., Muntjeeb, S., Doshi, P., Ottoor, D. (2021), Novel and Reliable Chemosensor Based on C. dots from Sunflower seeds for the Distinct Detection of Picric Acid and Bilirubin, Spectrochim. Acta. A. Mol. Biomol. Spectrosc., 250, 119354 (DOI: 10.1016/j.saa.2020.119354)

[25] Zhao, A., Chen, Z., Zhao, C., Gao, N., Ren, J., Qu, X. (2015), Recent advances in bioapplications of C-dots, Carbon, 85, 309–327 (DOI: 10.1016/j.carbon.2014.12.045)

[26] Xu, D., Lin, Q., Chang, H. (2020), Recent Advances and Sensing Applications of Carbon Dots, Small Methods., 4, 1900387 (DOI: 10.1002/smtd.201900387)

[27] Wen, X., Zhao, Z., Zhai, S., Wang, X., Li, Y. (2020), Stable nitrogen and sulfur co-doped carbon dots for selective folate sensing, in vivo imaging and drug delivery, Diam. Relat. Mater., 105, 107791 (DOI: 10.1016/j.diamond.2020.107791)

[28] Yen, Y.-T., Lin, Y.-S., Chen, T.-Y., Chyueh, S.-C., Chang, H.-T. (2019), Carbon dots functionalized papers for high-throughput sensing of 4-chloroethcathinone and its analogues in crime sites, R. Soc. Open Sci., 6, 191017 (DOI: 10.1098/rsos.191017)

[29] Sharma, V., Tiwari, P., Kaur, N., Mobin, S.M. (2021), Optical nanosensors based on fluorescent carbon dots for the detection of water contaminants: a review, Environ. Chem. Lett., 19, 3229–3241 (DOI: 10.1007/s10311-021-01241-8)

[30] Hasan, J., Crawford, R.J., Ivanova, E.P. (2013), Antibacterial surfaces: the quest for a new generation of biomaterials, Trends Biotechnol., 31, 295–304 (DOI: 10.1016/j.tibtech.2013.01.017)

[31] Schwartz, V.B., Thétiot, F., Ritz, S., Pütz, S., Choritz, L., Lappas, A., Förch, R., Landfester, K., Jonas, U. (2012), Antibacterial Surface Coatings from Zinc Oxide Nanoparticles Embedded in Poly(N-isopropylacrylamide) Hydrogel Surface Layers, Adv. Funct. Mater., 22, 2376–2386 (DOI: 10.1002/adfm.201102980)

[32] Sharma, V., Mohammad, A., Mishra, V., Chaudhary, A., Kapoor, K., Mobin, S.M. (2016), Fabrication of innovative ZnO

nanoflowers showing drastic biological activity, New J. Chem., 40, 2145–2155 (DOI: 10.1039/C5NJ02391B)
[33] Ventola, C.L. (2015), The Antibiotic Resistance Crisis, Pharm. Ther. 40, 277–283 (PMID: 25859123; PMCID: PMC4378521)
[34] Kaur, N., Tiwari, P., Kapoor, K.S., Saini, A.K., Sharma, V., Mobin, S.M. (2020), Metal–organic framework based antibiotic release and antimicrobial response: an overview, CrystEngComm. 22, 7513–7527 (DOI: 10.1039/D0CE01215G)
[35] Knoblauch, R., Geddes, C.D. (2020), Carbon Nanodots in Photodynamic Antimicrobial Therapy: A Review, Materials, 13, 4004 (DOI: 10.3390/ma13184004)
[36] Cieplik, F., Buchalla, W., Hellwig, E., Al-Ahmad, A., Hiller, K.-A., Maisch, T., Karygianni, L. (2017), Antimicrobial photodynamic therapy as an adjunct for treatment of deep carious lesions—A systematic review, Photodiagnosis Photodyn. Ther., 18, 54–62 (DOI: 10.1016/j.pdpdt.2017.01.005)
[37] Awak, M.M.A., Wang, P., Wang, S., Tang, Y., Sun, Y.-P., Yang, L. (2017), Correlation of carbon dots' light-activated antimicrobial activities and fluorescence quantum yield, RSC Adv., 7, 30177–30184 (DOI: 10.1039/C7RA05397E)
[38] A. Smith, N., Zhang, P., E. Greenough, S., D. Horbury, M., J. Clarkson, G., McFeely, D., Habtemariam, A., Salassa, L., G. Stavros, V., G. Dowson, C., J. Sadler, P.: Combatting AMR (2017), photoactivatable ruthenium(ii)-isoniazid complex exhibits rapid selective antimycobacterial activity, Chem. Sci., 8, 395–404 (DOI: 10.1039/C6SC03028A)
[39] M. Marković, Z., P. Jovanović, S., Z. Mašković, P., Danko, M., Mičušík, M., B. Pavlović, V., D. Milivojević, D., Kleinová, A., Špitalský, Z., Marković, B.M.T. (2018) Photo-induced antibacterial activity of four graphene based nanomaterials on a wide range of bacteria, RSC Adv., 8, 31337–31347 (DOI: 10.1039/C8RA04664F)
[40] Stanković, N.K., Bodik, M., Šiffalovič, P., Kotlar, M., Mičušik, M., Špitalsky, Z., Danko, M., Milivojević, D.D., Kleinova, A., Kubat, P., Capakova, Z., Humpoliček, P., Lehocky, M., Todorović Marković, B.M., Marković, Z.M. (2018), Antibacterial and Antibiofouling Properties of Light Triggered Fluorescent Hydrophobic Carbon Quantum Dots Langmuir–Blodgett Thin Films, ACS Sustain. Chem. Eng., 6, 4154–4163 (DOI: 10.1021/acssuschemeng.7b04566)
[41] Kováčová, M., Marković, Z.M., Humpolíček, P., Mičušík, M., Švajdlenková, H., Kleinová, A., Danko, M., Kubát, P., Vajďák, J., Capáková, Z., Lehocký, M., Münster, L., Todorović Marković, B.M., Špitalský, Z. (2018), Carbon Quantum Dots Modified Polyurethane Nanocomposite as Effective Photocatalytic

and Antibacterial Agents, ACS Biomater. Sci. Eng., 4, 3983–3993 (DOI: 10.1021/acsbiomaterials.8b00582)

[42] Marković, Z.M., Labudová, M., Danko, M., Matijašević, D., Mičušík, M., Nádaždy, V., Kováčová, M., Kleinová, A., Špitalský, Z., Pavlović, V., Milivojević, D.D., Medić, M., Todorović Marković, B.M. (2020), Highly Efficient Antioxidant F- and Cl-Doped Carbon Quantum Dots for Bioimaging, ACS Sustain. Chem. Eng., 8, 16327–16338 (DOI: 10.1021/acssuschemeng.0c06260)

[43] Bao, L., Zhang, Z.-L., Tian, Z.-Q., Zhang, L., Liu, C., Lin, Y., Qi, B., Pang, D.-W. (2011), Electrochemical Tuning of Luminescent Carbon Nanodots: From Preparation to Luminescence Mechanism, Adv. Mater., 23, 5801–5806 (DOI: 10.1002/adma.201102866)

[44] Melhuish, W.H. (1961) QUANTUM EFFICIENCIES OF FLUORESCENCE OF ORGANIC SUBSTANCES: EFFECT OF SOLVENT AND CONCENTRATION OF THE FLUORESCENT SOLUTE1, J. Phys. Chem., 65, 229–235 (DOI: 10.1021/j100820a009)

[45] Poddar, M., Sharma, V., Mobin, S.M., Misra, R. (2018), 1,8-Naphthalimide-Substituted BODIPY Dyads: Synthesis, Structure, Properties, and Live-Cell Imaging, Chem. Asian J., 13, 2881–2890 (DOI: 10.1002/asia.201800816)

[46] Carmichael, J., DeGraff, W.G., Gazdar, A.F., Minna, J.D., Mitchell, J.B. (1987), Evaluation of a tetrazolium-based semiautomated colorimetric assay: assessment of chemosensitivity testing, Cancer Res., 47, 936–942

[47] Sharma, V., Saini, A.K., Mobin, S.M. (2016), Multicolour fluorescent carbon nanoparticle probes for live cell imaging and dual palladium and mercury sensors, J. Mater. Chem. B., 4, 2466–2476 (DOI: 10.1039/C6TB00238B)

[48] Zhang, D., Wen, L., Huang, R., Wang, H., Hu, X., Xing, D. (2018), Mitochondrial specific photodynamic therapy by rare-earth nanoparticles mediated near-infrared graphene quantum dots, Biomaterials, 153, 14–26 (DOI: 10.1016/j.biomaterials.2017.10.034)

[49] Meng, A.-N., Chaihu, L.-X., Chen, H.-H., Gu, Z.-Y. (2017), Ultrahigh adsorption and singlet-oxygen mediated degradation for efficient synergetic removal of bisphenol A by a stable zirconium-porphyrin metal-organic framework, Sci. Rep., 7, 6297 (DOI: 10.1038/s41598-017-06194-z)

[50] Hu, Y., Yang, J., Tian, J., Yu, J.-S. (2015), How do nitrogen-doped carbon dots generate from molecular precursors? An investigation of the formation mechanism and a solution-based large-scale synthesis, J. Mater. Chem. B., 3, 5608–5614 (DOI: 10.1039/C5TB01005E)

[51] Sharma, V., Singh, S.K., Mobin, S.M. (2019), Bioinspired carbon dots: from rose petals to tunable emissive nanodots, Nanoscale Adv., 1, 1290–1296 (DOI: 10.1039/C8NA00105G)
[52] Wang, P., Zhang, D., Zhang, L., Fang, Y. (2013), The SERS study of graphene deposited by gold nanoparticles with 785nm excitation, Chem. Phys. Lett., 556, 146–150 (DOI: 10.1016/j.cplett.2012.11.018)
[53] Buiculescu, R., Stefanakis, D., Androulidaki, M., Ghanotakis, D., Chaniotakis, N.A. (2016), Controlling carbon nanodot fluorescence for optical biosensing, Analyst, 141, 4170–4180 (DOI: 10.1039/C6AN00783J)
[54] Li, D., Yuan, X., Li, C., Luo, Y., Jiang, Z. (2020), A novel fluorescence aptamer biosensor for trace Pb(II) based on gold-doped carbon dots and DNAzyme synergetic catalytic amplification, 221, 117056 (DOI: 10.1016/j.jlumin.2020.117056)
[55] Cao, C.-B., Lv, Q., Zhu, H.-S. (2003), Carbon nitride prepared by solvothermal method, Diam. Relat. Mater., 12, 1070–1074 (DOI: 10.1016/S0925-9635(02)00309-6)
[56] Thi Thanh Thuy, N., Hoang Huy, L., Thuy Vy, T., Thi Thanh Tam, N., Thi Lan Thanh, B., Thi My Lan, N. (2021), Green Synthesis of Silver Nanoparticles Using Plectranthus Amboinicus Leaf Extract for Preparation of CMC/PVA Nanocomposite Film, J. Renew. Mater., 9, 1393–1411 (DOI: 10.32604/jrm.2021.015772)
[57] Zhang, R., Yu, S., Shi, W., Wang, X., Cheng, J., Zhang, Z., Li, L., Bao, X., Zhang, B. (2017), Surface modification of piperazine-based nanofiltration membranes with serinol for enhanced antifouling properties in polymer flooding produced water treatment, RSC Adv., 7, 48904–48912 (DOI: 10.1039/C7RA09496E)
[58] Rajamanikandan, S., Biruntha, M., Ramalingam, G. (2021), Blue Emissive Carbon Quantum Dots (CQDs) from Bio-waste Peels and Its Antioxidant Activity, J. Clust. Sci., (DOI: 10.1007/s10876-021-02029-0)
[59] Fan, Y.Z., Zhang, Y., Li, N., Liu, S.G., Liu, T., Li, N.B., Luo, H.Q. (2017), A facile synthesis of water-soluble carbon dots as a label-free fluorescent probe for rapid, selective and sensitive detection of picric acid, Sens. Actuators B Chem., 240, 949–955 (DOI: 10.1016/j.snb.2016.09.063)
[60] Nagaraj, A., Munusamy, M.A., Ahmed, M., Kumar, S.S., Rajan, M. (2018), Hydrothermal synthesis of a mineral-substituted hydroxyapatite nanocomposite material for fluoride removal from drinking water, New J. Chem., 42, 12711–12721 (DOI: 10.1039/C8NJ02401D)
[61] Md Salim, R., Asik, J., Sarjadi, M.S. (2021), Chemical functional groups of extractives, cellulose and lignin extracted

from native Leucaena leucocephala bark, Wood Sci. Technol., 55, 295–313 (DOI: 10.1007/s00226-020-01258-2)
[62] Niu, J., Gao, H., Wang, L., Xin, S., Zhang, G., Wang, Q., Guo, L., Liu, W., Gao, X., Wang, Y. (2014), Facile synthesis and optical properties of nitrogen-doped carbon dots, New J. Chem., 38, 1522–1527 (DOI: 10.1039/C3NJ01068F)
[63] Schneider, J., Reckmeier, C.J., Xiong, Y., von Seckendorff, M., Susha, A.S., Kasák, P., Rogach, A.L. (2017), Molecular Fluorescence in Citric Acid-Based Carbon Dots, J. Phys. Chem. C., 121, 2014–2022 (DOI: 10.1021/acs.jpcc.6b12519)
[64] Miao, P., Han, K., Tang, Y., Wang, B., Lin, T., Cheng, W. (2015), Recent advances in carbon nanodots: synthesis, properties and biomedical applications, Nanoscale, 7, 1586–1595 (DOI: 10.1039/C4NR05712K)
[65] Dong, Y., Pang, H., Yang, H.B., Guo, C., Shao, J., Chi, Y., Li, C.M., Yu, T. (2013), Carbon-based dots co-doped with nitrogen and sulfur for high quantum yield and excitation-independent emission, Angew. Chem. Int. Ed Engl., 52, 7800–7804 (DOI: 10.1002/anie.201301114)
[66] Ortega-Liebana, M.C., Chung, N.X., Limpens, R., Gomez, L., Hueso, J.L., Santamaria, J., Gregorkiewicz, T. (2017), Uniform luminescent carbon nanodots prepared by rapid pyrolysis of organic precursors confined within nanoporous templating structures, Carbon, 117, 437–446 (DOI: 10.1016/j.carbon.2017.03.017)
[67] Jiao, Y., Gong, X., Han, H., Gao, Y., Lu, W., Liu, Y., Xian, M., Shuang, S., Dong, C. (2018), Facile synthesis of orange fluorescence carbon dots with excitation independent emission for pH sensing and cellular imaging, Anal. Chim. Acta., 1042, 125–132 (DOI: 10.1016/j.aca.2018.08.044)
[68] Wang, D., Wang, Z., Zhan, Q., Pu, Y., Wang, J.-X., Foster, N.R., Dai, L. (2017), Facile and Scalable Preparation of Fluorescent Carbon Dots for Multifunctional Applications, Engineering, 3, 402–408 (DOI: 10.1016/J.ENG.2017.03.014)
[69] Chandra, S., Bano, D., Pradhan, P., Singh, V.K., Yadav, P.K., Sinha, D., Hasan, S.H. (2020), Nitrogen/sulfur-co-doped carbon quantum dots: a biocompatible material for the selective detection of picric acid in aqueous solution and living cells, Anal. Bioanal. Chem., 412, 3753–3763 (DOI: 10.1007/s00216-020-02629-1)
[70] Ling, Y., Li, J.X., Qu, F., Li, N.B., Luo, H.Q. (2014), Rapid fluorescence assay for Sudan dyes using polyethyleneimine-coated copper nanoclusters, Microchim. Acta., 181, 1069–1075 (DOI: 10.1007/s00604-014-1214-9)
[71] Shang, L., Dong, S. (2009), Design of Fluorescent Assays for Cyanide and Hydrogen Peroxide Based on the Inner Filter

Effect of Metal Nanoparticles, Anal. Chem., 81, 1465–1470 (DOI: 10.1021/ac802281x)
[72] Zheng, Y., Wang, ·Shu, Li, R., Pan, L., Li, L., Qi, Z., Li, C. (2021), Highly selective detection of nitroaromatic explosive 2,4,6-trinitrophenol (TNP) using N-doped carbon dots, Res. Chem. Intermed., 47, 2421–2431 (DOI: 10.1007/s11164-021-04410-0)
[73] Chernousova, S., Epple, M. (2013), Silver as Antibacterial Agent: Ion, Nanoparticle, and Metal, Angew. Chem. Int. Ed., 52, 1636–1653 (DOI: 10.1002/anie.201205923)
[74] Liao, J., Li, W., Peng, J., Yang, Q., Li, H., Wei, Y., Zhang, X., Qian, Z. (2015), Combined Cancer Photothermal-Chemotherapy Based on Doxorubicin/Gold Nanorod-Loaded Polymersomes, Theranostics, 5, 345–356 (DOI: 10.7150/thno.10731)
[75] Dykman, L.A., Khlebtsov, N.G. (2016), Multifunctional gold-based nanocomposites for theranostics, Biomaterials, 108, 13–34 (DOI: 10.1016/j.biomaterials.2016.08.040)
[76] Zhou, Z., Song, J., Nie, L., Chen, X. (2016), Reactive oxygen species generating systems meeting challenges of photodynamic cancer therapy, Chem. Soc. Rev., 45, 6597–6626 (DOI: 10.1039/C6CS00271D)
[77] Fu, P.P., Xia, Q., Hwang, H.-M., Ray, P.C., Yu, H. (2014), Mechanisms of nanotoxicity: Generation of reactive oxygen species, J. Food Drug Anal., 22, 64–75 (DOI: 10.1016/j.jfda.2014.01.005)
[78] Wang, C., Yue, L., Wang, S., Pu, Y., Zhang, X., Hao, X., Wang, W., Chen, S. (2018), Role of Electric Field and Reactive Oxygen Species in Enhancing Antibacterial Activity: A Case Study of 3D Cu Foam Electrode with Branched CuO–ZnO NWs, J. Phys. Chem. C., 122, 26454–26463 (DOI: 10.1021/acs.jpcc.8b08232)
[79] Ge, J., Lan, M., Zhou, B., Liu, W., Guo, L., Wang, H., Jia, Q., Niu, G., Huang, X., Zhou, H., Meng, X., Wang, P., Lee, C.-S., Zhang, W., Han, X. (2014), A graphene quantum dot photodynamic therapy agent with high singlet oxygen generation, Nat. Commun., 5, 4596 (DOI: 10.1038/ncomms5596)
[80] Albert, K., Hsu, H.-Y. (2016), Carbon-Based Materials for Photo-Triggered Theranostic Applications, Mol. Basel Switz., 21, (DOI: 10.3390/molecules21111585)
[81] He, H., Zheng, X., Liu, S., Zheng, M., Xie, Z., Wang, Y., Yu, M., Shuai, X. (2018), Diketopyrrolopyrrole-Based Carbon Dots for Photodynamic Therapy, Nanoscale, (DOI: 10.1039/C8NR02643B)
[82] Peng, H., Jing, L., Xiansong, W., Zhe, W., Chunlei, Z., Meng, H., Kan, W., Feng, C., Zhiming, L., Guangxia, S., Daxiang, C., Xiaoyuan, C. (2012) Light-Triggered Theranostics Based on

Photosensitizer-Conjugated Carbon Dots for Simultaneous Enhanced-Fluorescence Imaging and Photodynamic Therapy, Adv. Mater., 24, 5104–5110 (DOI: 10.1002/adma.201200650)

[83] Zhao, D., Liu, X., Zhang, R., Xiao, X., Li, J. (2021), Preparation of two types of silver-doped fluorescent carbon dots and determination of their antibacterial properties, J. Inorg. Biochem, 214, 111306 (DOI: 10.1016/j.jinorgbio.2020.111306)

[84] Ciobanu, C., Massuyeau, F., Constantin, L., Predoi, D. (2011), Structural and physical properties of antibacterial Ag-doped nano-hydroxyapatite synthesized at 100°C, Nanoscale Res. Lett., 6, 613 (DOI: 10.1186/1556-276X-6-613)

[85] Abu Rabe, D.I., Al Awak, M.M., Yang, F., Okonjo, P.A., Dong, X., Teisl, L.R., Wang, P., Tang, Y., Pan, N., Sun, Y.-P., Yang, L. (2019), The dominant role of surface functionalization in carbon dots' photo-activated antibacterial activity, Int. J. Nanomedicine, 14, 2655–2665 (DOI: 10.2147/IJN.S200493)

[86] Khan, Z.M.S.H., Saifi, S., Shumaila, Aslam, Z., Khan, S.A., Zulfequar, M. (2020) A facile one step hydrothermal synthesis of carbon quantum dots for label -free fluorescence sensing approach to detect picric acid in aqueous solution, J. Photochem. Photobiol. Chem., 388, 112201 (DOI: 10.1016/j.jphotochem.2019.112201)

[87] Wang, X., Liu, Y., Zhou, Q., Sheng, X., Sun, Y., Zhou, B., Zhao, J., Guo, J. (2020), A reliable and facile fluorescent sensor from carbon dots for sensing 2,4,6-trinitrophenol based on inner filter effect, Sci. Total Environ., 720, 137680 (DOI: 10.1016/j.scitotenv.2020.137680)

[88] Li, N., Liu, S.G., Fan, Y.Z., Ju, Y.J., Xiao, N., Luo, H.Q., Li, N.B. (2018), Adenosine-derived doped carbon dots: From an insight into effect of N/P co-doping on emission to highly sensitive picric acid sensing, Anal. Chim. Acta., 1013, 63–70 (DOI: 10.1016/j.aca.2018.01.049)

[89] Kathiravan, A., Gowri, A., Srinivasan, V., Smith, T.A., Ashokkumar, M., Asha Jhonsi, M. (2020), A simple and ubiquitous device for picric acid detection in latent fingerprints using carbon dots, The Analyst, 145, 4532–4539 (DOI: 10.1039/D0AN00750A)

[90] Pal, A., Sk, M.P., Chattopadhyay, A. (2016), Conducting Carbon Dot–Polypyrrole Nanocomposite for Sensitive Detection of Picric acid, ACS Appl. Mater. Interfaces, 8, 5758–5762 (DOI: 10.1021/acsami.5b11572)

[91] Ju, Y.J., Li, N., Liu, S.G., Fan, Y.Z., Ling, Y., Xiao, N., Luo, H.Q., Li, N.B. (2019), Green Synthesis of Blue Fluorescent P-doped Carbon Dots for the Selective Determination of Picric Acid in an Aqueous Medium, Anal. Sci., 35, 147–152 (DOI: 10.2116/analsci.18P372)

[92] Wang, Y., Chang, X., Jing, N., Zhang, Y. (2018), Hydrothermal synthesis of carbon quantum dots as fluorescent probes for the sensitive and rapid detection of picric acid, Anal. Methods, 10, 2775–2784 (DOI: 10.1039/C8AY00441B)

[93] Li, J., Zhang, L., Li, P., Zhang, Y., Dong, C. (2018), One step hydrothermal synthesis of carbon nanodots to realize the fluorescence detection of picric acid in real samples, Sens. Actuators B Chem., 258, 580–588 (DOI: 10.1016/j.snb.2017.11.096)

[94] Sun, X., He, J., Meng, Y., Zhang, L., Zhang, S., Ma, X., Dey, S., Zhao, J., Lei, Y. (2016), Microwave-assisted ultrafast and facile synthesis of fluorescent carbon nanoparticles from a single precursor: preparation, characterization and their application for the highly selective detection of explosive picric acid, J. Mater. Chem. A, 4, 4161–4171 (DOI: 10.1039/C5TA10027E)

[95] Tian, M., Wang, Y., Zhang, Y. (2018), Synthesis of Fluorescent Nitrogen-Doped Carbon Quantum Dots for Selective Detection of Picric Acid in Water Samples, J. Nanosci. Nanotechnol., 18, 8111–8117 (DOI: 10.1166/jnn.2018.16342)

CHAPTER 4

Doxycycline Detection and Degradation in Aqueous Media via Simultaneous Synthesis of Fe-N@Carbon Dots and Fe_3O_4-Carbon Dot Hybrid Nanoparticles: One Arrow Two Hawk Approach

4.1. Introduction

Bacterial infections have been controlled effectively since the innovation of antibiotics. The versatile broad-spectrum antibiotics such as tetracyclines are gaining more and more interest in recent years due to their use in different areas such as human disease control, aquaculture, livestock, veterinary medicine, and to enhance animal growth [1–3]. The improved use of these antibiotics leads to increased concentration of drug residues in wastewater as 70-80% of the administered drug is either defecated or urinated [2, 4], so the effluents from animals or humans are presenting antibiotics to the environment up to a greater extent [5]. Due to the higher concentration of pharmaceuticals in water systems, the arising issues are a substantial global environmental concern [6, 7]. The drug residue in the aquatic system can cause genetic variation in microorganisms that may lead to drug resistance [4]. The gene exchange between agricultural or soil microorganisms and bacteria of clinical interest gives rise to drug resistance in pathogens, leading to the inception of superbugs [8]. So, removing pharmaceuticals from wastewater is the research area of utmost importance. To take the edge off toxicity and propagation of genes responsible for antibiotic resistance, the wastewater contaminated with antibiotics should be fairly decontaminated before letting it out into the natural surroundings. Various methods were

implemented, such as electrolysis, electrocoagulation, microalgal-decomposition, reverse osmosis, adsorption, ion exchange, membrane filtration, degradation, ozonation, etc. [9–13]. The shortcomings of conventional waste-water treatment methods were overcome by advanced oxidation technologies, among which Fenton oxidation technology is widespread for treating organic pollutants [14, 15]. The increased environmental availability of antibiotics jeopardizes the health and well-being of humans and poses a non-intended threat to other organisms as well [16]. The overuse of doxycycline and the inability to obey the withdrawal period in animals is the foremost reason for antibiotic residue in edible products like eggs, meat, and milk [17]. The intake of doxycycline-contaminated animal products leads to unintentional bioaccumulation of doxycycline that may cause profound adverse effects on human health such as liver problems, teeth damage, bowel diseases, and anaphylaxis [18]. This makes the determination of doxycycline residue essential, and the method that can determine doxycycline even in animal products such as milk has excellent potential in the sensing field. Various conventional methods are available for doxycycline sensing, such as high-performance liquid chromatography, liquid chromatography-mass spectrometry (LC-MS), electrochemistry, electrophoresis, surface plasmon resonance (SPR), microfluidic, etc. [17, 19–22]. Among these methods, many give highly accurate and reliable results. However, the requirement of high-priced instrumentation, specialized skill, tedious sample preparation, and long operation time limit their use and application. On that account, establishing plain, low-cost, and rapid inquisitive methods for doxycycline sensing would be worthwhile. Herein, to combat both the issues of doxycycline sensing and its degradation, we report for the first time the novel synthesis condition for synthesizing iron-nitrogen co-doped carbon dots (**Fe-N@CDs**) and iron oxide nanoparticles-carbon dot hybrid (**Fe_3O_4-CDs**) together. The "**Fe-N@CDs**" were used for doxycycline detection and "**Fe_3O_4-CDs**" for degradation. **Fe-N@CD**s selectively

detected doxycycline with a meager detection limit (LOD) and also detected them in milk samples. Similarly, the other formed product, i.e., **Fe_3O_4-CDs**, degrades doxycycline within 5 mins in the presence of shear forces applied by a home-based kitchen blender for the first time, thus making this system an outstanding prospect in the field of food and environment safety.

4.2. Results and discussion

The **Fe-N@CDs** (supernatant) and **Fe_3O_4-CDs** (settled powder) were synthesized after hydrothermal reaction following the method mentioned above. The formation of **Fe-N@CDs** occurred because of hydrothermal carbonization, whereas **Fe_3O_4-CDs** formation occurs because of both oxidation and reduction of Fe^{2+}. The detailed synthesis strategy for forming both **Fe-N@CDs** and **Fe_3O_4** NPs is shown in **Scheme 4.1.** In the following subsections, first **Fe-N@CDs** detailed characterization and its sensing behavior towards doxycycline are discussed, followed by **Fe_3O_4-CD's** detailed description and their applicability in degrading doxycycline.

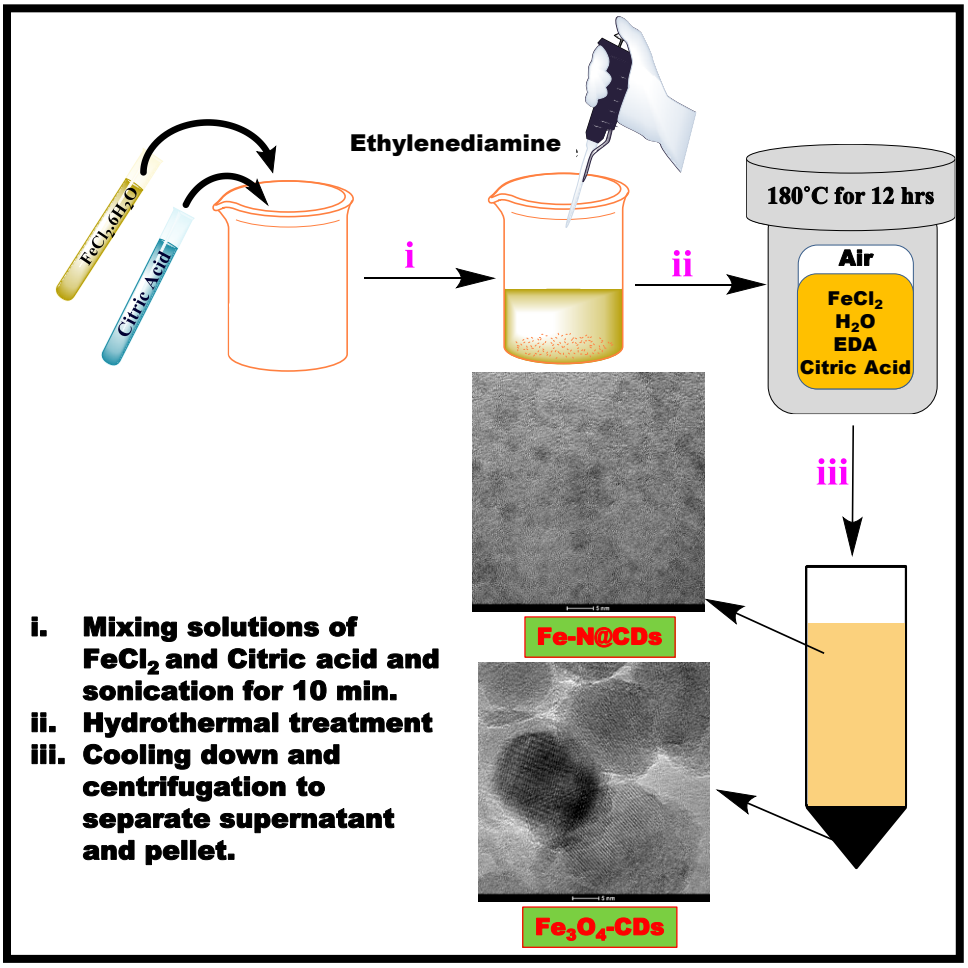

Scheme 4.1. Schematic illustration of the preparation of **Fe-N@CDs** and **Fe_3O_4-CDs.**

4.2.1. Structural, Morphological, and Surface Characterization of Fe-N@CDs

The **Fe-N@CDs** formed were fluorescent, having a QY value of around 47%. The plausible formation mechanism of **Fe-N@CDs** involved hydrolysis of citric acid (carbon precursor) at a very high temperature (~ 180 ^{o}C) followed by dehydration. Afterward, the carbon nuclei emerged by condensation and polymerization due to increased temperature. These carbon nuclei grew with temperature rise and reached a point where more growth led to their bursting, resulting in the formation of **Fe-N@CDs** (Hu et al., 2015, [26]. The HR-TEM images of **Fe-N@CDs** showed typical spherical particles, as shown in **Figure 4.1.a-b**. having a size in the range be 3.0±0.5 nm shown in **Figure 4.1.c**. The diffused SAED pattern revealed the poor crystallinity of the material **Figure 4.1.c(inset)**. The PXRD spectra of **Fe-N@CDs** in **Figure 4.1.d** showed a signature broader hump at 2θ=24.82°, indicating the formation of carbon dots [27]. The FT-IR spectrum of **Fe-N@CDs** is demonstrated in **Figure 4.1.e** offered a very strong band at 3356.32 cm^{-1} characteristics to the O-H stretch of the hydroxyl group. A comparatively weak band at 2131.03 cm^{-1} was also seen, attributing O-H stretching of the carboxyl group [27, 28]. At the same time, the stretching vibration of C-H has been seen at 2930 cm^{-1} [29]. The stretching vibration of primary amines gives rise to a strong peak at 1579 cm^{-1}. The phenolic OH bending was visualized at 1318 cm^{-1} [30]. Another band at 1482 cm^{-1} is also attributed to the phenyl ring [31]. OH, deformations of alcohols happened to form a peak at 1156 cm^{-1} [32]. The peak at 968 cm^{-1}, 819 cm^{-1}, and 585 cm^{-1} are assigned to the bending vibration of carbonyl, C-Cl stretch, and Fe-O vibration, respectively [33, 34].

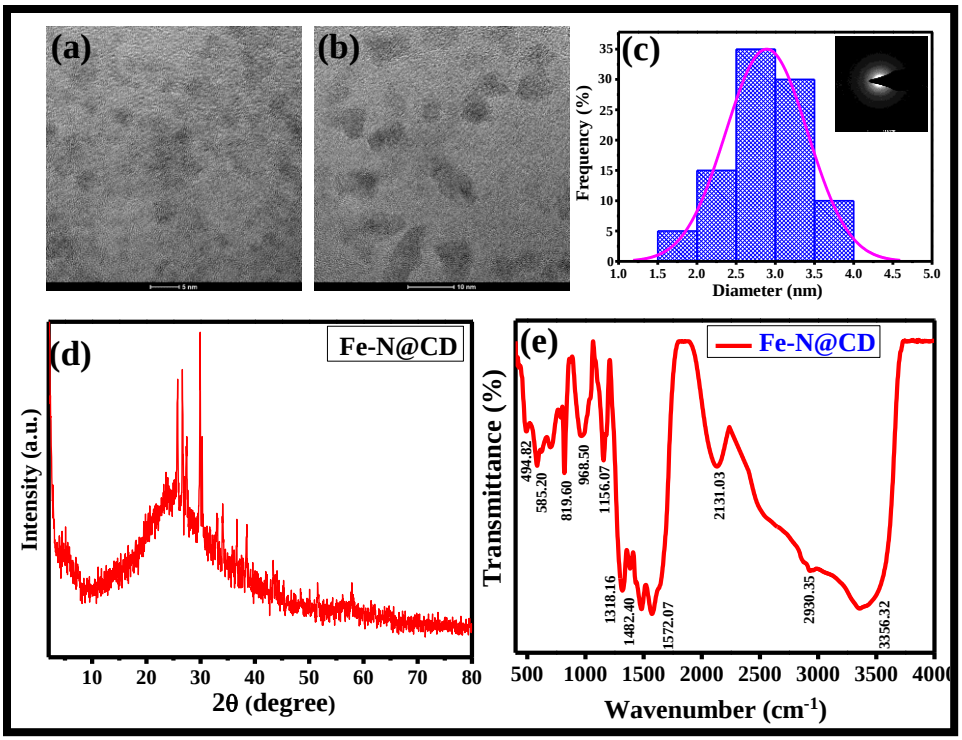

Figure 4.1. Structural and morphological characterization of **Fe-N@CDs**: HR-TEM (a-b), Size distribution histogram (c) with SAED patterns (inset). Powder X-ray diffractogram (d) and FT-IR spectrum (e).

The presence of different surface functional groups and the elemental composition of **Fe-N@CDs** were unraveled by XPS. The XPS survey scan of **Fe-N@CDs** in **Figure 4.2.a** showed signature peaks at 285.2eV, 530eV, 400.5eV, and 713eV, ascribed to C1s O1s, N1s, Fe2p. The high-resolution deconvoluted spectrum of C1s (**Figure 4.2.c**) showed three prominent peaks at 284.7 eV, 285.9 eV, and 288 eV attributed to C-C/C=C, C-O/C-N, and CONH functional groups [35, 36]. The O1s (**Figure 4.2.d**) deconvoluted spectrum also showed two peaks at 531.2eV and 533eV for C=O and C-O [37, 38]. The N1s (**Figure 4.2.e)** band contains two peaks at 399.4 eV and 401.1 eV corresponding to C-N and N-H [37]. The successful doping of Fe in carbon dots was investigated particularly by XPS (**Figure 4.2.b**). The peaks at 710.3 eV, 713.6 eV and 725.9 eV attributed to Fe2p3/2 of Fe^{2+}, Fe2p3/2 of $Fe^{3+}$and Fe2p1/2 of

Fe^{3+} respectively. The XPS spectra confirm the successful doping of both Fe and N atoms in the carbon lattice.

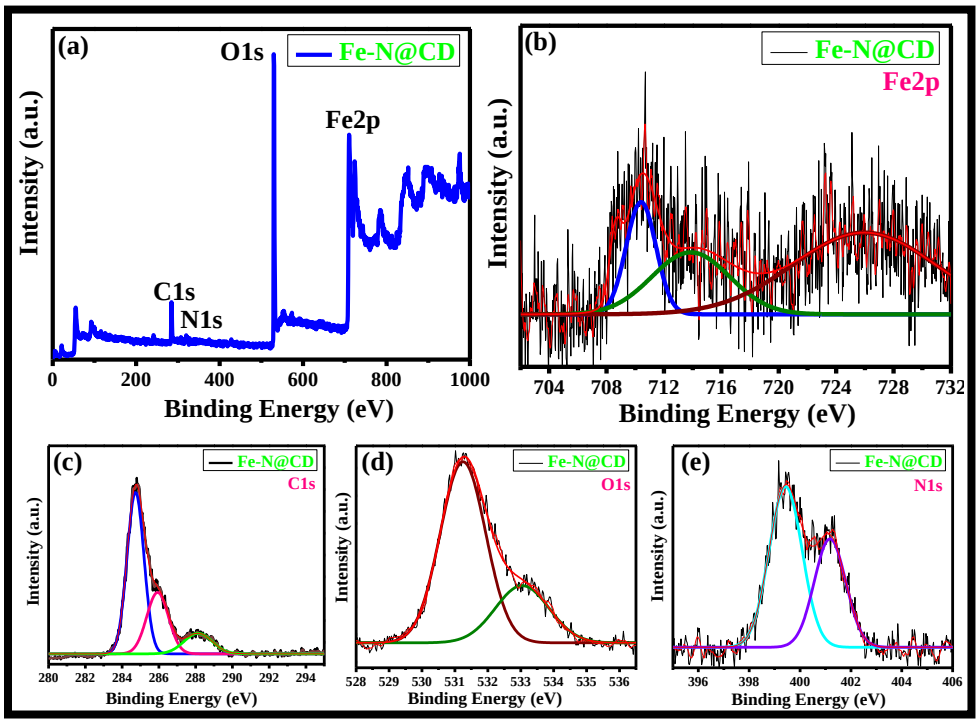

Figure 4.2. XPS survey spectrum of **Fe-N@CDs** (a), The high-resolution spectra of Fe2p(b), C1s (c), O1s (d), and N1s (e).

4.2.2. Optical Characterization of Fe-N@CDs

The optical characteristics of **Fe-N@CDs** were determined using UV-Vis and fluorescence spectroscopy. The distinctive peak at 345 nm (**Figure 4.3.a (UV-Absorbance)** in the UV-Vis spectrum arises due to the n-π* transition at the edge of the carbon lattice and occurs because of electronic transition between carbon and doped atoms. Moreover, the low strength broad absorbance trail till wavelength 550 nm is ascribed to the surface states of CDs associated with functional surface groups, giving rise to low energy sub-band gaps within n-π* bandgap [39]. The aqueous light brown colored solution of **Fe-N@CDs** brings about bright blue fluorescence, visible even with bare eyes on UV light irradiation (365 nm) by making use of a transilluminator (**Figure 4.3.c**). The same solution has emission

maxima at 450 nm (**Figure 4.3.a(Emission))** when excited using light of wavelength 360 nm. Due to functionalization, the surface state leads to trapping of the excited state energy, which gives rise to strong emission [40]. **Fe-N@CDs** showed excitation-dependent emission behavior as shown in **Figure 4.3.b**, and maximum emission was achieved at 450 nm with the excitation wavelength of 360 nm. The excitation-dependent emission nature with 0D carbon dot samples is ubiquitous, and this occurs because of the presence of different surface state distributions and varied particle sizes [41, 42].

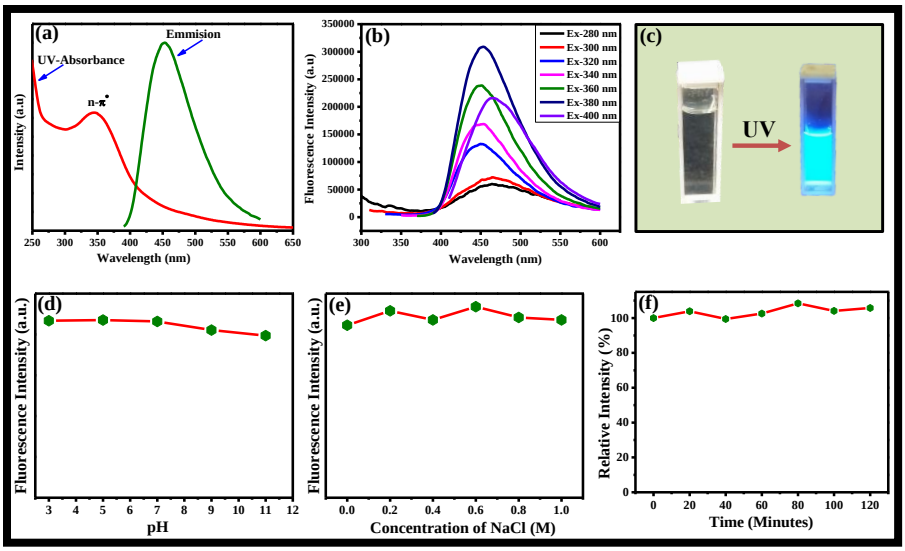

Figure 4.3. Photophysical characterization of Fe-N@CDs (a) UV–vis absorption spectra and emission spectra (b) Emission spectra obtained with varying excitation wavelength (c) **Fe-N@CDs** solution under visible light and UV light (360 nm) (d) Stability of **Fe-N@CDs** at various pH (e) with varying NaCl concentration (f) under UV irradiation for 120 min.

Moreover, the polydispersity in size and shape of carbon dots could also be another factor leading to such behavior of **Fe-N@CDs** [43]. To identify the stability of **Fe-N@CDs**, the related experiments were carried out in ambient conditions. There is barely any recognizable change in fluorescent intensities of **Fe-N@CDs** after UV irradiation for 120 min or after

treatment with different concentrations of NaCl up to 1M or at different *p*H and time (storage up to 60 days), exhibiting the commendatory stability and forbearance for hypersaline conditions, photobleaching, acidic and basic pH and prolonged storage time at room temperature (**Figure 4.3.d-f**), making them an excellent prospect for technological relevant systems. It is essential to mention that the **Fe-N@CDs** retain their original fluorescence properties ever after storage for months at standard temperature and pressure.

4.2.3. Ratio-metric Fluorescence Determination of Doxycycline Using Fe-N@CDs

The FTIR and XPS spectra confirmed the presence of both electrons donating and electron-accepting functional groups. The excellent fluorescence behavior of **Fe-N@CDs** inspired us to explore them as a fluorescent probe. **Fe-N@CDs'** change in fluorescence response was checked towards various antibiotics, biomolecules, and metal ions to substantiate this possibility. Interestingly, an appreciable fluorescence quenching in **Fe-N@CDs** was perceived selectively in the presence of doxycycline. The fluorescence intensity of **Fe-N@CDs** has descended to almost 50% upon the addition of 40 µg ml^{-1} of doxycycline. In contrast, after adding 100 µg mL^{-1} of doxycycline, the initial fluorescence of **Fe-N@CDs** gets decreases by around 80%, as shown in **Figure 4.4.a** demonstrating the potential prospect of **Fe-N@CDs** for doxycycline detection.

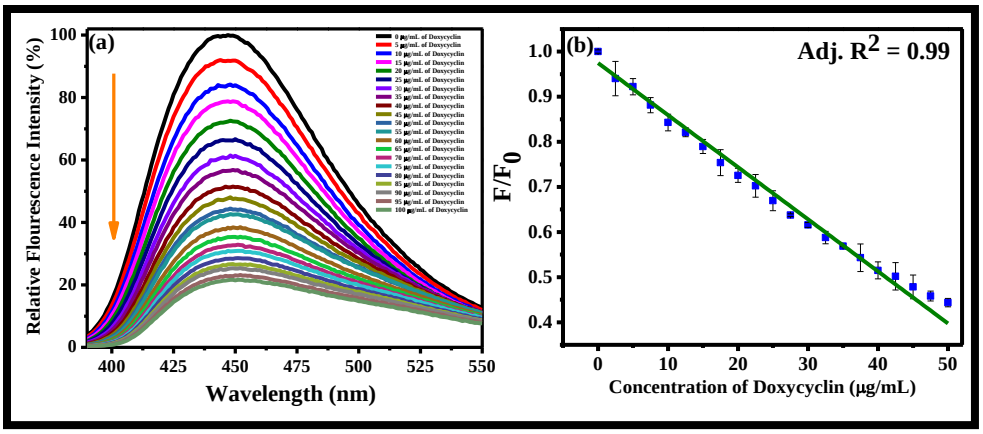

Figure 4.4. (a) The fluorescence spectra of **Fe-N@CDs** with different concentrations of doxycycline in the linear range (0 µg mL^{-1} - 100 µg mL^{-1}) (b) The linear plot shows the relationship of F/F_0 with the concentration of doxycycline.

After adding 100µg mL^{-1} of doxycycline, the initial fluorescence is decreased to 80 %. The fluorescence quenching efficiency was consistent with a doxycycline concentration range from 0µg mL^{-1}-100µg mL^{-1} and excellent linear co-relation between F/F_0 and the concentration of doxycycline, as shown in **Figure 4.4.b.** The correlation coefficient (R^2) was found to be 0.99. The corresponding limit of doxycycline detection was calculated as 66 ng mL^{-1} with a signal-to-noise ratio of 3. The observed data indicated the adequate precision of the prepared nanosensor. **Fe-N@CDs'** quick turn-off response towards doxycycline makes this method of doxycycline sensing meteoric. The performance of the synthesized sensor is compared with the recent reports on doxycycline sensing in **Table 4.3**.

4.2.4. Selectivity of Fe-N@CDs Towards Doxycycline Recognition and the Fluorescence Quenching Mechanism

Various target species have been chosen to check the selectivity of the presented nanosensor. The fluorescence performance of **Fe-N@CDs** was observed in the presence of multiple analytes, as shown in **Figure 4.5.a.**

Different antibiotics (norfloxacin, linezolid, penicillin, ofloxacin, cefixime, azithromycin, ciprofloxacin, metronidazole, and ampicillin), various "medically relevant" metal ions (K^+, Na^+, SO_2^{3-}, S^{2-}, PO_4^{3-}, Pb^{2+}, CH_3COO^-, HCO_3^-, Ca^{2+}) and several other biomolecules (Vitamin 6, Vitamin C, tryptophan, D-tyrosine, phenylalanine, creatinine, L-tyrosine, histidine, thiamine, cystine, and DOPA) (**Figure 4.5.b**) were chosen for checking the robustness of as prepared **Fe-N@CDs** based fluorescent nanosensors. A substantial change in fluorescence behavior of **Fe-N@CDs** was found only with doxycycline. Further, competitive selectivity studies were also carried out to determine the impact of other analytes on the sensing behavior of **Fe-N@CDs** (**Figure 4.5.a-b(inset)**). The obtained result showed exceptional sensitivity, selectivity, and specificity of **Fe-N@CDs** towards doxycycline.

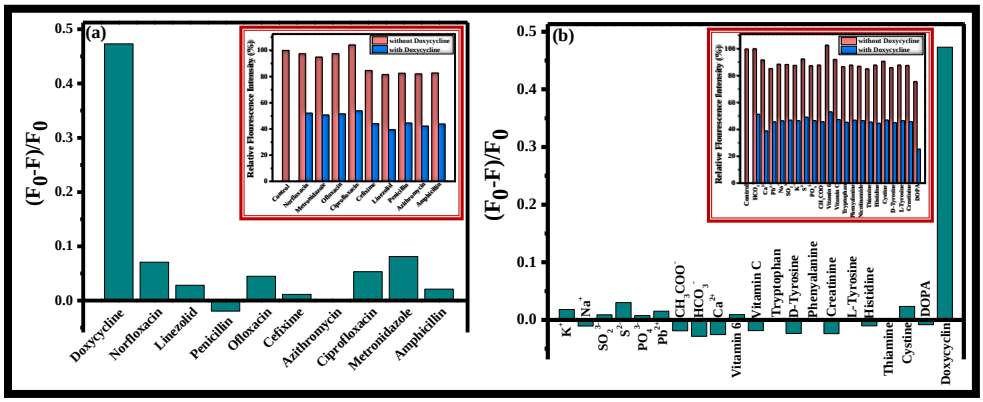

Figure 4.5. Selectivity in the sensing response of different antibiotics (a), metal ions, and biomolecules (b) with **Fe-N@CDs** (0.5mg mL^{-1} in water). The competitive selectivity of **Fe-N@CDs** towards doxycycline in the presence of other analytes

UV-Vis absorption and fluorescence spectra at different system temperatures were recorded to get detailed insights into the sensing mechanism. It has already been reported earlier that whenever any fluorescent probe shows quenching, it could be static or dynamic. In the static quenching, there is a chemical interaction between the fluorophore

and the quencher, which inhibits the formation of an excited state. At the same time, in dynamic, there is no such interaction between two species [18]. **Figure 4.6.a** represents the UV-vis spectra of **Fe-N@CDs**, doxycycline, and **Fe-N@CDs** + Doxycycline. No new peak was observed in the **Fe-N@CDs** + Doxycycline spectra, thus manifesting the quenching was dynamic in nature [44]. The fluorescent behavior was investigated at different temperatures, and the quenching constant (K_{sv}) was calculated using the Stern-Volmer equation (1).

$$F_0/F=K_{sv}[C]+1 \quad (1)$$

Table 4.1. Quenching constant (K_{sv}) at various temperatures

T(K)	K_{sv} (M^{-1})	R
298	**0.895×10^{-4}**	**0.99**
310	**1.0×10^{-4}**	**0.98**
323	**1.15×10^{-4}**	**0.98**

In the above equation, "F" corresponds to fluorescence of **Fe-N@CDs** at 450 nm, F_0 corresponds to fluorescence of **Fe-N@CDs** after the addition of doxycycline at 450 nm, K_{sv} is a quenching constant (M^{-1}), and C is the molar concentration of the analyte. As from **Table 4.1** and **Figure 4.6.b** clear increment in K_{sv} value and slope of Stern-Volmer plot was found with an increase in temperature. The increment in K_{sv} with temperature arises because of enhancement in a molecular collision occurring between the analyte (here doxycycline) and the fluorophore (**Fe-N@CDs**) and takes place specifically with dynamic quenching [44]

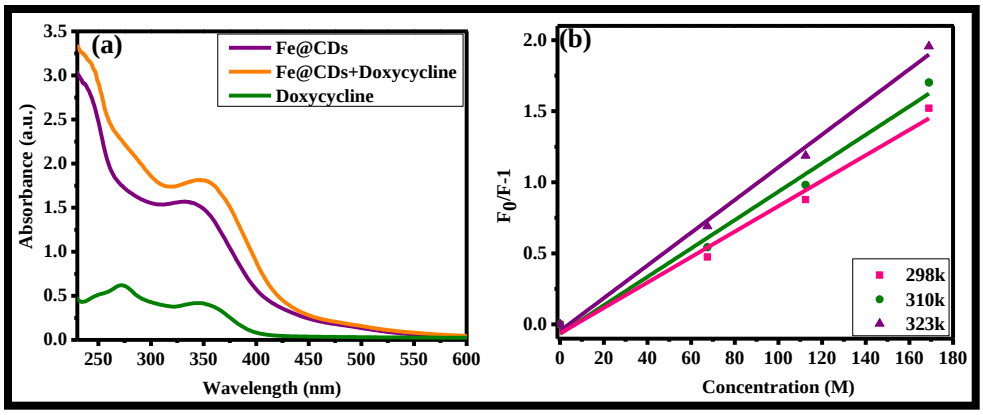

Figure 4.6. (a) UV-Vis spectrum of **Fe-N@CDs** solution, doxycycline alone, and the mixture of doxycycline and **Fe-N@CDs** (b) Stern–Volmer plots for **Fe-N@CDs**-Doxycycline combined at different temperatures.

4.2.5. Detection of Doxycycline in Milk Samples

To further authenticate the real-sample condition applicability of as prepared **Fe-N@CDs** nanosensor, doxycycline detection was checked in raw milk as available in the market. The pretreated sample of raw milk was spiked with different concentrations of doxycycline in the presence of **Fe-N@CDs.** The obtained results are summarized in **Table 4.2**. No doxycycline was detected in the milk sample alone, suggesting that the matrix effects had little intrusion on the sensor response. However, in the presence of **Fe-N@CDs**, doxycycline was recovered in the ranges from 98%-103% with a relative standard deviation of less than three. The very low LOD, high precision, and requirement of minimal pretreatment of actual sample broaden the application of **Fe-N@CDs** for facile detection of doxycycline.

Table 4.2. Doxycycline determination in milk samples (n=3)

Sample	Spiked (µM)	Detected (µM)	Recovery (%)	SD
1	**0**	**ND***		
2	**20**	**19.91**	**99.56**	**2.59**
3	**30**	**29.42**	**98.07**	**1.03**
4	**40**	**41.30**	**103.2**	**0.96**

* Not detected

4.2.6. Structural, Morphological, and Surface Characterization of Fe_3O_4-CDs

As discussed earlier, **Fe_3O_4-CDs** hybrid NPs were synthesized simultaneously with **Fe-N@CDs**. It is believed that **Fe_3O_4** NPs' formation occurs because EDA (used for the nitrogen doping in CDs) and hydrothermal conditions provide an environment to oxidize the iron precursor, which ultimately leads to nucleation and subsequent growth of **Fe_3O_4** NPs along with CDs. The role of EDA was justified further by performing different reactions. In reaction A, everything was kept the same except the hydrothermal condition; however, reaction B was devoid of EDA, and reaction C was carried out without citric acid but otherwise under identical conditions as mentioned earlier in the synthesis of **Fe_3O_4-CDs**. The results are shown in **Figure 4.8.b**. Only in reaction C, there is the formation of **Fe_3O_4** magnetic nanoparticles, whereas reactions A and B were failed to produce any such particles. From the TEM image, as shown in **Figure 4.7.b**, spherical **Fe_3O_4** NPs are seen with a lattice spacing of 0.33 nm (**Figure 4.7.a**) and size distribution in the range of 16-22 nm

(**Figure 4.7.c**). Also, the high-resolution TEM image revealed that CDs were wrapped over the **Fe_3O_4** NPs, forming a kind of core-shell structure. The SAED pattern further confirmed the crystalline nature of **Fe_3O_4-CDs** (**Figure 4.7.c(inset)**). The HR-TEM images were in line with previous work on **Fe_3O_4** carbon dot composite; however, in the present work, **Fe_3O_4-CDs** were synthesized in a single step [45].

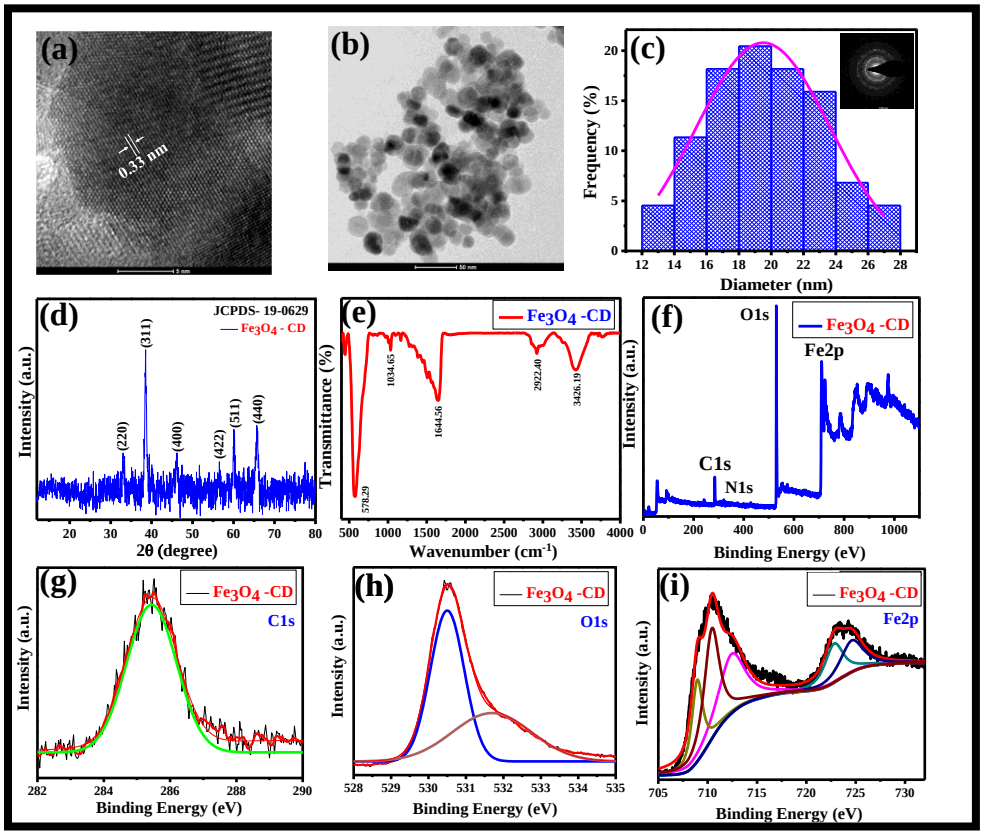

Figure 4.7. Structural and morphological characterization of **Fe_3O_4-CDs**: HR-TEM (a-b). Size distribution histogram (c) obtained from TEM image with respective SAED patterns (inset). Powder X-ray diffractogram (d), FT-IR spectra (e). XPS survey spectrum (f), The high-resolution spectra of C1s (g), O1s (h), and Fe2p(i).

Furthermore, the PXRD spectra (**Figure 4.7.d**) showed a signature peak of **Fe_3O_4** NPs and the data of the PXRD spectrum well matches with JCPDS

number- 19-0629 indicating the crystalline phase of magnetite [46]. It has to be mentioned here that possibly because of low content and poor crystallinity diffraction pattern from **Fe-N@CDs** didn't observe [47]. The FT-IR spectrum of **Fe_3O_4-CDs** recorded in the range of 400-4000 cm^{-1} confirmed the binding of CDs on the **Fe_3O_4** surface. As shown in **Figure 4.7.e**, five significant peaks at 3426.19 cm^{-1}, 2922.40 cm^{-1}, 1644.56 cm^{-1},1034.65 cm^{-1}, and 578.29 cm^{-1} were found, which could accurately be assigned to O-H stretching of hydroxyl group, C-H stretching vibration, aromatic C-C, C-N functional groups, and characteristic Fe-O vibration respectively [33, 48] The XPS survey spectrum (**Figure 4.7.f**) revealed the presence of C1s, O1s, N1s, and Fe2p with corresponding binding energies at 284.8eV 532 eV, 399.8 eV, and 710.8 eV [49, 50]. The high-resolution spectra of C1s (**Figure 4.7.g**) have a single peak attributed to aromatic or graphitic carbon [50]. The deconvoluted spectrum of O1s (**Figure 4.7.h**) exhibits two peaks at 530 eV and 531.4 eV. The former peak appeared for adsorbed oxygen, while later is due to the presence of hydroxide on the surface of magnetite particles [51]. The peaks of Fe2p3/2 and Fe2p1/2 (**Figure 4.7.i**) present at binding energies 710.3 eV and 723.8 eV could be deconvoluted into five peaks. The peak at binding energy 709 eV, 710.4 eV of Fe^{2+} and 712.7 eV, 724.8 eV of Fe^{3+} is well in accordance with previous literature reports indicating the successful formation of **Fe_3O_4** nanoparticles [52–55]. Thus, the FT IR and XPS spectrum strongly supported the presence of CDs on **Fe_3O_4** NPs, leading to the confirmation of **Fe_3O_4-CDs** hybrid nanostructure formation.

4.2.7. Magnetic Properties of Fe_3O_4-CDs

The magnetic behavior of **Fe_3O_4-CDs** was checked with VSM at 300 K. As shown in **Figure 4.8.a**; the **Fe_3O_4-CDs** showed a saturation magnetization value of 29.5 emu/g. Moreover, the obtained result showed zero coercivity, retentivity, and the absence of hysteresis loop confirmed the superparamagnetic nature of **Fe_3O_4-CDs**. Because of its significantly

less size, magnetic character, and presence of CDs (having several high-affinity surface functional groups), it motivated us to explore them for degradation/ adsorption of doxycycline.

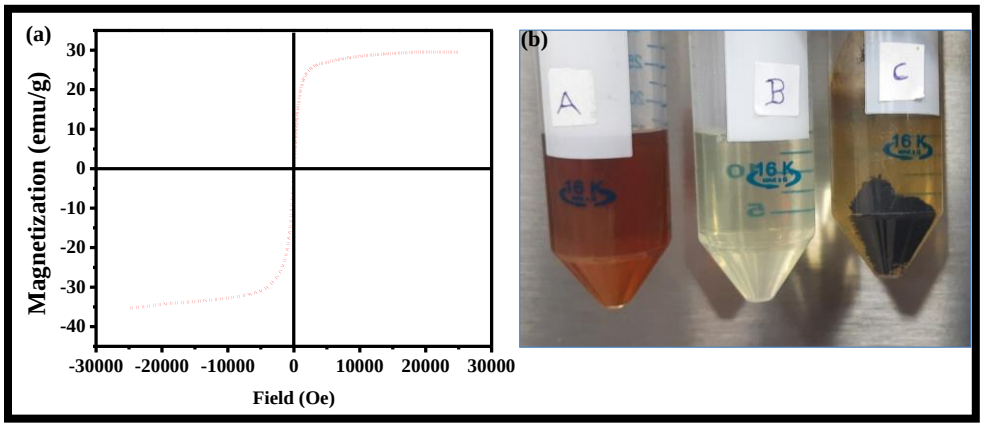

Figure 4.8. (a) VSM of **Fe_3O_4 -CDs** at room temperature (b) Images of the samples prepared under different reaction conditions.

4.2.8. Kitchen Blender Assisted Catalytic Activity of Fe_3O_4-CDs for the Degradation of Doxycycline

Further, the kitchen blender-assisted doxycycline degradation using **Fe_3O_4-CDs** was investigated. Since **Fe-N@CDs** have a selective affinity towards doxycycline by making non-radiative bonding thus, we thought to explore the other product formed "**Fe_3O_4-CDs**" for its degradation. With the application of a kitchen blender, the generation of shear forces led to a decrease in the absorbance value of doxycycline measured at 346 nm as shown in **Figure 4.9.a**, and in just after 5 min, around 70.26 % doxycycline degradation was achieved. It must be mentioned here that the degradation efficiency can improve by modulating the sheer force/cavitation time. With control condition, i.e., with only sheer force application (without **Fe_3O_4-CDs**), mere 11% degradation efficiency was achieved; however, in the presence of **Fe_3O_4-CDs**, the degradation efficiency was 70.26%, as shown in **Figure 4.9.b**. Higher degradation efficiency with **Fe_3O_4-CDs** occurs because of the nanohybrid's synergetic

effect and high shear forces. Moreover, the degradation efficiency of the present work was compared with other reported work, as shown in **Table. 4.4.**

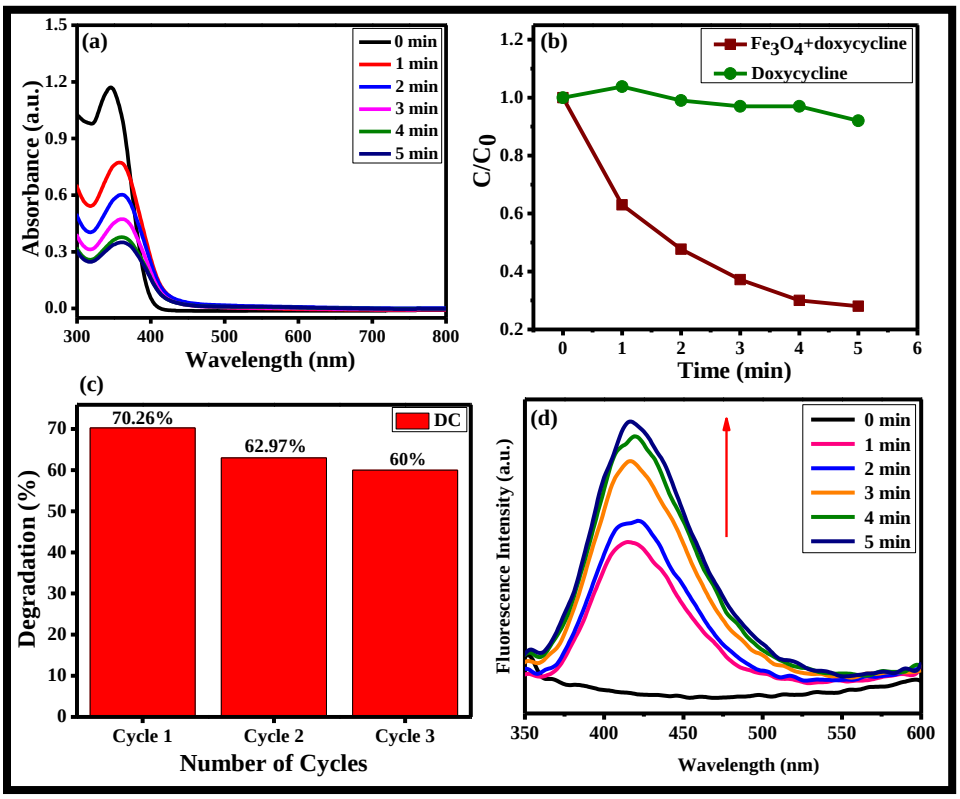

Figure 4.9. (a) UV-Vis spectra of doxycycline degradation by using kitchen blender under different time intervals (b) Variation in doxycycline concentration in solution during shear force-cum cavitation in terms of C/C_o with vibration time (c) Cycling experiment of doxycycline solution (50 mg 500mL^{-1}) by **Fe_3O_4-CDs**. (d) Fluorescence spectra of terephthalic acid after applying shear force, showing the formation of hydroxyl radicals by an increase in fluorescence intensity at 425 nm.

The ROS generated on applying shear force could degrade the adsorbed doxycycline. Hydroxyl radicles were measured using TA. The results obtained showed the enhancement of hydroxyl radicle on increasing the time of applied force. The maximum amount of TAOH formed when the whole mixture was blended for 5 mins. The possible degradation

mechanism of doxycycline with the application of shear forces in the presence of **Fe_3O_4-CDs** was also explored. The application of cavitation force gives mechanical stress to the material, which derives free charge carriers ($e^- + h^+$) to the surface. These e^- and h^+ react with OH^- and O_2 present in the system to produce ROS ($^{\cdot}OH/^{\cdot}O_2$) as described in the following eq. 3-12.

Fe_3O_4+Cavitation cum shear force $\rightarrow e^- + h^+$ (3)

$OH^- + h^+ \rightarrow {}^{\cdot}OH$ (4)

$O_2 + e^- \rightarrow O_2^-$ (5)

$2e^- + 2H^+ + O_2 \rightarrow H_2O_2$ (6)

$H_2O_2 + e^- + H^+ \rightarrow OH^- + {}^{\cdot}OH$ (7)

In the meantime, reduction and oxidation of ferrous ions takes place

$e^- + Fe^{3+} \rightarrow Fe^{2+}$ (8)

$h^+ + Fe^{2+} \rightarrow Fe^{3+}$ (9)

These ions and H_2O_2 in the solution start the Fenton-type pathway, giving rise to hydroxyl and hydroperoxyl radicals, ultimately degrading doxycycline (**Figure 4.10)**.

$Fe^{2+} + H_2O_2 \rightarrow Fe^{3+} + {}^{\cdot}OH + OH^-$ (10)

$Fe^{3+} + H_2O_2 + OH^- \rightarrow Fe^{2+} + OH_{\cdot 2} + H_2O$ (11)

Doxycycline + ROS ($^{\cdot}OH/^{\cdot}O_2$) $\rightarrow$ Degradation products ($CO_2 + H_2O$)

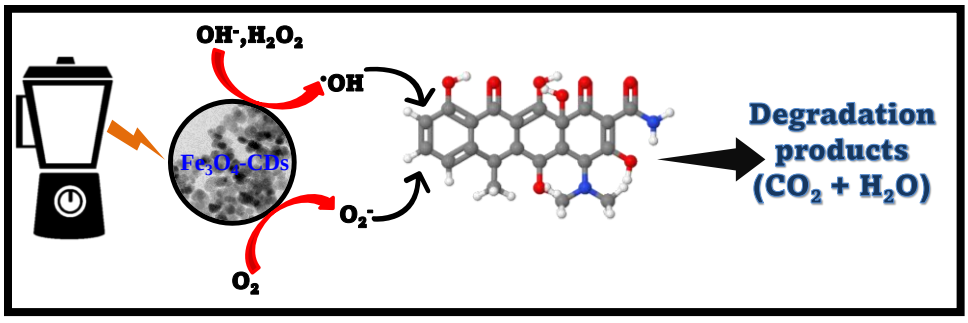

Figure 4.10. Doxycycline degradation mechanism.

The cyclic test was also performed to determine the reusability of **Fe_3O_4-CDs**, as shown in **Figure 4.11.a-c**. The degradation efficiency of doxycycline up to three cycles were around 70.26%, 62.97%, 60%, respectively interestingly no significant change in the PXRD pattern of **Fe_3O_4-CDs** collected after the third cycle was found as shown in **Figure 4.11.d**, suggesting the excellent recyclable and reusable attributes of **Fe_3O_4-CDs** and making this hybrid nanosystem a superb prospect for environmental remediation.

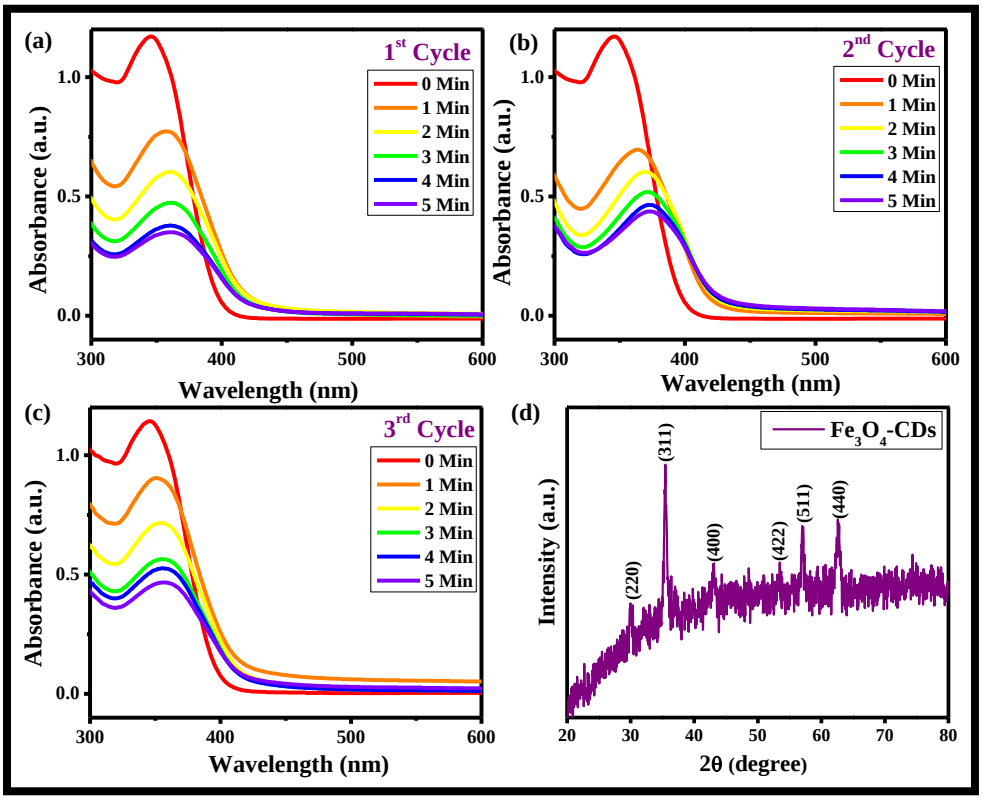

Figure 4.11. The recyclability of doxycycline by **Fe_3O_4-CDs** (a) First cycle (b) second cycle (c) Third cycle (d) PXRD pattern of **Fe_3O_4-CDs** after three consecutive cycles.

Table 4.3. Comparison of reported Doxycycline sensing methods with this work.

S.No.	Material	Method of sensing	LOD	Linearity Range	Ref.
1.	NCQDs	Fluorometric assay	87 nM	5 to 50 µM	[56]
2.	CuNCs	Fluorescence	270 nM	1–1000 µM	[57]
3.	BiOBr nanosheets	Photo-electrochemical	0.14 µM	0.50 µM to 1 mM	[58]
4.	CDs@MOF(Eu)	Fluorescence	0.1665 µg mL^{-1}	0–60 µM	[59]
5.	AOT-AgNPs	Chemo-sensing	0.2 µM	0.1 to 140 µM	[60]
6.	ZIF-8/NH2-MIL-53(Al)	Fluorescence	1.2 µg L^{-1}	NA	[61]
7.	CDs	Fluorescence	16.35 µM	10–1000 µM	[62]
8.	**Fe-N@CDs**	Fluorescence	66 ng mL^{-1}	0 mg mL^{-1} to 50 mg mL^{-1}	***This work***

Table 4.4. Comparison of reported Doxycycline degradation methods with this work

Catalyst	Pharma-ceuticals	Conc.	Volume used	Reaction time (min)	% Degradation achieved	Methods used	Ref.
Ag@LiNbO3/ PVDF	Tetracycline	0.2 mM	10 ml	120	69%	Ultra-sonication	[63]
Laccase	Chlor-tetracycline	2 mg	1L	120	80%	Ultra-sonication	[64]
p-n BiOI/ Bi_3O_4Cl	Tetracycline	-	-	180	73.5%	Photo-catalytic	[65]
Mn-doped CeO_2	Tetracycline, Chlor-tetracycline, Oxy-tetracycline.	-	-	60	98.6 %, 97.4%, 88.1 %	Fenton like photo catalytic reaction	[66]
Fe_3O_4-CDs	Tetracycline	50mg	500ml	5	70.26%	Kitchen blender	***This work***

4.3. Conclusions

In conclusion, the Fe-N co-doped carbon dots (**Fe-N@CDs**) and iron oxide carbon dot hybrid nanoparticles (**Fe_3O_4-CDs NPs**) were prepared simultaneously using the one-pot hydrothermal method. As synthesized, **Fe-N@CDs** have the maximum emission at 450 nm with the excitation wavelength of 360 nm and showed excitation-dependent emission nature. Moreover, these **Fe-N@CDs** demonstrated ultra-sensitive and accurate doxycycline detection in the linear range of 0 mg mL^{-1}- 50 mg mL^{-1} and LOD value of 66 ng mL^{-1}. **Fe-N@CDs** detected doxycycline in milk samples with excellent recovery. The study also came up with the efficient degradation of doxycycline for the first time in an aqueous medium using a simple kitchen blender's shear cum cavitation force with **Fe_3O_4-CDs** (second product formed with the same reaction). The Fenton-type reaction is followed for the degradation with excellent recyclability and reusability. The present work paves a new pathway in low-dimensional material synthesis with exciting applications in environmental remediations.

4.4. Experimental section

4.4.1. Materials and instrumentation

The chemicals used for all the experiments were either HPLC grade or analytical reagent grade. No chemical was purified further and used as purchased from Merck and sigma-Aldrich. Sartorius milli-Q system was employed to produce deionized water (DI) used throughout the experiments. For performing X-ray diffraction (XRD), RINT smart lab 2500 V X-ray diffractometer (Rigaku) was used with Cu Kα radiation (1.5406 Å). The UV-Vis and fluorescence spectra were measured on Shimadzu UV-1900 spectrophotometer and fluoromax spectrofluorometer. The fluorescence spectrophotometer set the emission and excitation slit width at 2 nm in a conventional 1 cm × 1 cm quartz cell. The IR spectra (400–4000 cm^{-1}) were obtained using the Bio-Rad FTS 3000MX instrument. X-ray photoelectron spectra (XPS) were recorded ESCA, Omicron Nano Technology. Transmission Electron Microscopy images were taken with FEI Tecnai G2- F20 Transmission Electron Microscope. To study the hysteresis loops, vibrating sample magnetometer model no. Lakeshore VSM 7410S (VSM) was used.

4.4.2. In-situ Synthesis of Fe-N@CDs and Fe_3O_4-CDs

Fe-N@CDs and **Fe_3O_4-CDs** were synthesized by the one-pot hydrothermal method. Firstly, 0.81g of $FeCl_2.6H_2O$ (0.2M) was dissolved in 15 mL of deionized water. Another solution was prepared by dissolving 1 gm of citric acid in 15 mL of deionized water. Both the solutions were mixed and sonicated for 10 min, into which 8 mL of ethylenediamine was added dropwise. The final solution was placed into a Teflon-lined stainless-steel autoclave, kept at 180˚C for 12 h. The resultant solution was cooled down at room temperature and centrifuged at 6000 rpm for 10 min. The larger particles (**Fe_3O_4-CDs**) were settled down, dried in a tube

furnace at 80˚C for 12 h., and stored for further use, whereas the supernatant (**Fe-N@CDs**) is stored separately for other studies.

4.4.3. Quantum yield calculations:

For calculating the quantum yield (QY), the method described in the manual by HORIBA Jobin Yvon IBH Ltd. "A Guide to Recording Fluorescence Quantum Yields" was followed. The equation (12) is utilized for calculations. The quinine sulfate, which is used as a standard, was dissolved using 0.1M H2SO4, whose quantum yield was found to be 0.54

$$\Phi_u = \Phi_{std} \times S_{sa} / S_{std} \times I_{std} / I_{sa} \times n^2_{sa} / \quad (12)$$

Φ_u is referred to QY of sample and Φ_{std} is QY of the standard, I_{std} and I_{sa} denote the absorbance of the standard and sample respectively at their respective λmax. To calculate the value of the slope of standard (S_{std}) and sample (S_{sa}), the graph was plotted with x and y coordinates using the integrated fluorescence intensity and the absorbance at various concentrations. The n_{std} and n_{sa} are the refractive indexes of solvent for the standard and the sample.

4.4.4. Fluorescence Quenching of Fe-N@CDs by Doxycycline and Selectivity Studies

An aqueous solution of **Fe-N@CDs** was initially prepared using the routine procedure followed for fluorescence studies for assessing doxycycline. To perform fluorescence spectroscopy, a 1 cm quartz cuvette was used, into which 3 mL of an as-prepared solution of **Fe-N@CDs** was poured, and fluorescence was recorded by exciting the sample at 380 nm. Emission was collected in the range of 390 nm - 550 nm. Next, a doxycycline solution was made afresh for sensing studies. Different concentration of doxycycline solution was added to **Fe-N@CDs** solution; the spectra of this mixture was recorded at $\lambda_{ex.}$ 380 nm excitation and λ_{em}. 390 nm -550 nm. All the experimental conditions were kept constant throughout the studies. The selectivity of **Fe-N@CDs** towards

doxycycline was checked by introducing various other antibiotics, norfloxacin, linezolid, penicillin, ofloxacin, cefixime, azithromycin, ciprofloxacin, metronidazole, ampicillin, metal ions, and other biomolecules.

4.4.5. Detection of Doxycycline in Raw Milk

The raw milk was procured from a local milk shop. The milk sample for detecting doxycycline was prepared following the procedure suggested by Song et al. 25. Briefly, the pH of the milk was lowered to 4.5 by using trichloroacetic acid. First, the raw milk was diluted 2.5 times using DI water. Further, 2 mL of 10% trichloroacetic acid was added to 15 mL of diluted milk and sonicated for 15 min at room temperature. This solution was centrifuged for 10 min at 12000 rpm to get a clear supernatant neutralized using 30% NaOH solution and again centrifuged to remove any deposits. This supernatant was spiked with different concentrations of doxycycline, and the sensing of same was performed by following the procedure stated in the previous section.

4.4.6. Kitchen Blender Assisted Degradation of Doxycycline

Typically, 30 mg of **Fe_3O_4-CDs** was added into a 50 mL doxycycline solution as a model pollutant (50 mg 500 mL^{-1}). The solution was stirred for 20 min to complete adsorption-desorption equilibrium. The solution was treated with a kitchen blender (500 w) with an operating speed of 20000 rpm. Periodically, 3 ml of aliquot was withdrawn after a 1 min time interval. The catalyst was separated by centrifugation. The supernatant was used to test the degradation efficiency using UV-Vis spectrophotometer by monitoring doxycycline's maximum absorption peak (λ_{max}) at 346 nm. The degradation efficiency was calculated using the equation ($C/C_0 \times 100\%$), Where C_0 and C represent the initial and final concentrations of doxycycline, respectively.

4.4.6. Determination of ROS

The ability of **Fe_3O_4-CDs** to generate reactive oxygen species (ROS) on applying shear force using a kitchen blender was checked using terephthalic acid (TA). The TA is a non-fluorescent compound that reacts with hydroxyl radicles and gives 2-hydroxyterephthalic acid (TAOH). The fluorescence was measured at 425 nm upon excitation with light of wavelength 315 nm. There is a direct correlation between the increase in intensity to the amount of hydroxyl radicles present. 0.5 mM terephthalic acid was used for the experiment under basic conditions. 30 mg of **Fe_3O_4-CDs** powder was used as a catalyst for the doxycycline solution of 50 mg $500mL^{-1}$. The fluorescence was checked after a time interval of 1 min till 5 min.

4.5. References

[1] Xu, J., Zhang, B., Jia, L., Bi, N., Zhao, T. (2020), Metal-enhanced fluorescence detection and degradation of tetracycline by silver nanoparticle-encapsulated halloysite nano-lumen, J. Hazard. Mater., 386, 121630 (DOI: 10.1016/j.jhazmat.2019.121630)

[2] Gu, J., Jia, H., Ma, S., Ye, Z., Pan, J., Dong, R., Zong, Y., Xue, J. (2020), Fe_3O_4-Loaded g-C3N4/C-Layered Composite as a Ternary Photocatalyst for Tetracycline Degradation, ACS Omega, 5, 30980–30988 (DOI:10.1021/acsomega.0c03905)

[3] Jia, L., Chen, R., Xu, J., Zhang, L., Chen, X., Bi, N., Gou, J., Zhao, T. (2021), A stick-like intelligent multicolor nano-sensor for the detection of tetracycline: The integration of nano-clay and carbon dots, J. Hazard. Mater., 413, 125296 (DOI: 10.1016/j.jhazmat.2021.125296)

[4] Yang, Y., Song, W., Lin, H., Wang, W., Du, L., Xing, W. (2018), Antibiotics and antibiotic resistance genes in global lakes: A review and meta-analysis, Environ. Int., 116, 60–73 (DOI: 10.1016/j.envint.2018.04.011)

[5] Alsager, O.A., Alnajrani, M.N., Abuelizz, H.A., Aldaghmani, I.A. (2018), Removal of antibiotics from water and waste milk by ozonation: kinetics, byproducts, and antimicrobial activity, Ecotoxicol. Environ. Saf., 158, 114–122 (DOI: 10.1016/j.ecoenv.2018.04.024)

[6] Ahmad, F., Zhu, D., Sun, J. (2021), Environmental fate of tetracycline antibiotics: degradation pathway mechanisms, challenges, and perspectives, Environ. Sci. Eur., 33, 64 (DOI: 10.1186/s12302-021-00505-y)

[7] Borghi, A.A., Palma, M.S.A. (2014), Tetracycline: production, waste treatment and environmental impact assessment, Braz. J. Pharm. Sci., 50, 25–40 DOI: 10.1590/S1984-82502011000100003)

[8] Peterson, E., Kaur, P. (2018), Antibiotic Resistance Mechanisms in Bacteria: Relationships Between Resistance Determinants of Antibiotic Producers, Environmental Bacteria, and Clinical Pathogens, Front. Microbiol., 9, 2928 (DOI: 10.3389/fmicb.2018.02928)

[9] Baran, W., Adamek, E., Jajko, M., Sobczak, A. (2018), Removal of veterinary antibiotics from wastewater by electrocoagulation, Chemosphere, 194, 381–389 (DOI: 10.1016/j.chemosphere.2017.11.165)

[10] Michelon, W., Matthiensen, A., Viancelli, A., Fongaro, G., Gressler, V., Soares, H.M. (2022), Removal of veterinary antibiotics in swine wastewater using microalgae-based process, Environ. Res., 207, 112192 (DOI: 10.1016/j.envres.2021.112192)

[11] Gopal, G., Ann Alex, S., Chandrasekaran, N., Mukherjee, A. (2020), A review on tetracycline removal from aqueous systems by advanced treatment techniques, RSC Adv., 10, 27081–27095 (DOI: 10.1039/D0RA04264A)

[12] Wang, X., Wang, A., Ma, J. (2017), Visible-light-driven photocatalytic removal of antibiotics by newly designed C3N4@MnFe2O4-graphene nanocomposites, J. Hazard. Mater., 336, 81–92 (DOI: 10.1016/j.jhazmat.2017.04.012)

[13] Khan, M.H., Bae, H., Jung, J.-Y. (2010), Tetracycline degradation by ozonation in the aqueous phase: proposed degradation intermediates and pathway, J. Hazard. Mater., 181, 659–665 (DOI: 10.1016/j.jhazmat.2010.05.063)

[14] Zhang, X., Ren, B., Li, X., Liu, B., Wang, S., Yu, P., Xu, Y., Jiang, G. (2021), High-efficiency removal of tetracycline by carbon-bridge-doped g-C3N4/Fe_3O_4 magnetic heterogeneous catalyst through the photo-Fenton process, J. Hazard. Mater., 418, 126333 (DOI: 10.1016/j.jhazmat.2021.126333)

[15] Fukushima, M., Tatsumi, K. (2001), Degradation Pathways of Pentachlorophenol by Photo-Fenton Systems in the Presence of Iron(III), Humic Acid, and Hydrogen Peroxide, Environ. Sci. Technol., 35, 1771–1778 (DOI: 10.1021/es001088j)

[16] Baquero, F., Martínez, J.-L., Cantón, R. (2008), Antibiotics and antibiotic resistance in water environments, Curr. Opin. Biotechnol., 19, 260–265 (DOI: 10.1016/j.copbio.2008.05.006)

[17] Choma, I., Grenda, D., Malinowska, I., Suprynowicz, Z. (1999), Determination of flumequine and doxycycline in milk by a simple thin-layer chromatographic method, J. Chromatogr. B. Biomed. Sci. App., 734, 7–14 (DOI: 10.1016/s0378-4347(99)00328-x)

[18] Feng, Y., Tan, L., Tang, Q., Zhong, W., Yang, X. (2018), Synthesis of Carbon Dots from PEG6000 and Papain for Fluorescent and Doxycycline Sensing, Nano, 13, 1850106 (DOI: 10.1142/S1793292018501060)

[19] Sczesny, S., Nau, H., Hamscher, G. (2003), Residue Analysis of Tetracyclines and Their Metabolites in Eggs and in the Environment by HPLC Coupled with a Microbiological Assay and Tandem Mass Spectrometry, J. Agric. Food Chem., 51, 697–703 (DOI: 10.1021/jf0258407)

[20] Attia, M.S. (2010), Spectrofluorimetric assessment of Ramipril using optical sensor Samarium ion–doxycycline complex doped in sol–gel matrix, J. Pharm. Biomed. Anal., 51, 7–11 (DOI: 10.1016/j.jpba.2009.08.017)

[21] Kazmi, S.A.R., Qureshi, M.Z., Masson, J.-F. (2020), Drug-Based Gold Nanoparticles Overgrowth for Enhanced SPR Biosensing of Doxycycline, Biosensors, 10, 184 (DOI: 10.3390/bios10110184)

[22] Sanderson, H., Ingerslev, F., Brain, R.A., Halling-Sørensen, B., Bestari, J.K., Wilson, C.J., Johnson, D.J., Solomon, K.R. (2005), Dissipation of oxytetracycline, chlortetracycline, tetracycline and doxycycline using HPLC–UV and LC/MS/MS under aquatic semi-field microcosm conditions, Chemosphere, 60, 619–629 (DOI: 10.1016/j.chemosphere.2005.01.035)

[23] Bao, L., Zhang, Z.-L., Tian, Z.-Q., Zhang, L., Liu, C., Lin, Y., Qi, B., Pang, D.-W. (2011), Electrochemical Tuning of Luminescent Carbon Nanodots: From Preparation to Luminescence Mechanism, Adv. Mater., 23, 5801–5806 (DOI: 10.1002/adma.201102866)

[24] Melhuish, W.H. (1961), QUANTUM EFFICIENCIES OF FLUORESCENCE OF ORGANIC SUBSTANCES: EFFECT OF SOLVENT AND CONCENTRATION OF THE FLUORESCENT SOLUTE1, J. Phys. Chem., 65, 229–235 (DOI: 10.1021/j100820a009)

[25] Song, J., Li, J., Guo, Z., Liu, W., Ma, Q., Feng, F., Dong, C. (2017), A novel fluorescent sensor based on sulfur and nitrogen co-doped carbon dots with excellent stability for selective detection of doxycycline in raw milk, RSC Adv., 7, 12827–12834 (DOI: 10.1039/C7RA01074E)

[26] Sharma, V., Kaur, N., Tiwari, P., Saini, A.K., Mobin, S.M. (2018), Multifunctional fluorescent “Off-On-Off” nanosensor for Au3+ and S2− employing N-S co-doped carbon–dots, Carbon, 139, 393–403 (DOI: 10.1016/j.carbon.2018.07.004)

[27] Tiwari, P., Kaur, N., Sharma, V., Mobin, S.M. (2020), A spectroscopic investigation of Carbon dots and its reduced state towards fluorescence performance, J. Photochem. Photobiol. Chem., 403, 112847 (DOI: 10.1016/j.jphotochem.2020.112847)

[28] Campos, B.B., Abellán, C., Zougagh, M., Jimenez-Jimenez, J., Rodríguez-Castellón, E., Esteves da Silva, J.C.G., Ríos, A., Algarra, M. (2015), Fluorescent chemosensor for pyridine based on N-doped carbon dots, J. Colloid Interface Sci., 458, 209–216 (DOI: 10.1016/j.jcis.2015.07.053)

[29] Chen, Y., Yang, Q., Xu, P., Sun, L., Sun, D., Zhuo, K. (2017), One-Step Synthesis of Acidophilic Highly-Photoluminescent Carbon Dots Modified by Ionic Liquid from Polyethylene Glycol, ACS Omega, 2, 5251–5259 (DOI: 10.1021/acsomega.7b01014)

[30] Boudouh, D., Ikram, R., Mohamed Jan, B., Simon Cornelis Metselaar, H., Hamana, D., Kenanakis, G. (2021), Synthesis, Characterization and Filtration Properties of Ecofriendly Fe_3O_4 Nanoparticles Derived from Olive Leaves Extract, Materials., 14, 4306 (DOI: 10.3390/ma14154306)

[31] Zhang, J., Zhao, X., Xian, M., Dong, C., Shuang, S. (2018), Folic acid-conjugated green luminescent carbon dots as a

nanoprobe for identifying folate receptor-positive cancer cells, Talanta, 183, 39–47 (DOI: 10.1016/j.talanta.2018.02.009)

[32] Adiani, V., Gupta, S., Ambolikar, R., Variyar, P.S. (2018), Development of rapid method to assess microbial quality of minimally processed pomegranate arils using FTIR, Sens. Actuators B Chem., 260, 800–807 (DOI: 10.1016/j.snb.2018.01.095)

[33] González-Gómez, M.A., Belderbos, S., Yañez-Vilar, S., Piñeiro, Y., Cleeren, F., Bormans, G., Deroose, C.M., Gsell, W., Himmelreich, U., Rivas, J. (2019), Development of Superparamagnetic Nanoparticles Coated with Polyacrylic Acid and Aluminum Hydroxide as an Efficient Contrast Agent for Multimodal Imaging, Nanomater. Basel Switz., 9, E1626 (DOI: 10.3390/nano9111626)

[34] Zhuo, S., Guan, Y., Li, H., Fang, J., Zhang, P., Du, J., Zhu, C. (2019), Facile fabrication of fluorescent Fe-doped carbon quantum dots for dopamine sensing and bioimaging application, Analyst, 144, 656–662 (DOI: 10.1039/C8AN01741G

[35] Li, H., Ye, S., Guo, J., Kong, J., Song, J., Kang, Z., Qu, J. (2019), The design of room-temperature-phosphorescent carbon dots and their application as a security ink, J. Mater. Chem. C, 7, 10605–10612 (DOI: 10.1039/C9TC03481A)

[36] Ren, G., Meng, Y., Zhang, Q., Tang, M., Zhu, B., Chai, F., Wang, C., Su, Z. (2018), Nitrogen-doped carbon dots for the detection of mercury ions in living cells and visualization of latent fingerprints, New J. Chem., 42, 6824–6830 (DOI: 10.1039/C7NJ05170K)

[37] Tao, S., Lu, S., Geng, Y., Zhu, S., Redfern, S.A.T., Song, Y., Feng, T., Xu, W., Yang, B. (2018), Design of Metal-Free Polymer Carbon Dots: A New Class of Room-Temperature Phosphorescent Materials, Angew. Chem. Int. Ed., 57, 2393–2398 (DOI: 10.1002/anie.201712662)

[38] Yang, P., Zhu, Z., Chen, W., Luo, M., Zhang, W., Zhang, T., Chen, M., Zhou, X. (2020), Nitrogen/sulfur Co-doping strategy to synthesis green-yellow emitting carbon dots derived from xylose: Toward application in pH sensing, J. Lumin., 227, 117489 (DOI: 10.1016/j.jlumin.2020.117489)

[39] Schneider, J., Reckmeier, C.J., Xiong, Y., von Seckendorff, M., Susha, A.S., Kasák, P., Rogach, A.L. (2017), Molecular Fluorescence in Citric Acid-Based Carbon Dots, J. Phys. Chem. C, 121, 2014–2022 (DOI: 10.1021/acs.jpcc.6b12519)

[40] Dong, Y., Pang, H., Yang, H.B., Guo, C., Shao, J., Chi, Y., Li, C.M., Yu, T. (2013), Carbon-Based Dots Co-doped with Nitrogen and Sulfur for High Quantum Yield and Excitation-Independent Emission, Angew. Chem. Int. Ed., 52, 7800–7804 (DOI: 10.1002/anie.201301114)

[41] Chun Li, Liu, W., Sun, X., Pan, W., Yu, G., Wang, J. (2018), Excitation dependent emission combined with different quenching manners supports carbon dots to achieve multi-mode sensing, Sens. Actuators B Chem., 263, 1–9 (DOI: 10.1016/j.snb.2018.02.050)

[42] Zhuo, S., Guan, Y., Li, H., Fang, J., Zhang, P., Du, J., Zhu, C. (2019), Facile fabrication of fluorescent Fe-doped carbon quantum dots for dopamine sensing and bioimaging application, Analyst, 144, 656–662 (DOI: 10.1039/C8AN01741G)

[43] Carbonaro, C.M., Chiriu, D., Stagi, L., Casula, M.F., Thakkar, S.V., Malfatti, L., Suzuki, K., Ricci, P.C., Corpino, R. (2018), Carbon Dots in Water and Mesoporous Matrix: Chasing the Origin of their Photoluminescence, J. Phys. Chem. C, 122, 25638–25650 (DOI: 10.1021/acs.jpcc.8b08012)

[44] Song, J., Li, J., Guo, Z., Liu, W., Ma, Q., Feng, F., Dong, C. (2017), A novel fluorescent sensor based on sulfur and nitrogen co-doped carbon dots with excellent stability for selective detection of doxycycline in raw milk, RSC Adv., 7, 12827–12834 (DOI: 10.1039/C7RA01074E)

[45] Majumdar, B., Sarma, D., Jain, S., Sarma, T.K. (2018), One-Pot Magnetic Iron Oxide–Carbon Nanodot Composite-Catalyzed Cyclooxidative Aqueous Tandem Synthesis of Quinazolinones in the Presence of tert-Butyl Hydroperoxide, ACS Omega, 3, 13711–13719 (DOI: 10.1021/acsomega.8b01794)

[46] Wardani, R.K., Dahlan, K., Wahyudi, S.T., Sukaryo, S.G. (2019), Synthesis and characterization of nanoparticle magnetite for biomedical application, AIP Conf. Proc., 2194, 020137 (DOI: 10.1063/1.5139869)

[47] Li, B., Wang, X., Guo, Y., Iqbal, A., Dong, Y., Li, W., Liu, W., Qin, W., Chen, S., Zhou, X., Yang, Y. (2016), One-pot synthesis of polyamines improved magnetism and fluorescence Fe_3O_4–carbon dots hybrid NPs for dual modal imaging, Dalton Trans., 45, 5484–5491 (DOI: 10.1039/C5DT04488J)

[48] Ding, Y.-Y., Gong, X.-J., Liu, Y., Lu, W.-J., Gao, Y.-F., Xian, M., Shuang, S.-M., Dong, C. (2018), Facile preparation of bright orange fluorescent carbon dots and the constructed biosensing platform for the detection of pH in living cells, Talanta, 189, 8–15 (DOI: 10.1016/j.talanta.2018.06.060)

[49] Ai, Q., Yuan, Z., Huang, R., Yang, C., Jiang, G., Xiong, J., Huang, Z., Yuan, S. (2019), One-pot co-precipitation synthesis of Fe_3O_4 nanoparticles embedded in 3D carbonaceous matrix as anode for lithium ion batteries, J. Mater. Sci., 54, 4212–4224 (DOI: 10.1007/s10853-018-3141-3)

[50] Kaur, N., Sharma, V., Tiwari, P., Saini, A.K., Mobin, S.M. (2019), “Vigna radiata” based green C-dots: Photo-triggered theranostics, fluorescent sensor for extracellular and intracellular

iron (III) and multicolor live cell imaging probe, Sens. Actuators B Chem., 291, 275–286 (DOI: 10.1016/j.snb.2019.04.039)

[51] Li, Z., Lin, H., Ding, S., Ling, H., Wang, T., Miao, Z., Zhang, M., Meng, A., Li, Q. (2020), Synthesis and enhanced electromagnetic wave absorption performances of Fe_3O_4@C decorated walnut shell-derived porous carbon, Carbon, 167, 148–159 (DOI: 10.1016/j.carbon.2020.05.070)

[52] Chandra, S., Das, R., Kalappattil, V., Eggers, T., Harnagea, C., Nechache, R., Phan, M.-H., Rosei, F., Srikanth, H. (2017), Epitaxial magnetite nanorods with enhanced room temperature magnetic anisotropy, Nanoscale, 9, 7858–7867 (DOI: 10.1039/C7NR01541K)

[53] Liu, D., Wu, C., Yan, M., Wang, J. (2018), Correlating the microstructure, growth mechanism and magnetic properties of FeSiAl soft magnetic composites fabricated via HNO3 oxidation, Acta Mater., 146, 294–303 (DOI: 10.1016/j.actamat.2018.01.001)

[54] Rajan, A., Sharma, M., Sahu, N.K. (2020), Assessing magnetic and inductive thermal properties of various surfactants functionalised Fe_3O_4 nanoparticles for hyperthermia, Sci. Rep., 10, 15045 (DOI: 10.1038/s41598-020-71703-6)

[55] Wu, H., Gao, G., Zhou, X., Zhang, Y., Guo, S. (2011), Control on the formation of Fe_3O_4 nanoparticles on chemically reduced graphene oxide surfaces, CrystEngComm., 14, 499–504 (DOI: 10.1039/C1CE05724C)

[56] Feng, X., Ashley, J., Zhou, T., Sun, Y. (2018), Fluorometric determination of doxycycline based on the use of carbon quantum dots incorporated into a molecularly imprinted polymer, Microchim. Acta., 185, 500 (DOI: 10.1007/s00604-018-2999-8)

[57] Yang, K., Wang, Y., Lu, C., Yang, X. (2018), Ovalbumin-directed synthesis of fluorescent copper nanoclusters for sensing both vitamin B1 and doxycycline, J. Lumin., 196, 181–186 (DOI: 10.1016/j.jlumin.2017.12.038)

[58] Cui, Z., Guo, S., Yan, J., Li, F., He, W. (2020), BiOBr nanosheets with oxygen vacancies and lattice strain for enhanced photoelectrochemical sensing of doxycycline, Appl. Surf. Sci., 512, 145695 (DOI: 10.1016/j.apsusc.2020.145695)

[59] Fu, X., Lv, R., Su, J., Li, H., Yang, B., Gu, W., Liu, X. (2018), A dual-emission nano-rod MOF equipped with carbon dots for visual detection of doxycycline and sensitive sensing of MnO_4, RSC Adv., 8, 4766–4772 (DOI: 10.1039/C7RA12252G)

[60] Siddiqui, A., Anwar, H., Ahmed, S.W., Naqvi, S., Shah, M.R., Ahmed, A., Ali, S.A. (2020), Synthesis and sensitive detection of doxycycline with sodium bis 2-ethylhexylsulfosuccinate based silver nanoparticle, Spectrochim.

Acta. A. Mol. Biomol. Spectrosc., 225, 117489 (DOI: 10.1016/j.saa.2019.117489)
[61] Li, C., Zhang, X., Wen, S., Xiang, R., Han, Y., Tang, W., Yue, T., Li, Z. (2020), Interface engineering of zeolite imidazolate framework−8 on two-dimensional Al−metal−organic framework nanoplates enhancing performance for simultaneous capture and sensing tetracyclines, J. Hazard. Mater., 395, 122615 (DOI: 10.1016/j.jhazmat.2020.122615)
[62] Su, Q., Wei, X., Mao, J., Yang, X. (2019), Carbon nanopowder directed synthesis of carbon dots for sensing multiple targets,, Colloids Surf. Physicochem. Eng. Asp., 562, 86–92 (DOI: 10.1016/j.colsurfa.2018.11.015)
[63] Singh, G., Sharma, M., Vaish, R. (2021), Flexible Ag@LiNbO3/PVDF Composite Film for Piezocatalytic Dye/Pharmaceutical Degradation and Bacterial Disinfection, ACS Appl. Mater. Interfaces, 13, 22914–22925 (DOI: 10.1021/acsami.1c01314)
[64] Pulicharla, R., Das, R.K., Brar, S.K., Drogui, P., Surampalli, R.Y. (2018), Degradation kinetics of chlortetracycline in wastewater using ultrasonication assisted laccase, Chem. Eng. J., 347, 828–835 (DOI: 10.1016/j.cej.2018.04.162)
[65] Huang, L., Yang, L., Li, Y., Wang, C., Xu, Y., Huang, L., Song, Y. (2020), p-n BiOI/Bi3O4Cl hybrid junction with enhanced photocatalytic performance in removing methyl orange, bisphenol A, tetracycline and Escherichia coli, Appl. Surf. Sci., 527, 146748 (DOI: 10.1016/j.apsusc.2020.146748)
[66] Wang, A., Zheng, Z., Wang, H., Chen, Y., Luo, C., Liang, D., Hu, B., Qiu, R., Yan, K. (2020), 3D hierarchical H2-reduced Mn-doped CeO2 microflowers assembled from nanotubes as a high-performance Fenton-like photocatalyst for tetracycline antibiotics degradation, Appl. Catal. B Environ., 277, 119171 (DOI: 10.1016/j.apcatb.2020.119171)

CHAPTER 5

A sustainable fluorescent system for the delivery of 5-fluorouracil in vitro, Co^{2+} ion detection, and live-cell imaging

5.1. Introduction

Nanomaterials have been studied extensively in recent years for their outstanding contributions to diagnosis and therapy. Various carbon-based nanomaterials were used extensively for bioimaging, sensing, drug delivery, antibacterial activity, photosensitizer, gene delivery, etc. [1–5]. The carbon dots emerge as a robust candidate for the carbon nanomaterial family and show great potential in theranostics [6–8]. Since the accidental discovery of carbon dots in 2004, it has been explored for activity in many applications, from optoelectronics, sensing, exfoliation, catalysis, energy storage, and environmental remediation to biomedical applications [9–16]. The excellent photophysical properties of carbon dots, and their highly biocompatible nature, provide it a higher position among the nanomaterials. Cancer is one of the leading causes of death [17]. Many cancer patients are still treated by using conventional chemotherapies. These therapies have multiple problems associated with like drug toxicity towards normal cells, lesser bioavailability of the drug, drug interaction with other biomolecules, non-specificity towards a particular type of cancer cells, etc. [18]. Various problems associated with chemotherapy can be overcome by using a specially designed drug delivery system [19, 20]. Maximum chemotherapeutic drugs are poorly soluble in water, so getting them entrapped or paired with an aqueous soluble delivery system will enhance their therapeutic efficacy.

The easy surface functionalization, resistance to photobleaching, and remarkable biocompatibility of carbon dots always make it interesting to

use them as fluorescent probes for bioimaging. Since the discovery of green fluorescent protein (GFP), it has been utilized as a probe to monitor biomolecule interactions, localization, and gene expression [21]. But its inability to resist photobleaching and less fluorescence encourage the researchers to develop other probes to be used successfully in bioimaging. The carbon dots are a desirable candidate with physicochemical properties as imaging agents. The pristine carbon dots could easily be modified to tune their optical properties and surface functionality for organelle or cell targeting. Carbon dots' highly fluorescent and biocompatible nature is also utilized to prepare in-vivo imaging probes. Since its discovery, the multipurpose carbon dots have also been used for sensing metal ions. Since then, the specific, selective, fast, and precise detection of metal ions using carbon dots-based sensors has been a growing area.

In this context, we demonstrate the synthesis of surface factionalized nitrogen-doped carbon dots as an effective drug carrier, bioimaging agent, and metal ion sensor. The as-synthesized carbon dots are reported to act as a carrier of the antimetastatic drug 5 Fluro uracil (5FU) and exhibited enhanced release in the tumor microenvironment. It helps improve drug efficacy and lessen the side effect on normal cells compared to conventional therapies. Therefore, the **N@PEGCDs** alone and the association of 5FU with them can serve as a new platform for bioimaging, sensing, and an intelligent drug delivery system.

5.2. Results and discussion

5.2.1 Preparation and Characterization of N@PEGCD and 5FU-N@PEGCDs

The nitrogen-doped carbon dots were obtained using trimesic acid and PEG as carbon sources and ethylenediamine for nitrogen doping via the hydrothermal method. The trimesic acid was used due to the presence of various functionality (-OH and -COOH), and PEG is used to impart biocompatibility to the product. The nitrogen doping can enhance quantum yield as well as bring about divergent surface states to improve the photostability for **N@PEGCDs**. The light-yellow mixture of precursors turns to brown color after hydrothermal treatment, evincing the formation of carbon dots. The hydrothermal treatment was carried out for 12 h at 200 ℃ to obtain fluorescent **N@PEGCDs**, as shown in **Scheme 1**. The quantum yield (QY) of the **N@PEGCDs** was calculated to be 43%. The enhanced QY is resultant of nitrogen doping [22].

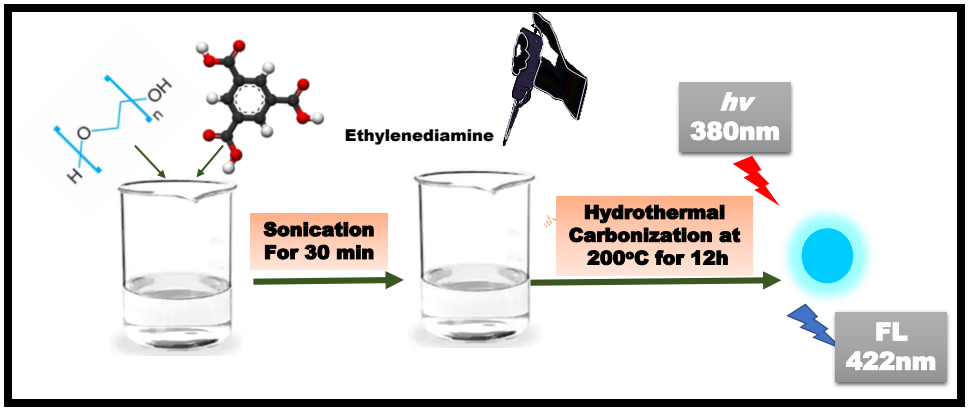

Scheme 5.1. Schematic illustration for synthesis strategy of **N@PEGCDs**

As explained in the experimental section, the **N@PEGCDs** were further conjugated with 5-FU, an anticancerous drug. The DLE was calculated to be 52.3%. It is believed that the functional group present on the surface of **N@PEGCDs** makes it a desirable candidate to interact easily with 5FU. The synthesis procedure is shown in **Scheme 2.**

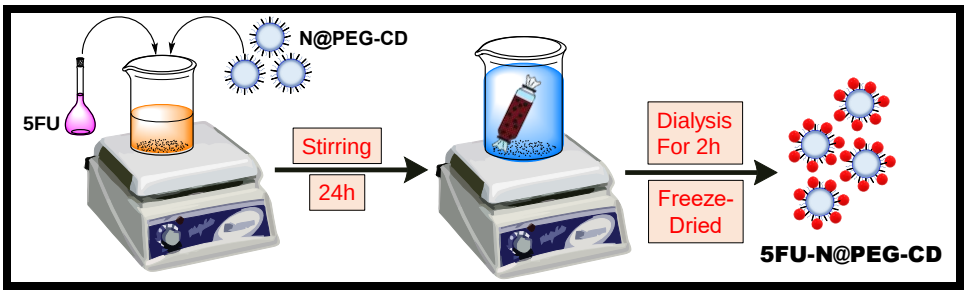

Scheme 5.2. Schematic illustration for synthesis strategy of **5FU-N@PEGCDs.**

To mechanism behind the synthesis of **N@PEGCDs** is demonstrated in **Figure 5.1**. The carboxyl group of trimesic acid firstly polymerizes with an amine of ethylenediamine and hydroxyl group of PEG to form a polymer through dehydration which further carbonizes and bursts to produce surface-functionalized fluorescent carbon dots [23].

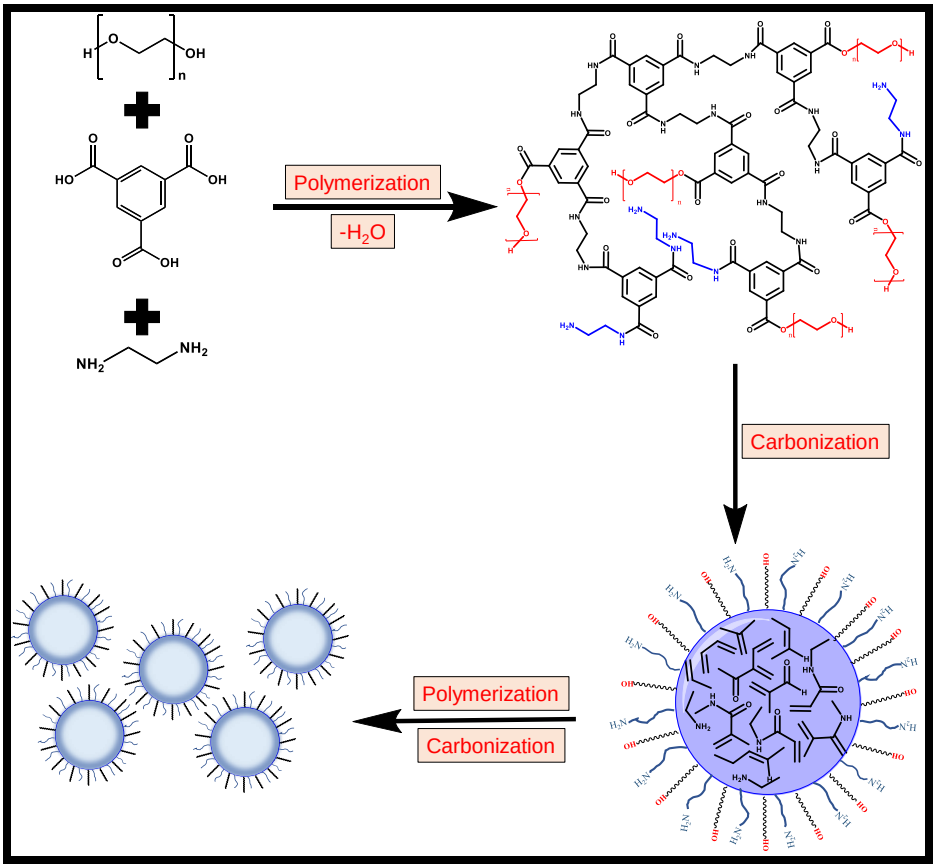

Figure 5.1. The mechanism of **N@PEGCDs** synthesis.

XRD, XPS, FTIR, and UV-vis spectroscopy were carried out to characterize the formed CDs. In PXRD (**Figure 5.2d**), the broad hump at 2θ=21.8° is found, suggestive of the amorphous nature of the material [24]. The d-spacing was calculated to be 4.0 Å which could be assigned to distorted sp^2 hybridization [25]. HR-TEM determined the morphology and size of **N@PEGCDs**. Most of the particles are spherical with an amorphous structure, which PXRD also supports. A few particles showed clear lattice fringes with a spacing of 0.26 nm (**Figure 5.2b**), suggestive of the graphite-like structure of formed CDs [26]. The size of CDs calculated from HR-TEM images ranges from 4.5 nm to 7 nm (**Figure 5.2c**). The SAED pattern shown in **Figure 2b (inset)** also supports the presence of little crystallinity in otherwise amorphous **N@PEGCDs**. The functional group present on the surface of **N@PEGCDs** was studied by FT-IR, as shown in **Figure 5.2e**. The broad peak at 3354 cm^{-1} was attributed to the stretching vibration of O-H [27], whereas the peak at 2914 cm^{-1} was anti-symmetric stretching of C-H [28]. Stretching vibration at 1634 cm^{-1} of C=O and 1103 cm^{-1} of C-O demonstrate oxygen-rich groups on the surface of **N@PEGCDs** [29]. The bending vibration of N-H [24] and C-N [30] was exhibited at 1571 cm^{-1} and 1353 cm^{-1}. The FT-IR data confirms the presence of amine and nitrogen-rich functionality on the surface of **N@PEGCDs**. The XPS spectra shown in **Figure 5.2f** revealed the presence of two high-intensity peaks at 284.4 eV and 532.4 eV assigned to C1s and O1s. Another low-intensity peak present at 398.6 suggested the presence of N1s in the elemental composition of **N@PEGCDs**. The deconvoluted spectra of C1s corresponding to sp^3 carbon C-N at 285.1 eV, the presence of C-O at 286.7 eV, and C=O at 287.8 eV [31–33]. The N1s high-resolution XPS spectra on deconvolution showed two peaks at 399.4 eV and 401 eV, denoting porphyrin C–N–C and aromatic N-C=O, respectively [34, 35]. In high-resolution spectra of O1s, the two peaks at

530.2 eV and 532 eV were ascribed to C=O and C-OH [36]. The high-resolution spectra of C1s, N1s, and O1s are shown in Figure 2. g-h.

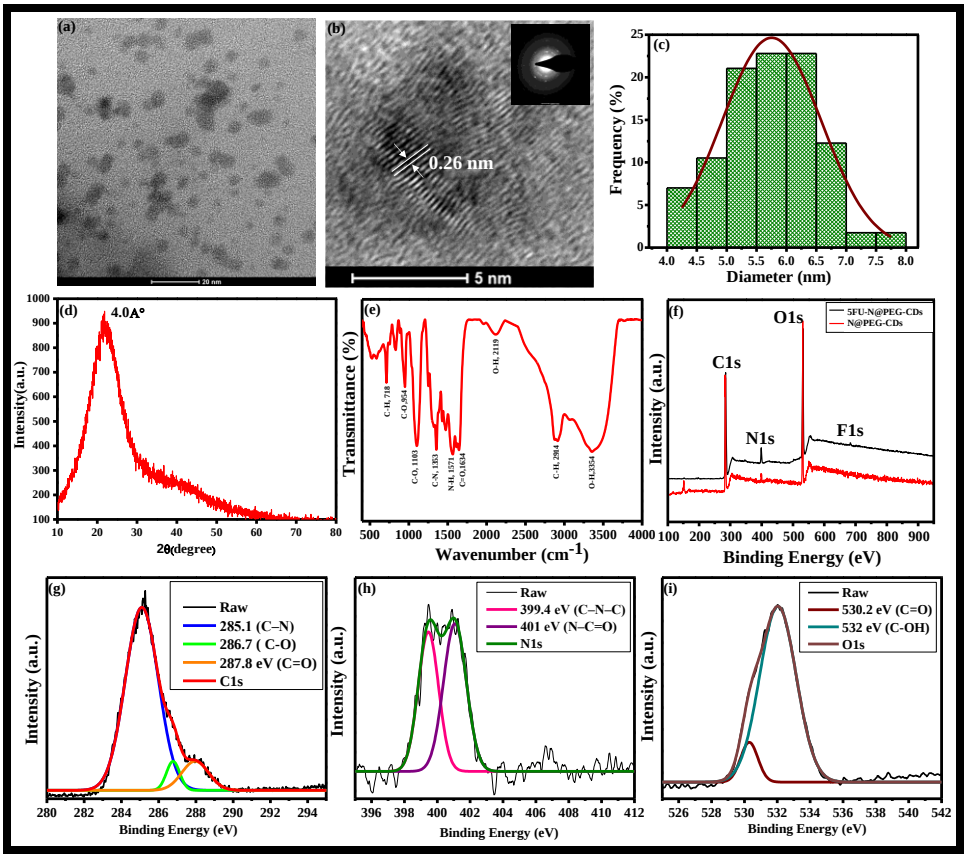

Figure 5.2. Structural and optical characterization of **N@PEGCDs** (a) TEM (b) HR-TEM (c) particle size distribution (d) PXRD (e) FT-IR (f) XPS survey scan of **N@PEGCDs** and **5FU-N@PEGCDs**. XPS high-resolution spectrum for **(g) N@PEGCDs**: C 1s, **(h) N@PEGCDs**: N 1s, **(i) N@PEGCDs**: O 1s.

The UV-vis spectrum of **N@PEGCDs** shown in **Figure 5.3a** reveals the presence of a shoulder at 286 nm attributed to the π- π* transition of C=C and C=N. Here, the carbonyl and carboxyl groups are assumed to be present on the surface of **N@PEGCDs**; however, the C=C originated from the polymeric domains situated at the core with sp^2 hybridization [37]. The different surface states of **N@PEGCDs** are also a reason for this shoulder

near-visible region [38]. The various functional groups present on the surface of **N@PEGCDs** is a crucial attribute that makes it a promising candidate to be used in multiple applications in different areas. For instance, the functionalized surface of **N@PEGCDs** was utilized for interaction with an anticancerous drug, 5FU, which is used to treat solid tumors. The inset of **Figure 5.3a** shows UV-Vis spectra of **5FU-N@PEGCDs** along with only 5FU. The drug-CD conjugate of **N@PEGCDs** and 5FU display a clear peak at 266 nm, which is the characteristic peak of 5FU, supporting the fact that 5FU has been loaded successfully on **N@PEGCDs**. The successful conjugation of 5FU with **N@PEGCDs** is also confirmed by XPS spectra of the **5FU-N@PEGCDs** conjugate, as shown in **Figure 5.2f**. The peak at 683.5 eV was assigned to F1s [41]. To determine the optical properties of **N@PEGCDs**, fluorescence spectroscopy was performed. The results shown in **Figure 5.3b** indicate the excitation-dependent emission behavior of **N@PEGCDs**. This behavior could be explained due to different surface states, polydispersity, carbon dot mixture, or the formation of aggregates [39, 40].

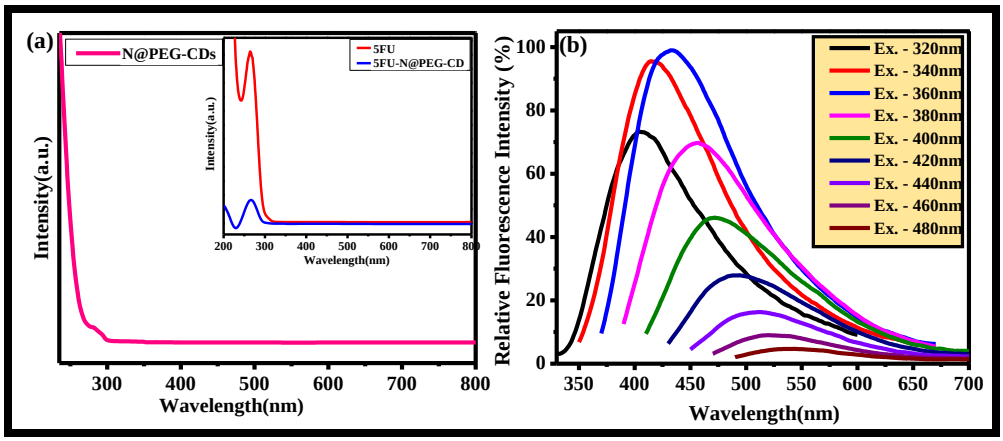

Figure 5.3. Optical characterization (a) UV-vis spectra of **N@PEGCDs**. The UV-spectra of 5FU and **5FU- N@PEGCDs** (inset) (b) Wavelength tuned emission of **N@PEGCDs**

5.2.2 Biocompatibility and Bio-Imaging using N@PEGCDs

The biocompatibility of **N@PEGCDs** was estimated using A375 (melanoma cancer cell line) up to 48 h by treating with concentrations ranging from 200 μg mL^{-1} to 1000 μg mL^{-1}. The results are shown in **Figure 5.4a** suggest the high biocompatible nature of **N@PEGCDs**. There is more than 85% cell viability even after 48 h. The outstanding biocompatibility and admirable optical properties make it a favorable fluorescent probe to be used as a bioimaging agent. On excitation with a blue laser of wavelength 405 nm, cells show blue fluorescence coming from the cytoplasmic region.

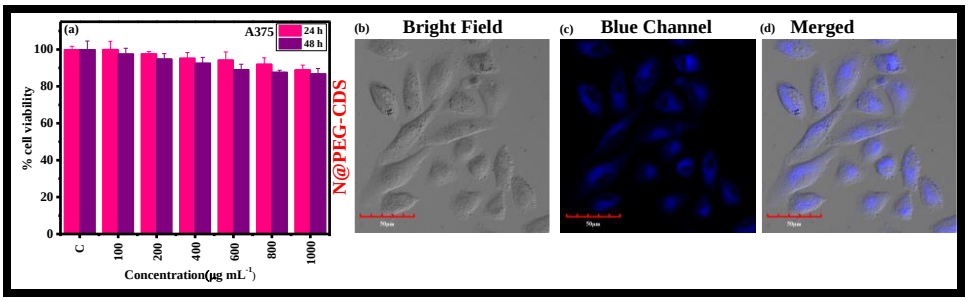

Figure 5.4. (a) Cytotoxicity assay of **N@PEGCDs** (100- 1000 μg mL^{-1}) Bio-imaging of A375 cells using **N@PEGCDs** (200μg mL^{-1}) at 37℃ for 6 h.

5.2.3 Fluorescence response of N@PEGCDs towards Co^{2+}ions, selectivity, and quenching mechanism

The presence of hydroxyl and carboxyl groups on the surface of **N@PEGCDs** gives it the ability of metal ion sensing. Interestingly, the prepared carbon shows an eminent response towards Co^{2+} ions (**Figure 5.5a**). The carbon dots have a dual ability of electron-accepting and donating, which is helpful in electron transfer from metal ions to carbon dots or vice versa. With the increase in the concentration of Co^{2+} in the system, the fluorescence of **N@PEGCDs** decreases gradually, and after a certain amount of Co^{2+} addition, the fluorescence response begins to slow

down, indicating the ligand sites on the surface of **N@PEGCDs** get occupied completely [42]. The **N@PEGCDs** showed a turn-off response towards Co^{2+} in the range of 0-1000 µM. An excellent linear relationship was found between fluorescence **N@PEGCDs** and the concentration of Co^{2+} in the range of 0-550 µM with adj. R^2 value of 0.98 (**Figure 5.5b**). To calculate the limit of detection (LOD) signal to noise ratio was set as 3. The LOD was 6.8 nm, which is much less than the allowed concentration of Co^{2+} in drinking water (40 µg ml^{-1}) [43]. The initial fluorescence of **N@PEGCDs** decreased to 8.5% after the addition of 1000 µM of Co^{2+} solution.

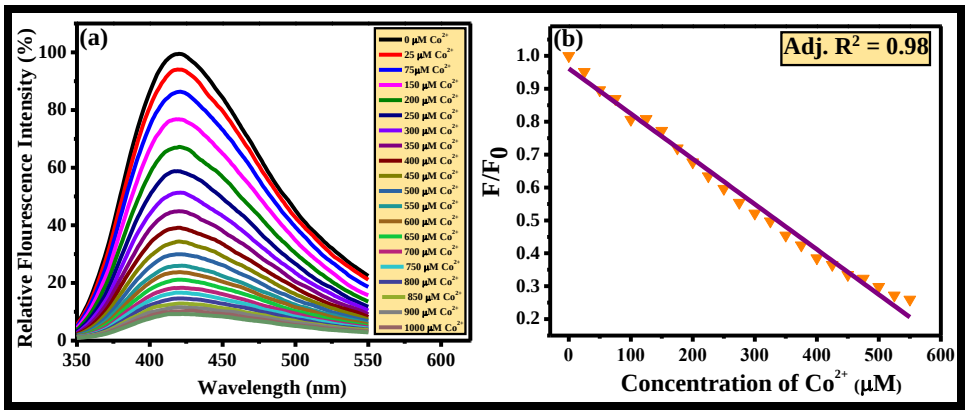

Figure 5.5. The fluorescence-based sensing response of **N@PEGCDs** (a) Relative fluorescence intensity with increasing concentrations of Co^{2+} (b) Linear correlation of concentrations of Co^{2+} with relative intensity.

The selectivity of **N@PEGCDs** towards Co^{2+} was determined in the presence of different anions and cations (Sn^{2+}, Cr^{2+}, Co^{2+}, Pb^{2+}, Cd^{2+}, Ag^{+}, Hg^{2+}, Bi^{3+}, Ni^{2+}, Na^{2+}, Cu^{2+}, Al^{3+}, Zr^{4+}, Zn^{2+}, Mn^{2+}, K^{+}, B^{3+}, V^{+}, Ba^{2+}, Ca^{2+}, Cl^{-}, I^{-}, Se^{2-}, SO_2^{3-}, S^{2-}, $S_2O_2^{5-}$, CO_3^{2-}, PO_4^{3-}, WO_4^{2-}, MoO_4^{2-}, HCO_3^{-}, NO_2^{-}, CH_3COO^{-}) As results illustrated in **Figure 5.6** shows that the response of **N@PEGCDs** towards Co^{2+} is maximum among all the metal ions. The other selected anions or cations exhibit significantly less or no fluorescence quenching of **N@PEGCDs** solution. The effect of different

ions on the ability of **N@PEGCDs** to sense Co^{2+} was also determined. It was concluded from the result of competitive selectivity studies in **Figure 5.6(inset)** that **N@PEGCDs** are selective towards Co^{2+}, and the presence of other anions and cations did not affect this property.

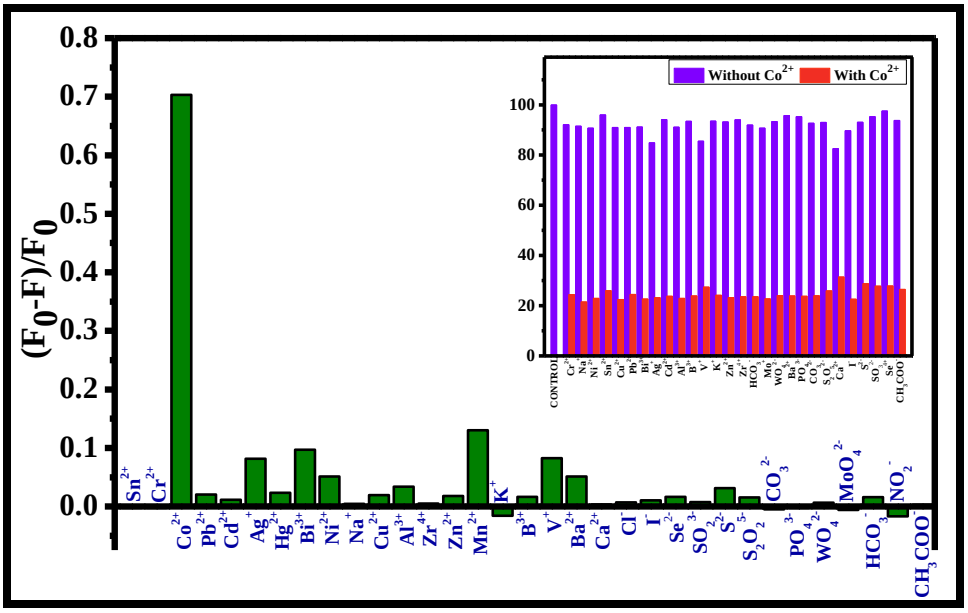

Figure 5.6. The selectivity in the sensing response of **N@PEGCDs** different anions and cations, Competitive selectivity study (inset)

There is evidence in previous studies that could be correlated to the sensing mechanism of **N@PEGCDs.** The fluorescence quenching of **N@PEGCDs** is by electron transfer between metal and fluorophore along with complex formation. The complex formation could be visualized by a change in the color of **N@PEGCDs** solution on the addition of metal ions from light yellow to brown, confirming the interaction between these two [44]. According to previous reports, this "turn-off" behavior of **N@PEGCDs** can be explained by the electron transfer mechanism and formation of the metal-fluorophore complex [45–47].

5.2.4 In vitro drug release profile, Cytotoxicity, and anticancer activity of 5FU-N@PEGCDs nanoconjugate

Any material used as a drug carrier should have a few qualities such as reduced cytotoxicity, controlled drug release, real-time monitoring, and stimulus-responsive delivery. To check the ability of **5FU-N@PEGCDs** to act as a drug delivery system, the drug release profile was studied at two different pH, one is 7.4 physiological pH, and another is 5.4 the pH around cancerous tumors (**Figure 5.7a**). The cumulative release of 5FU is higher at lower pH than physiological pH. This gives the **5FU-N@PEGCDs** delivery system the advantage of releasing more drugs around the tumor microenvironment. In addition, it could be inferred that the delivery of antineoplastic agent is in the presence of external stimuli, i.e., change of pH. The biocompatible nature of **N@PEGCDs** is already discussed earlier. The biocompatibility of **5FU-N@PEGCDs** has also been studied in HEK (human embryonic kidney cells), a standard cell line, and A375 (melanoma cells), a cancerous cell line for 24 h **(Figure 5.7b-c)**. The free 5FU was also used to determine the effect of conjugation on the cytotoxicity profile of the drug. The cell viability declines in normal and cancerous cells with free 5FU and **5FU-N@PEGCDs** nanoconjugate treatment. However, the toxicity of the free drug is more toward normal cells than **5FU-N@PEGCDs** nanoconjugate. At the highest treatment concentration of 8 μg ml^{-1}, 20% of the cells treated with free 5FU are viable, while the viability of **5FU-N@PEGCDs** treated cells is 30%. In contrast, when the cancerous A375 cells are treated with equivalent concentrations of free and conjugated drugs, the viability follows dose-dependent behavior. The drug conjugated with carbon dots kills more cancerous cells than the free drug. The equivalent concentration of both free and conjugated drugs kills approximately 70% and 80% of cells. The results also confirm that the conjugation of **N@PEGCDs** with 5FU doesn't alter its activity. This proposes the substantial prospective of **5FU-N@PEGCDs** in cancer treatment because its reduced cytotoxicity towards normal cells results in decreased adverse effects on patients hence better tolerance to the drug throughout the course of treatment.

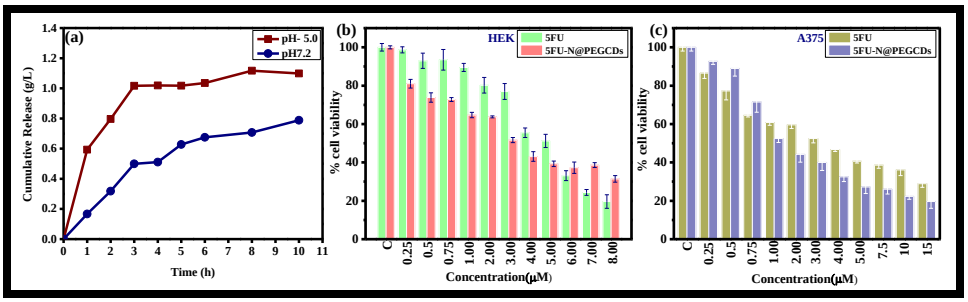

Figure 5.7. (a) In vitro release profile of 5-FU from **5FU-N@PEGCDs** nanoconjugate in different pH values. (b) Cytotoxicity results of Free 5-FU and **5FU-N@PEGCDs** to HEK cells (c) A375 cells at different concentrations for 24 h.

5.2.5 Cellular Interactions and mode of action of 5FU-N@PEGCDs nanoconjugate

It is evident from the previous results that **N@PEGCDs** were taken up by the cells. In the case of nanoconjugate, the **5FU-N@PEGCDs** could also be taken up by cells and release 5FU there, which kills the cell, or the drug gets released at the tumor site from **5FU-N@PEGCDs** and taken up by cells which kills the cells. In any case, the mode of action of **5FU-N@PEGCDs** for killing the cell was studied through various assays. The 5FU gets intruded into nucleoside metabolism and gets incorporated into cellular DNA or RNA, leading to the initiation of the apoptotic pathway to ultimately kill the cell [48]. The signs of morphological changes in nuclei, blebbing, chromatin fragmentation or condensation, and bi or multinucleation were investigated by Hoechst staining. The A375 cells after treatment with IC_{50} values of **5FU-N@PEGCDs** for 24 h were stained with Hoechst. The results are shown in **Figure 5.8**. The nucleus of non-treated cells are evenly stained, and cells treated with **N@PEGCDs** also show similar results, while the **5FU-N@PEGCDs** treated cells show a change in nucleus morphology. Their condensed and fragmented chromatin, cytoplasmic blebbing, and multi-nucleation are comparable to positive control.

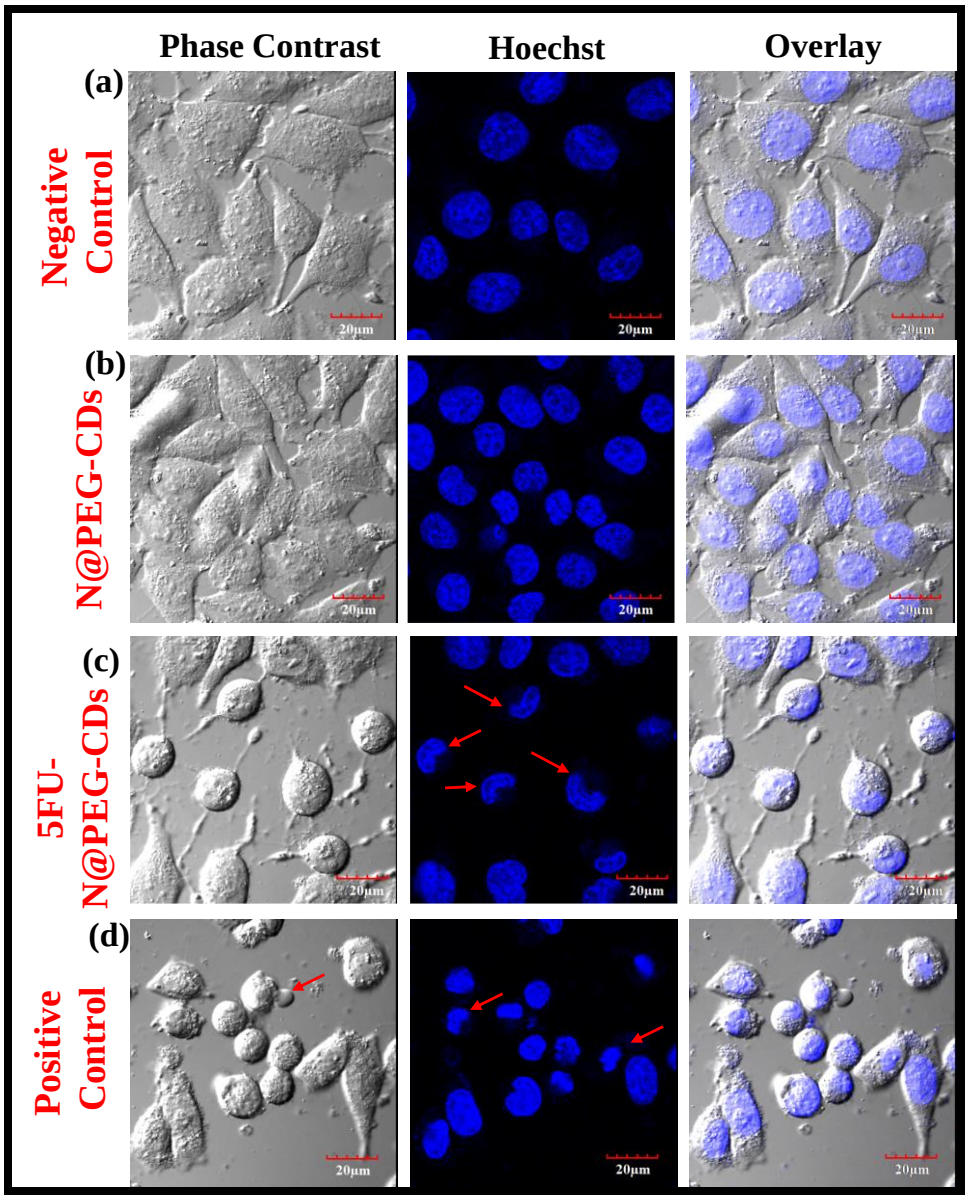

Figure 5.8. Confocal microscopic analysis of A375 cells treated with **N@PEGCDs** and **5FU-N@PEGCDs** along with positive and negative controls.

The reduced cell migration is another measure chosen to check the antiproliferative action of any drug or complex. The cell migration assay/wound healing assay was carried out using the A375 cells described earlier. The cancer cells invade neighboring tissues through migration

which occurs due to the action of many genes [49]. Many anticancerous drugs target these genes to inhibit the spread of metastatic cells from one organ to another. **Figure 5.9** depicts the delayed wound closure in the cells treated with **5FU-N@PEGCDs**. In negative control and **N@PEGCDs**, treated wounds heal almost 100% after 48 h, while approximately 45% of the wounded area remains in **5FU-N@PEGCDs** treated cells. So, it could be inferred that the **5FU-N@PEGCDs** suppress cell migration considerably.

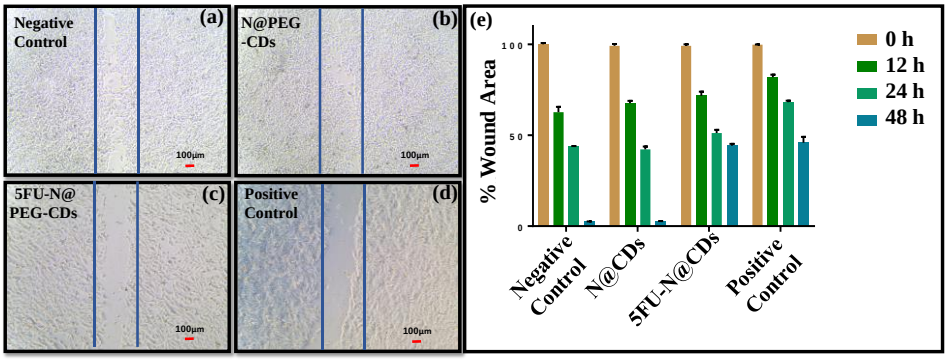

Figure 5.9. The wound-healing assay with the treatment of **N@PEGCDs** and **5FU-N@PEGCDs** (e) Graphical representation of % wound area remains from close at 0-48 h.

Chemotherapy often leads to the formation of reactive oxygen species (ROS), which could cause cell death through apoptosis. The treatment of cells with **5FU-N@PEGCDs** can also generate ROS in the treated cells. The generated ROS were determined by DCFDA assay. The enhancement of fluorescence in the treated cell is a clear indication of the presence of ROS, as shown in **Figure 5.10**. It further supports the assumption of cell death by apoptosis after **5FU-N@PEGCDs** treatment.

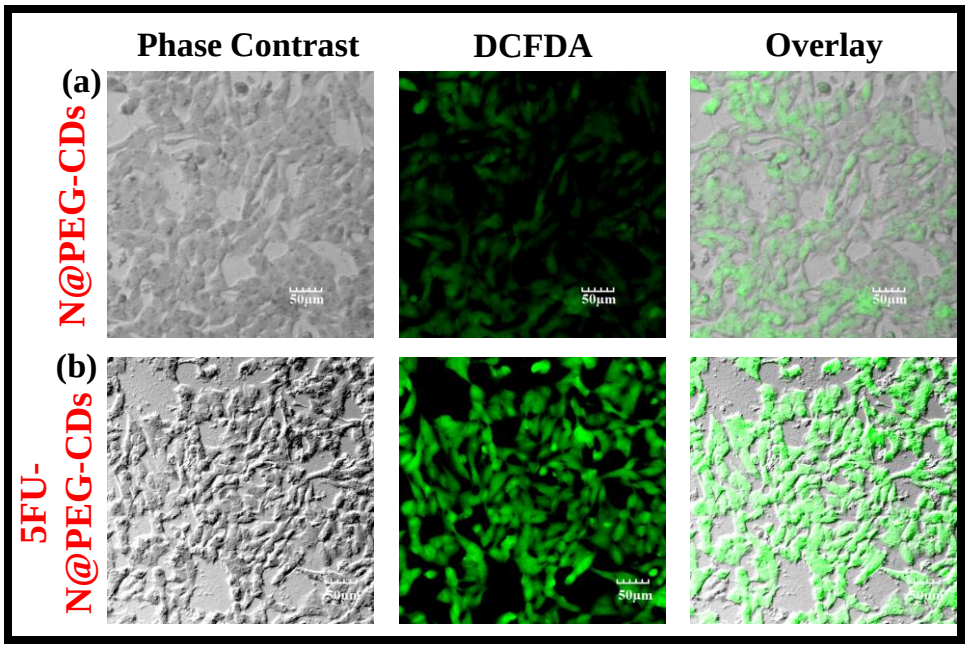

Figure 5.10. The confocal images of A375 cells after treatment with **N@PEGCDs** and **5FU-N@PEGCDs** and stained with DCFDA.

To dissect the apoptotic signaling pathway, we investigated the effects of **N@PEGCDs** and **5FU-N@PEGCDs** on apoptotic proteins in A375 and HEK cell lines by Western blotting. The apoptotic mitochondrial events are regulated by members of the Bcl-2 family of proteins [50]. Anti-apoptotic protein Bcl-XL is a member of the Bcl-2 family. It is a major transmembrane molecule of mitochondria that prevents apoptosis by blocking the release of mitochondrial contents like cytochrome C into cytosol; therefore, its expression was expected to be downregulated in apoptotic cells. As anticipated, the expression of anti-apoptotic protein Bcl-XL was down-regulated in **5FU-N@PEGCDs** treated cells (**Figure 11**). Next, we investigated the effects of **N@PEGCDs** and **5FU-N@PEGCDs** on a pro-apoptotic protein Poly (ADP-ribose) polymerase (PARP), which is involved in the repair of DNA damage. Therefore, cleavage of PARP by caspase-3 will inhibit the DNA repair mechanism leading to apoptosis [51]. Apoptosis was induced by exposing the cells to

5FU-N@PEGCDs treatment and confirmed by observing the cleavage of the PARP molecule to the characteristic 89 kDa C-terminal fragment. Together these results suggest that **5FU-N@PEGCDs** induce PARP mediated apoptosis.

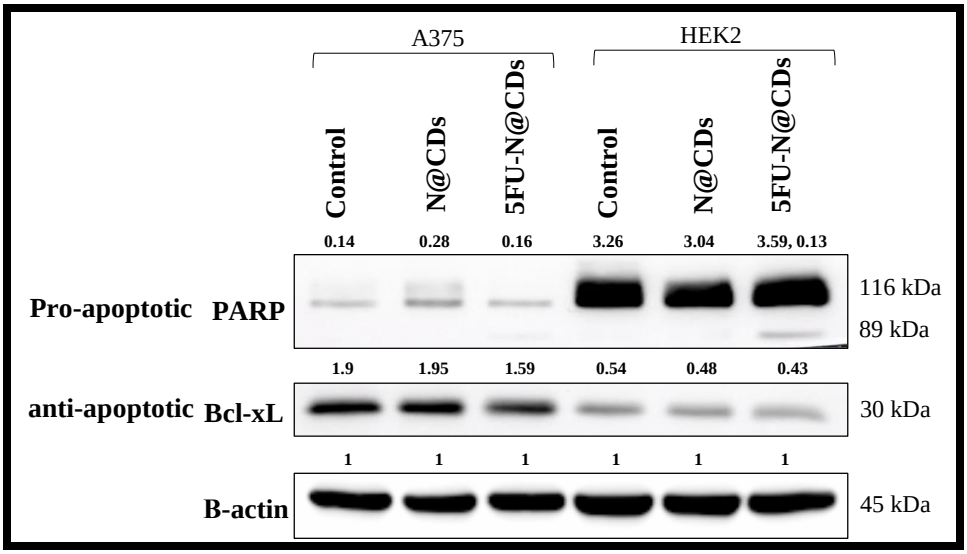

Figure 5.11. Western blot using protein extracted from A375 cells after treatment with **N@PEGCDs** and **5FU-N@PEGCDs**.

5.2.5 Cell death mechanism

The results herein demonstrated bring forth insights into cell death by apoptosis. The carbon dots loaded with 5FU are internalized to the cell by endocytosis. The drug release led to DNA damage, nuclear fragmentation, and ROS generation, activating the apoptotic signaling pathway. The apoptotic signals activate specific genes to cause cell death. The downregulation of BCL-xL could no longer prevent the release of mitochondrial content into the cytoplasm hence apoptosis. The cleaved PARP prevents DNA repair, which is again a favorable factor in apoptosis. The whole mechanism of cell death by apoptosis is summarized diagrammatically in **Figure 5.12**.

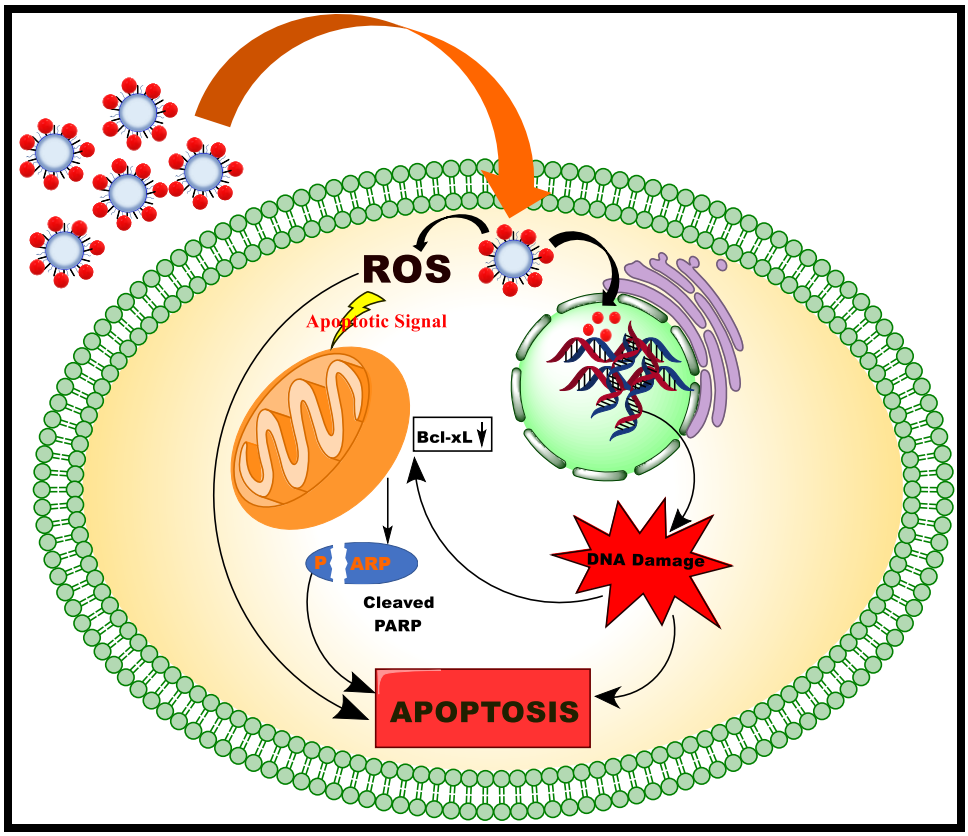

Figure 5.12 Mechanism of cell death by using drug-loaded carbon dots.

5.3. Conclusions

In this work, the facile preparation of nitrogen-doped carbon dots (**N@PEGCDs**) and a unique drug delivery system formulated by self-assembly of antimetastatic drug 5FU on the surface of carbon dots are illustrated. The **N@PEGCDs** were characterized thoroughly. The biocompatible **N@PEGCDs** were used as a fluorescent bioimaging probe and showed selective affinity to Co^{2+}. The LOD was calculated to be as low as 6 nM. The sensing response is selective, sensitive, and progressive. The electrostatic interaction of 5FU with **N@PEGCDs** made it less toxic to normal cells than a free drug, resulting in better drug tolerance. The mechanism behind the cell death caused by **5FU-N@PEGCDs** precisely indicates ROS's role, nuclear changes, and downregulation of anti-apoptotic and upregulation of pro-apoptotic factors in apoptosis. The

detailed mechanism of action is notable for future studies. This result will expedite the growth of carbon dots for their application in theranostics.

5.4. Experimental section

5.4.1 Materials and Instruments

The precursors for the synthesis of carbon dots were attained from sigma-Aldrich. The anions and metal salts were also procured from Sigma-Aldrich and Merck. The chemicals received were of analytical grade, requiring no further purification. The Deionized water (DI) obtained from Sartorius milli-Q system was used to perform all the experiments. The X-ray diffraction (XRD) was analyzed using a Rigaku, RINT 2500 V X-ray diffractometer with Cu Kα radiation (1.5406 Å). The Varian Cary 100 Bio UV-visible spectrophotometer was used to perform UV-visible spectroscopic studies. Fluoromax spectrofluorometer was used to conduct fluorescence studies. IR spectra (4000–400 cm^{-1}) and X-ray photoelectron spectroscopy (XPS) were recorded using Bio-Rad FTS 3000MX instrument and AXIS ULTRA respectively. TEM images were recorded using a FEI Tecnai G2- F20 Transmission Electron Microscope. The cellular imaging studies were carried out by using an Olympus laser scanning microscope. Synergy H1 Biotek microplate reader used for absorption studies of MTT assay.

5.4.2 Synthesis of N@PEGCDs

The hydrothermal carbonization process was drawn to obtain the nitrogen-doped carbon dots (**N@PEGCDs**), PEG and trimesic acid as carbon precursors, and ethylenediamine as nitrogen sources. A homogenous PEG and trimesic acid solution was prepared in DI water by sonication for 30 min. In this solution, the ethylenediamine was added dropwise and mixed. The whole mixture was poured into Teflon coated autoclave vial of 100 capacity and placed into a muffle furnace. The furnace was operated at 200 ℃ for 12 h. the resultant solution was cooled to room temperature, centrifuged to remove any large particles, collected in a clean vial, and

kept at room temperature. This obtained solution was lyophilized to remove water. After lyophilization, a light brown sticky material was obtained, which was stored to be re-suspended in DI water to be used hereafter.

5.4.3 Preparation of 5-Fluorouracil loaded N@PEGCDs

The simple stirring method is followed to prepare a nanoconjugate of **N@PEGCDs** and 5-fluorouracil (5-FU). The loading of 5-fluorouracil on **N@PEGCDs** was achieved by adding 800 mg L^{-1} 5-fluorouracil into the aqueous solution of **N@PEGCDs**. Both ingredients were allowed to react for 24 h by vigorous stirring at room temperature. The unconjugated 5-fluorouracil was removed by dialyzing from obtained solution using a dialyzing membrane of MWCO 2000Da for 3 h. The **5FU-N@PEGCDs** nanoconjugate solution was lyophilized for further characterization using various techniques. The Drug loading efficiency (DLE) and drug loading capacity (DLC) were calculated using the following equations.

$$DLE\ (\%) = [\{A_{(T)} - A_{(F)}\}/ A_{(T)}]\times 100$$

$A_{(T)}$ is the absorbance of the initially added amount of 5-FU in the solution, $A_{(F)}$ is the unconjugated amount of 5-FU, which is calculated by taking the absorbance of the solution outside the dialysis bag after 2 h of dialysis and $W_{(C)}$ is the total weight of the carrier which is **N@PEGCDs** added initially.

5.4.4 In-vitro release of 5-FU

To check the in vitro release of 5-FU from **5FU-N@PEGCDs**, two different pH conditions were evaluated, i.e., pH 7.4, which is physiological pH, and pH 5.0, which is the pH of cancerous tissue. The PBS and acetate buffers were used to achieve these pH conditions. The **5FU-N@PEGCDs** system was dialyzed against a buffer of different pH utilizing a dialysis membrane od MWCO 2000 Da at 37 ℃ for 24 h. The 2 mL solution was taken out from the buffer outside the dialysis membrane at regular intervals, and the release of 5-FU was determined using UV-vis

spectroscopy. To calculate the percentage of the released drug, following equation no. 3 was used.

Cumulative release (%) =Drug released/ total loaded drug content×100 (3)

5.4.5 Detection of $Co^{2+}$and selectivity studies.

The detection of Co^{2+} was carried out at room temperature using an aqueous solution of N@PEGCDs (1mg mL^{-1}). The stock solution of Co^{2+} (10 mM) was prepared in DI water. The fluorescence spectrum of **N@PEGCDs** was recorded at λex. 380 nm, which was used as control(F_0). The Co^{2+} was added serially (0-1000 μM), and a change in fluorescence was recorded. The solution of other anions and cations was prepared at the concentration of 10 mM. To determine the selectivity of the **N@PEGCDs** towards Co^{2+}, the other metal ions were added to the **N@PEGCDs** solution, and spectra of each one was recorded. All the sensing experiments were carried out at room temperature under the same conditions. The competitive selectivity of **N@PEGCDs** towards Co^{2+} was also determined in the presence of other cations and anions.

5.4.6 Cytotoxicity assay and bio-imaging

To perform the various cells related experiments, the cells were grown at 37 ℃ in a 5% CO_2 environment using Dulbecco's modified Eagle medium (DMEM) supplemented with 10% (v/v) FBS (fetal bovine serum) and 1% antibiotics penicillin/streptomycin, 10,000 U mL^{-1}.

The A375 (human melanoma cell line) and HEK (human embryonic kidney cell line) were grown and used for cellular studies.

The viability of both the cells (A375 and HEK) was checked in the presence of **N@PEGCDs**, **5FU-N@PEGCDs**, and 5-FU by a conventional MTT assay. The cells at the density of $1x10^4$ were seeded in 96 wells plate and grown for 24 h. Subsequently, the media was replaced by fresh media containing **N@PEGCDs**, **5FU-N@PEGCDs**, and 5-FU. The **N@PEGCDs** were checked for the concentration range from 200-1000 μg mL^{-1}, whereas the free 5-FU and **5-FU-N@PEGCDs** were tested for the concentration ranges from 0.25-16.0 μg mL^{-1} in triplicates. The

only media containing wells were taken as control. The treated and control cells were allowed to grow for the required time. After 24 h, the media was replaced with fresh media containing MTT of 5 mg mL^{-1}. The purple-colored formazan crystals were dissolved using 100 μL of DMSO per well, and the absorbance was recorded at 570 nm using a UV-plate reader. The percent cell viability was calculated using the following equation (4).

$$\% \text{ Cell Viability} = Abs_{(T)} / Abs_{(C)} \times 100 \quad \ldots\ldots (4)$$

For bio-imaging, A375 cells were grown in confocal dishes for 24 h following the same procedure and under similar conditions described earlier. After 24 h, the grown cells were washed once with PBS and then treated with **N@PEGCD** (250 μg mL^{-1}) for 4 h. To capture the cell images using a confocal microscope, the cells were prepared by first washing with PBS twice and then adding 2 mL of fresh DMEM media. The live-cell images were captured using blue and green laser sources.

5.4.7 Hoechst Staining

The morphological changes in the cells after treatment with **N@PEGCDs** and **5-FU-N@PEGCDs** were evaluated using Hoechst stain 33258. The A375 cells were grown in 6 well plate for 24 h. After 24 h, the cells were treated with the corresponding IC_{50} concentration of 5-FU as a positive control, **N@PEGCDs**, and **5-FU-N@PEGCDs**. The cells without any treatment were taken as a negative control. After 24 h of treatment, the cells were washed with PBS and stained using Hoechst stain (5μg mL^{-1}) for 30 min. The images were captured using a blue laser of a confocal microscope.

5.4.8 In-vitro scratch assay.

To access the effect of **N@PEGCDs** and **5-FU-N@PEGCDs** treatment on cell migration, the A375 cells were grown in 6 well plate until they achieved 100 % confluency. These fully confluent wells were wounded using a 200 μl pipet tip. The debris was removed by washing, and fresh media was added to all the wells containing IC_{50} concentration of **N@PEGCDs**, **5-FU-N@PEGCDs**, and 5-FU. The wounded region was

photographed using an inverted microscope at the interval of 0 h, 12 h, 24 h, and 48 h. To obtain the picture of the same point every time, the area was marked on the outer bottom of the dish.

5.4.9 DCFDA assay for ROS generation

2',7' –dichlorofluorescein diacetate (DCFDA) assay was performed to check ROS generation. The cells take up DCFDA, which gets oxidized by cellular reactive oxygen species (ROS) to generate fluorescent 2', 7' –dichlorofluorescein (DCF) with emission maxima 529 nm. The cells were grown in confocal dishes following the procedure described earlier. After 24 h, the cells were treated with DCFDA (10 μM in DMSO) for 30 min, followed by washing with PBS. A confocal microscope captured images at excitation of 488 nm, and emission signals were collected in the range of 490-560 nm.

5.4.10 Western Blotting

A375 and HEK2 (10^6) cells were seeded in six-well or 60 mm tissue culture plates. Cells were treated with IC_{50} (Concentration) **N@PEGCDs** and **5FU-N@PEGCDs** for 24 h. Then, cells were harvested, and protein samples were prepared by cell lysis using 80 to 100 μL of lysis buffer (1 M Tris, 2 M NaCl, 0.1 M EDTA, 100 mM DTT, 1% Triton X 100, Na3VO4·2H2O, 10% glycerol and PMSF) supplemented with a protease inhibitor cocktail. Proteins were electrophoresed in 10% SDS-PAGE, transferred to a PVDF membrane, and then membranes were incubated with primary rabbit anti-PARP and anti-BCL-xL IgG antibodies (dilution 1: 3000) overnight at 4 °C and followed by secondary goat anti-rabbit antibodies (1: 5000) for 2 h at room temperature. All the primary and secondary antibodies were procured from cell-signaling technologies (CST), Massachusetts, US. The membrane was developed using chemiluminescent solvents in the Vilber Fusion SOLO S Gel Doc system. The relative band densities were quantified relative to respective loading controls using the ImageJ software (National Institutes of Health, Bethesda, MD, USA).

5.5. References

[1] Jaleel, J.A., Pramod, K. (2018), Artful and multifaceted applications of carbon dot in biomedicine, J. Controlled Release, 269, 302–321 (DOI:10.1016/j.jconrel.2017.11.027)

[2] Guo, Y., Shen, M., Shi, X. (2021), Construction of Poly(amidoamine) Dendrimer/Carbon Dot Nanohybrids for Biomedical Applications, Macromol. Biosci., 21, 2100007 (DOI:10.1002/mabi.202100007)

[3] Yang, J., Zhang, X., Ma, Y.-H., Gao, G., Chen, X., Jia, H.-R., Li, Y.-H., Chen, Z., Wu, F.-G. (2016), Carbon Dot-Based Platform for Simultaneous Bacterial Distinguishment and Antibacterial Applications, ACS Appl. Mater. Interfaces, 8, 32170–32181 (DOI:10.1021/acsami.6b10398)

[4] Li, H., Yan, X., Qiao, S., Lu, G., Su, X. (2018), Yellow-Emissive Carbon Dot-Based Optical Sensing Platforms: Cell Imaging and Analytical Applications for Biocatalytic Reactions, ACS Appl. Mater. Interfaces, 10, 7737–7744 (DOI:10.1021/acsami.7b17619)

[5] Kaur, N., Tiwari, P., Mate, N., Sharma, V., Mobin, S.M. (2022), Photoactivatable carbon dots as a label-free fluorescent probe for picric acid detection and light-induced bacterial inactivation, J. Photochem. Photobiol. B, 229, 112412 (DOI:10.1016/j.jphotobiol.2022.112412)

[6] Hassan, M., Gomes, V.G., Dehghani, A., Ardekani, S.M. (2018), Engineering carbon quantum dots for photomediated theranostics, Nano Res., 11, 1–41 (DOI:10.1007/s12274-017-1616-1

[7] Du, J., Xu, N., Fan, J., Sun, W., Peng, X. (2019), Carbon Dots for In Vivo Bioimaging and Theranostics, Small, 15, 1805087 (DOI:10.1002/smll.201805087)

[8] Lin, J.-S., Tsai, Y.-W., Dehvari, K., Huang, C.-C., Chang, J.-Y. (2019). A carbon dot based theranostic platform for dual-modal imaging and free radical scavenging, Nanoscale, 11, 20917–20931 (DOI:10.1039/C9NR05746C)

[9] Xu, X., Ray, R., Gu, Y., Ploehn, H.J., Gearheart, L., Raker, K., Scrivens, W.A. (2004), Electrophoretic Analysis and Purification of Fluorescent Single-Walled Carbon Nanotube Fragments, J. Am. Chem. Soc., 126, 12736–12737 (DOI:10.1021/ja040082h)

[10] Tiwari, P., Sharma, V., Kaur, N., Ahmad, K., Mobin, S.M. (2019), Graphene Production: New Insights into Cannabis sativa Engineered Carbon Dots Based Exfoliating Agent for Facile Production of Graphene, ACS Sustain. Chem. Eng., 7, 11500–11510 (DOI:10.1021/acssuschemeng.9b01353)

[11] Sharma, V., Kaur, N., Tiwari, P., Saini, A.K., Mobin, S.M. (2018), Multifunctional fluorescent “Off-On-Off” nanosensor for Au^{3+} and S^{2-} employing N-S co-doped carbon–dots, Carbon, 139, 393–403 (DOI:10.1016/j.carbon.2018.07.004)

[12] Sharma, V., Kaur, N., Tiwari, P., Mobin, S.M. (2018), Full color emitting fluorescent carbon material as reversible pH sensor with multicolor live cell imaging, J. Photochem. Photobiol. B, 182, 137–145 (DOI:10.1016/j.jphotobiol.2018.04.006)

[13] Sharma, V., Tiwari, P., Kaur, N., Mobin, S.M. (2021), Optical nanosensors based on fluorescent carbon dots for the detection of water contaminants: a review, Environ. Chem. Lett., 19, 3229–3241 (DOI:10.1007/s10311-021-01241-8)

[14] Tiwari, P., Kaur, N., Sharma, V., Kang, H., Uddin, J., Mobin, S.M. (2019), Cannabis sativa-derived carbon dots co-doped with N–S: highly efficient nanosensors for temperature and vitamin B12, New J. Chem., 43, 17058–17068 (DOI:10.1039/C9NJ04061G)

[15] Hola, K., Zhang, Y., Wang, Y., Giannelis, E.P., Zboril, R., Rogach, A.L. (2014), Carbon dots—Emerging light emitters for bioimaging, cancer therapy and optoelectronics, Nano Today, 9, 590–603 (DOI:10.1016/j.nantod.2014.09.004)

[16] Hu, C., Li, M., Qiu, J., Sun, Y.-P. (2019), Design and fabrication of carbon dots for energy conversion and storage, Chem. Soc. Rev., 48, 2315–2337 (DOI:10.1039/C8CS00750K)

[17] World Health Organization (2018), World health statistics 2018: monitoring health for the SDGs, sustainable development goals, World Health Organization, Geneva

[18] Zimmermann, S., Dziadziuszko, R., Peters, S. (2014), Indications and limitations of chemotherapy and targeted agents in non-small cell lung cancer brain metastases, Cancer Treat. Rev., 40, 716–722 (DOI:10.1016/j.ctrv.2014.03.005)

[19] Liu, Z., Chen, K., Davis, C., Sherlock, S., Cao, Q., Chen, X., Dai, H. (2008), Drug Delivery with Carbon Nanotubes for In vivo Cancer Treatment, Cancer Res., 68, 6652–6660 (DOI:10.1158/0008-5472.CAN-08-1468)

[20] Wang, Q., Huang, X., Long, Y., Wang, X., Zhang, H., Zhu, R., Liang, L., Teng, P., Zheng, H. (2013), Hollow luminescent carbon dots for drug delivery, Carbon, 59, 192–199 (DOI:10.1016/j.carbon.2013.03.009)

[21] Li, H., Yan, X., Kong, D., Jin, R., Sun, C., Du, D., Lin, Y., Lu, G. (2020), Recent advances in carbon dots for bioimaging applications, Nanoscale Horiz., 5, 218–234 (DOI:10.1039/C9NH00476A)

[22] Tiwari, P., Kaur, N., Sharma, V., Mobin, S.M. (2020). A spectroscopic investigation of Carbon dots and its reduced state towards fluorescence performance, J. Photochem. Photobiol. Chem., 403, 112847 (DOI:10.1016/j.jphotochem.2020.112847)

[23] Yang, L., Jiang, W., Qiu, L., Jiang, X., Zuo, D., Wang, D., Yang, L. (2015), One pot synthesis of highly luminescent polyethylene glycol anchored carbon dots functionalized with a

nuclear localization signal peptide for cell nucleus imaging, Nanoscale, 7, 6104–6113 (DOI:10.1039/C5NR01080B)

[24] Li, F., Liu, C., Yang, J., Wang, Z., Liu, W., Tian, F. (2013), Mg/N double doping strategy to fabricate extremely high luminescent carbon dots for bioimaging, RSC Adv., 4, 3201–3205 (DOI:10.1039/C3RA43826K)

[25] Kaur, N., Sharma, V., Tiwari, P., Saini, A.K., Mobin, S.M. (2019), "Vigna radiata" based green C-dots: Photo-triggered theranostics, fluorescent sensor for extracellular and intracellular iron (III) and multicolor live cell imaging probe, Sens. Actuators B Chem., 291, 275–286 (DOI:10.1016/j.snb.2019.04.039)

[26] Huang, J.J., Zhong, Z.F., Rong, M.Z., Zhou, X., Chen, X.D., Zhang, M.Q. (2014), An easy approach of preparing strongly luminescent carbon dots and their polymer based composites for enhancing solar cell efficiency, Carbon, 70, 190–198 (DOI:10.1016/j.carbon.2013.12.092)

[27] Lin, F., Li, C., Chen, Z. (2018), Exopolysaccharide-Derived Carbon Dots for Microbial Viability Assessment, Front. Microbiol., 9,

[28] Li, L., Liao, L., Ding, Y., Zeng, H. (2017), Dithizone-etched CdTe nanoparticles-based fluorescence sensor for the off–on detection of cadmium ion in aqueous media, RSC Adv., 7, 10361–10368 (DOI:10.1039/C6RA24971J)

[29] Guo, Q., Luo, H., Zhang, J., Ruan, Q., Periasamy, A.P., Fang, Y., Xie, Z., Li, X., Wang, X., Tang, J., Briscoe, J., Titirici, M., Belen Jorge, A. (2020), The role of carbon dots – derived underlayer in hematite photoanodes, Nanoscale, 12, 20220–20229 (DOI:10.1039/D0NR06139E)

[30] Nie, Y., Guo, J., Deng, Y., Weng, W. (2020), Synthesis and application of fluorescent N,S co-doped carbon dots based on on-off-on quenching mode for the collaboration detection of iron ions and ascorbic acid, J. Saudi Chem. Soc., 24, 865–873 (DOI:10.1016/j.jscs.2020.09.003)

[31] Wang, Y., Su, Q., Yang, X. (2018), Exploration of the synthesis of three types of multicolor carbon dot originating from isomers, Chem. Commun., 54, 11312–11315 (DOI:10.1039/C8CC06116E)

[32] Wang, J., Wei, J., Su, S., Qiu, J. (2015), Novel fluorescence resonance energy transfer optical sensors for vitamin B 12 detection using thermally reduced carbon dots, New J. Chem., 39, 501–507 (DOI:10.1039/C4NJ00538D)

[33] Dey, D., Bhattacharya, T., Majumdar, B., Mandani, S., Sharma, B., K. Sarma, T. (2013), Carbon dot reduced palladium nanoparticles as active catalysts for carbon–carbon bond formation, Dalton Trans., 42, 13821–13825 (DOI:10.1039/C3DT51234G)

[34] Wu, P., Li, W., Wu, Q., Liu, Y., Liu, S. (2017), Hydrothermal synthesis of nitrogen-doped carbon quantum dots from microcrystalline cellulose for the detection of Fe^{3+} ions in an acidic environment, RSC Adv., 7, 44144–44153 (DOI:10.1039/C7RA08400E)
[35] Ding, Y., Zhang, F., Xu, J., Miao, Y., Yang, Y., Liu, X., Xu, B. (2017), Synthesis of short-chain passivated carbon quantum dots as the light emitting layer towards electroluminescence, RSC Adv., 7, 28754–28762 (DOI:10.1039/C7RA02421E)
[36] Pan, J., Sheng, Y., Zhang, J., Wei, J., Huang, P., Zhang, X., Feng, B. (2014), Preparation of carbon quantum dots/ TiO2 nanotubes composites and their visible light catalytic applications, J. Mater. Chem. A, 2, 18082–18086 (DOI:10.1039/C4TA03528C)
[37] Konar, S., Kumar, B.N.P., Mahto, M.Kr., Samanta, D., Shaik, M.A.S., Shaw, M., Mandal, M., Pathak, A. (2019), N-doped carbon dot as fluorescent probe for detection of cysteamine and multicolor cell imaging, Sens. Actuators B Chem., 286, 77–85 (DOI:10.1016/j.snb.2019.01.117)
[38] Cutrim, E.S.M., Vale, A.A.M., Manzani, D., Barud, H.S., Rodríguez-Castellón, E., Santos, A.P.S.A., Alcântara, A.C.S. (2021), Preparation, characterization and in vitro anticancer performance of nanoconjugate based on carbon quantum dots and 5-Fluorouracil, Mater. Sci. Eng. C, 120, 111781 (DOI:10.1016/j.msec.2020.111781)
[39] Ding, H., Ji, Y., Wei, J.-S., Gao, Q.-Y., Zhou, Z.-Y., Xiong, H.-M. (2017), Facile synthesis of red-emitting carbon dots from pulp-free lemon juice for bioimaging, J. Mater. Chem. B, 5, 5272–5277 (DOI:10.1039/C7TB01130J)
[40] Liu, H., Zhao, X., Wang, F., Wang, Y., Guo, L., Mei, J., Tian, C., Yang, X., Zhao, D. (2017), High-Efficient Excitation-Independent Blue Luminescent Carbon Dots, Nanoscale Res. Lett., 12, 399 (DOI:10.1186/s11671-017-2137-2)
[41] Goddeti, K.C., Kim, S.M., Lee, Y.K., Kim, S.H., Park, J.Y. (2014), Chemical Doping of TiO2 with Nitrogen and Fluorine and Its Support Effect on Catalytic Activity of CO Oxidation, Catal. Lett., 144, 1411–1417 (DOI:10.1007/s10562-014-1276-7)
[42] Kong, D., Yan, F., Han, Z., Xu, J., Guo, X., Chen, L. (2016), Cobalt (ii) ions detection using carbon dots as an sensitive and selective fluorescent probe, RSC Adv., 6, 67481–67487 (DOI:10.1039/C6RA12986B)
[43] Li, C.-L., Huang, C.-C., Prakash Periasamy, A., Roy, P., Wu, W.-C., Hsu, C.-L., Chang, H.-T. (2015), Synthesis of photoluminescent carbon dots for the detection of cobalt ions, RSC Adv., 5, 2285–2291 (DOI:10.1039/C4RA11704B)
[44] Zhao, C., Li, X., Cheng, C., Yang, Y. (2019), Green and microwave-assisted synthesis of carbon dots and application for

visual detection of cobalt (II) ions and pH sensing, Microchem. J., 147, 183–190 (DOI: 10.1016/j.microc.2019.03.029)

[45] Zhang, H., Chen, Y., Liang, M., Xu, L., Qi, S., Chen, H., Chen, X. (2014), Solid-phase synthesis of highly fluorescent nitrogen-doped carbon dots for sensitive and selective probing ferric ions in living cells, Anal. Chem., 86, 9846–9852 (DOI:10.1021/ac502446m)

[46] Dong, Y., Cai, J., You, X., Chi, Y. (2015), Sensing applications of luminescent carbonbased dots, Analyst, 140, 7468–7486 (DOI:10.1039/C5AN01487E)

[47] Atchudan, R., Edison, T.N.J.I., Chakradhar, D., Perumal, S., Shim, J.-J., Lee, Y.R. (2017), Facile green synthesis of nitrogen-doped carbon dots using Chionanthus retusus fruit extract and investigation of their suitability for metal ion sensing and biological applications, Sens. Actuators B Chem., 246, 497–509 (DOI:10.1016/j.snb.2017.02.119)

[48] Zhang, N., Yin, Y., Xu, S.-J., Chen, W.-S. (2008), 5-Fluorouracil: Mechanisms of Resistance and Reversal Strategies, Molecules, 13, 1551–1569 (DOI:10.3390/molecules13081551)

[49] Chambers, A.F., Groom, A.C., MacDonald, I.C. (2002), Dissemination and growth of cancer cells in metastatic sites, Nat. Rev. Cancer., 2, 563–572 (DOI:10.1038/nrc865)

[50] Cory, S., Adams, J.M. (2002), The Bcl2 family: regulators of the cellular life-or-death switch, Nat. Rev. Cancer, 2, 647–656 (DOI:10.1038/nrc883)

[51] Herceg, Z., Wang, Z.Q. (2001), Functions of poly(ADP-ribose) polymerase (PARP) in DNA repair, genomic integrity and cell death, Mutat. Res., 477, 97–110 (DOI:10.1016/s0027-5107(01)00111-7)

CHAPTER 6

Conclusions and Future Outlook

The present thesis aims to develop carbon dots-based optical and biomedical applications systems. Different types of doped cots are produced via the hydrothermal method. The dopants of the carbon dots were chosen carefully to tune the optical properties of carbon dots for their application in different areas such as antibacterial, optical sensor, theranostics, and bioimaging.

The carbon dots have various advantages over semiconductor quantum dots and other organic fluorophores like GFP in terms of high biocompatibility, resistance to photobleaching, facile synthesis, and remarkable optical properties for their use in bioimaging and optical sensing. The natural resources are full of carbon which has been exploited widely for the green synthesis of carbon-based nanomaterials. However, the purity and the low quantum yield of such green carbon dots are always a concern. In this regard, green carbon dots were derived from "*Vigna radiata*" sprouts whose quantum yield was optimized precisely by varying the synthesis conditions and the concentration of dopant.

Considering the change in properties of carbon dots after doping, gold, silver, and nitrogen-doped carbon dots were developed to be used for picric acid sensing and photo-mediated antibacterial activities. The rise in multi-drug resistant bacteria makes it inevitable to explore a new class of antibiotics, and carbon dots can undoubtedly be the way forward. However, the killing of pathogenic bacteria with the help of carbon dots needs more attention to be paid to.

The excessive use of antibiotics due to ever-increasing bacterial infections is a matter of concern globally. Tetracycline is a class of antibiotics that could be exploited at maximum for various purposes from the medical industry to horticulture. Its detection and degradation are of

utmost importance in human safety and environmental remediation. The carbon dot which can efficiently sense doxycycline, members of the tetracycline family have been synthesized. The in-situ composites of this carbon dot were utilized for doxycycline degradation.

The current work has also studied the use of carbon dots as a drug carrier. The mechanism behind enhanced drug tolerance in a normal cell, when conjugated with carbon dots, could be explored in detail, which can open the door to a new area of research altogether.

Since the carbon dots synthesized using green sources show better cytocompatibility, the major problem is the heterogenicity of the obtained carbon dots. The complex composition and difference in composition of green precursors when environmental conditions vary could be the main reason behind it. To gain homogeneity, the purification and separation routes should be investigated thoroughly. Moreover, the discovery of more naturally occurring carbon dots would prove helpful to get insights into their role, application, and advantages in our daily life.

The use of carbon dots for various metal ion sensing has been studied extensively in recent years. Their use in real-life samples was also explored with great interest. However, only a few reports are associated with the sensing response of carbon dots towards toxic metals like Cd^{2+}, Po^{3+}, As^{3+}, and Mn^{2+}. More efforts are needed to utilize carbon dots for sensing these metal ions. The fabrication of sensing devices for real-time use should also be looked into.

The carbon dots have been used in theranostics due to their fantastic optical properties and excellent biocompatibility. The surface state and functionality of carbon dots help design a fluorescent probe for diagnosis; however, the formation of ROS upon light irradiation makes them eligible for cancer and antibacterial therapy. More fine regulation of nonmedicinal carbon dots' properties leads to their use in various applications. The deep tissue penetration ability and less light-associated toxicity of NIR light

could be used as a clue to develop NIR responsive carbon dots for theranostics.

The ingrained features of carbon dots could be carefully monitored, explored, and exploited to prepare multimodal carbon dots. The single type of carbon dot could act as a complete package for treating a tumor by working as a PDT agent, PTT agent, drug carrier, and Gene carrier. The more stimulus-responsive carbon dots are needed to effectively combat diseases of the new era with lesser side effects. The microenvironment of the tumor site could be used as the required stimuli like pH, temperature, hypoxia, etc.

The cellular organelle targeting by fluorophore is used for cellular imaging to detect various diseases at an early stage. Carbon dots have shown the potential to target specific cellular organelles. The properties of carbon dots, which make them a particular organelle targeting agent, should be explored to achieve new milestones in this field. The progressive attitude of scientists towards carbon dots will soon make it a shining star in early diagnostics and treatment.

ANNEXURE 1

Tables A1

Table A1. Permissions for re-producing the materials.

Figure 1.1	Schematic representation of top-down and bottom-up methods of carbon dot preparation	Reproduced from Ref. [5]: Chapter 1, with permission from the Royal Society of Chemistry.
Figure 1.2	Schematic synthesis of c-dots. The microwave pyrolysis of citric acid and urea results in c-dot synthesis. The dialysis helps in cutting off different molecular weight fragments. A closed and an open vessel condition results in a blue carbon dot (bCD) and a green carbon dot (gCD).	Reproduced from Ref. [10]: Chapter 1, with permission from the Royal Society of Chemistry
Figure 1.3	(a) Hydrothermal preparation of c-dots using *Actinidia deliciosa* (b) Preparation of hydrophilic nitrogen-doped c-dots from biowaste using dwarf banana peel	Reproduced from Ref. [14,15]: Chapter 1, with permission from Elsevier.
Figure 1.4	Illustration of some green sources used to develop green c-dots.	Reproduced from Ref. [43]: Chapter 1, with permission from Springer.
Figure 1.5	The optical transitions in c-dots. (a) Fluorescence origination from the degree of surface oxidation (b) Structure and electronic transition diagram of c-dots.	Reproduced from Ref. [45]: Chapter 1, with permission from the Royal Society of Chemistry
Figure 1.6	Use of c-dots as a ratiometric fluorescent sensor in food safety.	Reproduced from Ref. [59]: Chapter 1, with permission from Taylor & Francis.
Figure 1.7	Biomedical applications of c-dots.	Reproduced from Ref [60]: Chapter 1, with permission from Wiley.

Figure 1.8	Mechanisms for antibacterial activity of c-dots.	Reproduced from Ref. [62]: Chapter 1, with permission from the Ivyspring International Publisher.
Figure 1.9	Multicolor imaging of A549 (A) HeLa cells (B) Microtubule imaging (C) Mitochondria targeting ability of c-dots (D).	Reproduced from Ref. [82]: Chapter 1, with permission from Elsevier.
Figure 1.10	Various ways of killing tumor cells via PDT.	Reproduced from Ref. [84]: Chapter 1, with permission from the Frontiers.
Figure 1.11	Use of c-dots as a photosensitizer in PDT.	Reproduced from Ref. [88,89]: Chapter 1, with permission from Wiley and Elsevier.
Figure 1.12	Doxorubicin delivery using folic acid functionalized c-dots.	Reproduced from Ref. [90]: Chapter 1, with permission from Wiley.
Figure 1.13	Targeted delivery of doxorubicin using c-dots nanohybrid with silica nanoparticles.	Reproduced from Ref. [91]: Chapter 1, with permission from Springer.